

International Advanced Researches and Engineering Journal

e-ISSN
2618-575X



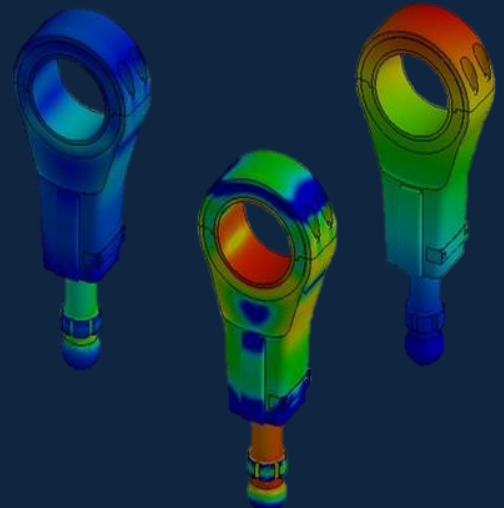
$$F=ma$$

$$E=mc^2$$

$$\int \frac{dy}{dx} dt$$

Volume	Issue
05	03

December, 2021





e-ISSN: 2618-575X

Available online at www.dergipark.org.tr/en

INTERNATIONAL ADVANCED RESEARCHES
and
ENGINEERING JOURNAL

Journal homepage: www.dergipark.org.tr/en/pub/iarej

International
Open Access



Volume 05
Issue 03

December, 2021

International Advanced Researches and Engineering Journal (IAREJ) is a double-blind peer-reviewed and publicly available online journal that has Editorial Board (<https://dergipark.org.tr/en/pub/iarej/board>). The editor in chief of IAREJ welcomes the submissions that cover theoretical and/or applied researches on **Engineering** and related science with Engineering. The publication language of the Journal is **English**. **Writing Rules** are given in Author Guidelines (<https://dergipark.org.tr/en/pub/iarej/writing-rules>). IAREJ publishes **original papers** that are research papers and technical review papers.

IAREJ publication, which is **open access**, is **free of charge**. There is no article submission and processing charges (APCs).

IAREJ is indexed & abstracted in:

Crossref (Doi beginning: 10.35860/iarej.xxxxxx)
Directory of Open Access Scholarly Researches (ROAD)
Directory of Research Journals Indexing (DRJI)
EBSCO
Google Scholar
Index Copernicus (ICI Journal Master List)
J-Gate
TUBITAK ULAKBIM TR Dizin (TR index)
WorldCAT

Authors are responsible from the copyrights of the figures and the contents of the manuscripts, accuracy of the references, quotations and proposed ideas and the Publication Ethics (<https://dergipark.org.tr/en/pub/iarej/page/4240>).

International Advanced Researches and Engineering Journal (IAREJ) allows the author(s) to hold the copyright of own articles.

©

IAREJ

15 December 2021



This is an open access issue under the CC BY-NC license (<http://creativecommons.org/licenses/by-nc/4.0/>).



e-ISSN: 2618-575X

Available online at www.dergipark.org.tr/en

INTERNATIONAL ADVANCED RESEARCHES
and
ENGINEERING JOURNAL

Journal homepage: www.dergipark.org.tr/en/pub/iarej

International
Open Access



Volume 05
Issue 03

December, 2021

Table of Contents

Research Articles	Pages
1. An automated Covid-19 respiratory sound classification method based on novel local symmetric Euclidean distance pattern and ReliefF iterative MRMR feature selector <i>Türker TUNCER, Emrah AYDEMİR, Fatih ÖZYURT, Sengul DOGAN, Samir Brahim BELHAOUARI, Erhan AKBAL</i>	334-343
2. Medical images fusion using two-stage combined model DWT and DCT <i>Ehsan AMİRİ, Mina RAHMANIAN, Saeed AMİRİ, Hadi YAZDANI PRAEE</i>	344-351
3. LUPU-Net: a new improvement proposal for encoder-decoder architecture <i>Saadet Aytaç ARPACI, Songül VARLI</i>	352-361
4. Design and implementation of FPGA-based arrhythmic ECG signals using VHDL for biomedical calibration applications <i>Fatih KARATAŞ İsmail KOYUNCU, Murat ALÇIN, Murat TUNA</i>	362-371
5. Detection of circuit components on hand-drawn circuit images by using faster R-CNN method <i>Mihriban GÜNAY, Murat KÖSEOĞLU</i>	372-378
6. Empirical and theoretical analysis of a modified isochronal test in a caspian region gas reservoir <i>Abdullah İŞÇAN</i>	379-386
7. Investigation of the availability of a new point load test device in characterization of rocks <i>Deniz AKBAY, Raşit ALTINDAĞ</i>	387-397
8. Prediction of cutting temperature in carbide cutting tool using finite element method <i>Mercy OZAKPOLOR, Cyril ALIYEGBENOMA, Dickson David OLODU</i>	398-404
9. Determination of mechanical performance of glass fiber reinforced and elastomer filled polyamide 6 composites <i>Hüseyin ÜNAL, Kemal ERMİŞ</i>	405-411
10. The production of open cell Ni-foam using KBr as spacer and oxidation shield via powder metallurgy technique <i>Mustafa Güven GÖK</i>	412-418
11. Knockdown factors for cylindrical shells caused by torsional Mode-I type geometric imperfections under axial compression <i>İbrahim KOCABAŞ, Haluk YILMAZ</i>	419-425
12. Harmonic response analysis of elliptically curved thin plates <i>Oğuzhan DAŞ</i>	426-434

13. Explicit dynamics finite element analyses of asymmetrical roll bending process <i>Tuncay KAMAŞ, Müfit SARIKAYA</i>	435-443
14. Analysis of Spatio-temporal rainfall trends and rainfall variability in Botswana between 1958 and 2019 <i>Hüseyin GÖKÇEKUŞ, Youssef KASSEM, Lorato Precious MPHINYANE</i>	444-453
15. Investigation of proper material selection for rainwater harvesting in squares having higher urban heat island effect potential: KBU Social Life Center example <i>Sibel TEMİZKAN, Merve TUNA KAYILI</i>	454-463
16. Investigating the construction parameters of deep mixing columns in silty soils <i>Yavuz YENGİNAR, Ahmed A.M.M. MOBARK, Murat OLGUN</i>	464-474
17. Dimensional optimization of two-phase flow boiling in microchannel heat sinks <i>Rahim JAFARI</i>	475-483
18. Structural analysis of embedded hollow tubes on straight and curved platforms under thermal loads <i>Mustafa Murat YAVUZ</i>	484-490



e-ISSN: 2618-575X

INTERNATIONAL ADVANCED RESEARCHES
and
ENGINEERING JOURNAL

Journal homepage: www.dergipark.org.tr/en/pub/iarejInternational
Open Access Volume 05
Issue 03

December, 2021

Research Article

An automated Covid-19 respiratory sound classification method based on novel local symmetric Euclidean distance pattern and ReliefF iterative MRMR feature selector

Turker Tuncer^a , **Emrah Aydemir**^{b,*} , **Fatih Ozyurt**^a , **Sengul Dogan**^a ,
Samir Brahim Belhaouari^c  and **Erhan Akbal**^a 

^a Firat University, Technology Faculty, Department of Digital Forensics Engineering, Elazig, 23100, Turkey^b Sakarya University, Management Faculty, Department of Management Information Systems, Sakarya, 54400, Turkey^c Hamad Bin Khalifa University, College of Science and Engineering, ICT Division, 34110, Doha, Qatar

ARTICLE INFO

Article history:

Received 17 March 2021

Revised 23 August 2021

Accepted 20 September 2021

Keywords:

Covid-19

LSEDP

Lung Disease Detection

Respiratory Sounds

RFMRMR

ABSTRACT

Covid-19 is a new variety of coronavirus that affects millions of people around the world. This virus infected millions of people and hundreds of thousands of people have passed away. Due to the panic caused by Covid-19, recently several researchers have tried to understand and to propose a solution to Covid-19 problem. Especially, researches in machine learning (ML) have been proposed to detect Covid-19 by using X-ray images. In this study, 10 classes of respiratory sounds, including respiratory sounds diagnosed with Covid-19 disease, were collected and ML methods were used to tackle this problem. The proposed respiratory sound classification method has been proposed in this study from feature generation network through hybrid and iterative feature selection to classification phases. A novel multileveled feature generating network is presented by gathering multilevel one-dimensional wavelet transform and a novel local symmetric Euclidean distance pattern (LSEDP). An automated hybrid feature selection method is proposed using ReliefF and ReliefF Iterative Maximum Relevancy Minimum Redundancy (RIMMR) to select the optimal number of features. Four known classifiers were used to test the capability of our approach for lung disease detection in respiratory sounds. K nearest neighbors (kNN) method has achieved an accuracy of 91.02%.

1. Introduction

An outbreak occurred in China Wuhan towards the end of 2019. This epidemic, which is transmitted from person to person very quickly, threatens the whole world. This virus was grouped as 2019 new coronavirus (2019-nCoV) and was named Covid-19 [1, 2]. Covid-19 is a virus belonging to the coronavirus family [3]. Coronaviruses are divided into 4 groups: gamma coronavirus, delta coronavirus, alphacoronavirus, and beta coronavirus [4, 5]. Alpha and beta coronaviruses infect the respiratory and central nervous functions of mammals. Gamma and delta coronavirus tend to infect birds. Alpha and Beta coronaviruses have different symptoms, especially in humans. There are some viruses such as HCoV-229E, HCoV-HKU1, HCoV-OC43 with milder symptoms [6-8]. However, viruses such as SARS-

CoV and MERS-CoV can cause fatal infections [9, 10].

Covid-19 virus, which belongs to the beta coronavirus family, also causes deadly respiratory infection disease, pneumonia, and kidney failure [5, 11, 12]. The most common symptoms of Covid-19 can be presented as sore throat, cough, fever, and fatigue. Covid-19, which is transmitted to large masses by inhalation, is a newly encountered virus type, so our immune system does not know what to respond to this virus [13]. Every patient with low immunity and chronic illness could be more affected by this virus. This disease has an incubation period. Generally, the effects that start on the 2nd day can be carried until the 14th day and they vary from person to person [14, 15]. This newly encountered virus has been extensively studied in the literature to both minimize its effects and increase the

* Corresponding author. Tel.: +90 264 295 7251; Fax: +90 264 295 7251.

E-mail addresses: turkertuncer@firat.edu.tr (T. Tuncer), emrahaydemir@sakarya.edu.tr (E. Aydemir), fatihozyurt@firat.edu.tr (F. Ozyurt), sdogan@firat.edu.tr (S. Dogan), sbelhaouari@hbku.edu.qa (S.B. Belhaouari), erhanakbal@firat.edu.tr (E. Akbal)

ORCID: 0000-0002-1425-4664 (T. Tuncer), 0000-0002-8380-7891 (E. Aydemir), 0000-0002-8154-6691 (F. Ozyurt), 0000-0001-9677-5684 (S. Dogan), 0000-0003-2336-0490 (S.B. Belhaouari), 0000-0002-5257-7560 (E. Akbal)

DOI: 10.35860/iarej.898830

© 2021, The Author(s). This article is licensed under the CC BY-NC 4.0 International License (<https://creativecommons.org/licenses/by-nc/4.0/>).

recognition of the virus. Some of these studies are listed below.

Huang et al. [10] proposed a method to describe the respiratory sounds of Covid-19 patients. An electronic stethoscope was presented in the study. Separation of abnormal sounds and normal sounds was confirmed by the analysis of 6 doctors in the proposed method. Aykanat et al. [16] proposed a method for classifying respiratory sounds. In the proposed method, they studied the classification of sounds received from an electronic stethoscope. The main aim of the study is to measure and classify lung sounds through an easy-to-use and cost-effective electronic stethoscope. For this purpose, 1630 test subjects were used. Two machine learning techniques, convolutional neural network (CNN) and support vector machine (SVM) were used to evaluate and classify the obtained sounds. In the study, 86.0% accuracy rate was calculated. Son [17] proposed a method for classifying lung sounds. In the study, a dataset of 85 samples was collected to measure the performance of proposed feature selection methods. Support vector machine, k-nearest neighbor, naïve bayes have been implemented as classifier for this dataset. F-measure, recall, precision parameters were used to evaluate the performance of the study and were calculated as 94.1%. Bardou et al. [18] compared 3 different methods on the classification of lung sounds. The first proposed method was based on the Mel-frequency cepstral coefficients method. The local binary pattern was used in the second approach. In the third method convolutional neural network was used. A comparison of these methods is presented in the study. In the study, normal, coarse crackle, fine crackle, monophonic wheeze, polyphonic wheeze, squawk, and stridor classes were used. According to the obtained results, CNN has been observed to achieve more successful results than other methods. Naves et al. [19] developed a pattern recognition system. The main purpose of the study is to classify lung sounds. There are 5 different sounds in Dataset: normal, fine crackle, coarse crackle, polyphonic wheezes, and monophonic. The accuracy rate obtained in the study was calculated as 98.1%. Kandaswamy et al. [20] proposed a new method for classifying lung sound signals. Wavelet transform and artificial neural networks were used for the analysis of audio signals. In the study, 6 classes as normal, crackle, wheeze, stridor, rhonchus, and squawk were used. Ucar and Korkmaz [21] proposed a deep learning-based method using chest X-rays. Accuracy, completeness, specificity, correctness, Matthew correlation coefficient, and F1 score parameters were used for the evaluation of the study. In the study, 3 classes as Covid-19, Pneumonia, and normal were used. Obtained accuracy rates were calculated as 100.0% for Covid-19, 96.73% for Pneumonia and 98.04% for normal. Narin et al. [22] proposed a method for Covid-19 detection. Convolutional neural network is chosen in the proposed method. Chest X-Ray Images [23] dataset was used to

evaluate the study. As the evaluation parameter, accuracy was selected and the accuracy rate was calculated as 98.0 for two classes (normal and Covid-19). Sethy and Behera [24] proposed a study for the diagnosis of Covid-19. In the study, the convolutional neural network method was used and the Kaggle Repository [3] dataset was chosen. The accuracy rate for normal and Covid-19 classes was calculated as 95.38%.

In the literature, many methods, research and ML (Machine Learning) methods have been proposed since Covid-19 is one of the hottest academic research areas. In general, researchers aimed to classify Covid-19 disease using normal or pneumonia chest X-ray images. But the characteristic of the respiratory sound of Covid-19 disease led to the idea of proposing Covid-19 diagnostic methods based on sound classification. Therefore, lung respiratory sounds belonging to 10 different classes, including Covid-19 were collected within the scope of this study and a new method is presented to help in the diagnosis of Covid-19.

2. Dataset

In this section, a data set was created by collecting lung respiratory sounds. These sounds, normally prepared for educational purposes, are used by medical professionals and healthcare providers. These respiratory sounds were shared by Medcool [25], EMTprep [26], Fouad [27] and Alhadapediatrics [28] on YouTube. These records were shared between 27.06.2018 and 10.04.2020. 657 sound recordings of 10 classes. Each of the 657 sound recordings consists of 2 or 3-second sounds. Firstly, each audio file was converted to wav file format. Then, the sounds carefully listened for segmentation. It was carefully checked that the same sound did not continue repeatedly during the fragmentation of the sound files. Table 1 demonstrates the attributes of the collected dataset.

3. Method

In this study, a new stable feature generation network and an automated iterative-hybrid feature selector is proposed. The proposed feature generation network uses a novel textural feature extractor and it is called LSEDP (Local Symmetric Euclidean Distance Pattern). In the proposed LSEDP, Euclidean distance is utilized for binary feature generation. As it is known from the literature, multileveled feature extractors have high performance for classification because they extract low, medium and high levels feature.

Therefore, 9-leveled DWT (Discrete Wavelet Transform) [29, 30] is considered to create levels and LSEDP extracts 256 features from each level and raw sound signal. RFIMRMR selects the most meaningful and informative features from the extracted 2560 features. Four shallow classifiers are used for classification and these are bagged tree (BT) [31], linear discriminant (LD) [32], kNN [33, 34] and support vector machine (SVM) [35].

Table 1. Type and Number of the collected Respiratory Sounds

ID	Sound Type	Number of observations	Number of videos
1	Vesicular Respiratory Sounds	83	7
2	Fine Crackles (Rales)	57	7
3	Wheezing (expiratory)	70	8
4	Rhonchi	72	8
5	Stridor	63	7
6	Coarse Crackles (Rales)	82	7
7	Bronchovesicular Respiratory Sounds	61	8
8	Bronchial Respiratory Sounds	65	5
9	Sounds of Coronavirus (Covid-19)	29	1
10	Healthy Person Respiratory	75	10
Total		657	68

The technical contributions are given below:

- A total of 657 new sound sets belonging to 10 classes were gathered from YouTube. The collected data set is presented publicly available for open access.
- A novel distance-based feature extractor (LSEDP) is presented. LSEDP and multileveled DWT are used together for presenting a multileveled feature generation network. This network generates low, medium, and

high-level features. ReliefF [36] and MRM (Maximum Relevancy Minimum Redundancy) are parametrical feature selectors. To select the best number of features, users/researchers generally set parameters one more time. The proposed RFIMRMR both uses the effectiveness of these feature selectors together and select the best number of features automatically. To obtain results comprehensively, four classifiers are used in 5 categories.

- A novel sound based Covid-19 detection method is presented and this method is a highly accurate method. The proposed method classified 10 respiratory sounds. Therefore, this method is a general diagnosis method, and it is demonstrated that this method could be used in medical applications.

3.1 The Proposed Respiratory Sound Classification Method

This study proposed a novel hand-crafted multileveled feature generation network and automatic features selector. A novel respiratory sound classification method is proposed by using four shallow classifiers. The schematically overview of the proposed method is shown in Figure 1.

To overview the proposed LSEDP and RFIMRMR based respiratory sound classification method, the procedure of this method is shown in Figure 2.

As can be seen from Figure 1 and 2, this method has three fundamental phases and these are explained in subsections.

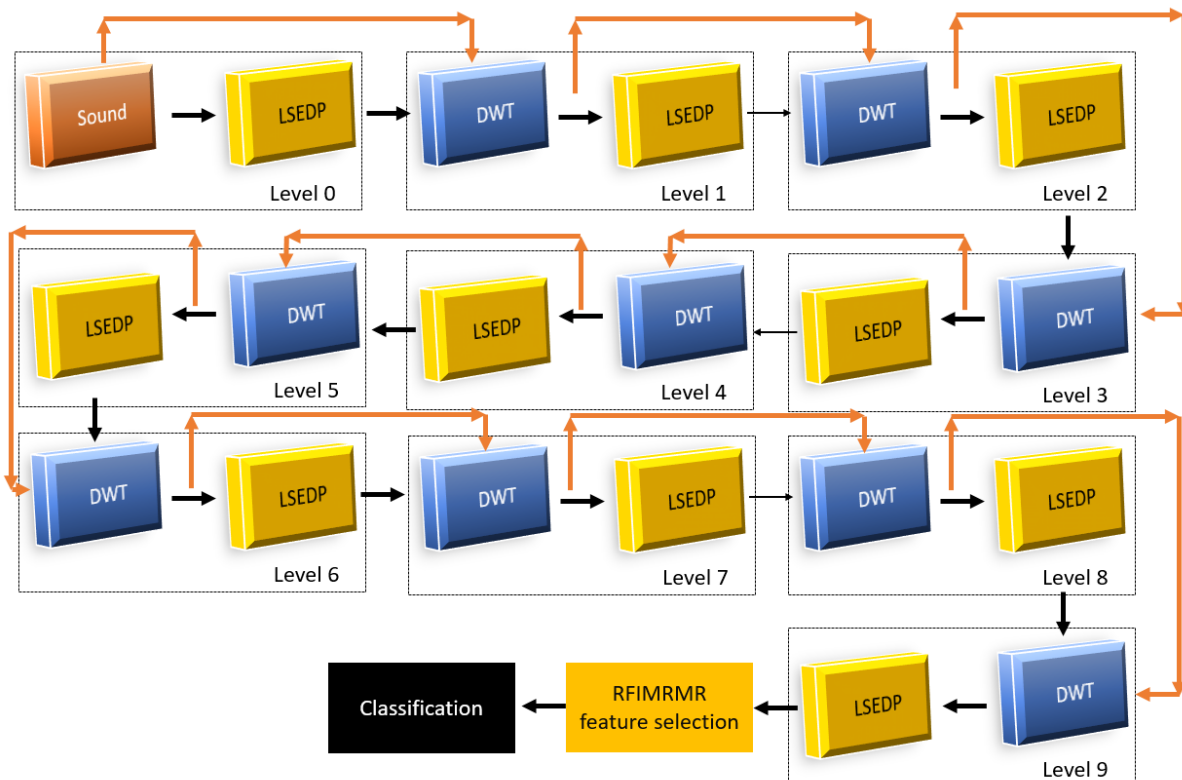


Figure 1. Graphical overview of the proposed method.

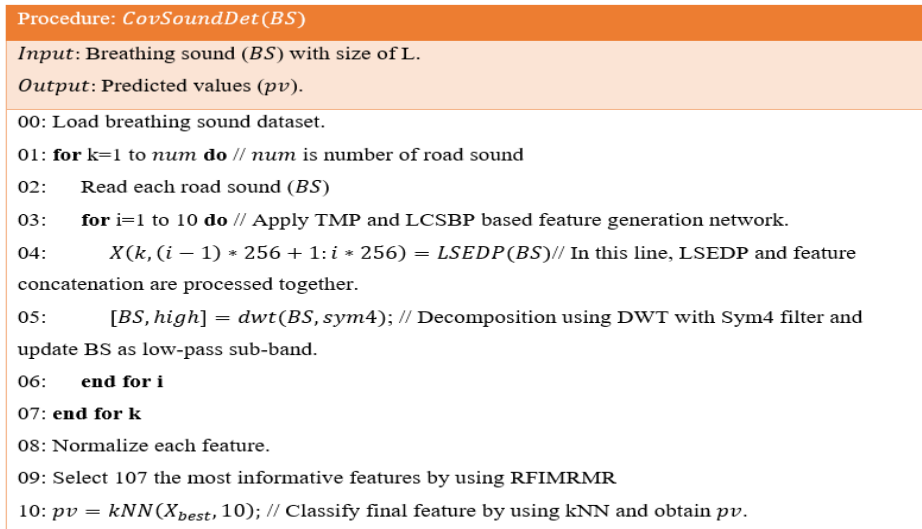


Figure 2. The procedure of the proposed respiratory sound classification based Covid-19 detection method.

3.2 Multileveled discrete wavelet transforms and local symmetric Euclidean distance pattern based feature generation network

The proposed multileveled DWT [29, 30] and LSEDP based feature generation network is aimed to extract meaningful and discriminating features from respiratory sounds. Textural feature extractors which are local binary pattern (LBP) [37] and ternary pattern (TP) [38, 39] are very effective for feature extraction on both images and signals. LBP and TP use signum and ternary functions to generate binary features and these bits are utilized to construct feature vector. Signum function is a basic comparison function and the ternary function is a parametrical feature generator and parameter setting process of ternary function is hard (ternary function uses threshold value and optimal threshold value finding is a non-polynomial problem). As it is known from the literature, there are many distance-based classifiers like kNNs. Also, some feature selectors use distance metrics, for instance, ReliefF [36] and Neighborhood Component Analysis (NCA) [40]. Therefore, a novel feature generator (LSEDP) is presented to use effectiveness of both textural feature extractors and distance metrics. DWT has been widely preferred transformations for signal processing. In this study, Symlet 4 (sym4) which is one of the filter of DWT decomposition method was used to construct level. Because sym4 filter is used for both decomposition and noise reduction. The proposed feature generator is inspired by deep networks. Thus, multileveled architecture is used. According to our experimental study, 9-levelled DWT was given the best result. That is why, 9-levelled DWT was applied to sound signals. The proposed LSEDP extracts 256 features from raw sound and low-pass filter coefficients of each level DWT. In total, 2560 features are generated by using the proposed LSEDP and DWT based generator as seen from Figure 1. Steps of this feature generator are listed in below.

Step 1: Load raw breathing sound (*BS*).

Step 2: Calculate 9 low-pass filter sub-bands of the *BS* by

applying 9-levelled DWT with sym4 filter.

$$[LowPass^1 HighPass^1] = DWT(BS, sym4) \quad (1)$$

$$[LowPass^i HighPass^i] = DWT(LowPass^{i-1}, sym4), i = \{2, 3, \dots, 9\} \quad (2)$$

where $LowPass^i$ and $HighPass^i$ are low-pass and high-pass filter coefficients of the i^{th} level DWT, $DWT(\dots)$ is one dimensional DWT function and *sym4* defines Symlet 4 filter.

Step 3: Generate features of the respiratory sound and low-pass filter of it by using the proposed LSEDP.

$$f^1 = LSEDP(BS) \quad (3)$$

$$f^{i+1} = LSEDP(LowPass^i), i = \{1, 2, \dots, 9\} \quad (4)$$

In Eqs. 3-4, $LSEDP(\dots)$ defines the used fundamental feature extractor. The LSEDP procedure is defined in sub-steps.

Step 3.1: Divide *BS* into 33 sized non-overlapping windows.

$$p = BS(j:j + 32), j = \{1, 2, \dots, L - 32\} \quad (5)$$

where *p* is window with size of 33 and *L* defines the length of the respiratory sound.

Step 3.2: Assign center as 17th value.

$$pc = p(17); \quad (6)$$

Step 3.3: Calculate distances of the symmetric values by using Euclidean distance, center value, and symmetric values.

$$d1(k) = \sqrt{(p(k) - pc)^2 + (p(33 - k) - pc)^2}, k \{1, 2, \dots, 8\} \quad (7)$$

$$d2(k) = \sqrt{(p(17 - k) - pc)^2 + (p(17 + k) - pc)^2}, \quad (8)$$

where $d1$ and $d2$ express first and second distances.

Step 3.4: Extract binary features (8-bit) by using first and second symmetric distances.

$$bit(k) = \begin{cases} 1, & d1(k) \geq d2(k) \\ 0, & d1(k) < d2(k) \end{cases} \quad (9)$$

Step 3.5: Calculate map signal value by using the extracted

8-bit binary features.

$$\text{map}(j) = \sum_{k=1}^8 \text{bit}(k) * 2^k \quad (10)$$

where map is constructed feature signal by using LSEDP.

Step 3.6: Calculate histogram of the map value to generate feature vector.

$$f(t) = 0, t = \{1, 2, \dots, 256\} \quad (11)$$

$$f(\text{map}(j) + 1) = f(\text{map}(j) + 1) + 1 \quad (12)$$

where f is the calculated feature vector by applying LSEDP.

Step 4: Concatenate the extracted features from each level.

$$\begin{aligned} \text{feat}(i * 256 + t) &= f^i(t), i = \{1, 2, \dots, 10\}, t \\ &= \{1, 2, \dots, 256\} \end{aligned} \quad (13)$$

where feat expresses final features with size of 2560. Eq. 13 denotes feature concatenation process mathematically.

3.3 ReliefF and iterative MRMR based feature selector

In this phase, a novel 2-leveled hybrid feature selector is presented. These feature selectors are ReliefF [36] and iterative MRMR. ReliefF is one of the distance-based feature selectors. It uses the Manhattan distance based fitness function and generates both positive and negative weights. Negative weighted features express redundant features. In the MRMR, sorted features indices are generated and it is called as idx . By using idx , features are selected parametrically. For automatic feature selection, a loss calculator should be used. As it is known from the literature, classifiers have been utilized as loss value generator. Four classifiers are used in this study, hence, variable tests are processed for feature generation.

Step 5: Generated ReliefF weights of the extracted 2560 features by using ReliefF weight generation function.

$$R^{\text{Weight}} = RF(\text{feat}, \text{target}) \quad (14)$$

where $RF(\dots)$ weight generation function of the ReliefF and R^{Weight} ReliefF weights with the length of 2560.

Step 6: Remove negative weighted features.

$$\begin{aligned} f^+(h) &= \text{feat}(i), \text{if } R^{\text{Weight}}(i) > 0, h \\ &= h + 1, h \leq i, i \\ &= \{1, 2, \dots, 2560\} \end{aligned} \quad (15)$$

where f^+ is selected positive weighted features.

Step 7: Calculate idx by using MRMR feature selection function and f^+ .

$$\text{idx} = \text{MRMR}(f^+, \text{target}) \quad (16)$$

Step 8: Select features iteratively by using idx and f^+ . To decrease the computational complexity of the proposed IMRMR, a range is defined. In this step, from 40 features to 500 features are used and loss values of these features are calculated. In this section, any classifier can be used as loss value generator.

$$\begin{aligned} X^{r-39}(i) &= f^+(\text{idx}(i)), i = \{1, 2, \dots, r\}, r \\ &= \{40, 41, \dots, 500\} \end{aligned} \quad (17)$$

$$\begin{aligned} \text{loss}^{r-39}(i) \\ = kNN(X^{r-39}, \text{target}, \text{Manhattan}, 10) \end{aligned} \quad (18)$$

where X^{r-39} is $(r - 39)^{\text{th}}$ selected features, loss^{r-39} expresses $(r - 39)^{\text{th}}$ loss value of the selected features. $kNN(\dots)$ denotes kNN classification method. In here, Manhattan distance based Fine kNN with 10-fold cross-validation was used.

Step 9: Find minimum loss value and select the best number of features by using the founded index, idx and f^+ .

$$[\text{minimum}, \text{index}] = \min(\text{loss}) \quad (19)$$

$$\text{index} = \text{index} + 39 \quad (20)$$

$$X_{\text{best}}(i) = f^+(\text{idx}(i)), i = \{1, 2, \dots, \text{index}\} \quad (21)$$

where X_{best} is the selected optimal features. The proposed RFIMRMR method selects 107 features for this study.

3.4 Classification

In the classification phase, MATLAB Classification Learner (MCL) is utilized to apply classifiers. In this study, four different classifiers are used, such as LD, SVM, kNN, and BT. 10-fold CV is selected for the used validation and test strategy. This is the last phase of the proposed method and is shown below as Step 10.

Step 10: Classify selected features (X_{best}) by using any of the used four shallow classifiers to illustrate discriminative attribute of the X_{best} .

The attributes of the used four classifiers are listed in Table 2.

4. Experiments

MATLAB2019a programming environment and MCL tool of this programming environment was used to implement the proposed LSEDP and RFIMRMR based Covid-19 sound classification method. Four shallow classifiers and source code of these classifiers were generated to obtain numerical results. Classification accuracy (CAC), unweighted average recall (UAR), unweighted average precision (UAP), F1-score ($F1$), and geometric mean (GM) were used to obtain numerical results [41-43]. These performance measurements have been widely preferred to evaluate the classification methods. To calculate these measurements, number of true positives (TP), true negatives (TN), false negatives (FN) and false positives (FP) should be used. Mathematical notations of these performance criteria are shown as below:

$$UAP = \frac{1}{N} \sum_{i=1}^N \frac{TP_i}{TP_i + FP_i}, i = \{1, 2, \dots, 10\} \quad (22)$$

$$UAR = \frac{1}{N} \sum_{i=1}^N \frac{TP_i}{TP_i + FN_i} \quad (23)$$

$$GM = \sqrt{\prod_{i=1}^N \frac{TP_i}{TP_i + FP_i}} \tag{24}$$

$$F1 = \frac{2 * UAP * UAR}{UAP + UAR} \tag{25}$$

$$CAC = \frac{TP_i + TN_i}{TP_i + TN_i + FP_i + FN_i} \tag{26}$$

In order to validate these results which are shown in Table 3, confusion matrices of the used four classifiers are shown in Figure 3 and 4.

5. Discussions

Covid-19 is a global problem and many people have suffered from this disease. Many treatment methods and vaccine studies have been proposed to solve Covid-19 problem. In this study, our aim is to detect Covid-19 with stethoscope sounds. Hence, 657 sounds with belonging to 10 classes were gathered from YouTube. A novel hand-crafted feature extraction network and an iterative 2-layer feature selector were proposed to classify these sounds automatically. A novel LSEDP feature extractor was presented to generate distinctive features from the collected sounds. The proposed LSEDP feature extraction network generated 2560 features. To select the most distinctive ones of the generated 2560 features, RFIMRMR feature selector was presented. The feature selection process of the RFIMRMR by using kNN was shown below.

Table 2. Attributes of the used four conventional classifiers

Classifier	Parameters and explanations
LD [32]	LD is a non-parametric classifier. In the MCL, we only can set covariance structure and it is set as Full.
SVM [35]	Kernel is 3 rd degree polynomial (Cubic) function, box constraint level (C) is 1 (it is default setting), multilevel method is selected as one-vs-all.
kNN [33, 34]	k is selected as 1 and distance metric is city block
BT [31]	BT is one of the ensemble methods in the MCL. Bag is selected as ensemble method, learner type is decision tree (DT), maximum number of split is 656 and 30 learners are used in this classifier.

Table 3. Measurements (%) of the proposed LSEDP and RFIMRMR based Covid-19 classification method

Classifier	UAP	UAR	GM	F1	CAC
LD	87.46	86.36	86.22	86.89	86.45
SVM	88.63	88.65	88.39	88.62	88.28
kNN	91.36	91.22	91.06	91.29	91.02
BT	88.61	87.18	86.91	87.82	87.21

Predicted Class

	1	2	3	4	5	6	7	8	9	10
1	71	2	1	0	0	2	0	7	0	0
2	1	47	0	1	0	6	0	0	2	0
3	2	1	59	1	0	5	0	2	0	0
4	0	3	2	61	0	2	2	2	0	0
5	0	0	2	1	59	0	0	0	1	0
6	4	7	0	1	0	68	0	2	0	0
7	1	3	0	7	0	1	49	0	0	0
8	3	0	3	0	0	2	0	56	1	0
9	0	0	1	1	0	0	0	2	25	0
10	0	0	1	1	0	0	0	0	0	73

LD

Predicted Class

	1	2	3	4	5	6	7	8	9	10
1	75	3	0	0	0	3	0	2	0	0
2	3	46	1	0	0	6	0	0	1	0
3	0	0	57	4	0	5	0	3	1	0
4	2	1	2	61	0	4	1	0	1	0
5	0	0	1	1	59	0	2	0	0	0
6	3	5	2	0	0	68	1	2	1	0
7	1	1	0	0	1	0	56	1	1	0
8	1	1	2	1	0	2	0	57	1	0
9	0	1	0	1	0	0	0	0	27	0
10	0	0	0	0	0	1	0	0	0	74

SVM

Figure 3. The confusion matrices of the LD and SVM

Predicted Class

	1	2	3	4	5	6	7	8	9	10
1	77	1	0	3	0	1	0	1	0	0
2	3	46	2	0	0	4	1	0	0	1
3	1	3	59	3	0	1	0	1	1	1
4	1	3	1	64	0	1	1	1	0	0
5	0	0	0	0	61	1	0	1	0	0
6	2	5	2	1	0	72	0	0	0	0
7	0	0	0	2	2	0	57	0	0	0
8	2	0	1	2	0	0	0	60	0	0
9	0	1	0	0	0	0	0	0	28	0
10	0	0	0	1	0	0	0	0	0	74

kNN

Predicted Class

	1	2	3	4	5	6	7	8	9	10
1	79	1	1	0	0	1	0	1	0	0
2	6	43	1	0	0	5	2	0	0	0
3	6	3	50	6	1	4	0	0	0	0
4	2	2	2	60	0	3	2	0	0	1
5	0	0	0	0	60	1	1	1	0	0
6	1	3	5	2	0	69	0	1	0	1
7	0	1	0	3	0	0	57	0	0	0
8	5	1	1	1	0	1	0	56	0	0
9	0	0	1	2	0	0	0	1	25	0
10	0	0	0	0	0	1	0	0	0	74

BT

Figure 4. The confusion matrices of the kNN and BT

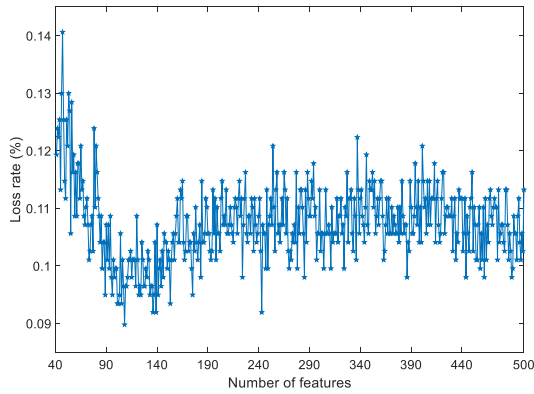


Figure 5. Graphical illustration of the proposed RFIMRMR feature selection process with a range of from 40 to 500 features

As can be seen from Figure 5, the best number of features can be selected automatically. The selected 107 features were forwarded to 4 conventional classifiers and 86.45%, 88.28%, 91.02, and 87.02% classification accuracies were calculated by using LD, SVM, kNN and BT classifiers respectively. To clear the demonstration of these results, confusion matrices of these classifiers were also shown. 9th class represents Covid-19 disease with belonging to 29 respiratory sounds. kNN classifiers reached 96.55% classification accuracy (there is only one misclassified observation) for Covid-19 detection. The kNN classifier is frequently preferred in different studies [44, 45]. LD,

SVM and BT classifiers also achieved 86.21%, 93.10% and 86.21% classification accuracies for Covid-19 detection respectively.

When the confusion matrix of the kNN method is examined, it can be seen that some diseases are almost never confused with other diseases, but only a small portion of some diseases can be confused. However, since the number of these mixed samples is very small, it can be said to be insignificant. Similar to the study here, 97% successful detections were obtained in the study for the detection of Covid-19 from the cough sound [46]. In another study, Covid-19 disease was tried to be detected from coughing, breathing and speaking sounds and a successful classification of 66.74% was obtained [47]. In another study, 80.7% AUC value was obtained from breathing and coughing sounds [48]. The studies here have shown that the success rate in this study is higher than its counterparts.

The main contributions of this paper are feature generation and selection methods. To show the distinctiveness of generated and selected 107 features, boxplot analysis was used. Boxplot has been widely used the statistical demonstration to illustrate separable attributes of the features. It shows quartiles (Q3-Q1 is shown as blue boxes), arithmetic average value (red line), upper and lower bounds, and abnormal values (red plus). Boxplots of the selected 107 features according to classes were shown in Figure 6 and 7.

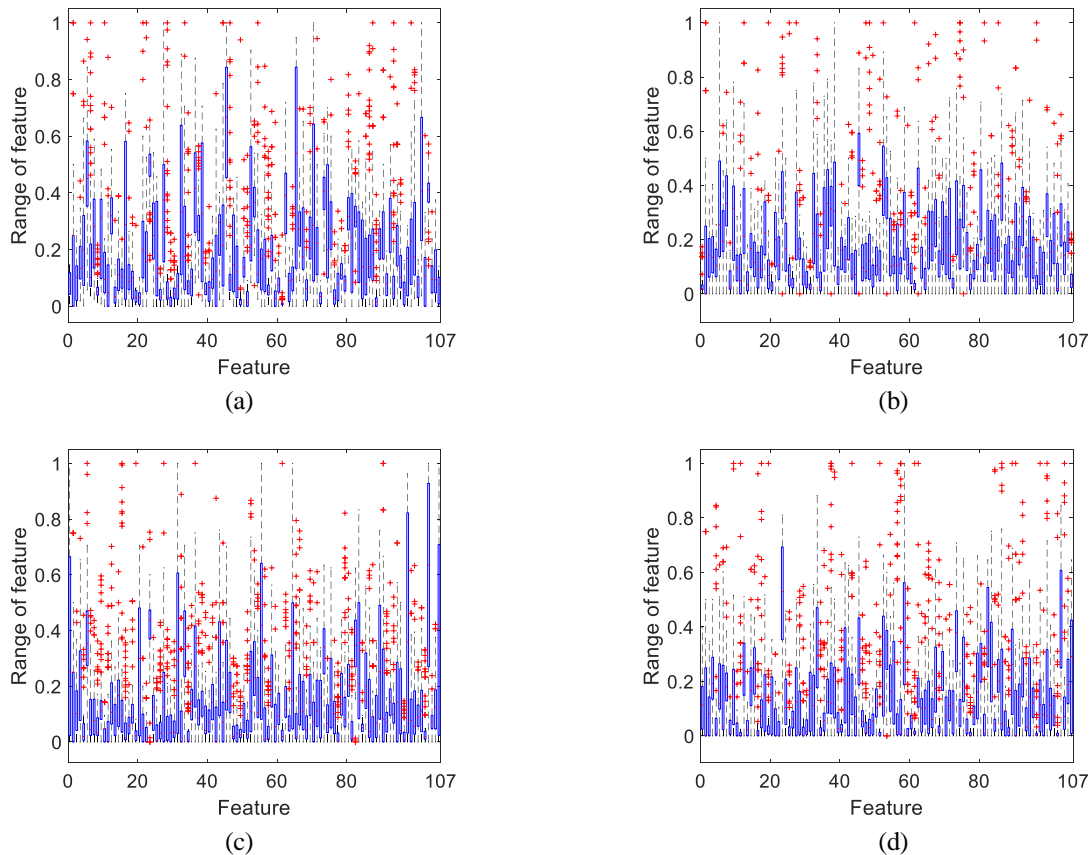


Figure 6. Boxplots of the extracted and selected 107 features by using the proposed LSEDP feature generation network and RFIMRMR feature selector. This figure shows statistical attributes of the (a) features of 1st class (b) features of 2nd class (c) features of 3rd class (d) features of 4th class

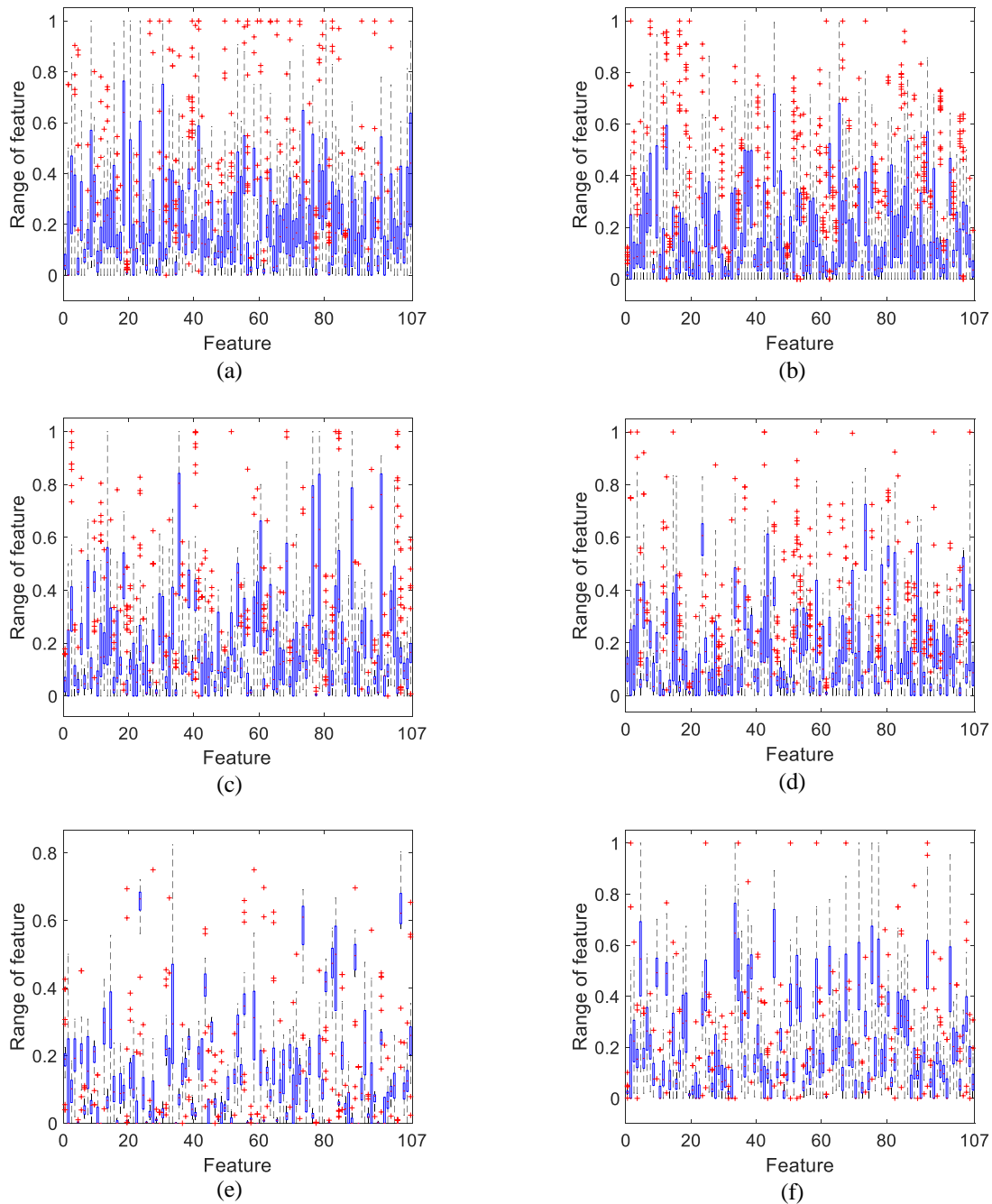


Figure 7. Boxplots of the extracted and selected 107 features by using the proposed LSEDP feature generation network and RFIMRMR feature selector. This figure shows statistical attributes of the (a) features of 5th class (b) features of 6th class (c) features of 7th class (d) features of 8th class (e) features of 9th class (f) features of 10th class

Figure 6 and 7 validated the obtained high success rates. The benefits of the proposed LSEDP and RFIMRMR based methods are shown below.

- A novel respiratory sound dataset was collected and it was publicly published. This dataset is heterogeneous.
- A novel textural and one-dimensional distance-based feature generator (LSEDP) was presented to extract salient features of the sounds. LSEDP and DWT were used together to provide a multilevel feature generation network, which is used the handcrafted method and a decomposition algorithm. The time complexity of this method was calculated as $O(n \log n)$.

- The problem of the most informative feature selection method was solved by this proposed method.
- The proposed LSEDP and RFIMRMR based feature generation and selection method is successful because four conventional/shallow classifiers achieved higher than 86% classification accuracies. By using the proposed methods, a high accurate respiratory sound classification method was presented.
- The proposed method classified of Covid-19 diagnosed respiratory sound with high performance.

In the literature, the lack of a publicly available respiratory sound data set is one of the limitations of the proposed

method. However, experimental results have shown that Covid-19 disease can be classified with high performance by using the proposed method.

6. Conclusion

This study aims to diagnose Covid-19 disease by using respiratory sounds. Therefore, a new respiratory sound dataset was collected in the first step. Then, a novel hand-crafted feature generation network and an iterative hybrid feature selector were proposed. The proposed LSEDP uses Euclidean distance to generate binary features. LSEDP aimed to use positive effect of the Euclidean distance for feature generation. To generate low, medium, and high levels features, 9-leveled DWT was used in the proposed feature generation network. To use effectiveness both ReliefF and MRMR, RFIMRMR was proposed and it solved the most discriminating numbers of features selection problem automatically. The proposed LSEDP feature generation network extracted 2560 features and RFIMRMR selected 107 most discriminative of them. These features were used input as 4 conventional classifiers and the best-resulted classifier was found as kNN (See Table 3). kNN reached the rates of 91.36%, 91.22%, 91.06%, 91.29% and 91.02%, UAP, UAR, GM, F1 and CAC respectively. It also classified Covid-19 with 96.55% classification accuracy. These results imply the success of the proposed method. A novel intelligent stethoscope can be developed by using the proposed method and novel datasets can be collected in the future works.

Declaration

The authors declared no potential conflicts of interest with respect to the research, authorship, and/or publication of this article. The authors also declared that this article is original, was prepared in accordance with international publication and research ethics, and ethical committee permission or any special permission is not required.

Author Contributions

T. Tuncer developed methodology. E. Aydemir collected dataset. F. Ozyurt performed the analysis. S.B. Belhaouari supervised and improved the study. S. Dogan and E. Akbal write and made proofreading of manuscript.





Acknowledgment

The authors would like to thank Qatar National Library, QNL, for supporting this study.

7. References

- Zhang, J.-f., et al., *SARS-CoV-2 turned positive in a discharged patient with COVID-19 arouses concern regarding the present standard for discharge*. International Journal of Infectious Diseases, 2020. **97**: p. 212-214.
- Pindiprolu, S.K.S. and S.H. Pindiprolu, *Plausible mechanisms of Niclosamide as an antiviral agent against COVID-19*. Medical Hypotheses, 2020. **140**: p. 109765.
- Shereen, M.A., et al., *COVID-19 infection: origin, transmission, and characteristics of human coronaviruses*. Journal of Advanced Research, 2020. **24**: p. 91-98.
- Tu, H., et al., *The epidemiological and clinical features of COVID-19 and lessons from this global infectious public health event*. Journal of Infection, 2020. **81**: p. 1-9.
- Saif, L.J., *Vaccines for COVID-19: perspectives, prospects, and challenges based on candidate SARS, MERS, and animal coronavirus vaccines*. Euro. Med. J., 2020. **24**: p. 1-7.
- Bellitti, P., et al., *A Wearable and Wirelessly Powered System for Multiple Finger Tracking*. IEEE Transactions on Instrumentation and Measurement, 2020. **69**(5): p. 2542-2551.
- Vellingiri, B., et al., *COVID-19: a promising cure for the global panic*. Science of the Total Environment, 2020. **725**: p. 138277.
- Singh, A., et al., *COVID-19: From bench to bed side*. Diabetes & Metabolic Syndrome: Clinical Research & Reviews, 2020. **14**(4): p. 277-281.
- Xie, M. and Q. Chen, *Insight into 2019 novel coronavirus—an updated interim review and lessons from SARS-CoV and MERS-CoV*. International Journal of Infectious Diseases, 2020. **94**: p. 119-124.
- Hui Huang, Y., et al., *The respiratory sound features of COVID-19 patients fill gaps between clinical data and screening methods*. medRxiv, 2020. **4**(7): p. 1-12.
- Abd El-Aziz, T.M. and J.D. Stockand, *Recent progress and challenges in drug development against COVID-19 coronavirus (SARS-CoV-2)-an update on the status*. Infection, Genetics and Evolution, 2020. **83**(1): p. 104327.
- Shoenfeld, Y., *Corona (COVID-19) time musings: Our involvement in COVID-19 pathogenesis, diagnosis, treatment and vaccine planning*. Autoimmunity Reviews, 2020. **19**(6): p. 102538.
- Chakraborty, I. and P. Maity, *COVID-19 outbreak: Migration, effects on society, global environment and prevention*. Science of The Total Environment, 2020. **728**: p. 138882.
- Taghizadeh-Hesary, F. and H. Akbari, *The Powerful Immune System Against Powerful COVID-19: A Hypothesis*. Medical Hypotheses, 2020. **140**: p. 109762.
- Ali, I. and O.M. Alharbi, *COVID-19: Disease, management, treatment, and social impact*. Science of The Total Environment, 2020. **728**: p. 138861.
- Aykanat, M., et al., *Classification of lung sounds using convolutional neural networks*. EURASIP Journal on Image and Video Processing, 2017. **2017**(1): p. 65.
- Don, S., *Random Subset Feature Selection and Classification of Lung Sound*. Procedia Computer Science, 2020. **167**: p. 313-322.
- Bardou, D., K. Zhang, and S.M. Ahmad, *Lung sounds classification using convolutional neural networks*. Artificial intelligence in medicine, 2018. **88**: p. 58-69.
- Naves, R., B.H. Barbosa, and D.D. Ferreira, *Classification of lung sounds using higher-order statistics: A divide-and-conquer approach*. Computer methods and programs in biomedicine, 2016. **129**: p. 12-20.
- Kandaswamy, A., et al., *Neural classification of lung sounds using wavelet coefficients*. Computers in biology and medicine, 2004. **34**(6): p. 523-537.

21. Ucar, F. and D. Korkmaz, *COVIDiagnosis-Net: Deep Bayes-SqueezeNet based Diagnostic of the Coronavirus Disease 2019 (COVID-19) from X-Ray Images*. Medical Hypotheses, 2020. **140**: p. 109761.
22. Narin, A., C. Kaya, and Z. Pamuk, *Automatic Detection of Coronavirus Disease (COVID-19) Using X-ray Images and Deep Convolutional Neural Networks*. Pattern Analysis and Applications, 2020. **24**: p. 1207-1220.
23. Uwadaira, Y., et al., *Logistic regression analysis for identifying the factors affecting development of non-invasive blood glucose calibration model by near-infrared spectroscopy*. Chemometrics and Intelligent Laboratory Systems, 2015. **148**: p. 128-133.
24. Sethy, P.K. and S.K. Behera, *Detection of coronavirus Disease (COVID-19) based on Deep Features*. Preprints, 2020. **22**.
25. Medzcool. *Lung and Breath Sounds*. [18 March 2020]; Available from: <https://www.youtube.com/watch?v=3Kkp6ZM35As&list=PL3n8cHP87ijAalXtLG2YbDpuwjxuJRR-A&index=9>.
26. EMTprep. *Lung Sounds Collection* [28 December 2019]; Available from: <https://www.youtube.com/watch?v=KRtAqeEGq2Q&feature=youtu.be>.
27. The Know Show. *Physiological pathological breath sounds*. [10 May 2013]; Available from: <https://www.youtube.com/watch?v=64bLgnv1mHA&feature=youtu.be>.
28. Alhadapediatrics. *Breath Sounds* [04 March 2010]; Available from: <https://www.youtube.com/watch?v=MzTcy6M3poM&feature=youtu.be>.
29. Tzanetakis, G., G. Essl, and P. Cook. *Audio analysis using the discrete wavelet transform*. in *Proc. Conf. in Acoustics and Music Theory Applications*. 2001.
30. Saravanan, N. and K. Ramachandran, *Incipient gear box fault diagnosis using discrete wavelet transform (DWT) for feature extraction and classification using artificial neural network (ANN)*. Expert systems with applications, 2010. **37**(6): p. 4168-4181.
31. Hothorn, T. and B. Lausen, *Bundling classifiers by bagging trees*. Computational Statistics & Data Analysis, 2005. **49**(4): p. 1068-1078.
32. Fraz, M., et al. *Retinal image analysis aimed at extraction of vascular structure using linear discriminant classifier*. in *2013 International Conference on Computer Medical Applications (ICCA)*. 2013. IEEE.
33. Liao, Y. and V.R. Vemuri, *Use of k-nearest neighbor classifier for intrusion detection*. Computers & security, 2002. **21**(5): p. 439-448.
34. Tahir, M.A., A. Bouridane, and F. Kurugollu, *Simultaneous feature selection and feature weighting using Hybrid Tabu Search/K-nearest neighbor classifier*. Pattern Recognition Letters, 2007. **28**(4): p. 438-446.
35. Lau, K. and Q. Wu, *Online training of support vector classifier*. Pattern Recognition, 2003. **36**(8): p. 1913-1920.
36. Robnik-Šikonja, M. and I. Kononenko, *Theoretical and empirical analysis of ReliefF and RReliefF*. Machine learning, 2003. **53**(1-2): p. 23-69.
37. Ojala, T., M. Pietikäinen, and T. Mäenpää. *A generalized local binary pattern operator for multiresolution gray scale and rotation invariant texture classification*. in *International Conference on Advances in Pattern Recognition*. 2001. Springer.
38. Zhang, Y., et al., *Revealing the traces of median filtering using high-order local ternary patterns*. IEEE Signal Processing Letters, 2014. **21**(3): p. 275-279.
39. Ren, J., X. Jiang, and J. Yuan. *Relaxed local ternary pattern for face recognition*. in *2013 IEEE international conference on image processing*. 2013. IEEE.
40. Raghu, S. and N. Sriraam, *Classification of focal and non-focal EEG signals using neighborhood component analysis and machine learning algorithms*. Expert Systems with Applications, 2018. **113**: p. 18-32.
41. Tuncer, T., S. Dogan, and F. Ertam, *Automatic voice based disease detection method using one dimensional local binary pattern feature extraction network*. Applied Acoustics, 2019. **155**: p. 500-506.
42. Rosenberg, A. *Classifying skewed data: Importance weighting to optimize average recall*. in *Thirteenth Annual Conference of the International Speech Communication Association*. 2012. Portland, OR, USA.
43. Bernecker, D., et al. *Representation learning for cloud classification*. in *German Conference on Pattern Recognition*. 2013. Springer.
44. Polat, Ö., *Determination of highly effective attributes in fold level classification of proteins*. International Advanced Researches and Engineering Journal, 2019. **3**(1): p. 32-39.
45. Cinar, A., B. Topuz, and S. Ergin, *A new region-of-interest (ROI) detection method using the chan-veese algorithm for lung nodule classification*. International Advanced Researches and Engineering Journal, 2021. **5**(2): p. 281-291.
46. Mouawad, P., T. Dubnov, and S. Dubnov, *Robust Detection of COVID-19 in Cough Sounds*. SN Computer Science, 2021. **2**(1): p. 1-13.
47. Sharma, N., et al., *Coswara--A Database of Breathing, Cough, and Voice Sounds for COVID-19 Diagnosis*. Inter Speech, 2020. **2768**: p. 1-5.
48. Nessiem, M.A., et al. *Detecting COVID-19 from Breathing and Coughing Sounds using Deep Neural Networks*. in *2021 IEEE 34th International Symposium on Computer-Based Medical Systems (CBMS)*. 2021. Aveiro, Portugal: IEEE.

**Research Article****Medical images fusion using two-stage combined model DWT and DCT****Ehsan Amiri^{a,*} , Mina Rahmanian^a , Saeed Amiri^a  and Hadi Yazdani Praee^b **^aDepartment of Computer Engineering, Andisheh Jahrom Institute of Higher Education, Jahrom, Iran^bDepartment of Computer Engineering, Faculty of Imam Mohammad Baqir Branch, Technical and Vocational University(TVU), Mazandaran, Iran**ARTICLE INFO***Article history:*

Received 07 April 2021

Revised 03 August 2021

Accepted 07 September 2021

Keywords:

Discrete cosine transform

Discrete wavelet transform

Image fusion

Medical images

ABSTRACT

The purpose of image enhancement is to improve the interpretation or perception of information in the image for viewers and the input of automated processing systems. Combining a multicenter image is a way of combining several images on a screen, focusing on different objects so that all objects appear in focus in the final image. Wavelet transform and cosine transform are used in many image processing applications, including image fusion. This paper's technique will combine DWT and DCT in two steps for medical MRI and PET images, eventually extracting the combined image. Input images are first divided into 8-pixel blocks in which DCT coefficients are extracted. After extracting the DCT coefficients, the first step of the combination takes place. The re-images will then be combined with the DWT conversion. According to the presented data, the proposed method achieved up to 5% better combination and, as a result, better image quality than the single-stage DWT and DCT methods.

1. Introduction

Image processing is now more commonly referred to as digital image processing. It is a computer science branch that deals with digital signal processing, representing images taken with a digital camera or scanned by a scanner. Image processing has two main branches: improving image and machine vision. Improving images includes blurring filters and increasing contrast to improve the visual quality of images and ensure that they are displayed correctly in the destination environment (such as printers or computer monitors). In contrast, machine vision uses methods that help them. And understanding the content of images to be used in works such as robotics and keratoconus detection [1, 2]. In a specific sense, image processing is any type of signal processing that is the input of an image, such as a photo or scene from a movie. The image processor's output can be an image or a set of special symbols or image-related variables.

Most image processing techniques consider the two-dimensional matrix as a signal processor and perform operations on the matrix. To date, multicenter image blending technology has proven to be a valuable method in surveillance and microscopic imaging [3]. Image fusion

methods can be divided into single-scale and multi-scale / multi-resolution methods [4]. Pyramid image analysis is the first method introduced in this field and includes reduction pyramid filter, gradient pyramid, Laplacian pyramid, ratio pyramid morphological pyramid, and contrast pyramid [5-10].

Discrete wavelet transform is much more advanced than pyramidal analysis. For example, it can process information required by the human visual system (HVS) [11]. Also, images combined with DWT can achieve better quality [12]. The wavelet has several examples, which are continuous wavelet transform (CWT) and fast wavelet transform (FWT) [13, 14].

Image enhancement aims to improve the interpretation or perception of the information in the image for human viewers or provide better input for automated processing systems. One of the most important quality factors in images is resolution [4]. In image processing, interpolation is used as a known method to increase resolution, referred to as using available data to estimate values in unknown places. Image resolution enhancement methods are based on various interpolations, three of which are the most popular interpolation methods called nearest-neighbor

* Corresponding author. Tel.: +98 917 391 8867;

E-mail addresses: e.e.amiri@gmail.com (E. Amiri), minarahmanian7@gmail.com (M. Rahmanian), saeed.amiri67@gmail.com (S. Amiri), hadi.yazdani62@gmail.com (H.Y. Praee)

ORCID: 0000-0001-6058-7083 (E. Amiri), 0000-0002-0444-427X (M. Rahmanian), 0000-0002-0232-4848 (S. Amiri), 0000-0002-6245-5014 (H.Y. Praee)

DOI: 10.35860/iaiej.910982

© 2021, The Author(s). This article is licensed under the CC BY-NC 4.0 International License (<https://creativecommons.org/licenses/by-nc/4.0/>).

interpolation, two-line interpolation, and two-cube interpolation.

Today, wavelet transform is used in many image processing applications, including feature extraction, image noise reduction, compression, face recognition, contrast enhancement, and resolution [15, 16]. It becomes. Decomposition of an image into different frequency ranges allows the separation of frequency components introduced by major shape changes or sub-factors within certain subbands. Considered wavelet-based hybrid models after examining items such as Xu and et al. [3] combined a multi-modal medical image using a matching pulse using an optimized QPSO algorithm, and Daniel Ebenser and et al. [4] worked on image composition using Gray Wolf optimization.

Therefore, to increase the quality of the enhanced images, preserving the edges is a vital issue. Therefore, image resolution enhancement using wavelet transform is a relatively new topic that many methods have recently been proposed in this field. Discretizing a continuous wavelet transform allows you to calculate it with a computer, but this is not a correct discrete conversion. The fact of the matter is that the wavelet series is, in fact, a sampled version of the CWT, and the information they provide, especially when it comes to signal reconstruction, is highly repetitive. This iteration, on the other hand, requires significant computational time and resources.

Combined models such as Xiao and et al. [8] worked on a multi-axis focused image based on edges and focused area extraction and achieved good results. El-Hosny and et al. [9] worked on an efficient DT-CWT medical image, and Ma and et al. [10] worked on an image composition method based on content recognition and achieved good results.

Hybrid models such as Nobariyan et al. [21] and Yin and et al. [18] have been able to get the right answer, but still, wavelet-based methods are better, such Meher and et al. [6] with studied area-based. Zhao and et al. [7] Worked on a local binary pattern based on a centralized metric based on multiple images. Gharbia and et al. [13] Worked on a multi-spectral method and panchromatic image fusion approach using fixed wavelet transform.

Discrete Wavelet Transform (DWT) provides sufficient information about both the parsing and the original signal's composition, with a significant percentage reduction in computation time. This article aims to medical images fusion (MRI and PET) to obtain a quality composite image for study and discover various diseases, especially cancer.

Section 2 describes the methods used to perform fusion, such as wavelet transform. In section 3, the proposed method is presented, and in section 4, the proposed method is evaluated with the help of a medical image database. Finally, in Section 5, a general conclusion of the article is given.

2. Research Methods

2.1 Discrete wavelet transform (DWT)

Wavelet transform obtains signals with different frequencies and provides appropriate information with the help of signal analysis. DWT uses two sets of functions, scale, and wavelet, related to low-pass filters, which are transient [13].

Signal analysis is performed with the help of different frequency bands over time. The main signal in the wavelet is $x[n]$, which is first calculated through a high-pass filter $g[n]$, and a low-pass filter, $h[n]$. After the filtering operation can delete half the sample according to Nyquist law. The signal at this stage has a maximum frequency of $f/2$ instead of f [15]. Can subscribe to the signal with two factors.

The desired formula for wavelet analysis is as follows:

$$y_{high}[k] = \sum x[n].g[2k - n] \quad (1)$$

$$y_{low}[k] = \sum x[n].h[2k - n] \quad (2)$$

In it, $y_{high}[k]$ and $y_{low}[k]$ are the output of the high-pass and low-pass filters, respectively, after subsampling [13].

This parsing halves the time resolution because only half of the samples specify the entire signal. Although this operation doubles the frequency resolution because it covers only half of the previous frequency band [6], it effectively halves the frequency's ambiguity. The introduced process is a sub-band coding that can repeat for further analysis. At each model level, filtering and sampling get half the number of samples and half the frequency band. According to Figure 1, $x[n]$ is the main decomposition signal, and $h[n]$ and $g[n]$ are high-pass and low-pass filters, respectively [17]. The signal bandwidth at each level is denoted by f in the figure.

The main frequencies in the signal appear as large oscillations in the area of the wavelet signal that contains certain frequencies. The difference between wavelet transform and Fourier transform is that time information is not lost in wavelet transform.

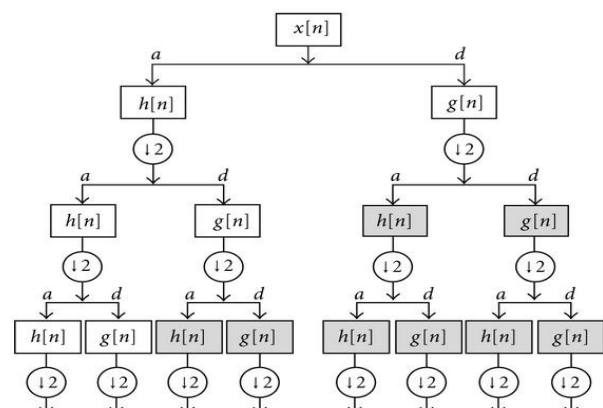


Figure 1. Wavelet with high-pass and low-pass filters [1]

The main signal information is more accurate at high frequencies than at low frequencies. For this reason, more samples are selected at this frequency. Localization will not be very accurate if low frequencies are considered. As a result, few samples are used to express the signal at these frequencies.

One of the platforms that makes the most of this wavelet conversion feature is image processing. You can calculate the DWT of each row for a given image and discard the coefficients below a certain threshold. Then, to recreate the original image's rows, he added the rows to the size of the deleted coefficients of zero and performed the inverse DWT.

It is also possible to parse the image into different frequency bands and use only certain bands to reconstruct the image [15].

2.2 Medical Images

MRI and PET are two diagnostic methods that include non-invasive techniques. "MRI" stands for Magnetic Resonance Imaging. This is a non-invasive method that uses a magnetic field to produce complete and extensive internal organs images [19-22]. MRI is used to monitor physical conditions such as cancer, tumors, and heart problems. This method uses a magnetic field and radio waves. Radio waves are generated to strike tissues that create a contrasting image when the limb is examined. The person being examined is placed under a powerful, ultra-cool magnifying glass, which captures images of the injured part of the body. These are designed to distinguish exactly between healthy and diseased tissues. MRI is used to produce accurate images of most parts of the body.

To diagnose problems such as Abnormal blood flow due to arterial blockage or any other type of injury, Bone or cartilage is also used to find abnormalities in skin tissue. The average MRI scan takes about 20 minutes to 50 minutes, depending on the organ's complexity [6].

"PET" stands for positron emission tomography technique. This technique has been used continuously since the late '50s. PET scanning is also a non-invasive procedure that uses tracer fluid introduced into the body, inhaled, or ingested by the patient.

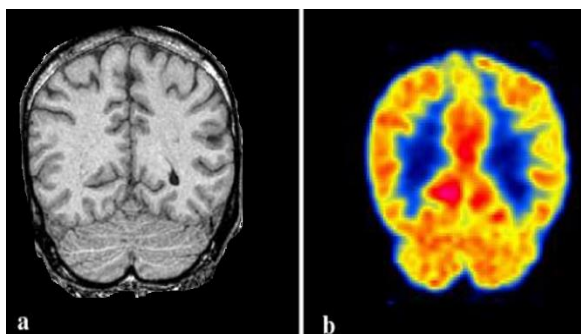


Figure 2. a) MRI image b) PET image [23]

This tracer fluid flows through the plasma throughout the body. A camera is installed that detects particles charged from the tracker fluid. Tracer fluid is a radioactive substance [6]. PET scanning uses nuclear drugs. It also determines the proper functioning of vital organs in the body. In this way, the body's sugar metabolism and oxygen consumption may also be judged. This scan is mainly used to diagnose nervous system disorders such as Alzheimer's and Parkinson's disease. It is also used to diagnose severe cancers and their spread in the body. The PET scan takes about half an hour.

3. Proposed Method

Advances in data collection and storage capabilities have led to large volumes of information in many sciences in recent decades. Researchers in various fields such as engineering, astronomy, biology, and economics face more and more observations every day. Compared to older and smaller data platforms, today's data platforms have created new data analysis challenges. Traditional statistical methods have lost their effectiveness today for two reasons. The first reason is the increase in the number of observations. The second and more important reason is the increase in the number of variables related to observation. The number of variables that must be measured for each observation is called the data dimension. Variable expressions are used more in statistics, while in computer science and machine learning, feature or adjective expressions are used more. Data platforms that are large, despite the opportunities they create, pose many computational challenges. One of the problems with large data sets is that most of the time, all the data features are not critical to finding the knowledge that lies in the data. For this reason, in many areas, reducing the size of the data remains a significant issue.

Data reduction methods are divided into several categories, the best of which are feature-based methods. The feature extraction draws the multidimensional space into a smaller space. In fact, by combining the values of the available properties, they create a smaller number of properties so that these properties have all (or more) of the information contained in the original properties. These methods are divided into two categories: linear and non-linear [24].

Among the linear methods, we can mention DFT and DWT, among which DWT has been considered. Feature selection methods try to reduce the data's size by selecting a subset of the primary attributes. Sometimes data analytics, such as classification, works better on reduced space than on main space. The DWT conversion was first created by a man named Alfred Haar.

Like the Fourier transform, this conversion is widely used and has been considered in many fields of science and engineering. Haar Wavelet conversion is more popular

than other DWT versions due to its ease of implementation and high execution speed. This conversion is such that a sequence will be n^2 long inputs.

These numbers are added together in pairs, and these sums are sent to the next step. The difference of each pair is also calculated and stored. This step is repeated, except that the sum of the previous step's pairs is added at the input. This process is repeated recursively to finally obtain a number that is the sum of all numbers. This number is returned along with the $(n-1)^2$ pair difference calculated at different stages of the algorithm as the output of this conversion. DCT and DWT techniques are both algorithms that operate on a frequency range. These techniques divide the image into fixed-size blocks to decide which should select the source image to form the final image.

This paper's technique combines these two algorithms and their improvements in using the criteria that select the best results. The technique described uses the magnitude of the difference as a criterion for selecting the combination of several blurred images in a good quality image. The difference is based on converting the image from the spatial amplitude to the frequency amplitude through DCT calculations. The blur input images are first divided into 8-pixel blocks in which the DCT coefficients are calculated according to the following Formula:

$$d_{k,l} = \frac{c(k)c(l)}{4} \sum_{i=0}^7 \sum_{j=0}^7 x_{i,j}(k,l) \quad (3)$$

$$x_{i,j}(k,l) = x_{i,j} \cos\left(\frac{(2i+1)k\pi}{16}\right) \cos\left(\frac{(2j+1)l\pi}{16}\right) \quad (4)$$

$$c(k) = \begin{cases} \frac{1}{\sqrt{2}} & k = 0 \\ 1 & \text{otherwise} \end{cases} \quad (5)$$

The result is an $8 * 8$ matrix of DCT coefficients. $Dn = \{Dn, k, l\}$ Different block sizes (other than $8 * 8$) can also be used to improve results.

The coefficients of each input image are used in the comparison, and the highest values are selected to construct the final image block.

Table 1. Proposed algorithm: DWT and DCT based image algorithm

1) Read the image
2) Apply the DCT function and obtain the parsing table
3) Apply the rules of composition
4) Inverse of DCT function
5) Apply DWT conversion to any image and composite image
6) Calculate the wavelet matrix based on the feature table obtained from the DWT conversion
7) Apply the rules of composition
8) Reverse DWT function to convert to image

The DC coefficient is an exception (0, 0) obtained by simple arithmetic mean between all DC coefficients from the input images. Finally, the image is created with inverse IDCT coefficients. After selecting a block, checking adjacent blocks (in a fixed size window) ensures better image quality of the merged image.

The second step of the proposed system is a wavelet-based system that, using the DCT method described, selects the best feature to combine the two images and then combines the two features of each image with the combination rules' help. And with the help of the wavelet conversion system, the combined image is obtained. The following diagram presents the proposed system, which includes wavelet transform and the use of DCT.

The algorithm consists of 8 steps, and in Table 1, these steps are listed.

In the first step, the images are read, and each image will be stored in the system as a table. The DCT function is applied to the image, and the property table is obtained. The table will feature the DCT coefficients resulting from the function. The combination of high band matrices is done with the help of the maximum function. With DWT conversion, the combined image and input images will be obtained as new feature tables.

In the end, with the help of the average function, the combination will be done, and the inverse wavelet will be obtained.

To provide facts and criteria in the field of accuracy for comparing different spatial evaluation methods and comparing the results of methods, we must have a precise definition of spatial quality. Based on this definition, both reality and different spatial evaluation methods can be analyzed. In general, spatial quality is detecting phenomena and their position with different sizes on satellite images. In images resulting from the merging of the displacement and change of position of different phenomena, we do not have the quality alone assuming accurate geometric correction. The boundaries of different phenomena (edges and borders) are determined and examined. These boundaries have changed in different images, and at the same limits, we can see blurring that is proportional to the spatial quality.

Thus, by measuring different dimensions, the spatial quality of different methods can be accurately determined. With this method, it is possible to study the change in the range of phenomena in different integration methods. It is observed that the differences in the dimensions of different phenomena in the resulting images in comparison with each other and comparison with the original image considering the resolution of the images are a maximum of two pixels. If we pay attention to the measurement method, One or two pixels are usually predictable due to misdiagnosis of the phenomena, so these small differences cannot be emphasized alone.

The main idea in data integration is to generate data from data that has good spectral resolution with the help of data with better spatial power, which has the benefits of both data. Still, this does not happen 100% in practice, and by improving the spatial resolution of multi-spectral data, a percentage of spectral information is lost. Details: In all merging methods, the resulting image is lower than the original images, both in terms of spatial quality and spectral.

To check the validity of the information obtained from the merger in two spatial and spectral dimensions and compare and evaluate different integration methods after the merger, using different quality evaluation methods, such as SNR, PSNR can be checked for quality. Results of payment integration, but it is necessary to mention here that not all of these methods have the accuracy and competence of evaluation. Each of these methods performs an evaluation based on a specific feature and criteria.

4. Tests and Results

In this paper, an image composition framework based on the DWT and DCT hybrid model is presented. The following are some assumptions about how the proposed method is calculated and how. The computational coefficients defined for the wavelet are adjusted based on the wavelet wave. Comparison methods include DCT, DWT, and other methods.

4.1 Evaluation Methods

In general, the purpose of an evaluation is to check the validity of the information obtained from the merger in both spatial and spectral dimensions, as well as to compare and evaluate different integration methods compared to the main multi-spectral and high-resolution images because during the integration process We will have different ratios of spatial properties of high-resolution image and spectral properties of multi-spectral image, i.e., in different stages of implementation of the algorithms used, these properties will change. Therefore, in this study, we study spatial

evaluation methods and select the appropriate method or methods in this field. Evaluation of the extent of these changes in image quality is done by two general methods of human comparison and computationally.

In mental methods, a comparison is based on the human visual system. Quantitative evaluation methods use a predefined criterion for comparison, divided into two main categories based on the reference image and independent of it based on the type of criterion. According to Wald, reference-based criteria such as Mapper can be introduced from the non-reference criteria that have recently received much attention, the PSNR (Peak Signal to Noise Ratio) index. PSNR is the most common way to measure image quality, where MAX is the maximum amount of pixels in the image.

$$PSNR = 10 \log (\text{Max}^2/\text{MSE}) \tag{6}$$

Here MSE (Mean Squared Error) is the average squared error in finding the number of pixels in an image. The higher the PSNR, the better the image reconstruction. Another indicator is an absolute error. This criterion calculates the distance between the main image and the combined image. The mean of absolute error has been used as a measure of proportionality to determine the correctness. The cost function will be calculated using the MAE error in Equation (7) as follows.

$$d(a,b) = \frac{1}{XY} \sum_i^X \sum_j^Y |a(i,j) - b(i,j)| \tag{7}$$

In Equation (7), a is the evaluation image, b is the target image of the same size, and (i, j) are the pixel coordinates.

The third indicator used to evaluate the combined image is the signal-to-noise ratio (SNR). The signal-to-noise ratio measures the amount of useful signal versus disturbing signal (or noise) in electrical systems. This number is the ratio of signal power to noise power and is expressed in decibels. The higher the index, the better the situation and the more useful the signal strength.

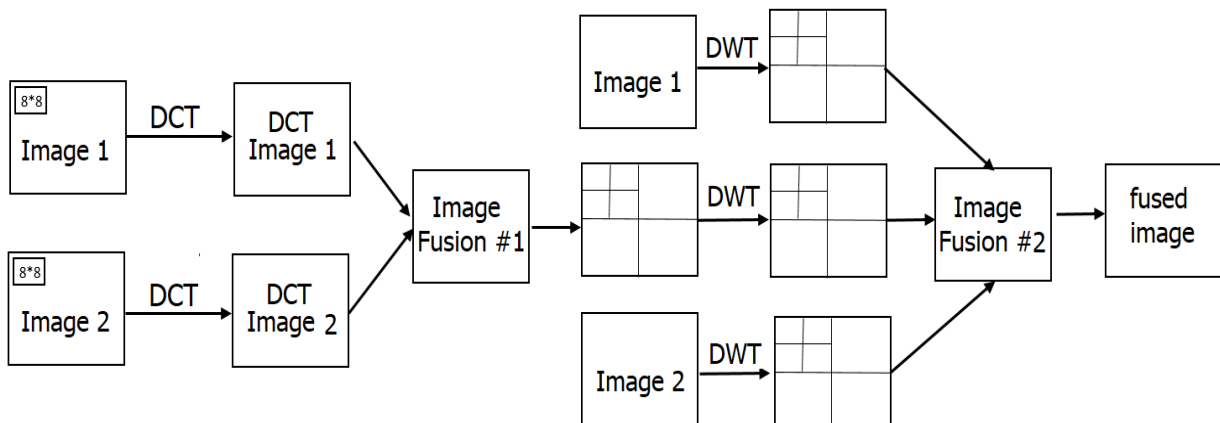


Figure 3. Proposed method image Fusion with DCT and DWT

Equation (8) shows how to calculate the SNR.

$$SNR = 10 \log \left(\frac{x^2}{y^2} \right) \quad (8)$$

According to this criterion, x is the average of the pixels, and y is the standard deviation.

All color images used in this test are 256×256 with RGB color input type and JPEG format. The simulation was performed on MATLAB R2018b on a personal computer with Intel Core i7, and the calculated results in terms of visual quality and the use of some criteria infusion. The desired values of our analysis scale are mentioned in the conclusion section, and also the results of the proposed fusion framework are compared with SWT methods.

4.2 Data Set

The test data included 150 images of two color domains, PET and black and white high-resolution MRI. Images have 256×256 pixels. All images are from the Harvard University website [25]. Brain images are classified into three groups (axial set images, normal coronary images, and Alzheimer's disease). Combining images to compare the algorithms introduced in this article Different images are introduced. For each group, we considered 50 images and the average of the results for comparison.

4.3 Review of Combination Methods

The input image has several problems because the thickness or density of the area to be measured varies.

Therefore, it is important to have a way that cannot be sensitive to this issue. To better understand the composition of the images, the combination is first done with the different methods mentioned (Figure 4).

Figure 5 is a fusion with the help of the proposed method. From the result, we can see that the proposed fusion method can preserve the high spatial resolution properties of the MRI image. Also, the combined image does not distort the spectral properties of the multi-spectral image. Tables 2, 3, and 4 present the composition results based on the image quality criteria. Also, due to the quantitative comparison of different blending techniques, most of the criteria can be obtained with the proposed method, shown in Tables 2, 3, and 4.

To examine each method according to the algorithms, it can be introduced as a table of their performance. Table 2 presents the results for determining the introduced algorithm's quality based on four main methods, and the selected image is MRI and PET image of the human brain in the first dataset.

Table 3 presents the results for the introduced algorithms' quality detection based on four main methods: the selected image, MRI image, and PET image related to the second dataset.

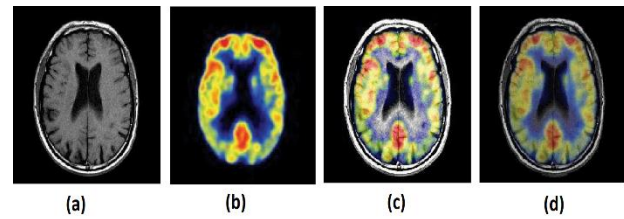


Figure 4. a and b MRI and PET images. d) Fusion of MRI and PET images by DCT method (h) Fusion of MRI and PET images by DWT method [26]

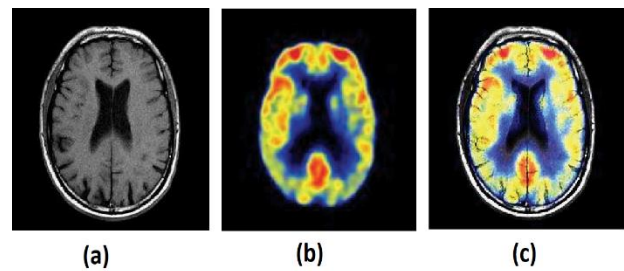


Figure 5. Combining MRI and PET images with the proposed method

Table 2. Results of the above algorithms for MRI and PET imaging of the human brain in the first dataset

Methods	PSNR(%)	MAE(%)	SNR(%)	MSE(%)
PCA	38.21	15.30	44.6	15.650
DWT	39.66	15.01	48.1	15.180
HIS[23]	39.72	14.86	46.02	14.76
SWT[27]	38.19	15.31	47.99	14.55
SWT-DWT[27]	39.34	14.69	46.63	14.23
YCbCr-DWT[22]	40.08	14.11	48.51	13.94
Proposed method	42.1	13.99	48.6	13.002

Table 3. Results of the above algorithms for MRI and PET image related to the second data set

Methods	PSNR(%)	MAE(%)	SNR(%)	MSE(%)
PCA	37.12	15.56	44.71	15.13
DWT	39.65	15.97	48.21	15.18
HIS[23]	39.78	14.63	46.03	14.77
SWT[26]	38.23	15.22	47.30	14.52
SWT-DWT[26]	39.44	14.66	46.60	14.27
YCbCr-DWT[22]	40.06	14.13	48.12	13.88
Proposed method	42.01	13.03	48.61	13.06

Table 4. Results of the above algorithms for MRI and PET image related to the third dataset

Methods	PSNR(%)	MAE(%)	SNR(%)	MSE(%)
PCA	38.54	15.56	44.55	15.62
DWT	39.12	15.44	48.09	15.17
HIS[23]	39.27	14.37	46.34	14.70
SWT[26]	38.65	15.12	47.98	14.51
SWT-DWT[26]	39.78	14.78	46.60	14.22
YCbCr-DWT[22]	40.90	14.23	48.56	13.90
Proposed method	42.21	13.87	48.59	13.009

Table 4 presents the results for quality detection of the introduced algorithms based on four main methods. The selected image, MRI image, and PET image are related to the third dataset.

According to the obtained results, it is clear that the obtained method has obtained a better answer up to about 5% compared to the other introduced algorithms.

5. Conclusion

Multiple images (spatial, spectral, temporal, and radiometric resolution) are ideal for many studies. Therefore, we try to optimize these factors as much as possible in the design of sensors. Still, due to the wide range of applications and technical problems in the design and manufacture of sensors, each sensor is suitable for a specific application and has limitations in other applications.

This is why there are so much variety and diversity in remote sensing imaging systems.

On the other hand, due to the need for data with specifications mentioned in specific applications and the need to use and use existing data from each region, most remote sensing researchers consider data integration or data fusion methods.

Image processing specialists are located. In general, data fusion is easier and more economical than designing and building an advanced sensor that has the power to separate spatially and spectrally. Hence, the use of both spatial and spectral information is undoubted without using data integration methods. They are not possible.

According to the data presented in Section 5, the proposed method was able to provide a somewhat better fusion than the other methods introduced. Also, the point that is evident in this method is that there is no need to manipulate the image in the early stages, which, unlike other methods, will not lead to image preprocessing challenges.

Declaration

The authors declared no potential conflicts of interest with respect to the research, authorship, and/or publication of this article. The authors also declared that this article is original, was prepared in accordance with international publication and research ethics, and ethical committee permission or any special permission is not required.

Author Contributions

E. Amiri and M. Rahmanian have defined the main subject. The model has been introduced and implemented by E. Amiri. S. Amiri was in charge of testing and analyzing the data. M. Rahmanian and H. Yazdani wrote the article, and E. Amiri supervised the article's writing.

References

- Seo, Y., Y. Choi, and J. Choi, *River stage modeling by combining maximal overlap discrete wavelet transform, support vector machines and genetic algorithm*. Water, 2017. **9**(7): p. 525.
- Amiri, E., et al., *Detection Of Topographic Images Of Keratoconus Disease Using Machine Vision*. International Journal of Engineering Science and Application, 2020. **4**(4): p. 145-150.
- Xu, X., et al., *Multimodal medical image fusion using PCNN optimized by the QPSO algorithm*. Applied Soft Computing, 2016. **46**: p. 588-595.
- Daniel, E., et al., *Optimum spectrum mask based medical image fusion using Gray Wolf Optimization*. Biomedical Signal Processing and Control, 2017. **34**: p. 36-43.
- Nair, R.R. and T. Singh, *Multi-sensor medical image fusion using pyramid-based DWT: a multi-resolution approach*. IET Image Processing, 2019. **13**(9): p. 1447-1459.
- Meher, B., et al., *A survey on region based image fusion methods*. Information Fusion, 2019. **48**: p. 119-132.
- Zhao, W., et al. *Local Binary Pattern Metric-Based Multi-focus Image Fusion*. in *International Symposium on Artificial Intelligence and Robotics*. 2018. Springer.
- Xiao, J., et al., *Multi-focus image fusion based on depth extraction with inhomogeneous diffusion equation*. Signal Processing, 2016. **125**: p. 171-186.
- El-Hoseny, H.M., et al., *An efficient DT-CWT medical image fusion system based on modified central force optimization and histogram matching*. Infrared Physics & Technology, 2018. **94**: p. 223-231.
- Ma, J. and D. Zhang, *An image fusion method based on content cognition*. Procedia computer science, 2018. **131**: p. 177-181.
- Manchanda, M. and R. Sharma, *An improved multimodal medical image fusion algorithm based on fuzzy transform*. Journal of Visual Communication and Image Representation, 2018. **51**: p. 76-94.
- Cabazos-Marín, A.R. and J. Álvarez-Borrego, *Automatic focus and fusion image algorithm using nonlinear correlation: Image quality evaluation*. Optik, 2018. **164**: p. 224-242.
- Gharbia, R., et al., *Multi-spectral and panchromatic image fusion approach using stationary wavelet transform and*

- swarm flower pollination optimization for remote sensing applications*. Future Generation Computer Systems, 2018. **88**: p. 501-511.
14. Farid, M.S., A. Mahmood, and S.A. Al-Maadeed, *Multi-focus image fusion using content adaptive blurring*. Information fusion, 2019. **45**: p. 96-112.
 15. Xu, X., Y. Wang, and S. Chen, *Medical image fusion using discrete fractional wavelet transform*. Biomedical signal processing and control, 2016. **27**: p. 103-111.
 16. Zhang, P., et al., *Infrared and visible image fusion using co-occurrence filter*. Infrared Physics & Technology, 2018. **93**: p. 223-231.
 17. Paramanandham, N. and K. Rajendiran, *Infrared and visible image fusion using discrete cosine transform and swarm intelligence for surveillance applications*. Infrared Physics & Technology, 2018. **88**: p. 13-22.
 18. Yin, W., et al., *Local binary pattern metric-based multi-focus image fusion*. Optics & Laser Technology, 2019. **110**: p. 62-68.
 19. Tian, J., G. Liu, and J. Liu, *Multi-focus image fusion based on edges and focused region extraction*. Optik, 2018. **171**: p. 611-624.
 20. Joshi, K., et al. *Multi-Focus Image Fusion Using Discrete Wavelet Transform Method*. in *International Conference on Advances in Engineering Science Management & Technology (ICAESMT)-2019, Uttarakhand University, Dehradun, India*. 2019.
 21. Ozsoydan, F.B., *Effects of dominant wolves in grey wolf optimization algorithm*. Applied Soft Computing, 2019. **83**: p. 105658.
 22. Nobariyan, B., et al., *A Novel Architecture of Medical Image Fusion Based on YCbCr-DWT Transform*. INTERNATIONAL ARAB JOURNAL OF INFORMATION TECHNOLOGY, 2018. **15**(5): p. 850-856.
 23. Daneshvar, S. and H. Ghassemian, *MRI and PET image fusion by combining IHS and retina-inspired models*. Information fusion, 2010. **11**(2): p. 114-123.
 24. Du, J., et al., *An overview of multi-modal medical image fusion*. Neurocomputing, 2016. **215**: p. 3-20.
 25. Harvard University website [cited 2020 29 June]; Available from: <http://www.med.harvard.edu/AANLIB/home.html>.
 26. Javed, U., et al., *MRI and PET image fusion using fuzzy logic and image local features*. The Scientific World Journal, 2014. **2014**.
 27. Diwakar, M., et al., *A comparative review: Medical image fusion using SWT and DWT*. Materials Today: Proceedings, 2020.

**Research Article****LUPU-Net: a new improvement proposal for encoder-decoder architecture****Saadet Aytac Arpacı^{a,*}  and Songül Varlı^a **^aComputer Engineering Department, Yıldız Technical University, Istanbul, 34220, Turkey**ARTICLE INFO***Article history:*

Received 19 May 2021

Revised 19 October 2021

Accepted 02 November 2021

Keywords:

Convolutional neural network

LU-Net

Retinal vessel

Semantic segmentation

Up sampling

U-Net

ABSTRACT

Many network designs in recent years have offered deeper layered solutions. However, models that achieve high-performance results with fewer layers are preferred due to causing less processing load for the system. The U-Net authors succeeded in efficiently creating a model with fewer layers. However, the U-Net architecture also requires improvement to become more efficient. For this purpose, we offer a novel encoder-decoder architecture based on the U-Net and the LU-Net. Furthermore, we propose using a reduced number of up-sampling operations, which were utilized together with the down-sampling operations intensively in the encoder section in our previous research, in the encoder part. The proposed architecture was evaluated on the IOSTAR dataset for the segmentation of retinal vessels. The preprocessing and data augmentation processes were applied to the images before training. The U-Net, LU-Net, and the proposed model were evaluated by using the accuracy, sensitivity, specificity, Dice, and Jaccard metrics. The proposed model achieved performance metric values such as an accuracy of 97.29%, a sensitivity of 81.10%, a specificity of 98.94%, a Dice coefficient of 84.66%, and a Jaccard coefficient of 73.41%. The proposed model obtained improved results compared with the other models, especially for test samples.

1. Introduction

Artificial neural network studies started in 1943 with [1] research, and these networks were introduced by [2] as the term "deep learning" in the year 2000. In the 1980s, the "Neocognitron" model, which could learn with a hierarchical multi-layered network, was proposed [3]. Later, the convolutional neural network (CNN) was developed based on the "Neocognitron" model.

CNN is a breakthrough in visual pattern recognition. Convolutional neural networks basically consist of three types of layers: 1) The convolution layer produces the feature maps (the activation maps); 2) the activation functions cause the values obtained from the layers to be kept within specific value ranges; 3) the down-pooling layer reduces spatial resolution.

Many architectures have been developed based on CNN. One of these architectures is the VGG16 classification model [4]. The VGG16 architecture uses 13 convolution layers and 3 x 3 convolution filters for feature extraction, a rectified linear unit (ReLU) layer follows each convolution layer, and the architecture has maximum

pooling layers for down-sampling. Fully connected layers are located in the last three layers [4].

With the semantic segmentation process, each pixel of an image is associated with a class tag. Thus, the desired region in the image is determined with its boundaries. One of the first samples of semantic segmentation was created by the Fully Convolutional Networks (FCN) authors [5]. The FCN authors [5] replaced the fully connected layers of existing CNN architectures such as VGG16 with the convolutional layers and used the transposed convolution for up-sampling. They did not add more decoder layers to the FCN architecture; therefore, the high-resolution features were disregarded by the model. This problem was solved with an improved encoder-decoder network. The U-Net [6] model, which was developed from the FCN architecture, was proposed in 2015. The U-Net contains some differences compared with the FCN: 1) The encoder-decoder sections are symmetrical; 2) it uses the "concatenation" operation instead of the "add" method to connect the encoder and decoder layers. Another encoder-decoder network architecture is SegNet [7], which was

* Corresponding author. Tel.: +90-212-383-5730.

E-mail addresses: saadeta99@gmail.com (S.A. Arpacı), svarli@yildiz.edu.tr (S. Varlı)

ORCID: 0000-0001-6226-4210 (S.A. Arpacı), 0000-0002-1786-6869 (S. Varlı)

DOI: 10.35860/iarej.939243

© 2021, The Author(s). This article is licensed under the CC BY-NC 4.0 International License (<https://creativecommons.org/licenses/by-nc/4.0/>).

proposed in 2017. The encoder part of this architecture is the same as the 13 convolution layers in the VGG16 network. The SegNet has 13 convolution layers in the decoder part corresponding to the encoder path. In the U-Net architecture, all activation maps are transferred to the corresponding decoder layer and concatenated with the up-sampled feature maps through the transposed convolution operation. The difference between SegNet with U-Net is that SegNet uses the pooling indices in the encoder section (calculated in the maximum pooling layer) for up-sampling in the corresponding layers in the decoder section. The up-sampled maps are then subjected to the convolution operation with the trainable filters to create the dense feature maps, as in U-Net. Some researches have been done in recent years with SegNet. For example, SegNet was used for retinal vessel segmentation in [8, 9] researches. The jump connections in the U-Net architecture can be seen as an advantage for the model to obtain more feature information. Even if the number of blocks of the model is reduced, the U-Net can achieve high performance at the pixel level [10-12]. The simple and flexible composition of the architecture allows efficient, new designs to be developed based on this model. For example, separate side paths were added to the encoder and the decoder sections in the M-Net [13] architecture. In this architecture, gradually reduced inputs with the maximum pooling operation in the first side path were given to the encoder section, and the outputs from the decoder section were given to the second side path. In the IterNet [14] architecture, the U-Net model was iteratively implemented to be four times deeper than the U-Net. Besides the raw input image, segmented vessel images were also used as input. Their model has achieved a 79.70% sensitivity rate on the CHASE-DB1 dataset [14]. The authors in [15] reference proposed an improvement to use the convolution operation instead of the maximum pooling process in the original U-Net model to retain more feature information. The authors in [16] reference used the bilinear interpolation function for the up-sampling operation. The theoretically expected situation in deep architectures is that if the number of layers of the network increases, the training error decreases. Contrary to this situation, the experiments were indicating the problem of the vanishing gradient. The Res-Net and the Dense-Net models tried to alleviate this problem. The input features were added as a shortcut link to the output of the next two convolutional layers in the Res-Net [17] model. The authors in [18, 19] references, who interpreted the Res-Net model differently, integrated their methods into the U-Net architecture for retinal vessels' segmentation. The MResU-Net [18] model has achieved an 81.01% sensitivity rate on the STARE dataset. The weighted ResUNet [19] model has achieved a 77.15% sensitivity rate on the DRIVE dataset. In the Dense-Net [20] model, each

layer in a block is connected with all previous layers. The Dense-Net was integrated into the U-Net model for retinal vessels' segmentation by [21, 22] researchers. The proposed model in [21] has achieved a 76.72% and an 89.67% sensitivity rate on the DRIVE and the CHASE-DB1 dataset, respectively. The proposed model in [22] reference has achieved a 79.86% sensitivity rate on the DRIVE dataset. The U-Net ++ authors [23] used the dense convolution blocks in the U-Net model's jump connections. The authors of the [24] reference proposed creating the dense feature maps in the U-Net model's encoder path and transferring them to the decoder path through the jump connections.

The authors of U-Net [6] demonstrated that the results of designs with many levels in applications could be accomplished with fewer layers as well. This situation provides an advantage in that it brings less processing load to achieve the result. However, the U-Net architecture also needs improvement to achieve more efficiency. For example, for cardiac ventricular segmentation, the LU-Net authors [25] proposed some improvements. In another improvement example, many feature maps obtained from the down-sampling and up-sampling operations were transferred to the decoder section of the U-Net in the reference [24] research, but here, as the number of layers increased, so did the processing load. Therefore, within this research, we tried the up-sampling operation applied in the reference [24] research in order to achieve results with less processing load. In continuation, the outcomes of the experiments were appraised by ours.

In this manuscript, we proposed a new model based on the U-Net, LU-Net architectures, and the reference [24] research for retinal vessel segmentation. This article has two essential contributions: Utilizing the up-sampling operation in the encoder part to get precise location information, and introducing a hybrid architecture improved with the up-sampling operation. The rest of this paper describes the proposed architecture, the used dataset, presents the experimental results, and the discussion section.

2. Materials and Methods

2.1 U-Net

The U-Net architecture comprises an encoder path on the left side and a decoder path on the right side. The encoder section is like a characteristic convolutional network architecture. Four down-sampling processes occur in the encoder path with a 2 x 2 max-pooling operation. Each block in the encoder path consists of two 3 x 3 convolution layers and a ReLU as the activation function. According to the number of feature maps in the first layer, the number of feature channels doubles after each down-sampling operation. The decoder path is symmetrical to the encoder path, and four up-sampling

operations occur in this section. The feature map size is increased in the decoder path by the 2 x 2 up-sampling process, and these feature maps are concatenated with the feature maps in the corresponding block in the encoder path. A more precise output is created by integrating the contextual information obtained from the encoder path with the localization information obtained from the decoder path, thanks to these jump connections, which are the reason for the segmentation success of the U-Net. In continuation of the up-sampling process, two 3 x 3 convolution operations occur, in which ReLU is applied as an activation function. At the output, a 1 x 1 convolution layer is used. The encoder path and decoder path are bridged by two 3 x 3 convolution layers [6].

2.2 LU-Net

For cardiac ventricular segmentation, the LU-Net authors [25] offered three improvement methods on the U-Net model. According to their application [25], first, the SE-Net [26] module, which is a feature weighting process, was applied before each pooling operation in the encoder path. When the feature maps pass to the SE-Net module, the global average pooling process performs to obtain the mean pixel value per channel, and the feature vector occurs. The feature vector enters two consecutive fully connected layers. In the first, linearity is achieved by the ReLU function, and in the second, a series of weight values between 0 and 1 is obtained by the sigmoid function. Finally, the weight values are multiplied by the activation maps to generate the new feature maps comprising the weight information. The LU-Net authors included the SE-Net module because it suppresses the ineffective information and gives more weight to the beneficial information on the channel, so the sensitivity of the network increases. In this way, the effectiveness of the

extracted features is increased, and the amount of calculation is reduced. Secondly, in the LU-Net research [25], the feature maps at various scales were obtained from the input (apart from the encoder path). Then these feature maps were concatenated with the output of the corresponding pooling layer in the encoder path. In this stage, a down-sampling process takes place with the convolution layer with a kernel size of 2 x 2 and a step size of 2 to obtain the feature maps of different scales. Thirdly, the deconvolution process in the decoder section of the U-Net was replaced with 3 x 3 and 1 x 1 convolution operations. Additionally, the up-sampling process was applied to the network model with the inverse unpooling operation. During U-Net's encoding and decoding processes, some important details are lost with the convolution and pooling operations, resulting in imperfect segmentation boundaries. To solve this problem, the authors of the LU-Net proposed the second and third improvements to the U-Net model [25].

2.3 Proposed Model

In this research, the U-Net [6], LU-Net [25] architectures, and the reference [24] research were used to create the proposed network model. Figure 1 shows the proposed LUPU-Net network.

Network architectures were modified such that: For the encoder part, we used the blocks in the encoder path of the LU-Net model up to the bridging section. Thus, the use of useful and effective information is provided. For the decoder path, we used the bridging section of the U-Net model and the blocks in the decoder path. Thus, the processing load that the convolution process would bring to the system is lightened. Each block in the network has two 3 x 3 convolution layers, and we used the ReLU as the activation function.

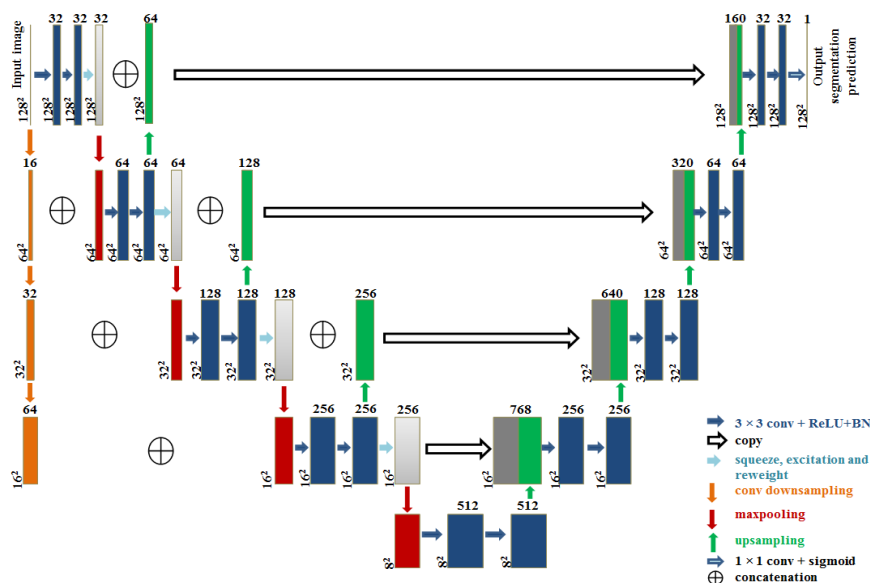


Figure 1. LUPU-Net model

For down-sampling in the encoder path, we used four 2×2 max-pooling operations, three convolutional down-sampling operations with a kernel size of 2×2 and a step size of 2.

We propose that the feature maps obtained by the up-sampling process from the blocks in each level of the encoder path pass to the decoder path through the jump connections. In this process, the up-sampling operation is applied to these feature maps before passing the feature maps to the SE-Net module. In continuation, these up-sampled feature maps are concatenated with feature maps obtained from the SE-Net module at the upper level. The precise localization information of the features in the encoder path concatenates with the contextual information obtained from the encoder path blocks. In this way, the segmentation of the images is made better. Later, all the feature maps are transferred from the encoder section to the decoder part.

The number of feature maps in the first layer of the LUPU-Net network is 32. After each down-sampling operation, the number of feature maps increases twice. During the training of the network, the pre-training process was not applied. In this research, the "UpSampling2D" class was used for up-sampling. As the optimization algorithm of the model, the Adam method [27] was used by starting it at a learning rate of 0.001. The batch normalization (BN) process was applied after the convolution layers to increase the convergence speed of the network. At the output, we used a convolution layer of 1×1 with the sigmoid activation function, which reduced all feature map information to a two-element vector. The performance of the model trained with 100 iterations was evaluated. Our segmentation research was carried out

using the Keras library [28], which uses the TensorFlow [29] framework on the backend.

2.4 Dataset

In this research, the IOSTAR dataset, which is publicly available on the website [30], was used. These high contrast images in the dataset based on the Scanning Laser Ophthalmoscopy (SLO) technique have a resolution of 1024×1024 pixels with a 45° FOV. The dataset contains 30 SLO images. The ground truth images were created by experts, and these images were included in the dataset. More information about the dataset is available in [31, 32] references.

2.5 Preprocessing

Since SLO images show retinal vascular structures with a stronger contrast, these images do not require preprocessing, but preprocessing was applied to the images in this experiment to get more vascular detail. Figure 2 shows the preprocessing stages. In this process [33], in the first stage, the images were converted to the HSV color space and the luminosity was adjusted by applying gamma correction to the value channel. Then the images were converted from the HSV color space to the RGB color space. In the second stage, the images were converted from the RGB color space to the LAB color space, and the CLAHE process was applied to the L channel to increase the vessel contrast. The image pixel values were normalized to the range [0-1]. 128×128 -size single-channel gray levels of the images were used in the evaluation of the models. The OpenCV library [34] was used during the preprocessing of the images.

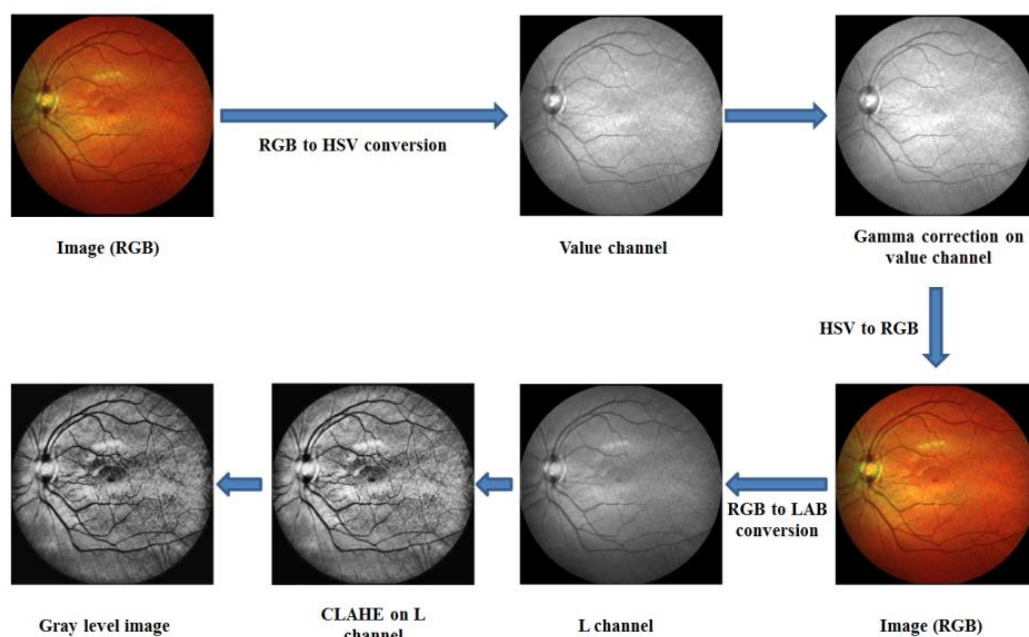


Figure 2. The preprocessing stages applied to the SLO images

The last 10 images in the IOSTAR dataset were used for testing. The data augmentation processes such as horizontal flipping, cropping a random area of the image, and rotating the image left and right by a maximum of 10° were applied to the 20 images. The 1000 images were obtained through the data augmentation process. The Augmentor library [35] was used for the data augmentation process. 20% of the dataset images were used for validation.

2.6 Evaluation Metrics

As used in the reference manuscript [36], accuracy as in Equation (1), sensitivity as in Equation (2), and specificity as in Equation (3) were used to measure the performance of the models in this research, as well. Furthermore, we measured the models' performance for the retinal vessels' segmentation with the Dice metric as in Equation (4) [37], and the Jaccard coefficient (IoU) as in Equation (5) [38]. The accuracy is the ratio of the sum of the number of pixels in the correctly defined vessel and background areas to the sum of the total number of pixels [36]. The sensitivity gives the rate of determination of the vessel area. The specificity gives the rate of determination of the background area. The Dice and Jaccard metrics measure the overlap between the segmented prediction image and the ground truth images. These metrics are calculated as follows:

$$\text{Accuracy} = \frac{TN + TP}{TN + TP + FP + FN} \quad (1)$$

$$\text{Sensitivity} = \frac{TP}{TP + FN} \quad (2)$$

$$\text{Specificity} = \frac{TN}{TN + FP} \quad (3)$$

$$\text{Dice} = \frac{2 * TP}{(2 * TP) + FP + FN} \quad (4)$$

$$\text{Jaccard} = \frac{TP}{TP + FP + FN} \quad (5)$$

TP, TN, FP, FN are the quantities of true positive, true negative, false positive, and false negative at the pixel level, respectively.

3. Results

The performance of the proposed network on vessel segmentation was evaluated using the IOSTAR dataset. Table 1 shows the evaluation metric values obtained on the IOSTAR data set with the U-Net, LU-Net, and LUPU-Net models. The accuracy, sensitivity, specificity, Dice, and

Jaccard metric values obtained with three models show minor differences. We used the same basic parameters, values, and classes for the three models in the experiments. For example, the activation function, the initial quantity of the feature maps, the down-sampling and up-sampling classes, the optimization function, the loss function, etc. The three models in the experiments differ only architecturally. Thus, we can explain the minor differences between the values.

Figure 3 shows the segmentation results obtained by three models for a test sample. Models can predict most retinal vessels.

In the result segmentation prediction images, the pixel values are obtained in the range of [0-1]; therefore, a binary thresholding process was applied to clarify the background and vessel separation with the values of 0 and 1. In this post-processing process, 0.10 was used as the threshold value. Table 2 shows the average accuracy, sensitivity, specificity, Dice, and Jaccard metric values obtained after the post-processing stage from the images in Figure 3.

Figure 4 shows graphically the average Dice similarity coefficients obtained from the models for ten test images. Figure 5 shows graphically the average Jaccard similarity coefficients obtained from the models for ten test images. The differences that did not appear in Table 1 metric value results became more apparent in the test samples. Figure 4 and Figure 5 show many test samples are segmented more efficiently by the LUPU-Net model. Therefore, the LUPU-Net increases the overlap between the ground truth and prediction images. These results show that the proposed architecture contributes to the improvement of retinal vessel segmentation.

4. Discussion

In this research, we created a hybrid network architecture based on the U-Net and the LU-Net models, and we applied a new improvement proposal based on the reference [24] research to this hybrid model. We used the IOSTAR dataset to measure the efficiency of this new model (LUPU-Net). Table 3 shows the outcomes of other studies [39-41] based on the U-Net architecture on the IOSTAR dataset and the results obtained from the LUPU-Net model. The findings show that the proposed model performed well in terms of pixel discrimination.

The researchers in reference [42] evaluated their proposed model for melanocytic lesion and retinal vessel segmentation without using image preprocessing. Their model has achieved a 94% Dice coefficient, an 88.2% Jaccard coefficient for melanocytic lesion segmentation, and an 82.6% Dice coefficient, a 70.8% Jaccard coefficient for retinal vessel segmentation. These comparative results show that the segmentation of a narrow and thin region is more difficult than a large region.

Table 1. The performance metric values obtained from the models

Models	Evaluation Metrics (%)				
	Accuracy	Sensitivity	Specificity	Dice	Jaccard (IoU)
U-Net	97.30	80.52	99.01	84.63	73.37
LU-Net	97.29	80.52	98.99	84.52	73.21
LUPU-Net	97.29	81.10	98.94	84.66	73.41

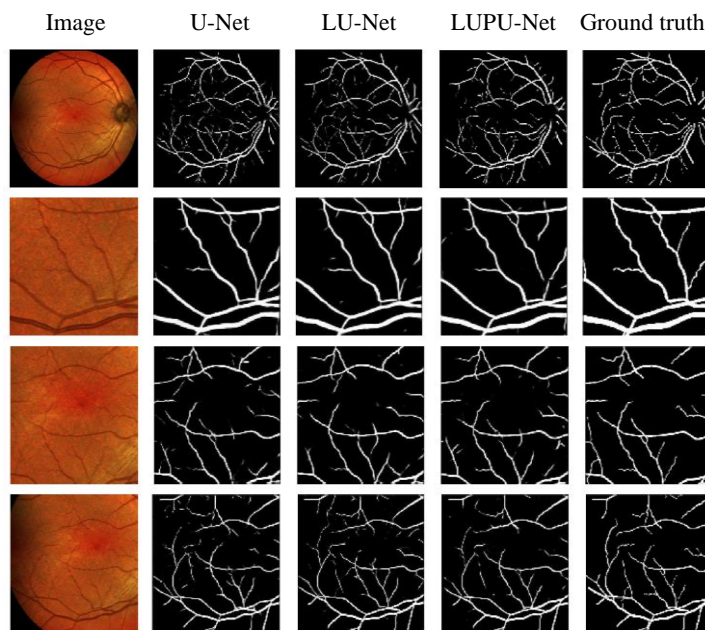


Figure 3. The segmentation results were obtained by three models for a test sample. The first column demonstrates the fundus images, the second column demonstrates the segmentation result images obtained by the U-Net model, the third column demonstrates the segmentation result images obtained by the LU-Net model, the fourth column demonstrates the segmentation result images obtained by the LUPU-Net model, and the fifth column demonstrates the ground truth images

Fundus photographs obtained with standard fundus cameras show complexities such as low contrast difference between the vessel and the non-vessel pixels, uneven background illumination, vessel width variation, brightness, and shape [43]. For this reason, many studies based on the U-Net [10, 11, 16, 19, 21, 22] have applied different preprocessing techniques to achieve more vascular detail. Compared with the standard fundus photographs, the images obtained by the SLO method are higher-quality images with high contrast and resolution. However, changes in vessel thicknesses, transitions and bifurcations in vessels, the low contrast difference between the vessel and the background for thin vessels are valid problems for the SLO images as well. For this reason, we applied image preprocessing to the IOSTAR dataset

images to obtain more vessel details. The researchers in [39- 41] did not use image preprocessing.

The authors of reference [39] segmented these images in the U-Net model by dividing the images into overlapping patches of 128 x 128 pixels. The authors of reference [41] created the datasets by only producing a small number of image patches without using any other data augmentation method. They evaluated the dataset segmentation by the U-Net model after 1000 epochs. The authors in reference [40] utilized the IOSTAR dataset without using any data augmentation process and changing the image size. They created a dense layered and densely connected architecture based on the Res-Net, Dense-Net, and U-Net models and evaluated the IOSTAR dataset segmentation after 300 epochs.

Table 2. The average metric values obtained after the post-processing stage of the images in Figure 3

Models	Evaluation Metrics (%)				
	Accuracy	Sensitivity	Specificity	Dice	Jaccard (IoU)
U-Net	95.45	84.50	96.74	79.57	66.31
LU-Net	95.19	84.25	96.56	78.78	65.14
LUPU-Net	95.60	83.22	97.12	80.03	66.84

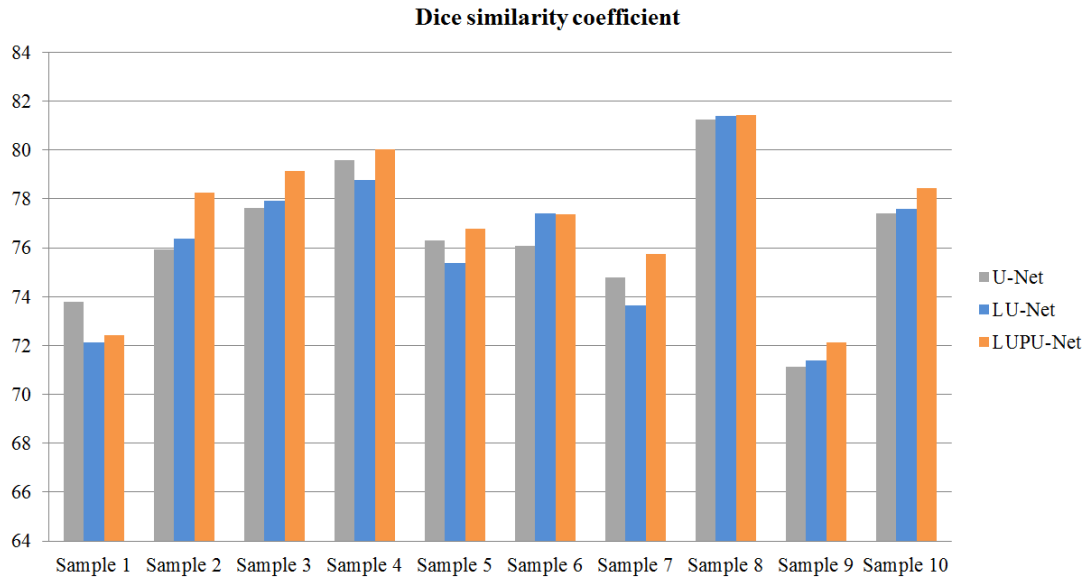


Figure 4. Models' average Dice similarity coefficients for ten test samples

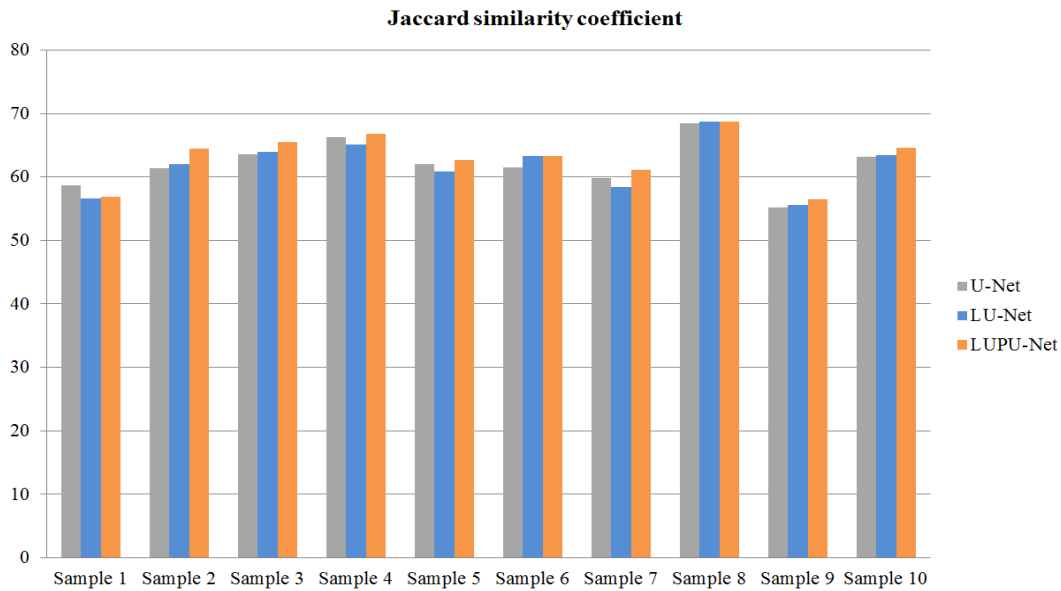


Figure 5. Models' average Jaccard similarity coefficients for ten test samples

Table 3. The performance metric values of our model and previous researches on the IOSTAR dataset

Researches	Evaluation Metrics (%)				
	Accuracy	Sensitivity	Specificity	Dice	Jaccard (IoU)
Meyer et al. (2017) [39]	96.95	80.38	98.01	-	-
Guo et al. (2020) [40]	97.13	80.82	98.54	-	-
Brea et al. (2020) [41]	95.00	86.00	95.00	71.00	-
This research (2021)	97.29	81.10	98.94	84.66	73.41

A sufficient quantity of augmented data with the correct method can create high-efficiency segmentation. The data augmentation methods generally applied to the images are flipping, rotation, translation, cropping, and elastic deformation [12, 15, 19, 24, 42, 44, 45]. However, investigations into different data augmentation methods like the translation-reflection technique [16], etc. have

been continued as well. Through the data augmentation methods we used in this research, a successful result was obtained. We used the batch normalization and data augmentation operations in the model to prevent the overfitting problem.

The feature maps obtained through the down-sampling and up-sampling operations were used by the authors of

reference [24]. They concentrated a lot of feature maps on the jump connections to use more feature information. Their model has achieved a 97.87% accuracy, an 84.11% sensitivity, a 99.39% specificity, an 88.70% Dice, a 79.69% Jaccard value. Within these results, we can say that the use of more feature information produces more successful results. However, this situation causes more processing load for the system. In this research, we tried a model using fewer operations. In this manner, the processing load to reach the result was reduced. Based on the research of [24] reference, we proposed using the up-sampling operation in the encoder section, and we evaluated our proposal together with a hybrid architecture based on the U-Net and the LU-Net. The LUPU-Net architecture improved results, particularly for test samples. These results are seen in Figure 4 and Figure 5. The data augmentation methods, the amount of data, the quality of the image, and using the various libraries, classes, optimization algorithms, loss functions, activation functions, etc., all have an impact on the model segmentation performance. Therefore, the models were evaluated under the same conditions.

The retinal vascular system provides important markers for the diagnosis of some diseases (diabetic retinopathy, hypertension, cardiovascular diseases) for ophthalmologists. Fast and accurate detection of changes in the vessels is a factor that increases the success of the diagnosis. The process of segmenting the retinal vasculature from the image for better examination is performed by trained experts traditionally, and this segmentation action is a time-consuming procedure. Even among professional experts, the segmentation of the same image differs significantly [43]. Therefore, the development of automated techniques in retinal vessel segmentation continues in order to support the clinician's decisions. We can say that the method we propose will contribute to the field of ophthalmology. However, we also recommend using the new method for other medical image segmentation applications in the future.

5. Conclusion

This paper introduces a novel method for segmentation. We created an encoder-decoder architecture and used the up-sampling operation in the encoder section. The encoder-decoder architecture proposed in this research, which was developed based on the U-Net, LU-Net models and our previous research, is a hybrid design. The proposed LUPU-Net architecture was evaluated on the IOSTAR dataset for retinal vessel segmentation. The preprocessing and data augmentation processes were applied to the images in the IOSTAR dataset before training. Under the same conditions, we compared the U-Net, LU-Net, and LUPU-Net models. The LUPU-Net architecture obtained improved results, especially for test samples.

The LUPU-Net model can also be evaluated on a variety of

retinal vessel datasets in the future. Furthermore, the LUPU-Net model can also be evaluated for different medical image segmentation tasks other than ophthalmology. Our proposal to use the up-sampling operation in the encoder section can be implemented into the other encoder-decoder architectures, and the results obtained from these models can be compared. The LUPU-Net model can be compared with the other traditional methods in the future.

Declaration

The authors declared no potential conflicts of interest with respect to the research, authorship, and/or publication of this article. The authors also declared that this article is original, was prepared in accordance with international publication and research ethics, and ethical committee permission or any special permission is not required.

Author Contributions

S. A. Arpacı performed the investigation, developed the software, wrote the original draft and improved the research. S. Varlı supervised and improved the research.

Nomenclature

<i>BN</i>	: Batch Normalization
<i>CNN</i>	: Convolutional Neural Network
<i>CLAHE</i>	: Contrast Limited Adaptive Histogram Equalization
<i>FCN</i>	: Fully Convolutional Networks
<i>FP</i>	: False Positive
<i>FN</i>	: False Negative
<i>HSV</i>	: Hue, Saturation, Value
<i>IoU</i>	: Intersection-Over-Union
<i>ReLU</i>	: Rectified Linear Unit
<i>Res-Net</i>	: Residual Network
<i>RGB</i>	: Red, Green, Blue
<i>SE-Net</i>	: Squeeze-and-Excitation Network
<i>SLO</i>	: Scanning Laser Ophthalmoscopy
<i>TP</i>	: True Positive
<i>TN</i>	: True Negative
<i>2D</i>	: Two-dimensional

References

1. McCulloch, W.S. and W. Pitts, *A logical calculus of the ideas immanent in nervous activity*. The Bulletin of Mathematical Biophysics, 1943. **5**: p. 115-133.
2. Aizenberg, I.N., N.N. Aizenberg, and J. Vandewalle, *Multi-Valued and Universal Binary Neurons: Theory, Learning and Applications*. 2000, USA: Kluwer Academic Publishers.
3. Fukushima, K., *Neocognitron: A self-organizing neural network model for a mechanism of pattern recognition unaffected by shift in position*. Biological Cybernetics, 1980. **36** (4): p. 193-202.
4. Simonyan, K. and A. Zisserman, *Very deep convolutional networks for large-scale image recognition*, in *3rd*

- International Conference on Learning Representations*, 2015, San Diego, CA: USA. p. 1-14.
5. Long, J., E. Shelhamer, and T. Darrell, *Fully convolutional networks for semantic segmentation*, in *The IEEE Conference on Computer Vision and Pattern Recognition*, 2015, Boston: USA. p. 3431-3440.
 6. Ronneberger, O., P. Fischer, and T. Brox, *U-Net: Convolutional networks for biomedical image segmentation*, in *Medical Image Computing and Computer-Assisted Intervention*, 2015, Munich: Germany. p. 234-241.
 7. Badrinarayanan, V., A. Kendall, and R. Cipolla, *SegNet: A deep convolutional encoder-decoder architecture for image segmentation*. *IEEE Transactions on Pattern Analysis and Machine Intelligence*, 2017. **39** (12): p. 2481-2495.
 8. Khan, T.M., S.S. Naqvi, M. Arsalan, M.A. Khan, H.A. Khan, et al., *Exploiting residual edge information in deep fully convolutional neural networks for retinal vessel segmentation*, in *International Joint Conference on Neural Networks*, 2020, Glasgow: United Kingdom. p. 1-8.
 9. Ozgunalp, U., R. Fan, and A. Serener, *Semantic segmentation of retinal vessels using SegNet*, in *28th Signal Processing and Communications Applications Conference*, 2020, Gaziantep: Turkey. p. 1-4.
 10. Xian-cheng, W., L. Wei, M. Bingyi, J. He, Z. Jiang, et al., *Retina blood vessel segmentation using a U-Net based convolutional neural network*, in *International Conference on Data Science*, 2018, Beijing: China. p. 1-11.
 11. Gao, X., Y. Cai, C. Qiu, and Y. Cui, *Retinal blood vessel segmentation based on the gaussian matched filter and U-Net*, in *10th International Congress on Image and Signal Processing, BioMedical Engineering and Informatics*, 2017, Shanghai: China. p. 1-5.
 12. Fu, W., K. Breininger, Z. Pan, and A. Maier, *Degenerating U-Net on retinal vessel segmentation*. [cited 2021 14 May]; Available from: https://doi.org/10.1007/978-3-658-29267-6_7.
 13. Mehta, R. and J. Sivaswamy, *M-Net: A convolutional neural network for deep brain structure segmentation*, in *IEEE 14th International Symposium on Biomedical Imaging*, 2017, Melbourne: Australia. p. 437-440.
 14. Li, L., M. Verma, Y. Nakashima, H. Nagahara, and R. Kawasaki, *IterNet: Retinal image segmentation utilizing structural redundancy in vessel networks*, in *IEEE Winter Conference on Applications of Computer Vision*, 2020, Colorado: USA. p. 3656-3665.
 15. Li, Q., S. Fan, and C. Chen, *An intelligent segmentation and diagnosis method for diabetic retinopathy based on improved U-Net network*. *Journal of Medical Systems*, 2019. **43**: p. 304.
 16. Cai, Y., Y. Li, X. Gao, and Y. Guo, *Retinal vessel segmentation method based on improved deep U-Net*, in *Chinese Conference on Biometric Recognition*, 2019, Zhuzhou: China. p. 321-328.
 17. He, K., X. Zhang, S. Ren, and J. Sun, *Deep residual learning for image recognition*, in *IEEE Conference on Computer Vision and Pattern Recognition*, 2016, Las Vegas: USA. p. 770-778.
 18. Li, D., D.A. Dharmawan, B.P. Ng, and S. Rahardja, *Residual U-Net for retinal vessel segmentation*, in *IEEE International Conference on Image Processing*, 2019, Taipei: Taiwan. p. 1425-1429.
 19. Xiao, X., S. Lian, Z. Luo, and S. Li, *Weighted Res-UNet for high-quality retina vessel segmentation*, in *9th International Conference on Information Technology in Medicine and Education*, 2018, Hangzhou: China. p. 327-331.
 20. Huang, G., Z. Liu, L. Van Der Maaten, and K.Q. Weinberger, *Densely connected convolutional networks*, in *IEEE Conference on Computer Vision and Pattern Recognition*, 2017, Honolulu: USA. p. 2261-2269.
 21. Cheng, Y., M. Ma, L. Zhang, C. Jin, L. Ma, and Y. Zhou, *Retinal blood vessel segmentation based on densely connected U-Net*. *Mathematical Biosciences and Engineering*, 2020. **17** (4): p. 3088-3108.
 22. Wang, C., Z. Zhao, Q. Ren, Y. Xu, and Y. Yu, *Dense U-Net based on patch-based learning for retinal vessel segmentation*. *Entropy*, 2019. **21** (2): p. 168.
 23. Zhou, Z., M.M. Rahman Siddiquee, N. Tajbakhsh, and J. Liang, *UNet++: A nested U-Net architecture for medical image segmentation*, in *4th International Workshop on Deep Learning in Medical Image Analysis*, 2018, Granada: Spain. p. 3-11.
 24. Arpacı, S.A. and S. Varlı, *Retinal vessel segmentation with differentiated U-Net network*, in *28th Signal Processing and Communications Applications Conference*, 2020, Gaziantep: Turkey. p. 1-4.
 25. Zhang, J., J. Du, H. Liu, X. Hou, Y. Zhao, et al., *LU-NET: An improved U-Net for ventricular segmentation*. *IEEE Access*, 2019. **7**: p. 92539-92546.
 26. Hu, J., L. Shen, and G. Sun, *Squeeze-and-excitation networks*, in *IEEE/CVF Conference on Computer Vision and Pattern Recognition*, 2018, Salt Lake City: USA. p. 7132-7141.
 27. Kingma, D.P. and J.L. Ba, *ADAM: A method for stochastic optimization*. [cited 2021 14 May]; Available from: <https://arxiv.org/pdf/1412.6980.pdf>.
 28. Keras library. [cited 2021 14 May]; Available from: <https://keras.io/>.
 29. TensorFlow library. [cited 2021 14 May]; Available from: <https://www.tensorflow.org/>.
 30. IOSTAR retinal vessel segmentation dataset. [cited 2019 5 April]; Available from: <http://www.retinacheck.org/download-iostar-retinal-vessel-segmentation-dataset>.
 31. Zhang, J., B. Dashtbozorg, E. Bekkers, J.P.W. Pluim, R. Duits, et al., *Robust retinal vessel segmentation via locally adaptive derivative frames in orientation scores*. *IEEE Transactions on Medical Imaging*, 2016. **35** (12): p. 2631-2644.
 32. Abbasi-Sureshjani, S., I. Smit-Ockeloen, J. Zhang, and B. Ter Haar Romeny, *Biologically-inspired supervised vasculature segmentation in SLO retinal fundus images*, in *12th International Conference Image Analysis and Recognition*, 2015, Niagara Falls: Canada. p. 325-334.
 33. Zhou, M., K. Jin, S. Wang, J. Ye, and D. Qian, *Color retinal image enhancement based on luminosity and contrast adjustment*. *IEEE Transactions on Biomedical Engineering*, 2018. **65** (3): p. 521-527.
 34. OpenCV library. [cited 2021 14 May]; Available from: <https://opencv.org/>.
 35. Bloice, M.D., C. Stocker, and A. Holzinger, *Augmentor: An Image Augmentation Library for Machine Learning*. [cited 2021 14 May]; Available from: <https://arxiv.org/abs/1708.04680>.
 36. Soomro, T.A., A. J. Afifi, J. Gao, O. Hellwich, M. Paul, and L. Zheng, *Strided U-Net Model: Retinal Vessels Segmentation using Dice Loss*, in *Digital Image Computing*:

- Techniques and Applications*, 2018, Canberra: Australia. p. 1-8.
37. Sorensen, T., *A method of establishing groups of equal amplitude in plant sociology based on similarity of species content and its application to analyses of the vegetation on Danish commons*. Biologiske Skrifter, 1948.5: p.1–34.
 38. Jaccard, P., *Lois de distribution florale dans la zone alpine*. Bull. Société Vaudoise Sci. Nat., 1902. **38**: p. 69–130.
 39. Meyer, M.I., P. Costa, A. Galdran, A.M. Mendonça, and A. Campilho, *A deep neural network for vessel segmentation of scanning laser ophthalmoscopy images*, in *International Conference on Image Analysis and Recognition*, 2017, Montreal: Canada. p. 507-515.
 40. Guo, C., M. Szemenyei, Y. Yi, Y. Xue, W. Zhou, et al., *Dense residual network for retinal vessel segmentation*, in *IEEE International Conference on Acoustics, Speech and Signal Processing*, 2020, Barcelona: Spain. p. 1374-1378.
 41. Brea, L.S., D.A. De Jesus, S. Klein, and Tv. Walsum, *Deep learning-based retinal vessel segmentation with cross-modal evaluation*, in *Proceedings of the Third Conference on Medical Imaging with Deep Learning*, 2020, Montreal: Canada. p. 709-720.
 42. Kim, J.U., H.G. Kim, and Y.M. Ro, *Iterative deep convolutional encoder-decoder network for medical image segmentation*, in *39th Annual International Conference of the IEEE Engineering in Medicine and Biology Society*, 2017, Jeju: Korea (South). p. 685-688.
 43. Khan, K.B., A.A. Khaliq, A. Jalil, M.A. Iftikhar, N. Ullah, et al., *A review of retinal blood vessels extraction techniques: challenges, taxonomy, and future trends*. Pattern Analysis and Applications, 2019. **22** (3): p. 767-802.
 44. Oliveira, A., S. Pereira, and C.A. Silva, *Augmenting data when training a CNN for retinal vessel segmentation: How to warp?*, in *IEEE 5th Portuguese Meeting on Bioengineering*, 2017, Coimbra. p. 1-4.
 45. Arpacı, S.A. and S. Varlı, *Diabetic retinopathy classification with deep learning*, in *4th International Scientific Research Congress*, 2019, Yalova: Turkey. p. 311-321.



Research Article

Design and implementation of FPGA-based arrhythmic ECG signals using VHDL for biomedical calibration applications

Fatih Karataş^{a,*} , İsmail Koyuncu^b , Murat Alçın^c  and Murat Tuna^d 

^aAfyon Kocatepe University, Graduate School of Natural and Applied Sciences, Afyonkarahisar 03200, Turkey

^bAfyon Kocatepe University, Faculty of Technology, Department of Electrical and Electronics Engineering, Afyonkarahisar 03200, Turkey

^cAfyon Kocatepe University, Faculty of Technology, Department of Mechatronics, Afyonkarahisar 03200, Turkey

^dKırklareli University, Technical Sciences Vocational High School, Department of Electrical and Energy, Kırklareli 39000, Turkey

ARTICLE INFO

ABSTRACT

Article history:

Received 16 April 2021

Revised 21 June 2021

Accepted 08 July 2021

Keywords:

Arrhythmia

Calibration

ECG

FPGA

Signal Processing

VHDL

Biomedical applications are one of the important research areas of recent years. One of these fields of study is biomedical signals. In this study, the Normal Sinus Rhythm and three arrhythmic ECG signals (Ventricular Tachycardia, Ventricular Paced and Atrial Flutter), one of the vital sign signals, were designed and implemented to work on FPGA chips using the Xilinx-Vivado program with VHDL. Matlab-based ECG signals were taken as a reference and compared with the results obtained from the FPGA-based ECG signals design. Then, the structure used in the design and the test results obtained from the study have been presented. The designed ECG signals were synthesized for the Zynq-7000 XC7Z020 FPGA and observed from the oscilloscope using the 14-channel AN9767 DA module. FPGA chip resource consumption values obtained after the Place-Route process are presented. According to the results, the maximum operating frequency of Normal Sinus Rhythm and Ventricular tachycardia signals on the FPGA was 657.614 MHz and the maximum operating frequency of the Ventricular Paced and Atrial Flutter signals on the FPGA was 651.827 MHz. The maximum MSE value obtained from FPGA-based ECG signal design is 1.2319E-02. In this study, it has been shown that the FPGA-based ECG signal generation system, which is implemented as hardware, can be designed using FPGA chips and can be safely used in biomedical calibration applications. Other arrhythmic ECG signals can be designed and implemented using similar methods in future studies.

1. Introduction

Situations such as heart health, trying to solve problems related to heart health and early diagnosis in every period of life are issues that should be highlighted. One of these issues is Electrocardiography (ECG) and the signals of these values constitute the data groups that should be followed in the first place about the patient [1].

Calibration is a series of measurements used to measure the accuracy, determine and document deviations of another test and measuring instrument using a measurement standard or system of known accuracy under specified conditions. The importance of calibration becomes clearer if we estimate what it will cost in a sector that is difficult to return, such as health, because a medical device that makes an erroneous measurement adversely

affects the diagnostic process. With calibration: The accuracy of all measurements performed is ensured. Production quality is increased to the desired level. Any deviations and errors that may arise during the production stages are detected and corrected in advance. It is ensured that the products are compatible with other company products. The possibility of competition increases. The opportunity to catch and use advanced technology is provided. The manufactured product is in compliance with international standards. Unfair profit from the customer or gaining unfair advantage to the customer is prevented. Our health is evaluated with correct diagnosis and treatment opportunities. All devices used in health institutions must be subjected to a calibration process within certain periods. The devices used for this purpose are called medical calibrator devices. The calibrator whose design is

* Corresponding author. Tel.: +90-272- 218-14-60; Fax: +90-272- 218-14-62.

E-mail addresses: fatihkaratas@usr.aku.edu.tr (F. Karataş), ismailkoyuncu@aku.edu.tr (İ. Koyuncu), muratalcin@aku.edu.tr (M. Alçın), murattuna@klu.edu.tr (M. Tuna)

ORCID: 0000-0003-1877-5552 (F. Karataş), 0000-0003-4725-4879 (İ. Koyuncu), 0000-0002-2874-7048 (M. Alçın), 0000-0003-3511-1336 (M. Tuna)

DOI: 10.35860/iarej.918874

© 2021, The Author(s). This article is licensed under the CC BY-NC 4.0 International License (<https://creativecommons.org/licenses/by-nc/4.0/>).

mentioned in this study is the ECG Simulator [2].

Field Programmable Gate Arrays (FPGA) are widely accepted in medical systems due to their capabilities such as rapid prototyping, reprogramming, parallel processing and high performance of a concept that requires co-design as hardware or software [3].

Very successful studies are carried out with FPGA chips in the field of signal processing using digital hardware [4].

In the literature, the signals used in the studies of the ECG and vital signs signals on FPGA chips: These are analog signals recorded with medical devices such as ECG, patient monitor, or rhythm holer [5].

Hundreds of signal samples taken at various times from people with different types of ailments in different regions were used from national/international databases [6].

Studies conducted in this area are generally in the form of taking ECG signals from databases, which were previously recorded from the patient, non-artificial, real signals and applying them to FPGA chips with the help of Analog Digital Converter (ADC) and Digital Analog Converter (DAC) [7]. Studies on these signals received from the patient; Heart rate calculation [8], detection of rhythm disturbances [9], detection of peak on the signal [10], normalization of noisy ECG signals by applying filters such as Finite Impulse Response (FIR) [11], Quadrature Mirror Filters (QMF) and Infinite Impulse Response (IIR) [12], ECG signal filtering in FPGA [13], classification of ECG signals with the Discrete Wavelet Transform (DWT) method for the detection of the QRS (The three graphs (Q wave, R wave, and S wave) found in a typical ECG are a combination of the deviation) complex [14].

ECG Simulators are commonly performed with microcontrollers [15–20]. However, these do not work in parallel like FPGA chips, they work in series.

As can be seen in the literature research, the studies of vital signs and ECG signals using FPGA technology are in the form of recording these signals from the human body through a medical device, storing them in databases and taking them from there and using them if needed.

In this study, four ECG signals (Normal Sinus Rhythm, Ventricular Tachycardia, Ventricular Paced and Atrial Flutter) are modeled by presenting a new approach on FPGA [21]. In the first place, ECG signals were mathematically designed and observed in Matlab. Then, ECG signals have been modeled for using in FPGA chips in Xilinx-Vivado with Very High-Speed Integrated Circuits (VHSIC) Hardware Description Language (VHDL), which is a structural hardware description language. After that, these signals were compared with Matlab-based signals and the error values obtained from the comparison were presented. Information was given about the FPGA chip and DAC used in the design. Oscilloscope images of the obtained signals are shown.

The working frequencies of the FPGA-based ECG signal generation system and the chip statistics obtained from the design are presented. In the second part of the study, information about ECG signals, FPGA chips and system components are given. In the third part, FPGA-based ECG signal design and FPGA chip statistics obtained from the design are given. In the last part, the results obtained from the design are evaluated.

2. Background Information

2.1 ECG Signal

The process of recording and interpreting the systole and diastole phases of the atrium and ventricles of the heart, the electrical activity that occurs during the stimulation and transmission of the heart on a moving millimeter paper by magnifying the electrical potential created by the heart tissue is called Electrocardiography, the recording device is called Electrocardiograph and the signal obtained is called Electrocardiogram [22].

This Non-invasive method has been developed to examine the operation of the heart muscle and the neural conduction system of the heart, to diagnose and then to apply the correct treatment, heart enlargement, reduction in the amount of blood to the heart, observation of problems in the heart valves, new or old heart damage, heart rhythm problems. Also, it can provide important information about many cardiac and pericardial diseases that carry the risk of premature death. Therefore, ECG, signal processing and modeling are considered as some of the most important issues in biomedical applications [23].

ECG signal; It is a normal sinus rhythm as shown in Figure 1 consisting of waves, segments and intervals. Waves; P, Q, R, S, T and U wave. Segments; PR-Segment and ST-Segment. Intervals; QT-interval, PR-interval, RR-interval. These values vary in arrhythmic signals [24]. In this study, Normal Sinus Rhythm (NSR) and three arrhythmic ECG signals (Ventricular Tachycardia, Ventricular Paced and Atrial Flutter) were used as a reference in FPGA design. NSR is shown in Figure 2, Ventricular Tachycardia in Figure 3, Ventricular Paced in Figure 4, and Atrial Flutter in Figure 5, respectively [25].

2.2 Development FPGA Board and System Components

FPGAs are digital Integrated Circuits (IC) with re-programmable features, whose hardware structure can be changed by the user/designer according to the desired function after production. It stands out with its features such as parallel processing, low power consumption, rapid initial prototyping, high operating frequency and high performance compared to other platforms [26]. FPGA chips can be programmed in coding languages such as VHDL, Verilog, Handel-C and System C [27].

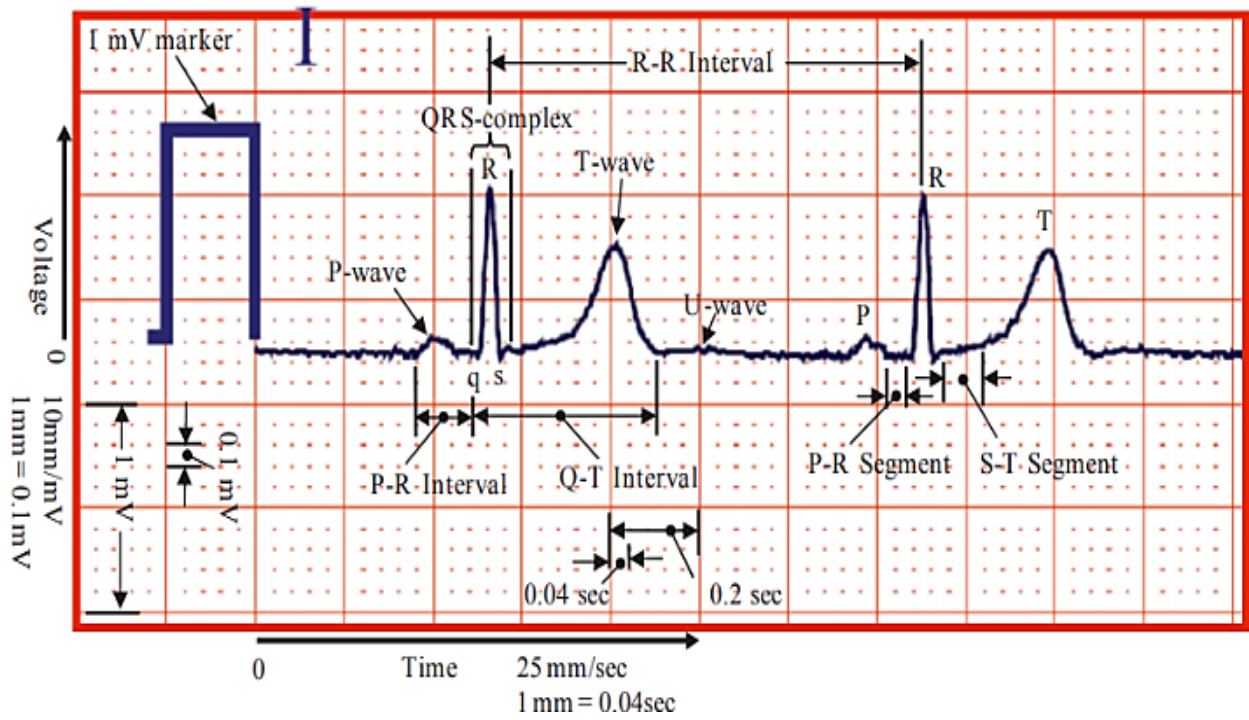


Figure 1. Typical ECG of a normal person



Figure 2. Normal Sinus Rhythm (NSR)



Figure 4. Ventricular Paced



Figure 3. Ventricular Tachycardia

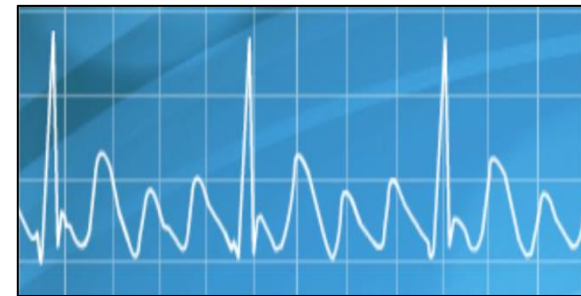


Figure 5. Atrial Flutter

An FPGA consists of three programmable components: configurable logic blocks (CLB), input-output blocks (IOB) and interconnection networks. It consists of various elements such as Look-Up Table (LUT) where logical functions can be created, Flip-Flops where single-bit information can be stored and Multiplexers that direct the information flow. Figure 6 shows the FPGA components [28].

FPGA chips are widely used in many areas in recent years. These working areas are; Artificial Neural Networks (ANN) [29], fuzzy logic applications [30], chaotic oscillator design

[31], Pseudo and True Random Number Generators [32], robotics [33], space, aviation and defense industry [34], purpose-built integrated prototypes such as Application Specific Integrated Circuit (ASIC), audio, automotive industry, press and media, consumer electronics, data center, high-performance computing and data storage industry, video and image processing, wired/wireless communication, biomedical applications and medical devices [35-39].

This study was carried out using the Zynq-7000 SoC XC7Z020 FPGA development board shown in Figure 7 and the 14-bit AN9767 DAC module shown in Figure 8.

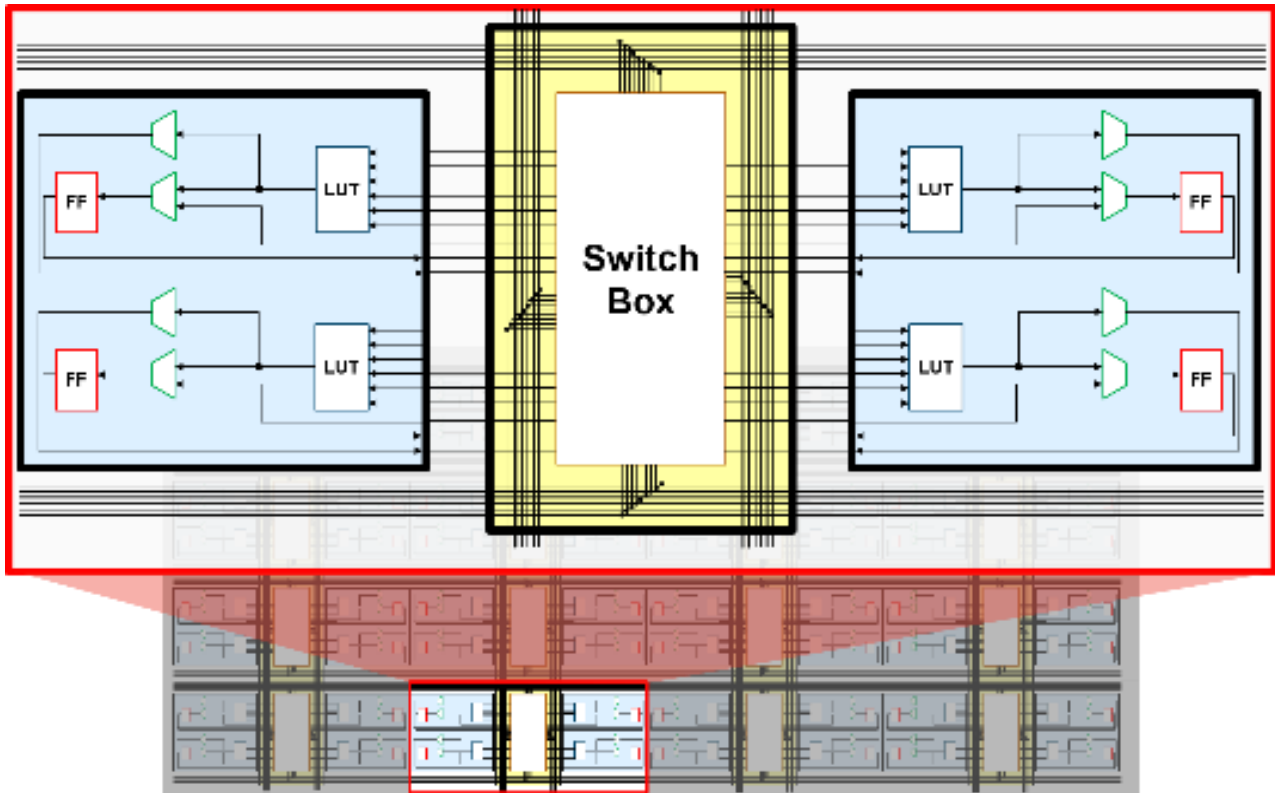


Figure 6. FPGA architecture

The AX7020 FPGA development board uses Xilinx's Zynq7000 series of chips, model XC7Z020-2CLG400I, in a 40-pin FPGA package. The ZYNQ7000 chip can be divided into a Processor System part (PS) and a Programmable Logic part (PL). On the AX7020 development board, the PS and PL sections of the ZYNQ7000 are equipped with a wealth of external interfaces and devices for user convenience and functional verification [40].

3. FPGA-based design of ECG Signals

The system is designed as a block that generates an ECG signal according to parameters in Xilinx-Vivado software using VHDL. The working logic of the system as follows; The results of the mathematical equations created within the scope of the study (functions that calculate ECG values) are recorded in LUTs (Look-Up Table). Then, by creating a phase register, the phase register increases with every rising clock signal and this increased value is modeled to load the values in the LUT and transfer them to the output. This situation is repeated in each period during the clock.

Firstly, Normal Sinus Rhythm (NSR) with 72 bpm heart rate, Ventricular Tachycardia signal with 210 bpm heart rate, Ventricular Paced signal with 75 bpm heart rate and Atrial Flutter signal with 150 bpm heart rate have been modeled in Matlab in accordance with time and amplitude values. The NSR signal modeled in Matlab is shown in Figure 9, the Ventricular Tachycardia signal in Figure 10, the Ventricular Paced signal in Figure 11, and the Atrial Flutter signal in Figure 12.



Figure 7. ALINX AX7020: Zynq-7000 SoC XC7Z020 FPGA Development Board

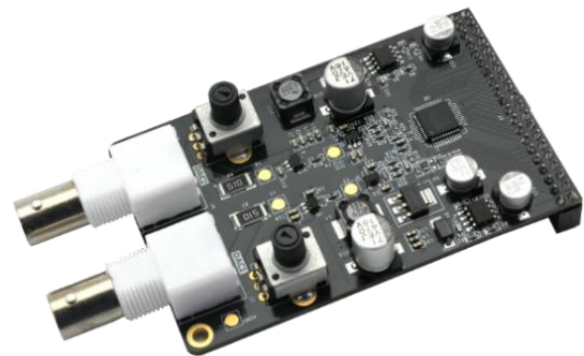


Figure 8. 14-bit Dual Port DAC Output Module AN9767

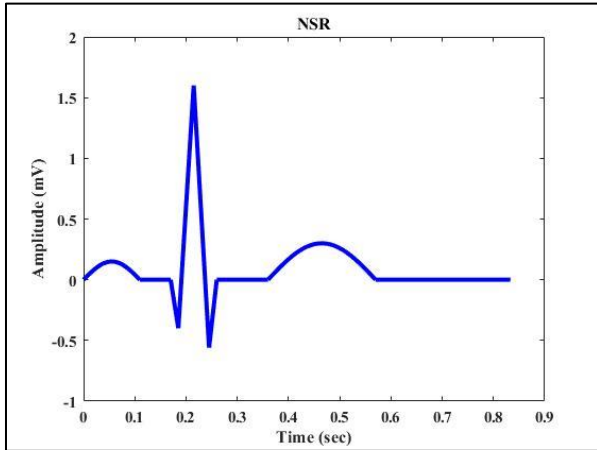


Figure 9. Normal Sinus Rhythm (NSR) with 72 bpm heart rate in Matlab

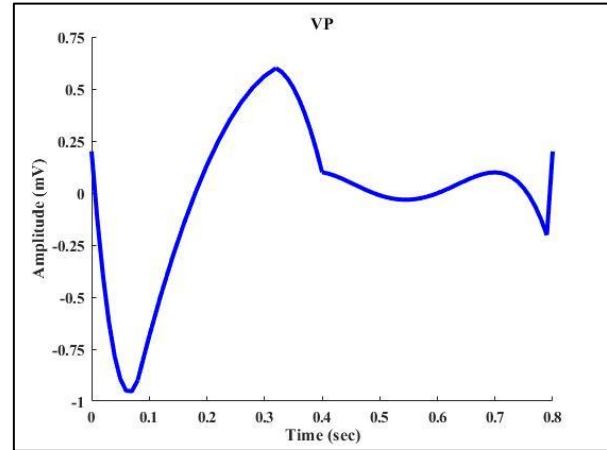


Figure 11. Ventricular Paced signal with 75 bpm heart rate in Matlab

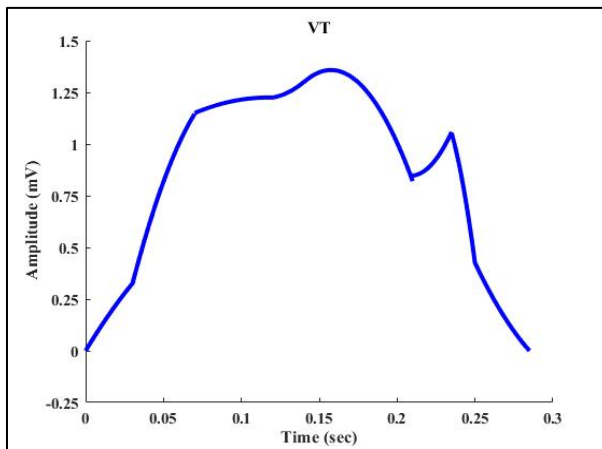


Figure 10. Ventricular Tachycardia signal with 210 bpm heart rate

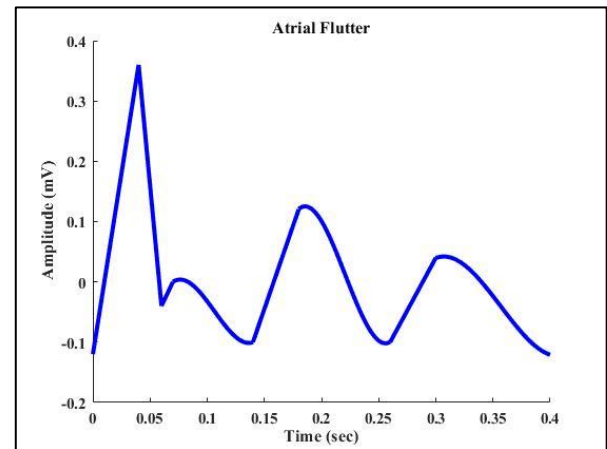


Figure 12. Atrial Flutter signal with 150 bpm heart rate in Matlab

The mathematical equation of the P wave generation of the ECG signal, which is called Normal Sinus Rhythm and whose heart rate is designed as 72 bpm per minute, is shown in Equation (1) in Table 1. In addition, the generations of PR-segment, QRS complex, ST-segment and T wave are illustrated in Equation (2), Equation (3), Equation (4) and Equation (5), respectively. The stationary period from the last part of the T wave to the beginning of the P wave of the next ECG signal is given in Equation (6). The amplitude and time parameters of the NSR are shown in Table 2 and Table 3, respectively.

Then, these four ECG signals were designed in the Xilinx-Vivado program using VHDL. The signals observed on the Vivado simulation screen, namely the NSR signal, are shown in Figure 13, the Ventricular Tachycardia signal in Figure 14, the Ventricular Paced signal in Figure 15, and the Atrial Flutter signal in Figure 16.

The first-order block diagram of the top module of the FPGA-based ECG signal generation system designed to operate on the FPGA chip is given in Figure 17. The second-order block diagram of the system for NSR and the block producing the ECG Signal are given in Figure 18.

Table 1. Mathematical equations for the NSR designed in Matlab

$x_1 = 0:0.005:p_int$ $y_1 = p_peak * \sin(x_1 * \frac{\pi}{p_int})$	(1)
$x_2 = p_int:0.01:pr_int$ $y_2 = 0 * x_2$	(2)
$q_1 = pr_int + 0.015$ $x_3 = pr_int:0.005:q_1$ $y_3(Q\ wave) = -26.667 * x_3 + 4.53333$ $r_1 = pr_int + 0.045$ $x_4 = q_1:0.005:r_1$ $y_4(R\ wave) = 66.667 * x_4 - 12.733$ $s_1 = pr_int + 0.075$ $x_5 = r_1:0.005:s_1$ $y_5(S_1\ wave) = -72 * x_5 + 17.08$ $s_2 = pr_int + qrs_int$ $x_6 = s_1:0.005:s_2$ $y_6(S_2\ wave) = 37.333 * x_6 - 9.706$	(3)
$t_1 = pr_int + qrs_int + st_seg$ $x_7 = s_2:0.01:t_1$ $y_7 = 0 * x_7$	(4)
$t_2 = pr_int + qt_int$ $x_8 = t_1:0.005:t_2$ $y_8 = t_peak * \sin((x_8 - t_1) * \frac{\pi}{t_2 - t_1})$	(5)
$delay = h - t_2$ $x_9 = t_2:0.01:h$ $y_9 = 0 * x_9$	(6)

Table 2. Amplitude parameters of NSR

NSR parameters	Amplitude (mV)
P wave (p_peak)	0.15
Q wave (q_peak)	0.40
R wave (r_peak)	1.60
S wave (s_peak)	0.56
T wave (t_peak)	0.30

Table 3. Time parameters of NSR

NSR parameters	Time (sec.)
P wave (p_int)	0.11
PR-interval (pr_int)	0.17
PR-segment (pr_seg)	0.06
ST-segment (st_seg)	0.10
QT-interval (qt_int)	0.40
QRS complex (qrs_int)	0.09
T wave (t_int)	0.21

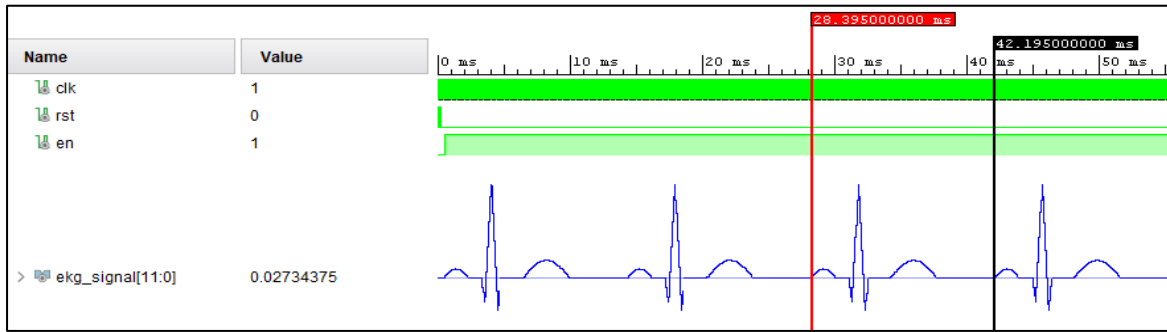


Figure 13. Vivado Simulation of NSR

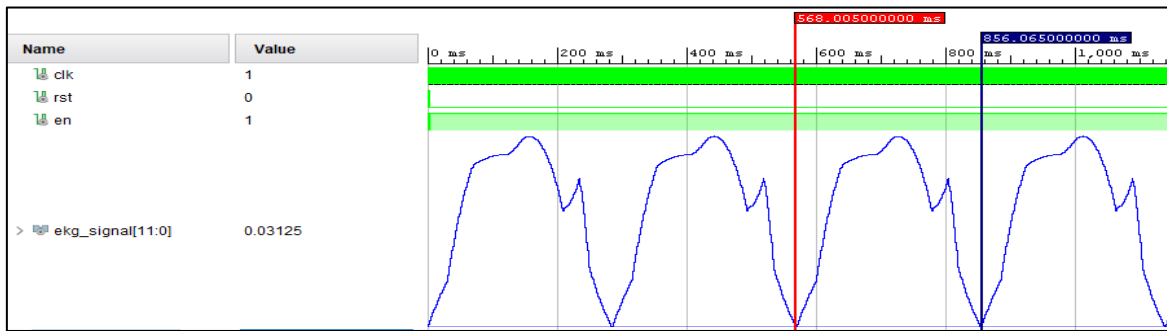


Figure 14. Vivado Simulation of Ventricular Tachycardia

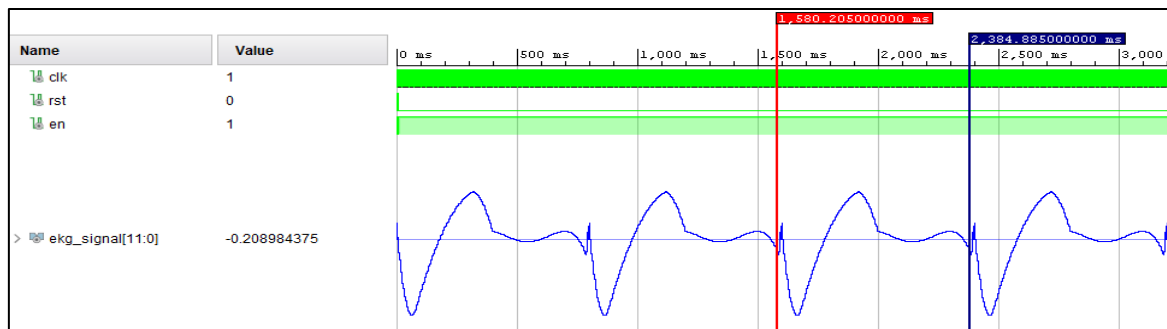


Figure 15. Vivado Simulation of Ventricular Paced

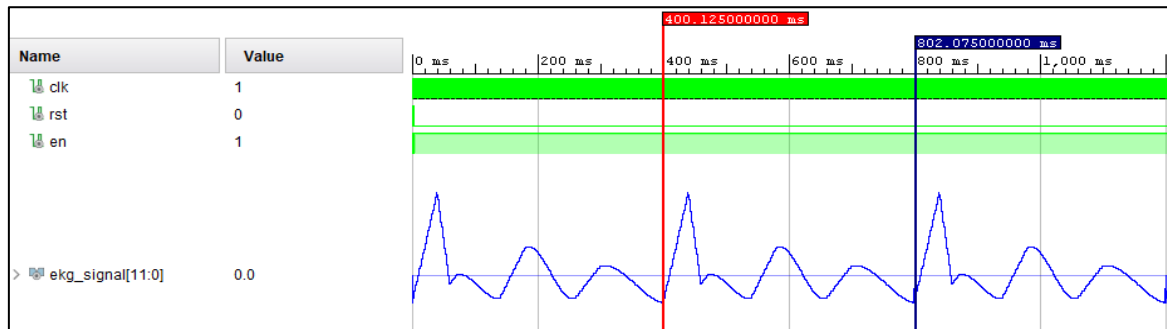


Figure 16. Vivado Simulation of Atrial Flutter

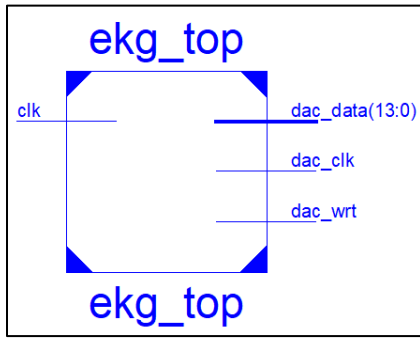


Figure 17. The first-order block diagram of the system top module

The designed ECG signals were synthesized for Zynq-7000 XC7Z020 FPGA and observed over the

oscilloscope using the 14-channel AN9767 DA module. The NSR signal observed from the oscilloscope is given in Figure 19, the Ventricular Tachycardia signal in Figure 20, the Ventricular Paced signal in Figure 21, and the Atrial Flutter signal in Figure 22, respectively.

Matlab-based ECG signals were taken as a reference and compared with the results obtained from the FPGA-based ECG signals design and this comparison is shown in Table 4. As a result of this comparison, the maximum MSE value for the NSR signal obtained from the FPGA-based ECG signal design is 1.2319E-02, the MSE value for the Ventricular Tachycardia signal is 8.5333E-07, the MSE value for the Ventricular Paced signal is 2.9538E-05, and the Atrial Flutter MSE value is 3.3255E-03.

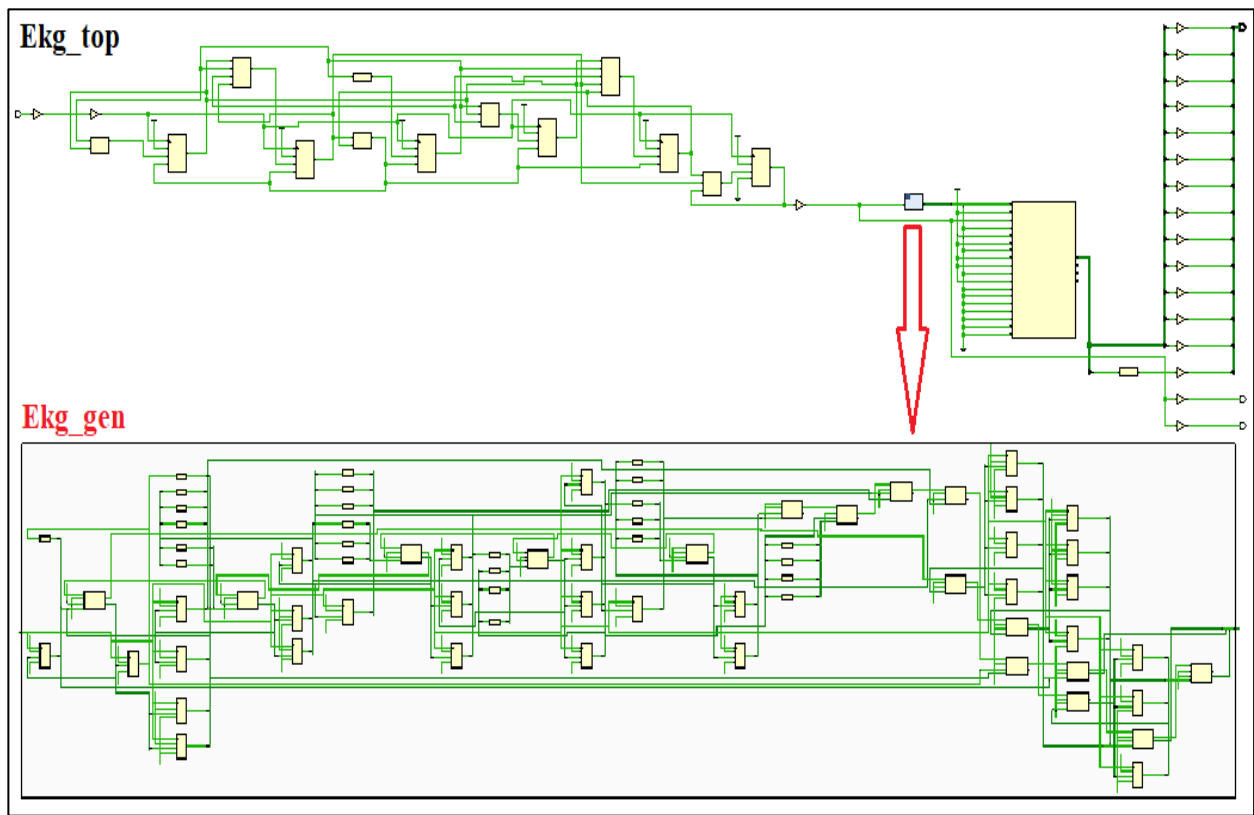


Figure 18. The second-order block diagram of the system for NSR and the block generating the ECG Signal



Figure 19. NSR observed on oscilloscope



Figure 20. Ventricular Tachycardia observed on oscilloscope



Figure 21. Ventricular Paced observed on oscilloscope



Figure 22. Atrial Flutter observed on oscilloscope

The usage statistics for the Zynq-7000 chip of the FPGA-based ECG signal generation system obtained after the Place-Route process are given in Table 5. According to the results, the maximum operating frequency of NSR and VT signals on FPGA was determined as 657.614 MHz. The maximum operating frequency of VP and Atrial Flutter on FPGA has been determined as 651.827 MHz.

4. Conclusions

In this study, Normal Sinus Rhythm, one of the vital signs for biomedical calibration applications and three arrhythmic ECG signals (Ventricular Tachycardia, Ventricular Paced and Atrial Flutter) were designed and implemented to work on FPGA chips using the Xilinx-Vivado program with VHDL. These signals were first mathematically modeled in Matlab and the accuracy of the obtained graphics was compared and evaluated in accordance with the literature. Later, in the Xilinx-Vivado program, using VHDL, the verified signals in Matlab were designed. Matlab-based ECG signals were taken as a reference and compared with the results obtained from the FPGA-based ECG signals design. As a result of this comparison, the maximum MSE value obtained from the FPGA-based ECG signal design is 1.2319E-02. The designed ECG signals were synthesized for Zynq-7000 XC7Z020 Alinx FPGA and observed from the oscilloscope using the 14-channel AN9767 DAC module. FPGA chip resource consumption values obtained after the Place-Route process are presented.

Table 4. The comparison of Normal Sinus Rhythm in Matlab and Vivado

NSR	Time (sec.)		Amplitude (mV)	
	Matlab & Vivado		Matlab	Vivado
P wave	0.00000	0.00000	0.00000	0.00000
	0.00500	0.02135	0.02148	0.02148
	0.01000	0.04225	0.04101	0.04101
	0.02000	0.08109	0.08007	0.08007
	0.03000	0.11336	0.11328	0.11328
	0.03500	0.12618	0.12695	0.12695
	0.04000	0.13644	0.13671	0.13671
	0.04500	0.14392	0.14453	0.14453
	0.05000	0.14847	0.14843	0.14843
	0.05500	0.15000	0.15039	0.15039
	0.06000	0.14847	0.14843	0.14843
	0.07000	0.13644	0.13671	0.13671
	0.08000	0.11336	0.11328	0.11328
	0.09000	0.08109	0.08007	0.08007
	0.09500	0.06231	0.06445	0.06445
	0.10000	0.04225	0.04101	0.04101
	0.10500	0.02134	0.02148	0.02148
	PR segment	0.11000	0.00183	0.00000
0.17000		0.00000	0.00000	0.00000
QRS wave	0.17500	-0.13339	-0.13281	-0.13281
	0.18000	-0.26673	-0.26367	-0.26367
	0.18500	-0.40006	-0.41796	-0.41796
	0.20000	0.60040	0.61328	0.61328
	0.20500	0.93373	0.93945	0.93945
	0.21000	1.26707	1.26367	1.26367
	0.22000	1.24000	1.25976	1.25976
	0.23000	0.52000	0.49804	0.49804
	0.23500	0.98800	0.96679	0.96679
	0.24000	-0.20000	-0.20507	-0.20507
	0.25000	-0.37270	-0.37890	-0.37890
	0.25500	-0.18610	-0.19726	-0.19726
ST segment	0.26000	0.00000	0.00000	0.00000
	0.36000	0.00000	0.00000	0.00000
T wave	0.37000	0.04470	0.42968	0.42968
	0.39000	0.13020	0.12890	0.12890
	0.41000	0.20410	0.20507	0.20507
	0.42000	0.23450	0.23437	0.23437
	0.44000	0.27930	0.27929	0.27929
	0.45000	0.29250	0.29296	0.29296
	0.46000	0.29920	0.29882	0.29882
	0.47000	0.29920	0.29882	0.29882
	0.48000	0.29250	0.29296	0.29296
	0.50000	0.25980	0.25976	0.25976
	0.51000	0.23450	0.23437	0.23437
	0.52000	0.20410	0.20312	0.20312
	0.53000	0.16900	0.16992	0.16992
	0.54000	0.13200	0.13281	0.13281
	0.55000	0.08840	0.08789	0.08789
0.56000	0.04470	0.04492	0.04492	
Stationary period	0.57000	0.00000	0.00000	0.00000
	0.83000	0.00000	0.00000	0.00000

According to the results, the maximum operating frequency of Normal Sinus Rhythm and Ventricular tachycardia signals on the FPGA was 657.614 MHz and the maximum operating frequency of the Ventricular Paced and Atrial Flutter signals on the FPGA was 651.827 MHz. With this study, it has been shown that the hardware designed FPGA-based ECG signal generation system can be designed using FPGA chips, can be utilized safely in biomedical calibration applications and can be used in ECG Simulators used for calibration tests of medical devices in the field of cardiology.

Table 5. The usage statistics for the Zynq-7000 chip of FPGA based ECG signal generation system

Logic Utilization / Usage rate	NSR	Ventricular Tachycardia	Ventricular Paced	Atrial Flutter
Number of BUFCTRLs	2 / %6.25	2 / %6.25	2 / %6.25	2 / %6.25
Number of Slice LUTs	39 / %0.073	39 / %0.073	40 / %0.075	40 / %0.075
Number of Slice Registers	38 / %0.035	38 / %0.035	39 / %0.036	39 / %0.036
Maximum Operating Frequency (MHz)	657.614	657.614	651.827	651.827
Mean Squared Error (MSE)	1.2319E-02	8.5333E-07	2.9538E-05	3.3255E-03

In future studies, other arrhythmic ECG signals can be modeled using similar methods and also vital sign signals such as SPO₂, ETCO₂ and blood pressure can be added to increase the variety of signals to be used for calibration.

Declaration

The author(s) declared no potential conflicts of interest with respect to the research, authorship and/or publication of this article. The author(s) also declared that this article is original, was prepared in accordance with international publication and research ethics and ethical committee permission or any special permission is not required.

Author Contributions

All the authors have equally contributed.

Acknowledgment

This study is sponsored by the Scientific and Technological Research Council of Turkey (TUBITAK) with project number 119E659.

References

- Do Vale Madeiro, J.P., Cortez, P.C., Salinet, J.L., Pedrosa, R.C., da Silva Monteiro Filho, J.M., and Brayner, A.R.A., *Classical and Modern Features for Interpretation of ECG Signal*, Developments and Applications for ECG Signal Processing: Modeling, Segmentation, and Pattern Recognition, Elsevier, 2019. p. 1–28.
- Yang, S., Lam, B., and Ng, C.M.N., *Calibration of Electrocardiograph (ECG) Simulators*. NCSLI Measure, 2018. **12**(1): p. 46–53.
- Koyuncu, İ., Özcerit, A.T., Pehlivan, İ., and Avarođlu, E., *Design and implementation of chaos based true random number generator on FPGA*. In 2014 22nd IEEE Signal Processing and Communications Applications Conference, 2014. p. 236–239.
- Meyer-Base, U., *Introduction., Digital Signal Processing with Field Programmable Gate Arrays*, Berlin, Heidelberg, 2014. p. 1–52.
- Life in the fast lane. *ECG Library Basics*. [cited 2021 11 February]; Available from: <https://litfl.com/ecg-library/>.
- PhysioNet. *The research resource for complex physiologic signals. Physio Bank ATM, MIT, and BIH Arrhythmia Database*. [cited 2021 11 February]; Available from: <https://archive.physionet.org/>.
- Kumar, S., Singh, G., and Kaur, M., *FPGA Implementation of Electrocardiography (ECG) Signal Processing 1*. An International Journal of Engineering Sciences, 2016. p. 2229–6913.
- Desai, V., *Electrocardiogram (ECG/EKG) using FPGA*, San Jose State University, Computer Science, Master's Thesis, USA, 2012. p. 11-15.
- Madiraju, N.S., Kurella, N., and Valapudasu, R., *FPGA Implementation of ECG Feature Extraction Using Time Domain Analysis*. Electrical Engineering and Systems Science, Signal Processing (eess.SP); Hardware Architecture (cs.AR), 2018. arXiv:1802.03310
- Agrawal, A., and Gawali, D.H., *FPGA-Based Peak Detection of ECG Signal Using Histogram Approach*, International Conference on Recent Innovations in Signal Processing and Embedded Systems, RISE 2017, Institute of Electrical and Electronics Engineers Inc., 2017. p. 463–468.
- Alhelal, D., and Faezipour, M., *Denoising and Beat Detection of ECG Signal by Using FPGA*. International Journal of High Speed Electronics and Systems, 2017. **26**(3): p. 1740016.
- Su, W., Liang, Y., Li, M., and Li, Y., *The Research and FPGA Implementation of ECG Signal Preprocessing*, International Conference on Biomedical and Health Informatics, IFMBE Proceedings, Springer Verlag, Singapore, 2018. p. 167–168.
- Popa, R., *ECG Signal Filtering in FPGA*, 2019 6th International Symposium on Electrical and Electronics Engineering, ISEEE 2019, Galati, Romania, 2019. p. 1-6.
- Egila, M.G., El-Moursy, M.A., El-Hennawy, A. E., El-Simary, H.A., and Zaki, A., *FPGA-Based Electrocardiography (ECG) Signal Analysis System Using Least-Square Linear Phase Finite Impulse Response (FIR) Filter*. Journal of Electrical Systems and Information Technology, 2016. **3**(3): p. 513–526.
- Shirzadfar, H., and Khanahmadi, M., *Design and Development of ECG Simulator and Microcontroller Based Displayer*. Journal of Biosensors & Bioelectronics, 2018. **9**(3): p. 1–9.
- Cho, S., Lee, Y., and Chang, I., *Designing a Novel ECG Simulator: Multi-Modality Electrocardiography into a Three-Dimensional Wire Cube Network*. IEEE Technology and Society Magazine, 2016. **35**(1): p. 75–84.
- Paul, A.D., Urzoshi, K.R., Datta, R.S., Arsalan, A., Azad, A.M., *Design and Development of Microcontroller Based ECG Simulator*, In: Osman, N.A.A., Abas, W.A.B.W., Wahab, A.K.A., Ting, HN. (eds) 5th Kuala Lumpur International Conference on Biomedical Engineering, IFMBE Proceedings, Berlin, Heidelberg, 2011. **35**: p. 292-295.
- Jun-an, Z., *The Design of ECG Signal Generator using PIC24F*, Procedia Engineering, International Conference on Advances in Engineering, 2011. **24**: p. 523-527.
- Chien, J.R.C., *Design of a Programmable Electrocardi-*

- ogram Generator Using a Microcontroller and the CPLD Technology, IECON Proceedings (Industrial Electronics Conference), IEEE Computer Society, 2007. p. 2152–2157.
20. Caner, C., Engin, M., and Engin, E.Z., *The Programmable ECG Simulator*. Journal of Medical Systems, 2008. **32**(4): p. 355–359.
 21. Karatas, F., Koyuncu, I., Alçın, M., and Tuna, M., *Design of FPGA-based ECG Signal Using VHDL*, 1st International Hazar Scientific Research Congress, IKSAD Publishing, Baku, Azerbaijan, 2020. p. 114–127.
 22. John, A.D., and Fleisher, L.A., *Electrocardiography: The ECG*. Anesthesiology Clinics of North America, 2006. **24**(4): p. 697–715.
 23. Alemzadeh-Ansari, M.J., Editor(s): Maleki, M., Alizadehasl, A., Haghjoo, M., *Chapter 3 Electrocardiography*, Practical Cardiology, 2018. p. 17-60.
 24. Wagner, G., *Chapter 6-Basic Electrocardiography*, Editor(s): Saksena, S., Camm, A.J., Boyden, P.A., Dorian, P., Goldschlager, N., *Electrophysiological Disorders of the Heart*, Churchill Livingstone, 2005. p. 95-128.
 25. SkillStat. *Free ECG Simulator*. [cited 2021 12 February]; Available from: <https://www.skillstat.com/tools/ecg-simulator/>.
 26. Tlelo-Cuautle, E., Rangel-Magdaleno, J., de la Fraga, L. G., Tlelo-Cuautle, E., Rangel-Magdaleno, J. de J., and De la Fraga, L. G., *Introduction to Field-Programmable Gate Arrays., Engineering Applications of FPGAs*, Springer International Publishing, 2016. p. 1–32.
 27. Alcin, M., Tuna, M., Erdogmuş, P., and Koyuncu, I., *FPGA-based Dual Core TRNG Design Using Ring and Runge-Kutta-Butcher based on Chaotic Oscillator*. Chaos Theory and Applications, 2021. **3**(1): p. 20–28.
 28. Moysis, L., Tutueva, A., Volos, C., and Butusov, D., *A Chaos Based Pseudo-Random Bit Generator Using Multiple Digits Comparison*. Chaos Theory and Applications, 2020. **2**(2): p. 58–68.
 29. Alçın, M., Pehlivan, İ., and Koyuncu, İ., *Hardware Design and Implementation of a Novel ANN-Based Chaotic Generator in FPGA*. Optik - International Journal for Light and Electron Optics, 2016. **127**(13): p. 5500–5505.
 30. Karataş, F., Koyuncu, İ., Tuna, M., and Alçın, M., *Bulanık Mantık Üyelik Fonksiyonlarının Fpga Üzerinde Gerçeklenmesi*. Bilgisayar Bilimleri ve Teknolojileri Dergisi, 2020. **1**(1): p. 1-9.
 31. Akgul, A., Calgan, H., Koyuncu, I., Pehlivan, I., and Istanbulu, A., *Chaos-Based Engineering Applications with a 3D Chaotic System without Equilibrium Points*. Nonlinear Dynamics, 2015. **84**(2): p. 481–495.
 32. Akgül, A., Arslan, C., Arıcıoğlu, B., *Design of an Interface for Random Number Generators based on Integer and Fractional Order Chaotic Systems*. Chaos Theory and Applications, 2019. **1**(1): p. 1–18.
 33. Pan, J., Luan, F., Gao, Y., and Wei, Y., *FPGA-Based Implementation of Stochastic Configuration Network for Robotic Grasping Recognition*. IEEE Access, 2020. **8**: p. 139966–139973.
 34. Fu, H., Osborne, W., Clapp, R. G., Mencer, O., and Luk, W., *Accelerating Seismic Computations Using Customized Number Representations on FPGAs*. Eurasip Journal on Embedded Systems, 2009. **382983**: p. 1-13.
 35. Koyuncu, I., Cetin, O., Katircioglu, F., and Tuna, M., *Edge Dedection Application with FPGA Based Sobel Operator*, 23rd Signal Processing and Communications Applications Conference (SIU), IEEE, Malatya, Turkey, 2015. p. 1829–1832.
 36. Taşdemir, M.F., Koyuncu, I., Coşgun, E., and Katircioglu, F., *Real-Time Fast Corner Detection Algorithm Based Image Processing Application on FPGA*, International Asian Congress on Contemporary Sciences-III, IKSAD Publishing, Konya, Türkiye, 2020. p. 1–6.
 37. Arshad, Shaukat, S., Ali, A., Eleyan, A., Shah, S., and Ahmad, J., *Chaos Theory and its Application: An Essential Framework for Image Encryption*. Chaos Theory and Applications, 2020. **2**(1): p. 17–22.
 38. Chowdhury, S.R., Chakrabarti, D., and Saha, H., *FPGA Realization of a Smart Processing System for Clinical Diagnostic Applications Using Pipelined Datapath Architectures*. Microprocessors and Microsystems, 2008. **32**(2): p. 107–120.
 39. Tuncer, T., Avaroglu, E., Türk, M., and Ozer, A.B., *Implementation of non-periodic sampling true random number generator on FPGA*. Informacije Midem, 2015. **44**(4): p. 296–302.
 40. Alinx Electronics Technology, *ZYNQ FPGA Development Board AX7020 User Manual*. [cited 2021 9 February]; Available from: <http://www.alinx.com/en/>.



Research Article

Detection of circuit components on hand-drawn circuit images by using faster R-CNN method

Mihriban Günay^a  and Murat Köseoğlu^{b,*} 

^aMunzur University, Department of Electrical-Electronics Engineering, 62000, Tunceli, Turkey

^bİnönü University, Department of Electrical-Electronics Engineering, 44280, Malatya, Turkey

ARTICLE INFO

Article history:

Received 25 March 2021

Revised 21 May 2021

Accepted 01 June 2021

Keywords:

Circuit components
Classification,
Deep learning
Faster R-CNN
Hand-drawn circuits
Object detection

ABSTRACT

In this study, one of deep learning methods, which has been very popular in recent years, is employed for the detection and classification of circuit components in hand-drawn circuit images. Each circuit component located in different positions on the scanned images of hand-drawn circuits, which are frequently used in electrical and electronics engineering, is considered as a separate object. In order to detect the components on the circuit image, Faster Region Based Convolutional Neural Network (R-CNN) method is used instead of conventional methods. With the Faster R-CNN method, which has been developed in recent years to detect and classify objects, preprocessing on image data is minimized, and the feature extraction phase is done automatically. In the study, it is aimed to detect and classify four different circuit components in the scanned images of hand-drawn circuits with high accuracy by using the Python programming language on the Google Colab platform. The circuit components to be detected on the hand-drawn circuits are specified as resistor, inductor, capacitor, and voltage source. For the training of the model used, a data set was created by collecting 800 circuit images consisting of hand drawings of different people. For the detection of the components, the pretrained Faster R-CNN Inception V2 model was used after fine tuning and arrangements depending on the process requirements. The model was trained in 50000 epochs, and the success of the trained model has been tested on the circuits drawn in different styles on the paper. The trained model was able to detect circuit components quickly and with a high rate of performance. In addition, the loss graphics of the model were examined. The proposed method shows its efficiency by quickly detecting each of the 4 different circuit components on the image and classifying them with high performance.

1. Introduction

Each discipline may have its own terms and notations in which these terms are expressed visually. Especially in applied sciences, visuals where the terms correspond in real terms are needed. The figures of the terms are described by the way of drawings. The prevalence of drawings in many engineering fields shows that visuality is at the forefront. Drawings and visuality are also important in electrical and electronics engineering. Because in electrical and electronics engineering, a circuit diagram is drawn first, and then various analyses are made on it. This circuit diagram can be created by hand drawing or any drawing program. Although hand drawing is seen as a primitive method, it is generally the first preferred method. When an electrical and electronics engineer wants

to design a circuit, initially the circuit components to be used in the circuit are decided. Then, a draft drawing is made on a paper by using the determined circuit components, and numerical values are assigned to each component. After this step, the mathematical calculations are made due to the aim of the circuit on the completed draft drawing. If the results are as expected, the circuit is set up for testing in a simulation program or in a real laboratory environment. However, it is time-consuming and tedious for engineers to redraw a hand-drawn circuit by using a circuit drawing program on the computer. Taking an image of the circuit drawn on the paper and transferring it directly to the simulation program through an interface or software provide a great advantage to engineers. In this way, the workload of the engineers is

* Corresponding author. Tel.: +904223774797; Fax: +904223410046.

E-mail addresses: mihribangunay@munzur.edu.tr (M. Günay), murat.koseoglu@inonu.edu.tr (M. Köseoğlu)

ORCID: 0000-0002-0932-1981 (M. Günay), 0000-0003-3774-1083 (M. Köseoğlu)

DOI: 10.35860/iarej.903288

© 2021, The Author(s). This article is licensed under the CC BY-NC 4.0 International License (<https://creativecommons.org/licenses/by-nc/4.0/>).

reduced, there is no need to draw the circuit on the computer again, and they save time. The creation of such a software and its success in the detection of the circuit components from the hand-drawn circuit images have great importance in the aspect of engineering science. Depending on the rapid advancement of science and technology, researchers tend to develop such applications that facilitate human life in recent years. Several applications based on different methods in the object detection and classification have made significant contributions to the literature on this subject. Also, there are many studies in the literature on this subject, which have become popular in recent years.

Some researchers have focused on the recognition and classification of hand-drawn circuits and circuit components, since great successes have been achieved in handwritten number recognition and handwritten character recognition studies in the literature. Machine learning-based and deep learning-based methods have been used in the studies on the detection and classification of hand-drawn circuits and circuit components.

For this purpose, the HOG method was used in the recognition of the components on the hand-drawn circuit, and the machine learning-based SVM and KNN methods were used in the classification of the circuit components. Liu and Xiao [1] first divided the hand-drawn circuit into sections using a topology-based segmentation method and then classified the components in the circuit with SVM. The classification success for each circuit component classified in the circuit was over 90%. Moetesum et al. [2] firstly applied segmentation and various preprocesses to the circuit to classify the circuit components on the hand-drawn circuit. After the segmentation process, they suggested using the histogram of directed gradient properties (HOG) method to detect the circuit components, and the SVM method to classify them. In the study, 10 different hand-drawn circuit components were classified, and the average classification success rate was 92%. Angadi and Naika [3] performed certain preprocesses on hand-drawn circuit diagrams with image processing techniques. They suggested using the SVM method in the classification stage, which is the decision-making stage in determining the hand-drawn circuit diagram. Dewangan and Dhole [4] achieved 90% success rate in the classification they made by using scanned images of 90 hand-drawn circuits using KNN method. Naika et al. [5] used the HOG method in the recognition of 10 different hand-drawn electronic components and the SVM method in the classification stage. In the study, a data set consisting of 2000 images was used. As a result of the study, the rate of success in recognizing electronic components was 96.9%.

With the rapid developments in the field of deep learning in recent years, many studies have been carried

out by using deep learning-based methods. Deep learning-based methods have been used in hand-drawn electronic component recognition studies since the beginning of 2020. Wang et al. [6] used deep learning-based convolutional neural networks method to classify 3 different hand-drawn electronic components. The success rate of the method used in the study in classifying hand-drawn diode, resistor and capacitor images was stated as 90%. CNN, which is one of the deep learning-based methods, is generally used in the image classification [7]–[10]. The Faster R-CNN method, which was developed to determine the objects and the position of the objects on the images, is a new deep learning-based method. In the literature, there are many studies in which high performance was achieved by detecting objects using Faster R-CNN. Sardogan et al. [11], in their study, created a data set by collecting diseased and healthy apple leaf images. Using the Faster R-CNN method, they identified and classified the diseased and healthy leaves in the image. The proposed method achieved an average success rate of 84.5% in this study. Cömert et al. [12] first prepared a dataset containing 1200 apple images. After the training phase was completed with the images in the dataset, they detected the rotten area on the apple using the Faster R-CNN method. As a result of the study, they achieved an average of 84.5% success. Ren et al. [13] made some changes and adjustments in the Faster R-CNN method and used it for object detection in optical remote sensing images. Julca-Aguilar and Hirata [14] suggested using the Faster R-CNN method to detect symbols found in handwritten graphics and mathematical expressions. Yang et al. [15] conducted an experimental study using the Faster R-CNN method in handwritten text recognition studies. As a result of the study, they stated that the average success rate of the method used in character recognition was 97%.

In this article, the Faster R-CNN method, which is a deep learning-based object detection method, is proposed for the detection of circuit components in a hand-drawn circuit image. A data set was created by collecting the hand-drawn circuit images. After the labeling processes in the data set were completed, the pretrained Faster R-CNN model was selected. The training process was carried out using the selected model. Finally, the model is tested on various hand-drawn test circuits and the resulting loss plots are evaluated.

The main contributions of this study can be expressed as follows: It is demonstrated that basic circuit components, which are hand-drawn by different people, can be classified with a great accuracy by using Faster R-CNN method. Also, it is shown that this method is quite useful for the applications, where object detection and high speed is needed.

2. Material and Method

2.1 Data set

As the first step of the study, a data set including 800 hand-drawn circuits has been prepared. In this kind of studies, the data set is generally created in two ways. The first way is to use a ready-prepared data set that can be found on various web platforms. The second way is to use a data set created by the participants of a specific study. Since this study is about the hand-drawn circuit images and it is difficult to find an available data set intended for such a study, a data set specific to this study was created with the scanned images of circuits drawn by different people manually. The circuits were drawn on a white A4 paper by many people in different styles. Scanned images of 800 hand-drawn circuits were collected to create a data set to be used in the study. Since the scanned images were of high size, first the images were resized and reduced. 80% of the collected 800 images was reserved for training while the remaining 20% was reserved for validation.

Four different components have been defined to be detected in the hand-drawn circuit images. These are voltage source, resistor, inductor, and capacitor. Figure 1 contains sample images from the circuit components in the dataset.

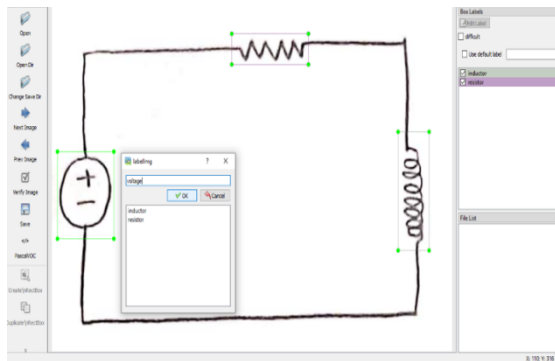


Figure 1. Sample images of the classes in the dataset

CLASSES				
				Inductor
				Resistor
				Capacitor
				Voltage

Figure 2. Sample images of the classes in the dataset

Since the aim of the study is to determine the circuit components on the images, different from the classification studies, the location of each circuit component is needed. For this reason, the circuit components on the images in the data set are labeled using the LabelImg program which is a graphical image annotation tool written in Python [16]. Figure 2 shows the labeling process of all the components in the images in the dataset with the LabelImg program.

2.2 Deep Learning and Convolutional Neural Networks

Deep learning is a newer field than artificial intelligence and machine learning. Unlike classical learning methods, deep learning is closer to the human brain because it consists of multi-layered neural networks [17], [18]. Since human is the creature in the nature that is the best at learning and applying the knowledge, the recent studies focus on developing novel learning algorithms similar to ones used by human brain. Considering the mentioned reasons, the deep learning method is frequently preferred for the studies on object detection and image processing by the researchers. Due to the widespread use of deep learning in different areas, various deep learning models specific to the field have been developed. Each of the developed models differs from each other and is used to solve problems in different areas. It is a great advantage to use deep learning approaches in classifying the images according to the categories and detecting the objects on the image, since it has high performance feature extraction ability.

At the beginning of 2012, the convolutional neural network architecture, which is a useful deep learning model in visual recognition, has been developed to use in specific fields. CNN architectures are mostly preferred in the education and classification stages of image processing studies. A basic CNN model is usually designed by using convolution layer, activation function, relu layer, pooling layer and fully connected layers [19]. For classification in the CNN model, a classification layer selected by the user is added to the backside of the fully connected layer. The number of layers to be used may differ depending on the model to be applied. There are many CNN-based ready-made models used in several studies, and these models differ according to the parameters such as the number of layers used, the order of the layers, and the learning rate. In addition, some users have designed their own CNN models instead of using ready-made models to use in their own studies. The main reasons for the increase in CNN usage in many different areas can be explained as follows: It is easy to apply, fast in training and testing stages and has efficient feature extraction stages occurring automatically through layers.

3. Proposed Faster R-CNN Method

The CNN algorithm estimates the class of a given image and yields as an output [20]. It is possible also to estimate the class of the object on an image using CNN. However, it is not possible to find the position of the object on the image by using CNN. For this purpose, a new model called R-CNN, which is one of the deep learning methods based on CNN, has been created to solve the object detection problem on the image [21]. In the R-CNN method, firstly, 2000 different regions are suggested with the selective search algorithm on the image. All proposed regions are transferred to the CNN model named Convnet, and feature map of each region is drawn. SVM method is used to classify by considering the extracted features. Finally, a bounding box plot is required to indicate the location of the object, and a regression model is used for this purpose. In the R-CNN method, training is completed in approximately 84 hours. The estimated time for a single image is about 47 seconds. In the R-CNN method, the training is slow and takes a long time, since CNN is applied for all the proposed regions. The scientists, who designed the R-CNN model, realized the disadvantages of R-CNN model and created a new model called Fast R-CNN [22]. While creating Fast R-CNN, some changes were made in R-CNN. In Fast R-CNN, unlike R-CNN, after CNN is applied to the image, 200 different regions are suggested by using the selective search algorithm. The ROI is then passed through the pooling layer to ensure the images are equal in size. Finally, the Softmax classifier is used to classify the desired objects. In the Fast R-CNN method, the training is completed in approximately 8.75 hours. The estimated time for a single image is 2.3 seconds. When the Fast R-CNN and R-CNN methods are

compared, it has been stated in the literature that the speed performance of Fast R-CNN is better than R-CNN. As a result of the changes made to increase and speed up the performance of the Fast R-CNN model in 2017, a new model named Faster R-CNN was proposed [23]. In this method, CNN is applied to the image in the first step, as in Fast R-CNN. In the second step, the selective search algorithm is used. Thanks to the RPN algorithm used, the zone proposition phase has been accelerated. Thanks to the Faster R-CNN method, it has become possible to detect the objects on the image in a fast way with high-performance. The application steps of Faster R-CNN method are shown in Figure 3 with block diagrams [24], [25]. In this article, Inception V2 model [26], one of the pretrained Faster R-CNN models, has been preferred to detect circuit components on hand-drawn circuits.

As seen in Figure 3, after the model is selected, CNN is applied to extract the feature map of the input image. RPN is used for region propositions using extracted feature maps. Features and proposed regions are passed through the ROI pooling layer. Features and suggested regions at the exit of the ROI pooling layer will be the same size. Then, a bounding box is drawn around the object on the image at the output and the class of the object is estimated by using the Softmax function.

In the Faster R-CNN method, the number of preprocessing steps on the images is small compared to other object detection and machine learning methods that are available in the literature. The preprocessing steps are few in this method, the method is realized successfully and quickly despite the high-level features of the image to be processed.

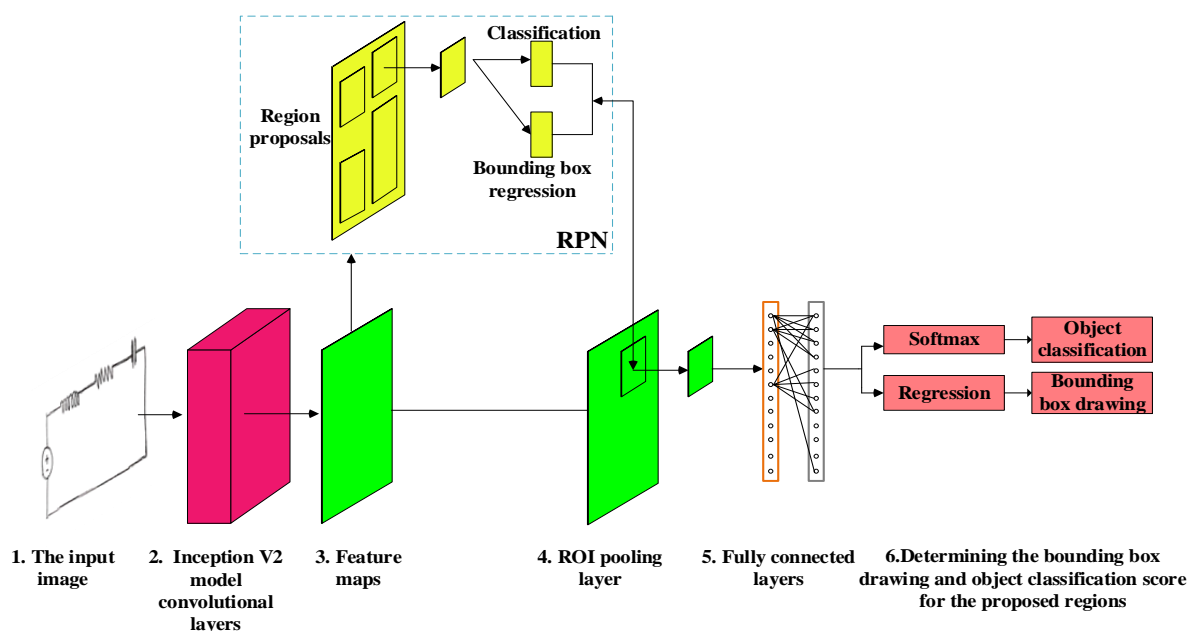


Figure 3. Representation of Faster R-CNN architecture

4. Experimental Results

In this study, a certain way has been followed to detect and classify circuit components found in hand-drawn circuit images. The steps followed in the study are shown in Figure 4.

Before using the pretrained Inception V2 model, the data set was created as a first step. After creating the data set, certain preprocesses were applied. All the images in the data set were resized as $200 * 200$ pixels, and all images were brought to the same size. Within the composed data set, two separate files were created for training and testing. 80% of the images in the data set were transferred to the train folder and the remaining 20% to the test folder. Then all the images in the data set were labeled. An xml file was created for each image in the train and test folder. The xml file contained the class information and coordinate information of the objects. All xml files in train and test folder were converted into a single csv file. After the preliminary preparations for the application were completed, Google Colab [27] cloud environment was preferred to use the Faster R-CNN model. The application of the proposed hand-drawn circuit component detection system was realized after necessary adjustments and arrangements were made on the Inception V2 model, which was pretrained by using Python software language. NVIDIA Tesla K80 GPU, offered free of charge by Google Colab, was used as the graphics card.

The model has been trained in 50000 epochs. The positions of the circuit components on the hand-drawn circuits having different styles can vary in each image. Also, depending on the purpose of the circuit, these four components may not be present in each circuit. Because each designed circuit and each component in the circuit has a task to perform. Considering the situation of the circuit components in different positions on the circuit, the

trained model was analyzed on various hand-drawn circuits. Figure 5 shows the real-time detection of circuit components on 4 different hand-drawn circuit images. As seen in Figure 5, the trained model has identified the components on the circuits by drawing a rectangular frame with different color tones. In addition, the model made an estimation in percent ratio for the label of the component detected with each rectangular frame drawn.

Loss functions were examined in the study to evaluate the performance of the trained Faster R-CNN Inception V2 model in detecting the components on hand-drawn circuits. In loss function graphs, the lower the loss means the higher the accuracy rate of the model. Therefore, when evaluating the success of the model, the loss is expected to decrease gradually as the number of epochs increases.

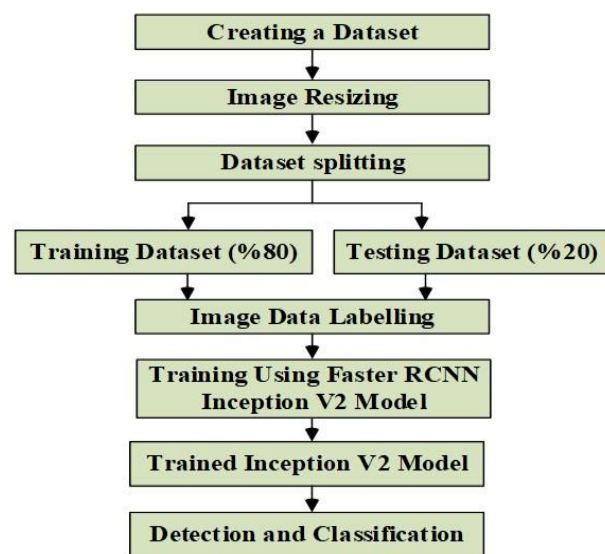


Figure 4. The steps followed to detect the circuit components in hand-drawn circuits

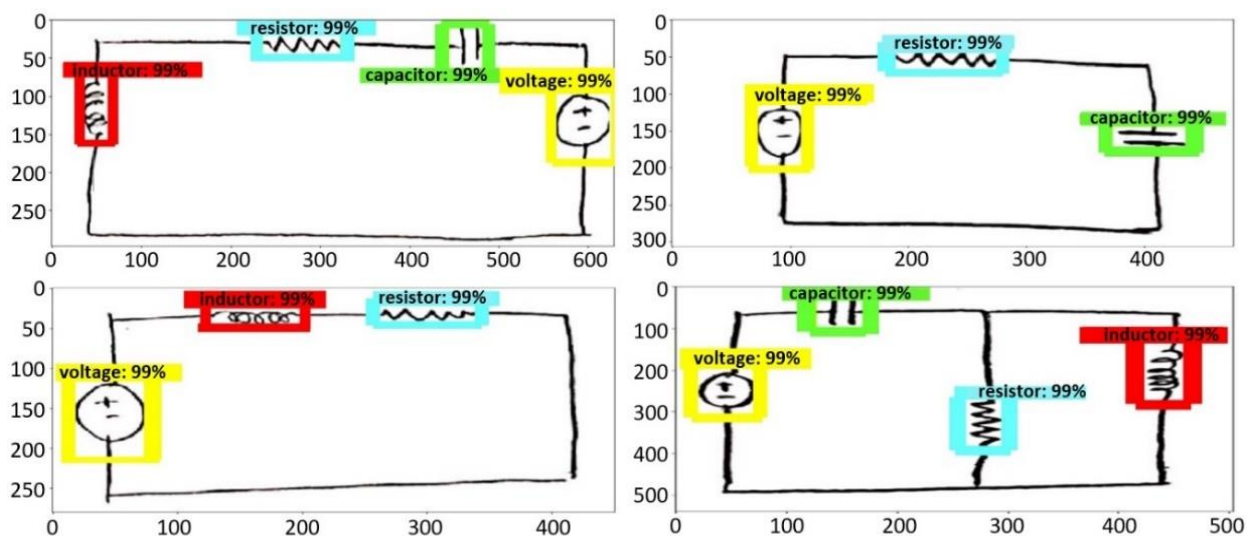


Figure 5. Real-time detection of components in the different circuit images tested

In Figure 6, various loss functions of the model that detect the components in the 50000 epoch trained hand-drawn circuit are given. The total loss function of the model is given in Figure 6 (a). The total loss function shows the overall loss of the model. When Figure 6 (a) is examined, the total loss has decreased to 0.06 at the end of 50,000 epochs. The classification loss function of the model is given in Figure 6 (b). The classification loss function shows the loss of the model at the classification stage. When Figure 6 (b) is examined, the loss in classification has decreased to 0.03 at the end of 50000 epochs.

In Figure 6 (c), the loss function of the model to determine the positions of the circuit components is given. As seen in Figure 6 (c), at the end of 50000 epochs, the localization loss has decreased to 0.02. When the loss graphs showing the performance of the model are examined, a gradual decrease in the loss is observed and after a while the loss started to remain constant. Considering the total loss graph, the model loss was a minimum of 0.048. As the number of epochs increased, the loss of model gradually decreased to less than 0.1. This shows that the model will have a high accuracy rate in real-time detections.

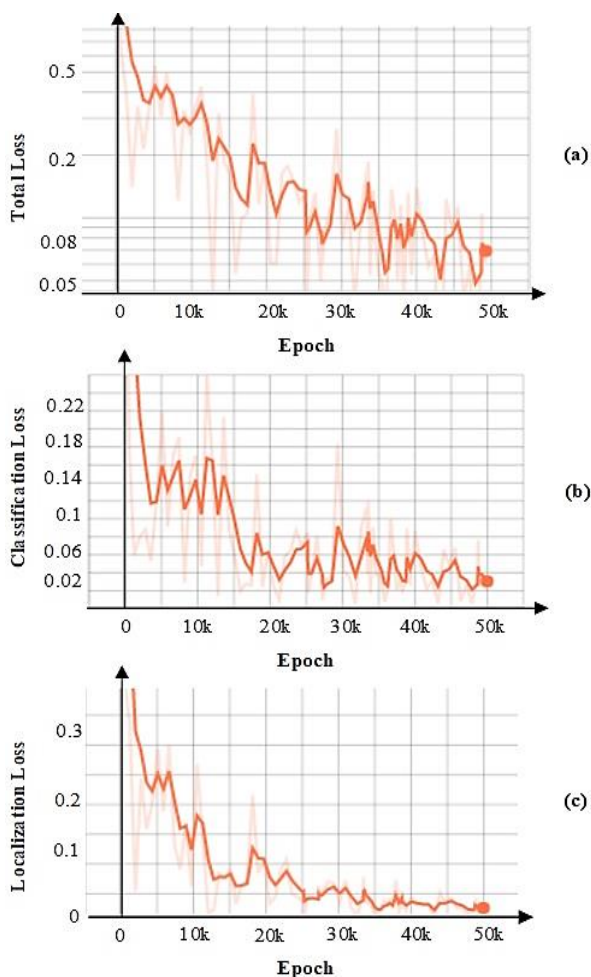


Figure 6. Loss function graphics for a) Total loss, b) Classification loss, c) Localization loss

5. Conclusions

In this study, the Faster R-CNN object detection method is used to detect circuit components from various hand-drawn circuit images. A lot of image data is needed to train the Faster R-CNN architecture, which is a deep learning model. In the study, the Inception V2 Faster R-CNN architecture, which was pretrained with a hand-drawn circuit data set and has a high success rate, was employed for object detection and classification. For this purpose, the necessary settings and arrangements were made by choosing a pretrained model in the study. Then, the model was trained with the data set created for the study with the images of 800 circuits drawn in several styles by many different people. The trained Faster R-CNN model has been applied, and the results were analyzed for many hand-drawn circuits where circuit components are designed in different positions. Softmax was preferred as the classification function. According to the results obtained, it has been observed that the method used has a high success rate in the detection of hand-drawn circuit components both in series and parallel RLC circuits. In the next studies, it will be focused on the detection of these components separately in hand-drawn circuits created by using semiconductor circuit components together with passive circuit components. In the next stage, it is planned to take photos of the circuits drawn on paper and transfer them to simulation programs such as Pspice, Proteus and Multisim through an interface to be developed.

Declaration

The authors declared no potential conflicts of interest with respect to the research, authorship, and/or publication of this article. The authors also declared that this article is original, was prepared in accordance with international publication and research ethics, and ethical committee permission or any special permission is not required.

Author Contributions

M. Günay collected the data and conducted the experiments based on the mentioned methodology. All the authors contributed to the analysis and writing phases. M. Köseoğlu supervised the work and provided some improvements. The work has been derived from M. Günay's ongoing master thesis, and M. Köseoğlu is the thesis supervisor.

References

1. Liu, Y. and Y. Xiao, *Circuit sketch recognition*. Department of Electrical Engineering Stanford University Stanford, CA, 2013.
2. Moetesum, M., et al., *Segmentation and recognition of electronic components in hand-drawn circuit diagrams*. EAI

- Endorsed Transactions on Scalable Information Systems, 2018. **5**(16).
3. Angadi, M. and R.L. Naika, *Handwritten circuit schematic detection and simulation using computer vision approach*. International Journal of Computer Science and Mobile Computing, 2014. **3**(6): p. 754-761.
 4. Dewangan, A. and A. Dhole, *KNN based hand drawn electrical circuit recognition*. International Journal for Research in Applied Science & Engineering Technology, 2018. **6**(6): p. 1111-1115.
 5. Dinesh, R., *Handwritten Electronic Components Recognition: An Approach Based On HOG+ SVM*. Journal of Theoretical & Applied Information Technology, 2018. **96**(13).
 6. Wang, H., T. Pan, and M.K. Ahsan, *Hand-drawn electronic component recognition using deep learning algorithm*. International Journal of Computer Applications in Technology, 2020. **62**(1): p. 13-19.
 7. Seveli, O. and N. Kemalöglu, *Turkish Sign Language digits classification with CNN using different optimizers*. International Advanced Researches and Engineering Journal, 2020. **4**(3): p. 200-207.
 8. Lee, H. and H. Kwon, *Going Deeper With Contextual CNN for Hyperspectral Image Classification*. IEEE Trans Image Process, 2017. **26**(10): p. 4843-4855.
 9. Coşkun, M., et al., *Face recognition based on convolutional neural network*. In *2017 International Conference on Modern Electrical and Energy Systems (MEES)*. 2017. IEEE.
 10. Li, Q., et al., *Medical image classification with convolutional neural network*. In *2014 13th international conference on control automation robotics & vision (ICARCV)*. 2014. IEEE.
 11. Sardoğan, M., Y. Özen, and A. Tuncer, *Faster R-CNN Kullanarak Elma Yaprağı Hastalıklarının Tespiti*. Düzce Üniversitesi Bilim ve Teknoloji Dergisi, 2020: p. 1110-1117.
 12. Cömert, O., M. Hekim, and A. Kemal, *Faster R-CNN Kullanarak Elmalarda Çürük Tespiti*. Uluslararası Mühendislik Araştırma ve Geliştirme Dergisi. **11**(1): p. 335-341.
 13. Ren, Y., C. Zhu, and S. Xiao, *Deformable faster r-cnn with aggregating multi-layer features for partially occluded object detection in optical remote sensing images*. Remote Sensing, 2018. **10**(9): p. 1470.
 14. Julca-Aguilar, F.D. and N.S. Hirata, *Symbol detection in online handwritten graphics using faster R-CNN*. In *2018 13th IAPR International Workshop on Document Analysis Systems (DAS)*. 2018. IEEE.
 15. Yang, J., P. Ren, and X. Kong, *Handwriting Text Recognition Based on Faster R-CNN*. In *2019 Chinese Automation Congress (CAC)*. 2019. IEEE.
 16. *GitHub - tzutalin/labelImg: ? LabelImg is a graphical image annotation tool and label object bounding boxes in images*. [cited 2021 March 18]; Available from: <https://github.com/tzutalin/labelImg>.
 17. Yuan, Z., Y. Lu, and Y. Xue, *Droiddetector: android malware characterization and detection using deep learning*. Tsinghua Science and Technology, 2016. **21**(1): p. 114-123.
 18. Bengio, Y., *Learning deep architectures for AI*. 2009: Now Publishers Inc.
 19. LeCun, Y., Y. Bengio, and G. Hinton, *Deep learning*. nature, 2015. **521**(7553): p. 436-444.
 20. Lei, X. and Z. Sui, *Intelligent fault detection of high voltage line based on the Faster R-CNN*. Measurement, 2019. **138**: p. 379-385.
 21. Girshick, R., et al., *Rich feature hierarchies for accurate object detection and semantic segmentation*. in *Proceedings of the IEEE conference on computer vision and pattern recognition*. 2014.
 22. Girshick, R., *Fast r-cnn*. In *Proceedings of the IEEE international conference on computer vision*. 2015.
 23. Ren, S., et al., *Faster r-cnn: Towards real-time object detection with region proposal networks*. arXiv preprint arXiv:1506.01497, 2015.
 24. Lin, G., et al., *Smoke detection on video sequences using 3D convolutional neural networks*. Fire Technology, 2019. **55**(5): p. 1827-1847.
 25. Lei, J., et al., *Efficient power component identification with long short-term memory and deep neural network*. EURASIP Journal on Image and Video Processing, 2018. **2018**(1): p. 1-14.
 26. Szegedy, C., et al., *Rethinking the inception architecture for computer vision*. In *Proceedings of the IEEE conference on computer vision and pattern recognition*. 2016.
 27. *Welcome to Colaboratory - Colaboratory*. [cited 2021 March 5]; Available from: https://colab.research.google.com/notebooks/intro.ipynb#scrollTo=5fCEDCU_qrC0.



Research Article

Empirical and theoretical analysis of a modified isochronal test in a caspian region gas reservoir

Abdullah Gürkan İşçan ^{a,*} 

^aCyprus International University, Department of Petroleum and Natural Gas Engineering, Lefkoshia, 99258, Cyprus

ARTICLE INFO

Article history:

Received 18 February 2021

Revised 30 July 2021

Accepted 11 September 2021

Keywords:

Absolute open flow potential

Gas well testing

Modified isochronal test

Reservoir

ABSTRACT

A deliverability test performed in a gas well is one of the fundamental steps to determine the flow potential of the wells in reservoir surveillance. Dynamic reservoir models need robust AOF (Absolute Open Flow), productivity index, permeability for calibration, history matching, and predictions. In this study, a gas well in a Pliocene sandstone gas reservoir was validated using the “Modified Isochronal Testing” method. This study aims to mitigate the efforts done to estimate the phenomenon of flow potential of the gas wells. Hence, the field development activities can be leveraged to a more efficient stage technically and economically. In this study, AOF, Productivity Index (PI), and the permeability of the tested interval were calculated. The validation of the permeability with log and core data increases the confidence level of the work done. AOF is the key performance indicator to define the gas well productivity at zero sand face pressure which is a measure of ranking the production potential of gas wells. The AOF values support the determination of the number of wells to be drilled and the design of the surface facilities. In this study, pressure and time data were obtained and they were analyzed by empirical and theoretical methods. These two methods used in analysis gave very close AOF values; 10.15MMSCF/D (empirical) and 10.67 MMSCF/D (theoretical), respectively. The permeability was calculated as 3.42 md, which is in line with the log permeability of 3.70 md and core permeability of 3.40 md.

1. Introduction

Gas well testing is composed of three major schemes: pressure transient, deliverability, and production analysis. Although they are all related to each other, the most important data collection is the pressure by time at different flow rates. This study focuses on gas well deliverability tests. These deliverability tests were used to determine the production capability of a well under specific reservoir conditions as mentioned by Brown [1]. In this study, Absolute Open Flow (AOF), Inflow Performance Relation (IPR), productivity index (PI), and the permeability of the gas well were calculated using the theory described by Lee [2]. The calculated test permeability, log permeability, and the core of the tested interval matched with each other. The required time to create the reservoir pressure before the achievement of flow for a needed period of time is not practical as mentioned by Lee et al. [3]. Thus, an industry-accepted modification is needed to reduce test times. The aim of the

modified isochronal test is to obtain similar data as in an isochronal test without longer stabilization periods to reach the reservoir pressure. The modified isochronal test is carried out similarly to an isochronal test except that the shut-in periods are of equal duration. The final stabilized flow point often is required after the final flow that will be used in the determination of the well performance coefficient (C).

Specifically, the modified isochronal test is a successive version of single-point tests planned to determine stabilized deliverability characteristics without forcing the well flow for the time required to reach the stabilized conditions as noted by Lee and Wattenberger [4]. The deliverability tests are described as flow-after-flow tests, single point tests, isochronal tests, and modified isochronal tests with and without a stabilized point. It is expected to enhance the deliverability evaluation of gas reservoirs in order to facilitate the early evaluation of gas well deliverability in complex gas reservoirs with low

* Corresponding author. Tel.: +90 392 671 1111.

E-mail addresses: aiscan@ciu.edu.tr (A.G. İşçan)

ORCID: 0000-0003-1647-2451 (A.G. İşçan)

DOI: 10.35860/iarej.880198

© 2021, The Author(s). This article is licensed under the CC BY-NC 4.0 International License (<https://creativecommons.org/licenses/by-nc/4.0/>).

permeability and strong heterogeneity as well as calculation of the absolute open flow potential as mentioned by Xi et al. [5]. Shoaib et al. [6] stated that pulse tests which include the application of a cyclic sequence of alternating rates are the harmonic tests. They can be conducted during the ongoing production period. The isochronal test is carried out through the sequential production of the well without stabilization followed by shutting-in the well and allowing it to build-up to the average reservoir pressure before the beginning of the next production phase. In isochronal tests, each shut-in period needs to last until the stabilization time. However, this causes delays, and improper stabilization of the data leads to misinterpretations. On the other hand the modified isochronal test differs from the isochronal test in terms of the equal durations of each successive flow and shut-in periods. The modified isochronal test does not require the pressure to be stabilized at each flow and shut-in, except for the initial shut-in, to determine the reservoir pressure. Therefore, it is more practical and faster compared to isochronal test. As the permeability gets higher, the stabilization time gets shorter. Stabilization time is defined as the time needed to observe almost no change or very little change in pressure with respect to time. The determination of IPR (Inflow Performance), well performance coefficient (C), the inverse slope of gas deliverability curve (n), and AOF are the major parameters that can be calculated using the pseudo pressure approach which widely used in the industry as mentioned by Mohamd and Fatooh [7]. Although most of the gas reservoirs are clastic/sandstone as lithology, there are cases where tight carbonate reservoirs can be encountered as noted by Jiang et al. [8]. In such cases, similarly, conventional deliverability theory and equation in sandstone reservoirs are still used except for the coefficients of the equation which are sensitive to the reservoir data. Sergeev [9] emphasized that the adaptive interpretations of gas well deliverability tests facilitate the possibility of generating bottom-hole pressure and flow rate data at different test stages together with the IPR curve. In general, the idea is estimating the formation pressure and the flow coefficients. The modified isochronal and isochronal gas well testing techniques are often used in the industry. Especially, the modified isochronal deliverability method is generally in the unsteady state since it is not needed for the reservoir to reach the steady state during the test phase as stated by Aziz [10]. Having considered the basic concepts of modified isochronal test mentioned above, in this study, it was considered to implement a modified isochronal test analysis since the permeability of the reservoir is as low as 3-5 md. Otherwise, the successive shut-in stabilization periods would have been too long to be efficient if the isochronal test had been conducted here.

This paper aims to present a structured plan and the analysis of the test data using empirical and theoretical approaches based on the well-known textbook sources [1-4] and [28-30]. The analysis of the real field data revealed reasonable results which match the log and the core data. Therefore, this paper establishes a link between the theory and real field data application. When new gas wells are drilled, their potential needs to be determined for further field development activities. Deliverability gas well testing measures the production capabilities of a gas well under specific bottom-hole pressures and reservoir conditions. Although this study focuses on gas production techniques and reservoir approaches, it is also recommended to conduct calorific value and biomass analyses of the produced gas to be able to validate the gas for energy deliverability and quality aspects as a future activity as mentioned by Ozyuguran et al. [11].

In general, three-four month extended flow tests are costly and they cause time and money losses in terms of making a quick decision. However, the modified isochronal test, applied in this study, is relatively shorter up to a few days. The planning of the test is crucial, otherwise time and money losses emerge. Thus, successful or representative data cannot be obtained.

In this study, a pressure gauge which can acquire 2 data at 30 seconds (0.008333 hours) was used. This data resolution helps to visualize the pressure profile and the stabilization. Unless the resolution is planned carefully, the obtained data would not provide an opportunity to make a "sound" analysis. Moreover, since the electric power should not be interrupted during the test, a backup battery is recommended at the downhole gauge beside the electric power cable. This study focuses on the executed modified isochronal test which has five flow and three shut-in periods. Each of the four equal duration flow and three shut-in period durations is 15 hours. There is an extended flow period of 60 hours. The total duration of the test is 165 hours.

In general, it has been seen that the literature studies calculated the reservoir properties with dynamic testing. However, the calculated data have not been validated with log or core data. In this paper, the calculated permeability was validated with log and core, which increased the level of confidence. On the other hand, implementation of the textbook theory over the real field data rather than laboratory-driven data makes a significant difference in this paper compared to the literature.

Hashemi et al. [12] studied the well testing in horizontal wells. Near wellbore behaviors of gas and condensate wells were evaluated to find preliminary results throughout their study by means of different mobility zones stemming from condensate drop out. Wu et al. [13] investigated the multi-factor control for unconsolidated sandstone gas reservoir for productivity testing. They studied the combination of testing

reservoir, pipe string type, sea area and the required minimum testing flow rate during cleaning up process. A test working system was designed based on critical flow test rates. Bakyani et al. [14] analyzed gas condensate wells. They aimed to optimize the flow performance by means of tubing equations and inflow performance relation (IPR). Igwilo et al. [15] reviewed a case study of horizontal well to optimize the gas production. In their study, it was aimed to evaluate the solution methods to identify the rates of the lift gas and the optimum gas production rates. Nodal analysis was applied to enhance the flow rate and to determine the constraints for the solution. Meunieur et al. [16] studied normalized pseudo variables in gas well testing. In their study, two methods were proposed to find rate-dependent skin, permeability, mechanical skin, and well deliverability.

The first method was the logarithmic convolution of pressure with flow rate. The second method was a transient flow-after-flow test with a short duration where they obtained close results. Solaimani et al. [17] analyzed the horizontal gas wells in tight formations. They investigated the sensitivity of the productivity to reservoir properties. A modified backpressure test method was used to identify the productivity of horizontal gas wells where pressure dependent viscosity and anisotropy exist. In their study, process conversion- flowing pressure correction was used to convert the modified backpressure test process into the isochronal test. The comparison of the productivity values before and after conversion yielded good productivity results. The benefit was gained especially in tight gas reservoirs. Gomaa et al. [18] studied the well testing analysis of unconventional gas reservoirs. They identified the Absolute Open Flow potential (AOF) and production performance coefficient (C) in a tight gas reservoir via flow-after-flow test. In their study, the improvement of permeability was emphasized after the fracturing operation. Brar and Aziz [19] investigated the utilization of the modified isochronal test to calculate the deliverability information without stabilized flow data. Their paper aimed to present two techniques to estimate stabilized deliverability output using isochronal data obtained from the modified isochronal test. They reported that reasonable permeability thickness product and skin factors were the outcomes of their research. Sarfraz and Tiab [20] studied the pressure build-up and drawdown in gas condensate reservoirs under two-phase flow conditions by a pseudo pressure approach integrated to changes of phases with pressure and physical properties. It was mentioned that the effective permeability could be used to estimate the well performance in pseudo-steady-state and Absolute Open Flow Potential. Franco et al. [21] studied optimized isochronal test. They applied multi rate well test to eliminate the shut-in time in gas well testing over transient and pseudo steady state flow. The edge point of their study is no stabilization time is required to reach the reservoir pressure. Instead, they developed a mathematical method using

transient flow equation. Wjayanti et al. [22] utilized commercial software for the analysis of deliverability tests. They identified the (AOF) Absolute Open Flow potential, skin and permeability through the analysis of the Modified Isochronal Test. The delivered analysis graphs are similar to those which were generated in the in-house study. Putri et al. [23] investigated the production capability of a gas reservoir by means of modified isochronal gas deliverability test. The wells were flown to atmospheric pressure. They identified the Absolute Open Flow potential, well performance flow coefficient (C) and the inverse slope of gas deliverability curve (n). They aimed to estimate ability of a well to produce gas at surface by determining the (AOF) Absolute Open Flow potential.

This study contributes the literature through establishing a link between the oil and gas industry by using real field data and the textbook theory. The determination of the number of wells to be drilled and the design of the surface facilities for gas processing rely on the AOF data. Therefore, the study supports the economic planning. The confirmation of the calculated permeability through log and core data imposes the cross-check of the data by means of different sources in the literature. Moreover, dynamic reservoir models (reservoir simulations) of gas wells need the AOF, pay zone productivity, permeability for modeling calibration, history matching, and predictions. Especially, a low permeability well as depicted in this study needs a long time for stabilization. The modified isochronal test does not require stabilized pressure after each flow period. This time gain is a great advantage in terms of obtaining and analyzing data for a more practical and economical testing. The correct determination of the AOF, PI, and permeability help to estimate the flow potential of the gas wells for supporting the field development activities.

2. Basic Reservoir Information

The total hydrocarbon system is the Oligocene–Miocene Maykop/Diatom Total Petroleum System (TPS). The source rock is generally type-II and type-III kerogen. The reservoir is Pliocene which includes the Middle Pliocene Productive series referred to as the Red Bed Series. The Productive Series is composed of upper and lower conglomeratic Pereryva Suite.

The Red Bed Series constitutes the major reservoirs mentioned for the same reservoir by Iscan [24]. They are composed of highly fluvio-deltaic clastic sequences that include interbedded conglomerate to mudstones. The type log of the productive gas reservoir displays 43 m upper conglomerate and 5m siltstone and mudstone with relatively higher shale volume. The tested well in this study penetrates the reservoir at -5,412 fts (5912ft MD). The average porosity is 17% and the average permeability is 3.7 md, while the highest permeability is up to 7 md (Figure 1).

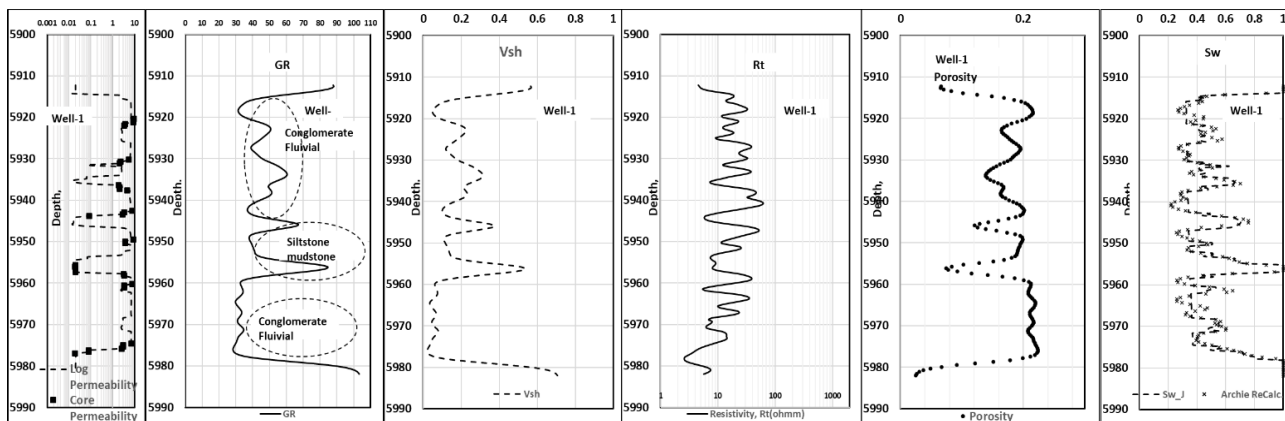


Figure 1. Type log of the reservoir

The core permeability was measured using flood experiments as per the methods by Iscan et al. [25]. These measurements revealed an average of 3.4 md which is in line with the log and the well testing permeabilities. This is a good and reliable argument that increases the confidence of the well-test data validated by means of log and cores as a major difference from most of the literature study so far.

The tested interval is 5,912-5,955 ft MD (43ft). There is a sharp reduction in porosity and permeability as well as resistivity towards 5,955 ft MD. The saturation log yields 100% water saturation at this depth. Although this behavior might be due to tightness, the bottom portion below 5,955 ft was not perforated and was not tested against the risk of a water zone. However, the reservoir properties get more prolific right after this depth. Therefore, it is planned to perforate this bottom zone in the future to further investigate the reservoir.

The top structural depth map of the reservoir is displayed in Figure 2. Based on laboratory MICP (Mercury Injection Capillary Pressure) data, the FWL is in a range of -5,481-5,530 fss. Saturation data matches the saturation log better at a deeper FWL which is uncertain as this section was not tested.

3. Test Planning -Test Data and Data Analysis Method

This Section includes the real data which were acquired in the field. The analysis and the interpretation of these data were summarized in 3.1 Test Planning - Test Data, 3.2 Test Data Analysis Method, and 3.3 Permeability Calculation.

3.1 Test Planning - Test Data

To be able to proactive, the testing phase planning was initiated prior to the completion of the well. The power requirements, downhole temperatures, and most importantly the pressure-time recorders were supplied and brought to the well site. The well test rates and test durations were summarized together with end-point flowing and shut-in pressures (Table 1). The pressure-time data acquisition was planned as twice at 30 seconds. Therefore, thousands of

pressure-time data were collected during the entire test phase of 165 hours.

The flowing bottom-hole pressure gradually decreases from 3,277 psi to 2,697 psi as the flow periods evolve. The successive flow and shut-in periods are 15 hours. There is an observed reduction in the successive shut-in periods after each of the interim flow periods which is a typical diagnostic of the modified isochronal testing. The initial reservoir pressure is 3,400 psi.

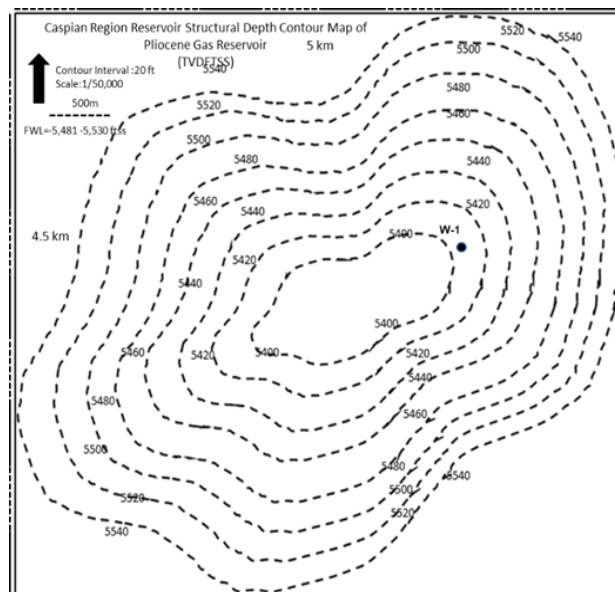


Figure 2. Top Structural Depth Map of the Gas Reservoir

Table 1. Modified isochronal test data summary

Test	Duration (hours)	P _{wf} or P _{ws} (psia)	q _g (MMscf/D)
First Flow	15	3,277	2.5
First shut-in	15	3,350	
Second Flow	15	3,178	3.1
Second shut-in	15	3,310	
Third flow	15	3,024	4.35
Third shut-in	15	3,275	
Fourth flow	15	2,783	6
Extended flow (stabilized)	60	2,697	5.2

The stabilized flow rate of 5.2 MMSCF/D was achieved by a flowing bottom-hole pressure of 2,697 psi at the end of a 60-hour testing period. The overall test rate profile by time data is summarized in Figure 3. It is planned to utilize the build-up data in another study to demonstrate the pressure build-up analysis by using the pseudo pressures concept. Each one of the flowing and shut-in periods is of 15 hours at flow rates ranging from 2.5 to 6 MMSCF/D (Figure 3). The rates are successively increased at each of the flow periods except for the stabilized extended flow. The extended flow data is used for the determination of the Well Performance Coefficient (C). The other four points are used to calculate the inverse slope of gas deliverability curve. The combination of all of these data lead to the calculation of the Absolute Open Flow Potential.

As it is seen the pressure does not stabilize at the end of each successive flow and shut-in period. This shows how the modified isochronal test differs from the isochronal one. There is a slight reduction in the pressure at the end of each of the 15-hour shut-in periods (Figure 4). If it was an isochronal test instead, pressure stabilization would have to be reached. However, in that case, the shut-in durations would have been different from each other and much longer waiting periods would have been unavoidable.

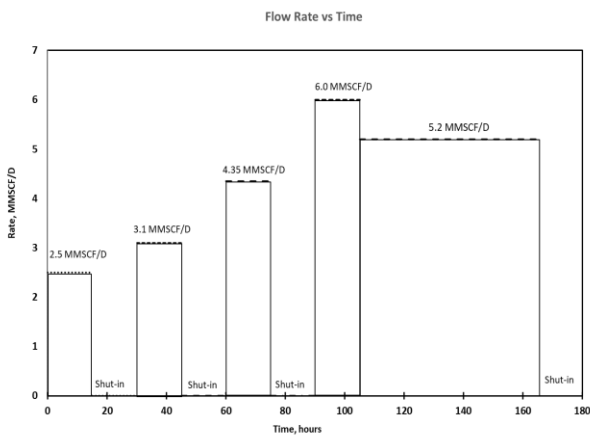


Figure 3. Rate vs time profile of the modified isochronal test

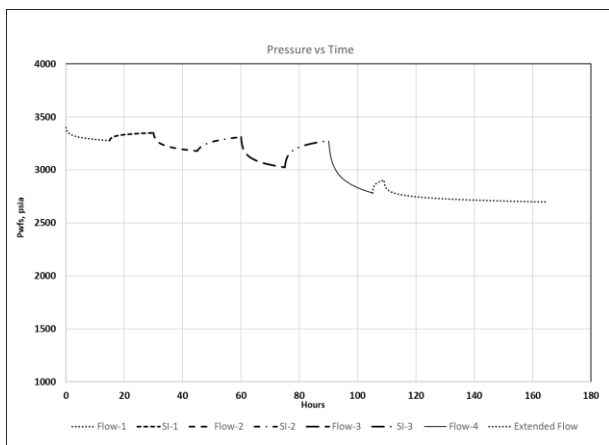


Figure 4. Pressure vs time profile of the modified isochronal test

3.2 Test Data Analysis Method

The data analysis was carried out using empirical and theoretical two methods based on well-known textbooks [1-4] and [28-30].

3.2.1 Empirical Method

The empirical method requires the plot of the square of delta pressure vs gas flow rate on a log-log paper. This plot provides an empirical correlation of the well test data. It is not recommended to extend the plot at a large distance beyond the obtained data to eliminate the risk of having misleading results. The empirical analysis relates flow rate with the square of the pressures as in Equation (1) which is known as back pressure equation. This equation is based on the empirical equation which was presented by Rawlins and Schellhardt [26].

$$q_{sg} = C(P_S^2 - P_{wf}^2)^n \tag{1}$$

As described in Brown [1] and Lee [2], the raw test data were processed by taking squares of the consecutive shut-in and flowing pressures as well as dividing the pressure difference by the corresponding flow rates (Table 2). Therefore, (Table 2) is the processing of the raw data which lead to the production of Figure 5 and Figure 6.

Lee [2] defined the theoretical rate at which the well could produce as the Absolute Open Flow Potential (AOF) if the flowing bottom-hole pressure was the atmospheric one.

$$slope = \frac{[\log(P_4^2 - P_{wf4}^2) - \log(P_2^2 - P_{wf2}^2)]}{[\log q_4 - \log q_2]} \tag{2}$$

$$slope = 1.48 = 1/n \tag{3}$$

$$n = 0.67 \tag{4}$$

The stabilized rate is 5.2 MMscf/D with a stabilized flowing bottom-hole pressure of 2,697 psi. The well performance coefficient C was calculated using this stabilized flow data and the reciprocal of the slope as “n” (Figure 5). The value of the C was calculated as 1.77 x10⁻⁴ by using Equations (2)-(4).

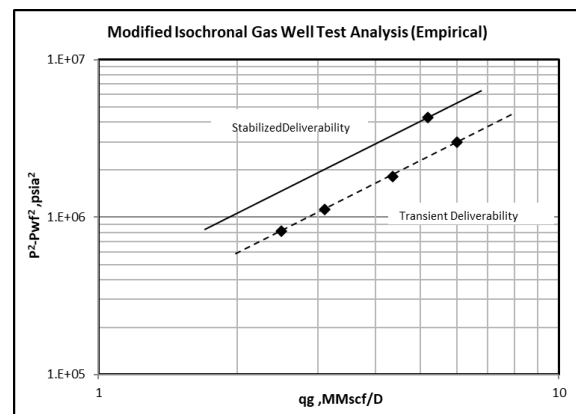


Figure 5. Empirical modified isochronal test deliverability

Donohue and Ertekin [28] utilized and presented this theory. In their study, they applied a case example with the utilization of the Equations (1) and (4). The typically characteristic test plots were also mentioned in their study which are similar to Figure 3, Figure 4 and Figure 5 of this paper. This proves the validity of the methodology which was applied in this study.

3.2.2 Theoretical method

The theoretical method is based on the background of Houpeurt [27] flow calculated using Equation (5) as described in Lee and Wattenberger [4]. The form of the equation in pseudo pressure terms is:

$$\Delta P_p = P_p(P_s) - P_p(P_{wf}) = a_t q + b q^2 \quad (5)$$

This form of Houpeurt's [27] equation is presented in pressure squared terms. The derivation is directly done from the diffusivity equation assuming that $\mu_g z$ is constant over the studied pressure interval. Equation (6) is presented for pseudo-steady flow as in the following:

$$\Delta P^2 = P_s^2 - P_{wf}^2 = a q + b q^2 \quad (6)$$

The solution of Equation (6) is done by dividing each side of the equation by gas flow rate (q) leading to Equation (7).

$$\frac{\Delta P^2}{q} = \frac{P_s^2 - P_{wf}^2}{q} = a + b q \quad (7)$$

Then, a graph of $(P_s^2 - P_{wf}^2)/q$ vs $a + b q$ is plotted linearly where slope of the equation is "b". The vertical intercept of the line is not directly "a" as in the isochronal test because the initial plot is made with the four points without the stabilization. Therefore, the $(P_s^2 - P_{wf}^2)/q$ vs $a + b q$ plot needs to be used for slope "b" calculation only. The "a" needed to be calculated using the stabilized point of $q = 5.2$ MMSCF/D and $(P_s^2 - P_{wf}^2)/q = 823,798$. Then, the vertical intercept "a" was calculated as 576,637 using the stabilized point (Figure 6). After the determination of "a" and "b", the Absolute Open Flow Potential (AOF) was calculated by setting the P_{wf} as atmospheric pressure. The calculated AOF values from the empirical and theoretical methods are compared with each other.

$$\Delta P^2 = P_s^2 - P_{wf}^2 = a q + b q^2 = 576637 q + 47531 q^2 \quad (8)$$

When the P_{wf} is set as 14.17 psi by definition of AOF, the flow rate q is solved as 10.67 MMSCF/D for the above quadratic Equation (8) as mentioned in Lee and Wattenberger [4]. Ikoku [29] described the Inflow performance curves as with the implementation of back pressure equation.

The theory and the applications of the deliverability equations of this study were validated with the deliverability testing and well production potential analysis methods as

discussed by Chaudry [30] where a mathematical review of the deliverability concept was carried out.

3.3 Permeability Calculation

Permeability calculation requires the determination of the Productivity Index (PI). The PI is defined as the stabilized flow rate divided by the pseudo drawdown pressure Equation (9).

$$PI = \frac{q_{sg}}{\varphi_s - \varphi_{wf}} \quad (9)$$

The pseudo pressure term " φ " is defined as the pressure square divided by viscosity. Therefore, $P_s^2 - P_{wf}^2$ vs q_s was plotted as IPR (Inflow Performance Relation) (Figure 7). Then, the gas flow rate is calculated practically by the $PI \times (P_s^2 - P_{wf}^2)/\mu_{gave}$ as detailed in Equation (10).

Table 2. Processing of the modified isochronal test data

q _g (MMscf/D)	P ² -P _{wf} ² (psia) ²	(P ² -P _{wf} ²)/q _g	Test points
2.5	822,768	329,107	1
3.1	1,119,877	361,251	2
4.35	1,808,980	415,857	3
6	2,983,658	497,276	4
5.2	4,283,752	823,798	stabilized point

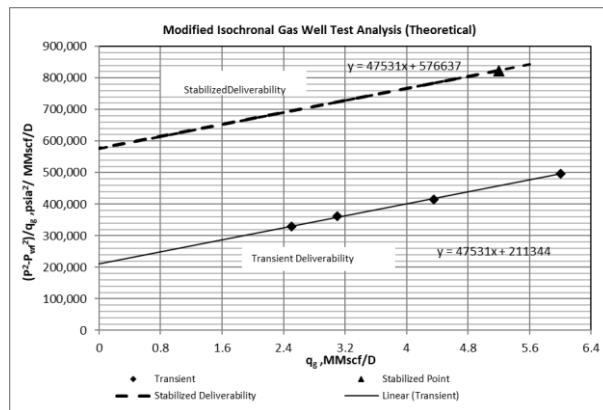


Figure 6. Theoretical deliverability of modified isochronal test

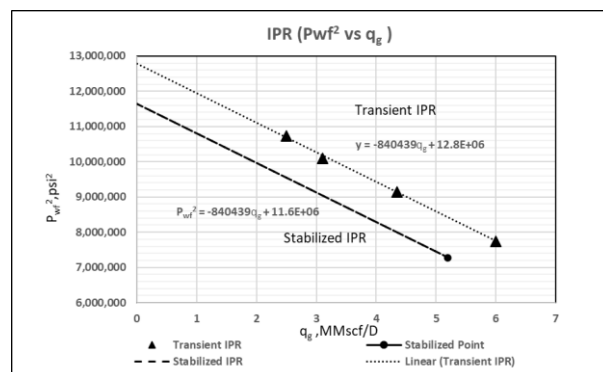


Figure 7. IPR curve for the gas well

Hence, the parameters except for the pressure square terms divided by average viscosity are the productivity index (PI). The slope obtained from Figure 7 is substituted into Equation (10) as applied in Brown [1]. Then, the corresponding permeability is calculated. The slope of the line was divided by average viscosity and its reciprocal was calculated as the PI (Figure 7). Then, the PI was calculated as 0.0227 scf/d/psi²/cp.

$$q_{sc} = \frac{703 \times 10^{-6} kh (P_s^2 - P_{wf}^2)}{T \mu_{gave} Z_{ave} \left\{ \ln \left(\frac{r_e}{r_{wf}} \right) - 0.75 + S + a' q \right\}} \quad (10)$$

All of the parameters which were used and calculated in the study were mentioned in section 8. The permeability was calculated as 3.42 md using the Equation (10) and the parameter in Table 3 (input parameters) which matched with the average log permeability of 3.70 md presented in Figure 1.

4. Conclusions

In this study, raw data was obtained and its analysis was carried out using the modified isochronal test. The entire test duration was 165 hours. The study provides a link between the theory and the real field application. In addition, economical and technical benefits are also provided regarding the field and facility development through the analysis of the data as well as the calibration and robustness of the dynamic simulation models. The conclusions of the study is presented under five items below.

- The Absolute Open Flow Potential (AOF) values were calculated using both empirical and theoretical approaches. The empirical method yielded an AOF value of 10.15 MMSCF/D, while the theoretical method resulted in 10.67 MMSCF/D. The percentage difference between the two methods was determined as 4.8%.
- The performance coefficient (C) of the deliverability equation was calculated as 1.77×10^{-4} .

Table 3. Input reservoir parameters of the gas reservoir

Ps, psi	3,400
Phi	0.17
h, ft	43
T, F	180
rw, ft	0.3
q _{sg} , MSCF/D	5,200
P _{wfs} , psi	2,697
Sg	0.7
μ _g , cp	0.019
z	0.88
re, ft	2083
a' q	0
S	0

- The inverse of the slope of the gas deliverability curve was determined as 0.67. The stabilized rate was determined as 5.2 MMSCF/D at a stable flowing bottom-hole pressure of 2,697 psi.
- The productivity index (PI) of the well was calculated as 0.0227 scf/d/psi²/cp. The permeability was calculated as 3.42 md through the tested interval of 43 ft. This test-driven permeability matched with the log permeability of 3.70 md and the core permeability of 3.4 md.
- The determination of AOF (Absolute Open Flow) by using two methods facilitated understanding the production potential of the gas wells in the fields for further technical and economic field development activities.

The tested interval is 5,912-5,955 ft MD (43 ft). There is a sharp reduction in porosity and permeability as well as resistivity towards 5,955 ft MD. The saturation log yields 100% water saturation at this depth. Although this behavior might be due to tightness, the bottom portion below 5,955 ft was not perforated and was not tested against the risk of a water zone. There is a plan to perforate the bottom portion of the well below 5,955 ft MD for testing the potential of this lower interval considering that hydrocarbon might have existed.

Declaration

The author declared no potential conflicts of interest with respect to the research, authorship, and/or publication of this article. The author also declared that this article is original, was prepared in accordance with international publication and research ethics, and ethical committee permission or any special permission is not required. This study is not a part of a graduate or undergraduate thesis study.

Author Contributions

A.G. İşcan is responsible for all sections of the study.

Nomenclature

- AOF* : Absolute Open Flow Potential, MMscf/d
 MMscf/d: Million Standard Cubic Feet per Day
 Mscf/d : Thousand Standard Cubic Feet per Day
P_s : Sandface Pressure, psi
P_{wf} : Flowing Bottom hole Pressure, psi
 Δ*P* : Pressure Difference Between the Reservoir Pressure and Flowing Well Bottom Hole Pressure, psi
PI : Productivity Index , scf/d/psi²/cp
q_{sg} : Stabilized Gas Flow Rate, MMscf/d
q_{sc} : Calculated Gas Flow Rate, MMscf/d
C : Well Performance Coefficient
n : The Inverse Slope of Gas Deliverability Curve
a or a_t : Theoretical Gas deliverability Vertical Intercept
b : Theoretical Gas Deliverability Slope

Φ	: Porosity fraction
k	: Permeability, md
h	: Tested Interval Thickness, ft
T	: Formation Temperature, R
r_w	: Wellbore Radius, ft
r_e	: Drainage Radius, ft
S_g	: Gas Specific Gravity
μ_g	: Average Gas viscosity, cp
z	: Gas Compressibility Factor
S	: Skin Factor
$a q$: Non-Darcy Term
φ	: Pseudo pressure term, psi ² /cp
P_p	: Pseudo Pressure Term Identification

References

- Brown, K., *The Technology of Artificial Lift Methods*. 1984, USA: PennWell Publishing Company.
- Lee, J., *Well Testing*. 1982, USA: SPE AIME.
- Lee, J., Rollins, J.B. and Spivey, J.P., *Pressure Transient Testing*. 2003, Richardson TX USA: SPE Textbook Series.
- Lee, J. and Wattenberger, R., *Gas Reservoir Engineering*. 1996, Richardson TX, USA: Henry L. Doherty Memorial Fund of AIME.
- Xi, F., X.Peng, Q. Li, X. Zhao, P. Zhang, and D. Pan, *A new method for evaluating the unstable deliverability of gas wells in gas formation testing phase*. Natural Gas Industry B, 2020. **7**(6): p. 614-623.
- Shoaib, M., D. Viberti, S.B. Eloisa, and F. Verga, *Harmonic pulse testing for gas well deliverability Assessment*. Geingegneria Ambientale e Mineraria, 2019. **158**(3): p. 53-60.
- Mohamd, I.S. and S.K., Fatooh, *Gas wells deliverability determination using flow after-flow test analysis*. Journal of Applied Science, 2020. **4**: p.26-43.
- Jiang, L., C. Xiancaho, G. Ping, and Z. Jingchao, *Tight carbonate gas well deliverability evaluation and reasonable production proration analysis*. J Petrol Explor Prod Technol., 2021. **11**: p.2999-3009
- Sergeev, V.L., N.T. Phuonget, and A.I. Krainov, *Adaptive interpretation of gas well deliverability tests with generating data of the IPR curve*. J. Phys., 2017.: Conf. Ser. **803** (012136): p.1-6.
- Aziz, K., *Theoretical basis of isochronal and modified isochronal back-pressure testing of gas wells*. Journal of Canadian Petroleum Technology, 2013. **6**(01): p. 20-22.
- Özyuğuran, A., S. Yaman, and Küçükbayrak, S., *Prediction of calorific value of biomass based on elemental analysis*. International Advanced Researches and Engineering Journal. 2018; **2**(3): p. 254-260.
- Hashemi, A., L. Nicolas, and C. Gringarten, *Well test analysis of horizontal wells in gas-condensate reservoirs*. SPE Res Eval & Eng, 2006. **9**(01): p. 86-99, SPE 89905-PA.
- Wu, M., H. Liang, M. Zhang, D. Sun, and P. Zhong, *Productivity testing design method of multi-factor control for unconsolidated sandstone gas reservoir*. Engineering, 2016. **8**(11): p. 815-822.
- Bakyani, A., A. Rasti, S. Qazvini, and F. Esmailzadeh, *Gas condensate wells simulation to optimize well flow performance using tubing equations coupled with inflow-performance-relation (IPR) curve*. Open Access Library Journal, 2018. **5**(5): p. 1-17.
- Igwilo, K., E. Okoro, A. Nwude, A. Mamudu, and C. Onuh, *A review on gas well optimization using production performance models: A case study of horizontal well*. Open Journal of Yangtze Oil and Gas, 2018. **3**(1): p. 57-67.
- Meunier, D.F., C.S. Kabir, and M.J. Wittmann, *Gas well test analysis: use of normalized pseudovariables*. SPE Form Eval, 1987. **2**(04): p. 629-636. SPE-13082-PA.
- Soleimani, R., Y. Jahanpeyma, and M. Salehian, *Analysis of horizontal well productivity in tight gas formations and its sensitivity to reservoir properties*. J Petrol Explor Prod Technol, September 2019. **9**: p. 1237-1244.
- Gomaa, S., A. Attia, A. Abdelhady, S. Khaled, M. Elwageeh, A.N. Elhoshoudy, M. Omran, A. Essam, M. Osama, A. Ashraf, and C. Wagdy, *Well testing analysis of unconventional gas reservoirs: real case study of tight gas carbonate reservoir, apollonia formation, western desert, egypt*. International Journal of Petroleum and Petrochemical Engineering (IJPPE), 2019. **5**(1): p. 1-5.
- Brar, G.S. and K. Aziz, *Analysis of modified isochronal tests to predict the stabilized deliverability potential of gas wells without using stabilized flow data*. Journal of Petroleum Technology (JPT), 1978. **30**(02): p. 297-304, SPE-6134-PA.
- Sarfraz, A.J. and T. Djebbar, *Pressure drawdown and buildup analysis in gas condensate reservoirs*. Paper presented at the SPE Western Regional/AAPG Pacific Section Joint Meeting, Anchorage, Alaska, May 2002. SPE-76780-MS.
- Franco, F., A. Rinchon, and M. Useche, *Optimized isochronal testing*, Society of Petroleum Engineers - Abu Dhabi International Petroleum Exhibition and Conference 2018, ADIPEC 2018.
- Wijayanti, P., L. Said, and P.J. Singh, *Analysis of determining deliverability test and transient pressure in the PW-02 well of Alpha fields by using Ecrin software*. Journal of Physics : Conference Series, 2019. **1402**(5): p.1-6.
- Putri, N.A., A. Fattahanisa, A. Ristawati, and R. Setiati, *Production capability prediction of a reservoir gas by using gas deliverability analysis to supply gas energy in Indonesia*. IOP Conf. Series: Earth and Environmental Science 780. 2021: 012016.
- Iscan, A.G., *Water saturation calculation using fractional flow and production logging data in a caspian region sandstone petroleum reservoir*. J. Petrol. Sci. Eng. 2021. **200**(05): p.108355
- Iscan, A.G., F. Civan, M.V. Kok, *Alteration of permeability by drilling fluid invasion and flow reversal*. J. Petrol. Sci. Eng. 2007. **58** (1-2): p.272-244.
- Rawlins, E.L. and Schellhardt, M.A., *Backpressure data on natural gas wells and their application to production Practices*. 1935 (7). Monograph Series, USBM.
- Houpeurt, A., *On the flow of gases in porous media*. Revue de L' Institut Francais du Petrole, 1959. **15**(11): p. 1468-1684.
- Donohue, D. and Ertrekin, T., *Gas Well Testing Theory, Practice & Regulation*. 1982, Springer Netherlands.
- Ikoku, C.U., *Natural Gas Production Engineering*. 1992, Krieger Publishing Company.
- Chaudry, A., *Gas Well Testing Handbook* 2003, Elsevier and Gulf Publishing.

**Research Article**

Investigation of the availability of a new point load test device in characterization of rocks

Deniz Akbay ^{a,*}  and Raşit Altındağ ^b 

^aÇanakkale Onsekiz Mart University, Çan Vocational School, Department of Mining and Mineral Extraction, Çan, Çanakkale, 17400, Turkey

^bSüleyman Demirel University, Faculty of Engineering, Department of Mining Engineering, Isparta, 32260, Turkey

ARTICLE INFO*Article history:*

Received 18 April 2021

Revised 04 June 2021

Accepted 17 June 2021

Keywords:

Natural stone

Point load index

Rock characterization

Test device

ABSTRACT

Difficulties in determining rock properties have led to the developed and increased use of index test methods predicting them. Index test methods are mostly simple, cheap, and easy to apply but there are some restrictions due to these specifications. The most used method to determine the strength values of rocks indirectly is the point load index. The main aim of this study is primarily investigating the usability of modified test device instead of classical test device. For this, laboratory tests were carried out on rocks with different strength values (3 igneous, 1 metamorphic, 3 sedimentary). The point load index tests were carried on 15 different classical test devices and on a modified test device which the limitations of the classical test device were eliminated. Analysis of the obtained results was carried out by the simple regression method. It was determined the modified test device can be used reliably instead of the classical test devices. Besides, while determining the strength tests the stress distributions on the samples were examined with the finite element method.

1. Introduction

Classification of rock mass is very important in engineering projects in terms of project design. Different methods are used to obtain this information in engineering applications. The most preferred one of these is the experimental method. Experimental methods consist of experiments involving index and engineering properties that are used to identify and correlate the rock mass and the ground, which are performed according to the related standards. However, for some experiments, rock procurement, preparation, and testing are costly and time-consuming. In such cases, to predict the required parameter, simpler, faster, easier, relatively cheaper test methods that do not require a sample preparation process may be preferred. The first and most used mechanical parameter that comes to mind to determine the strength properties of rock material is uniaxial compressive strength (UCS). In cases where UCS cannot be determined, the first and most used mechanical parameter that comes to mind to predict UCS is the point loading index (PLI). For this reason, many researchers have been

studying on predicting the UCS of rocks using PLI indirectly. As a result of these studies, the researchers presented more than 100 equations that were predicting UCS using PLI [1]. In rocks of different geological origin and structure to predict the UCS of the rock its PLI value must multiply by a coefficient ranging from 3 to 71 [1]. However, it has not been revealed clearly which coefficient will be used for which rock in predicting UCS, so the studies in this area have continued.

For the first time in the literature, Andrea et al. [2] mentioned PLI as point load tensile strength and defined it “point load tensile strengths were obtained by applying a compressive point load to the surface of a cylindrical core perpendicular to the axis of the core”. They emphasized as a result of their study that PLI alone can be reliably sufficient to predict UCS. They determined a linear and strong relationship between UCS and PLI. For years after, the researchers used PLI to predict the UCS of the rocks. First Broch and Franklin [3] and Bieniawski [4] investigated the correlation between UCS and PLI in their studies. After that, many studies were carried out in which

* Corresponding author. Tel.: +90-286-416-7705; Fax: +90-286-416-3733.

E-mail addresses: denizakbay@comu.edu.tr (D. Akbay), rasitaltindag@sdu.edu.tr (R. Altındağ)

ORCID: 0000-0002-7794-5278 (D. Akbay), 0000-0002-5397-7312 (R. Altındağ)

DOI: 10.35860/iarej.918874

© 2021, The Author(s). This article is licensed under the CC BY-NC 4.0 International License (<https://creativecommons.org/licenses/by-nc/4.0/>).

different coefficients were proposed. They carried out the experiments on different rock samples and on different sample shapes. Singh and Singh [5] examined the relations between PLI and UCS using quartzite rocks. Rusnak and Mark [6] made a study that was involving the load frame and PLI tests of coal. Akram and Bakar [7] performed PLI tests on different rock types to consider the relationships between the UCS and the PLI. Basu and Kamran [8] tested usability of PLI to predict UCS on schistose rocks. Heidari et al. [9] aimed to compare all of the PLI test methods and their applicability in practice. Singh et al. [10] made a study to confirm the relationship between PLI and UCS for core samples of igneous, sedimentary, and metamorphic origin rock types. Elhakim [11] used PLI as a describing parameter like UCS for weak and very weak calcareous sandstones. Liang et al. [12] They made experiments on irregular samples to compare and verify the empirical relation between UCS and PLI for different rock types. Alitalash et al. [13] researched relationships between the PLI and UCS for rock samples. Wong et al. [14] investigated the relations of the UCS with PLI on irregular volcanic rock samples for of different grain sizes and weathering grades. Akbay and Altındağ [15] made experiments on 15 different test devices on the same samples to investigate the errors and the limitations of the PLI test method and device. Al-Jassar and Hawkins [16] studied the correlations between PLI and geotechnical properties on the carboniferous limestone various sized samples. Çobanoğlu and Çelik [17] made a study to estimate UCS from PLI, P-wave velocity and Schmidt hardness using multiple regression analysis. Minaeian and Ahangari [18] examined the relationship between PLI and UCS and tensile strength of weak conglomerates. Ferentinou and Fakir [19] investigated the correlations of the UCS and indirect tests such as PLI for some sedimentary and igneous rocks using the technology of artificial intelligence Teymen [20] made an experimental study to determine the relations between mechanical properties and index properties such as PLI. Khajevand and Fereidooni [21] used PLI and block punch strength tests to estimate the mechanical properties of rocks in their study. Brook [22] suggested a size correction for PLI test method in his study. Abbs [23] made a statistical study and showed that PLI was poorly suited to weak carbonate rocks. Norbury [24] reviewed published papers reporting test procedures and case histories and underlined PLI is a useful test as a cheap reliable index test. Khanlari et al. [26] researched on different experimental techniques to classify the strength of anisotropic foliated rocks and pointed at that porosity and water absorption are the dominant parameters on the mechanical properties of rocks such as PLI. Smith [27] investigated the usability of the PLI for weak rocks in dredging applications. Look and Griffiths [28] looked for an answer in their study the usability of

PLI to provide guidance on design parameters for various tunnels and bridge foundations. Quane and Russel [29] developed rock strength as an ancillary tool for mapping variations in welding intensity using PLI. Basu and Aydin [30] researched the properties of cone penetration test with weathering in granitic samples, to improve the prediction ability prediction of UCS of PLI. Kabilan et al. [31] examined the relationships between UCS and PLI based on joint asperity and orientation of rocks. Also, there are many studies in the literature that were researched the relationships between PLI and other rock properties. Ren et al. [32] established a correlation of failure load between half-core and core samples with a fit size suggestion and size correction factor. Mesutoğlu and Özkan [33] made a study to determine the material characteristics of coal and inner burdens using relationships between the Schmidt hardness and PLI values. Guevara-Lopez et al. [34] developed prediction models for the UCS of rocks based on the PLI. Jamshidi et al [35] suggested a new parameter (PMP) based on physical and mechanical properties of rocks to estimate the brittleness of sandstones and calculated the PMP of sandstones based on the ratio of PLI to porosity. Şahin et al. [36] studied on prediction models for the UCS from the PLI on half-cut core samples.

In this study, the PLI tests were carried out on 15 different classical PLI test devices and a modified PLI test device which the limitations were removed (Figure 1). Seven different rock types (three sedimentary, one metamorphic, three igneous) used in the experiments. The classical PLI test device was modified to eliminate the limitations and errors determined by Akbay and Altındağ [31]. Thus, the ability of PLI obtained from the modified PLI test device to predict physical and mechanical properties was analyzed.

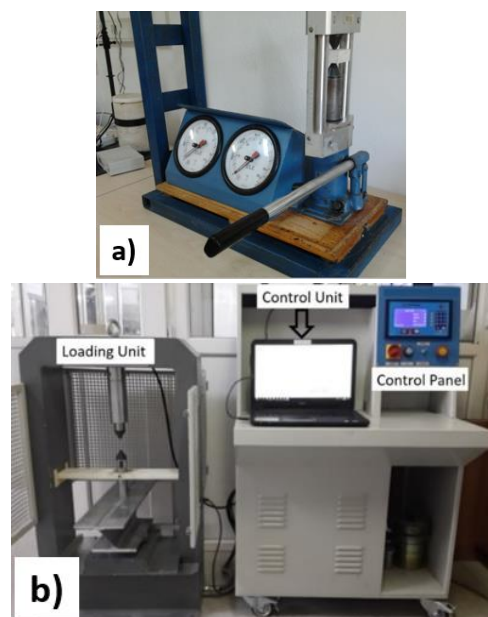


Figure 1. a) The classical test device and b) the modified test device

In the studies carried out so far, the results obtained from a single test device (with known errors/limitations) have been compared with the other properties of the rocks. The main reason is using a test device with known errors/limitations why the results obtained in these studies, in which heterogeneous rock material was investigated, showed such a large distribution from each other.

In such a situation, the number of samples should be increased and even the experiment should be repeated in different devices in order to reach the closest results to the real. In this study, it was shown that the results to be obtained by using a test device that was eliminated from its errors/ limitations instead of these would be sufficient. You should repeat the PLI tests on at least 15 different devices to achieve the nearest true PLI. This will take a lot of time and will be costly and you will need a large number of test samples. Or it will be enough to carry out tests just on the modified test device to reach the reliable results on a limited number of samples in less time.

2. Materials and Methods

Seven different rock types were used in this study and rock blocks were taken from marble processing plants located in different regions of Turkey (Table 1). The investigated natural stones show a wide range of strength and are generally used for building, facing, and flooring applications. All the test specimens were prepared according to the related standards recommended by the International Society for Rock Mechanics and Rock Engineering (ISRM) and Turkish Standards Institution (TSE). For the mineralogical and petrographic examinations of the rock samples used in the study, thin sections were prepared in the laboratory and mineralogical analyses were made with a microscope. The fresh surface images of the rocks used in the analyses are given in Figure 1.

2.1 Sample Description

For the mineralogical and petrographic examinations of the rock samples used in the study, thin sections were prepared in the laboratory and mineralogical analyses were made with a microscope. The fresh surface images of the rocks used in the analyses are given in Figure 2.

Limestone-1:

The dominant mineral is calcite. Calcites are anhedral fine-grained and occasionally found in medium grains. There are randomly formed thin and medium cracks in the rock. The cracks observed in the rock are mostly filled by thin and medium-sized secondary calcites. The rock shows the micritic character (Figure 2a).

Table 1. Geographical and geological origins of the rocks used in this study

Sample	Sample Code	Origin	Region
Limestone-1	LS-1	Sedimentary	Isparta
Limestone-2	LS-2	Sedimentary	Isparta
Limestone-3	LS-3	Sedimentary	Antalya
Marble	M	Metamorphic	Muğla
Andesite	A	Igneous	Isparta
Granite	G	Igneous	Aksaray
Diabase	D	Igneous	Kayseri

Limestone-2:

The dominant mineral in the rock is dolomite. Crystals are semi-essentially shaped. The crystals are medium-grained and there are coarse grains in places. Dolomite is also observed as vein filling in less observed cracks in the rock. The rock shows micritic and sparitic texture (Figure 2b).

Limestone-3:

The dominant mineral is calcite. Calcite crystals are generally rhombic and euhedral and sometimes seen as subhedral. Calcites are fine and medium grain size. The rock has a massive appearance, and no fractures or cracks are observed. However, it may contain some melt gaps. The rock consists of sparitic texture (Figure 2c).

Marble:

The rock consists of calcite minerals. Calcites are observed in medium and coarse grain sizes. Crystals exist in subhedral and anhedral forms. Rhomboedric cleavage and polysynthetic twinning are commonly observed in calcites. The rock generally shows a homogeneous feature without fractures or cracks. The rock is in granoblastic texture (Figure 2d).

Andesite:

The rock is phenocrystalline mainly composed of amphibole (hornblende), plagioclase, and pyroxene (augite) minerals. On the other hand, there are sanidine and opaque minerals. The rock shows porphyritic, pilotaxitic, and glomeroporphyritic texture characteristics. Amphiboles are euhedral and subhedral. They are generally hexagonal in shape and cleavage. Brownish interference-colored amphiboles have brownish and dark brown pleochroism. Most of these crystals have become opaque by oxidizing along the edge planes. Pyroxene crystals are observed in the form of thin, long, rod-like crystals. These crystals with a greenish interference color have low pleochroism. Plagioclases have been observed as phenocrysts, generally semi-shaped, plate-like crystals. While it typically shows polysynthetic twinning, it rarely shows zoned extinction. Kaolinization is evident in the rock, in the phenocrysts of sanidine, and in the whole section (Figure 2e).

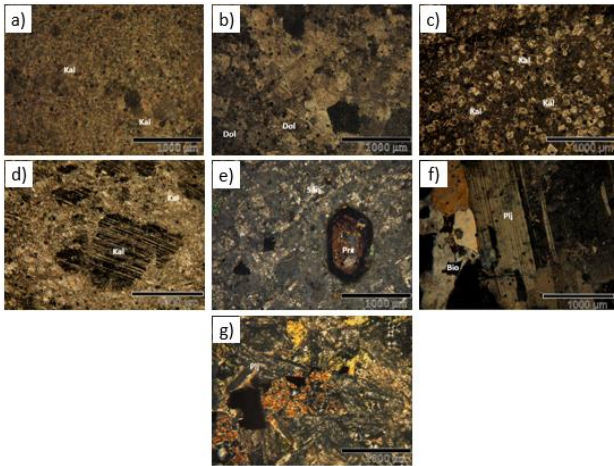


Figure 2. The images of the samples under the polarizing microscope a) limestone-1, b) limestone-2, c) limestone-3, d) marble, e) andesite, f) granite, g) diabase

Granite:

Dominant minerals in the rock are plagioclase (oligoclase), alkali feldspar (orthoclase), and quartz. There are fewer amounts of biotite and hornblende. Plagioclases are euhedral and subhedral. It commonly shows polysynthetic twinning and rarely shows zoned extinction. It is generally separated, and clay formation is observed. Orthoclase mineral is less common than plagioclase. Biotites are thin and long rod-like and plate-like shapes. Biotites with brown interference color have brownish pleochrism. Quartz is in the form of anhedral crystals. It is seen as transparent and transparent. They rarely show undulating extinction (Figure 2f).

Diabase:

The dominant mineral in the rock is plagioclase and amphibole. There are opaque minerals scattered around. Plagioclases mostly do not show their optical properties due to alteration, but they are grayish-brown in color. They have been observed as long and rod-like crystals. They rarely show polysynthetic twinning. Amphiboles are subhedral and anhedral. Chloritization is generally observed in amphibole

minerals (Figure 2g).

2.2 Physical and Mechanical Properties

To describe the investigated rocks in this study some physical and mechanical properties tests were performed in the laboratory. Density, unit volume weight; apparent porosity, and total porosity [37], water absorption percent by weight [38], sound speed propagation [39], Bohme abrasion strength [40], the uniaxial compressive strength [41], Brazilian tensile strength [42], flexural strength under concentrated load [43], and flexural strength under constant moment [44] of the investigated rocks were determined with the related standards and suggested methods. All tests were carried on at least ten samples. The test results were presented in Table 2 and Table 3.

3. Point Load Index Tests

Seven different rock types were used in this study and rock blocks were taken from marble processing plants located in different regions of Turkey (Table 1). The investigated natural stones show a wide range of strength and are generally used for building, facing, and flooring applications. All the test specimens were prepared according to the related standards recommended by ISRM [45]. Figure 3 shows the PLI values obtained from 15 different devices and modified devices together. It is seen in Figure 3 how far the values obtained from 15 different devices deviate from each other. The dashed line on the figure is a line drawn from the modified device value. It can be said that this line approximately represents the average of the values obtained from 15 different devices. In Table 4, average PLI values and standard deviation values obtained from 15 different devices and modified device are given. It is seen that especially the standard deviations of the PLI values obtained from the modified test device are smaller than the standard deviations of the PLI values obtained from 15 different test devices.

Table 2. The physical properties of rocks [1]

Sample Code	d_0		UVW		WAW		AP		TP	V_p		BAR	
	(g/cm ³)		(g/cm ³)		(%)		(%)		(%)	(m/s)		cm ³ /50cm ²	
	\bar{x}	SD	\bar{x}	SD	\bar{x}	SD	\bar{x}	SD	\bar{x}	\bar{x}	SD	\bar{x}	SD
LS-1	2.770	0.007	2.756	0.016	0.124	0.053	0.343	0.148	0.484	6627	38	10.5	0.6
LS-2	2.851	0.009	2.714	0.009	1.173	0.119	3.183	0.313	4.788	5456	688	10.0	0.7
LS-3	2.734	0.005	2.561	0.012	2.375	0.290	6.081	0.720	9.311	5038	451	14.6	0.2
M	2.725	0.002	2.713	0.001	0.076	0.015	0.206	0.040	0.440	6144	723	9.1	0.9
A	2.608	0.002	2.303	0.019	3.281	0.297	7.552	0.632	11.704	4875	91	9.9	0.1
G	2.673	0.005	2.644	0.002	0.218	0.004	0.576	0.011	1.082	5367	156	4.5	0.4
D	2.994	0.012	2.904	0.030	0.656	0.076	1.902	0.204	3.011	5101	152	4.5	0.5

d_0 : density; UVW: unit volume weight; WAW: water absorption percent by weight; AP: apparent density; TP: total porosity; V_p : ultrasonic wave velocity; BAR: Bohme abrasion resistance; \bar{x} : average; SD: standard deviation

Table 3. The mechanical properties of rocks [1]

Sample Code	σ_c (MPa)		σ_t (MPa)		$\sigma_{fs(c)}$ (MPa)		$\sigma_{fs(cm)}$ (MPa)	
	\bar{x}	SD	\bar{x}	SD	\bar{x}	SD	\bar{x}	SD
LS-1	110.6	11.1	8.4	1.3	11.6	2.5	14.2	2.7
LS-2	103.9	12.3	8.0	1.8	8.0	1.7	13.1	2.2
LS-3	64.2	10.8	8.9	0.9	10.8	1.1	17.4	1.4
M	72.1	5.0	8.5	1.7	13.5	2.0	21.0	0.8
A	102.4	11.5	10.0	0.6	15.7	0.8	22.9	1.4
G	154.0	8.6	10.0	1.3	17.7	1.1	31.7	2.5
D	144.5	15.8	11.6	1.4	17.2	2.3	24.9	1.7

σ_c : uniaxial compressive strength; σ_t : Brazilian tensile strength; $\sigma_{fs(c)}$: flexural strength under concentrated load; $\sigma_{fs(cm)}$: flexural strength under constant moment; \bar{x} : average; SD: standard deviation

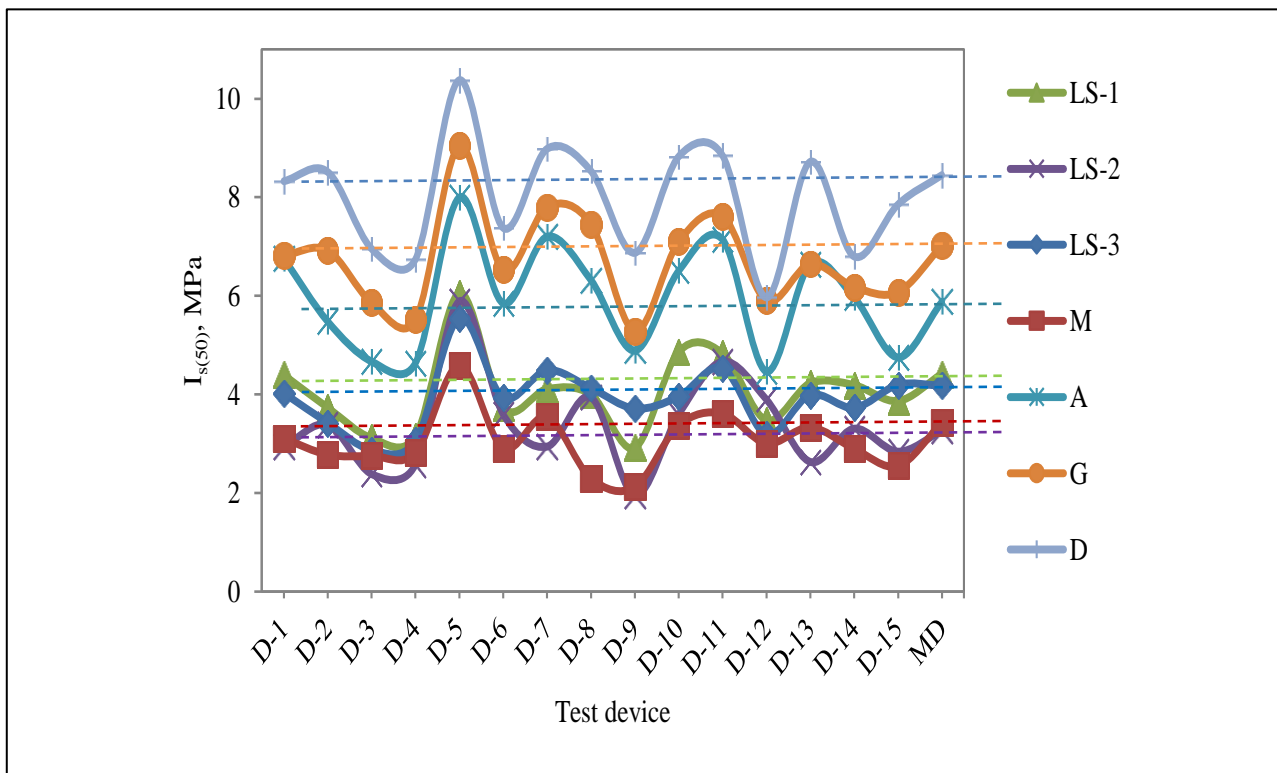


Figure 3. PLI values of the rocks obtained from 15 different PLI test devices and modified test device (D: test device; MD: modified test device)

4. Results and Discussions

4.1 Experimental Study

Relationships between PLI values and physical and mechanical properties of the studied rocks were analyzed by the simple regression method and distribution graphs were created (Figure 4 and 5). Significant relationships were found between PLI values (obtained from both 15 different test devices and modified test device) and physical and mechanical properties as expected. It is seen in Table 5, the correlation coefficients of the relationships between PLI values obtained from both 15 different test devices and modified test device and determined rock properties were very close. When Figures 4-5 are examined, it is seen that the strongest relationship is between PLI and Brazilian tensile strength with a correlation coefficient of $r = 0.96$, the weakest

relationship is between PLI and V_p with a correlation coefficient of $r = 0.52$ and $r = 0.46$. The correlation coefficients and their direction and type of relationships between PLI and physical and mechanical properties are given in Table 5. Brazilian tensile strength, flexural strength under concentrated load, and flexural strength under constant moment experiments apply for predicting the tensile strength of rocks. In this study when Table 5 is examined it is seen the correlation coefficients (r) between PLI and Brazilian tensile strength, flexural strength under concentrated load, and flexural strength under constant moment values of the studied rocks are higher than the correlation coefficient (r) between PLI and UCS. This should be interpreted as PLI is more capable of predicting tensile strength than predicting UCS.

Table 4. The PLI values obtained from different test devices [1]

Sample Code	The average values obtained from 15 different test devices		Modified test device		Difference between $I_{s(50)}$ values	Difference between SD values
	$\bar{x} I_{s(50)}$ (MPa)	SD	$\bar{x} I_{s(50)}$ (MPa)	SD	%	%
LS-1	3.95	0.86	4.22	0.24	7	-72
LS-2	3.29	1.27	2.76	0.98	-16	-23
LS-3	3.84	0.40	4.14	0.22	8	-45
M	2.97	0.31	3.31	0.20	11	-35
A	5.87	0.72	5.77	0.73	-2	1
G	6.64	0.63	6.96	0.23	5	-63
D	7.92	0.92	8.25	0.66	4	-28

\bar{x} : average; SD: standard deviation

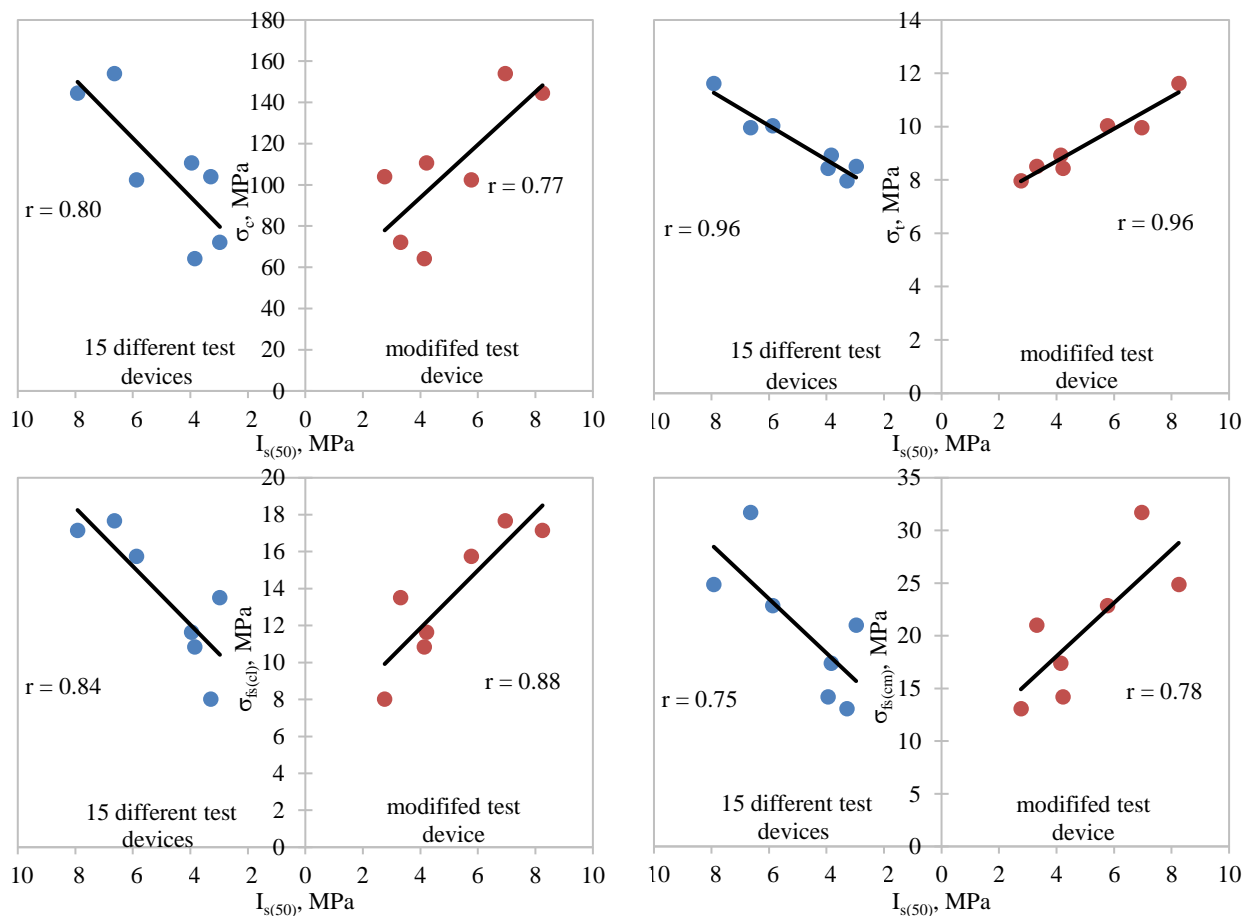


Figure 4. Relationships between PLI and some mechanical properties

4.2 Numerical Study

In the strength tests applied to rock samples in different shapes and sizes, the stress distributions formed on the rock samples were analyzed with ANSYS Workbench 2020 R1. For Young's modulus and poisson's ratio values required for static stress analysis, the default values defined for the limestone embedded in the software were used. For Young's modulus and poisson's ratio values required for static stress analysis, the default values defined for the limestone embedded in the software were used. The elastic modulus was to be assumed 38 GPa and Poisson's ratio was assumed to be 0.3 [45]. In the analysis, all different shaped and sized

samples were subjected to load of the amount required to achieve maximum stress of 5 MPa on cross-section, since the software used was academic version and there were limitations. While performing static stress analysis, Von mises stresses give good results in ductile materials, whereas principal stresses should be considered for brittleness materials such as limestone, marble, granite, etc. As a result of the analysis, maximum principal stress distributions on the surface and inside of the sample for each different test sample are given in Figure 6-10. The positive values show tensile stresses and the negative ones show compressive stresses.

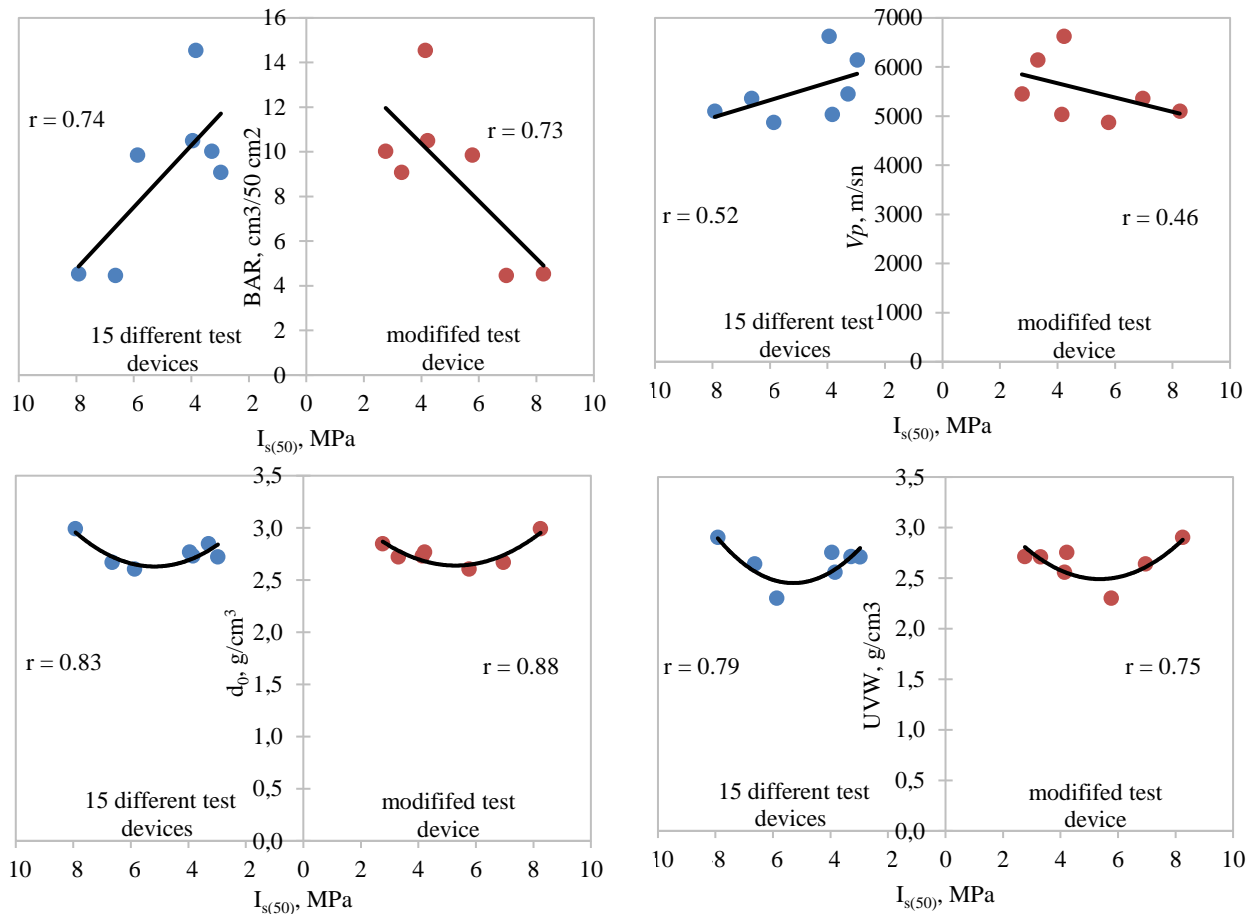


Figure 5. Relationships between PLI and some physical properties

Table 5. Correlations between PLI and physical and mechanical properties of rocks

Associated property	Correlation coefficient (r)		Form - direction
	15 different test devices	Modified test device	
$I_{s(50)}$ - σ_c	0.80	0.77	Positive linear
$I_{s(50)}$ - σ_t	0.96	0.96	Positive linear
$I_{s(50)}$ - $\sigma_{fs(cl)}$	0.84	0.88	Positive linear
$I_{s(50)}$ - $\sigma_{fs(cm)}$	0.75	0.78	Positive linear
$I_{s(50)}$ -BAR	0.74	0.73	Negative linear
$I_{s(50)}$ - V_p	0.52	0.46	Negative linear
$I_{s(50)}$ - d_0	0.83	0.88	Second-degree polynomial
$I_{s(50)}$ -UVW	0.79	0.75	Second-degree polynomial

$I_{s(50)}$: point load index; σ_c : uniaxial compressive strength; σ_t : Brazilian tensile strength; $\sigma_{fs(cl)}$: flexural strength under concentrated load; $\sigma_{fs(cm)}$: flexural strength under constant moment; BAR: Bohme abrasion resistance; V_p : ultrasonic wave velocity; d_0 : density; UVW: unit volume weight

In Figures 6 and 7, it is seen that the vertical applied load induces horizontal tensile stress and the distribution of this tensile stress occurs along a plane running parallel to the load application direction. The failure occurs at the centre of the specimen when the maximum tensile strength of the rock is exceeded. Since the tensile strength of rocks is lower than their compressive strength.

In Figures 8 and 9, a vertical load from the middle of the specimen standing on two supports or vertical loads are applied from two different points close to the middle point. Here, both compression and tensile forces occur in the

sample. Compression force occurs on the upper surface of the sample where the load is applied, while tensile stress occurs on the lower surface of the sample. Since the tensile strength of the rocks is lower than the compressive strength, the failure occurs when the tensile strength of the rock is exceeded.

However, when Figure 10 is examined, it is seen that tensile stresses are concentrated in a region close to the lower surface of the sample due to the vertical force applied to the upper surface of the sample.

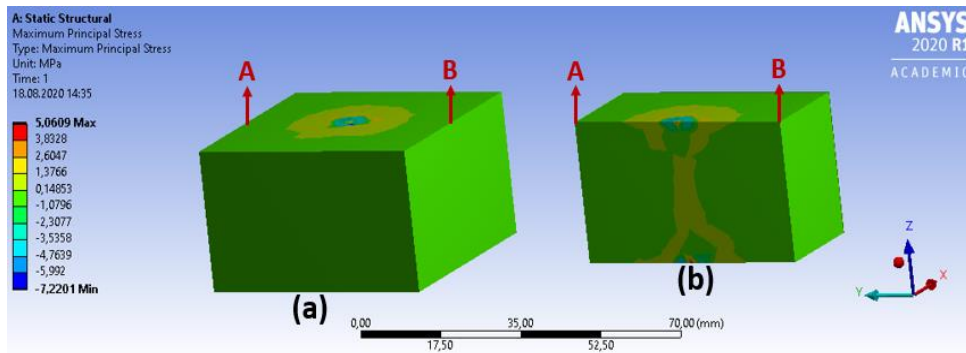


Figure 6. The stress distribution in block point index load tests; a) sample surface, b) section A-B

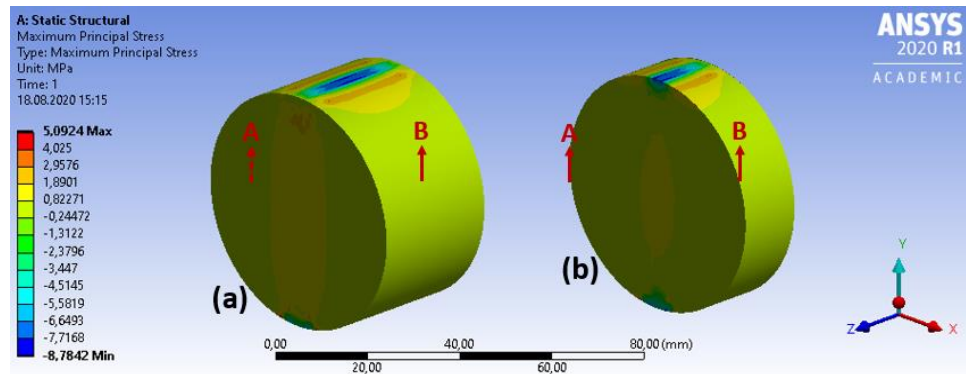


Figure 7. The stress distribution in Brazilian tensile strength tests; a) sample surface, b) section A-B

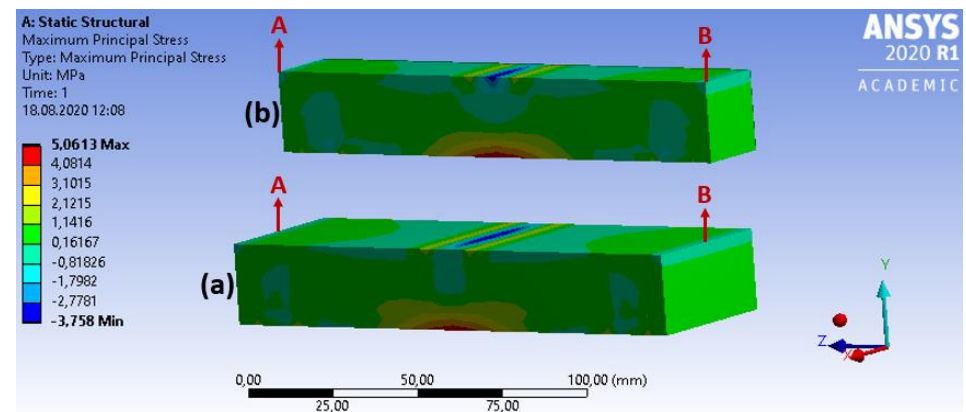


Figure 8. The stress distribution in flexural strength under concentrated load tests; a) sample surface, b) section A-B

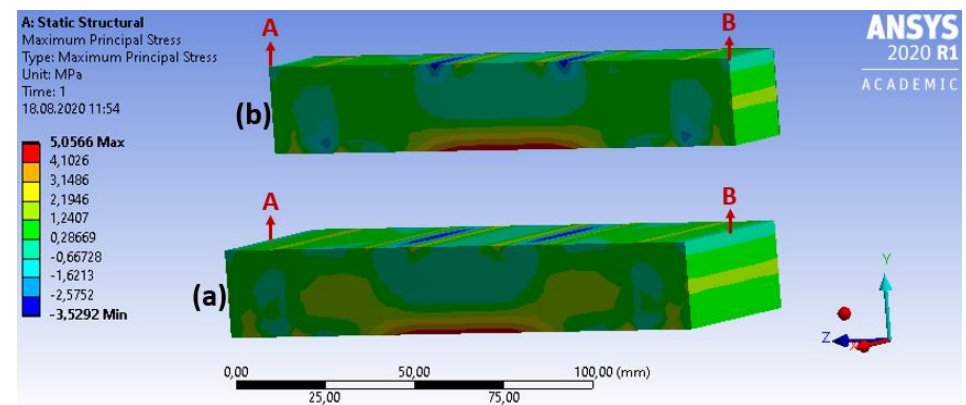


Figure 9. The stress distribution in flexural strength under constant moment tests; a) sample surface, b) section A-B

But in the compressive strength test, the failure occurs when the compressive strength of the rock exceeds along a failure plane. In other words, unlike the test methods

mentioned above, the compressive strength of the sample must be exceeded for the failure to occur.

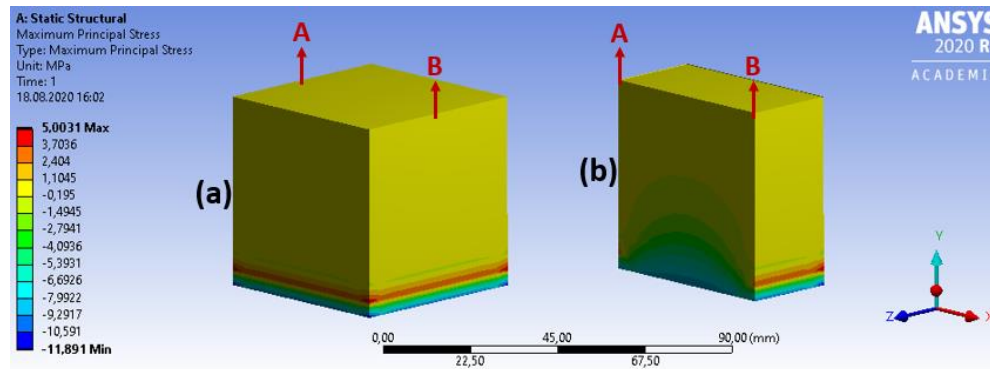


Figure 10. The stress distribution in uniaxial compressive strength tests; a) sample surface, b) section A-B

5. Conclusions

The aim of this study is primarily investigating the useability of modified test device instead of classical test device.

As a result of this study, you should repeat the PLI tests on at least 15 different devices to achieve the nearest true PLI. This will take a lot of time and will be costly and you will need a large number of test samples. Or it will be enough to carry out tests just on the modified test device. Also, significant relationships were found between PLI values (obtained from both 15 different test devices and modified test device) and physical and mechanical properties as expected. It is noticed, the correlations of the relations between PLI values obtained from both 15 different test devices and modified test device and determined rock properties were very close. These results also prove the PLI values obtained from the modified test device can be used reliably in predicting rock properties.

Several regression analyses were conducted between the PLI and some physical and mechanical properties using the laboratory test results of this study. According to the results obtained from the analysis, it is established that the strongest relationship is between PLI and Brazilian tensile strength. The performance of each correlation has been measured using linear and nonlinear regression analyses.

The results of the numerical analysis also support the analytical results obtained. The numerical analysis explains the failure mechanisms of each strength test.

Declaration

The authors declared no potential conflicts of interest with respect to the research, authorship, and/or publication of this article. The authors also declared that this article is original, was prepared in accordance with international publication and research ethics, and ethical committee permission or any special permission is not required.

Author Contributions

D. Akbay and R. Altındağ contributed to the formation of the idea. D. Akbay performed the design and literature review. D. Akbay and R. Altındağ provided the materials

used and examined the results. R. Altındağ checked the spelling and checked the article in terms of content.

Acknowledgment

This work supported by the Scientific and Technological Research Council of Turkey (TUBITAK) under Research Project (project no 116R070) and Suleyman Demirel University OYP Coordination Unit Project (project no OYP-05286-DR-13), Turkey.

References

- 1 Akbay, D., *Designing A New Testing Apparatus For Preventing The Errors in Point Load Index Test*, in: *Mining Engineering 2018*, Süleyman Demirel University: Turkey. p. 201.
- 2 Andrea, D.V.D., R.L. Fischer, and D.E. Fogelson, *Prediction of Compressive Strength From Other Rock Properties*. 1965, USA: Department of the Interior, Bureau of Mines.
- 3 Broch, E. and J. A. Franklin, *The Point-Load Strength Test*. *International Journal of Rock Mechanics and Mining Sciences*, 1972. **9**: p. 669–697.
- 4 Bieniawski, Z.T., *The point-load test in geotechnical practice*. *Engineering Geology*, 1975. **9**(1): p. 1–11.
- 5 Singh, V.K. and D.P. Singh, *Correlation between point load index and compressive strength for quartzite rocks*. *Geotechnical and Geological Engineering*, 1993. **11**(4): p. 269–272.
- 6 Rusnak, J. and C. Mark, *Using the Point Load Test To Determine the Uniaxial Compressive Strength of Coal Measure Rock*. in *Proceedings of the 19th International Conference on Ground Control in Mining*, Morgantown, West Virginia., 2000. p. 362–371.
- 7 Akram, M. and M.Z.A. Bakar, *Correlation between uniaxial compressive strength and point load index for salt-range rocks*. *Pakistan Journal of Engineering and Applied Sciences*, 2007. **1**(50): p. 1–8.
- 8 Basu, A. and M. Kamran, *Point load test on schistose rocks and its applicability in predicting uniaxial compressive strength*. *International Journal of Rock Mechanics and Mining Sciences*, 2010. **47**(5): p. 823–828.
- 9 Heidari, M., G.R. Khanlari, M.T. Kaveh, and S. Kargarian, *Predicting the uniaxial compressive and tensile strengths of gypsum rock by point load testing*. *Rock Mechanics and Rock Engineering*, 2012. **45**(2): p. 265–273.
- 10 Singh, T.N., A. Kainthola, and A. Venkatesh, *Correlation*

- between point load index and uniaxial compressive strength for different rock types. *Rock Mechanics and Rock Engineering*, 2012. **45**(2): p. 259–264.
- 11 Elhakim, A.F., *The use of point load test for Dubai weak calcareous sandstones*. *Journal of Rock Mechanics and Geotechnical Engineering*, 2015. **7**(4): p. 452–457.
 - 12 Liang, W., K. Hou, Z. Yang, and H. Sun, *Evaluation of Uniaxial Compressive Strength by Point Load Tests for Irregular Specimens of Different Rock Types*. *Electronic Journal of Geotechnical Engineering*, 2015. **20**(13):, p. 11265–11271.
 - 13 Alitallesh, M., M. Mollaali, and M. Yazdani, *Correlation between uniaxial strength and point load index of rocks*. in *The 15th Asian Regional Conference on Soil Mechanics and Geotechnical Engineering*, Fukuoka, Kyushu, Japan, 2015. p. 282–285.
 - 14 Wong, R.H.C., K.T. Chau, J.H. Yin, D.T.W. Lai, and G.S. Zhao, *Uniaxial compressive strength and point load index of volcanic irregular lumps*. *International Journal of Rock Mechanics and Mining Sciences*, 2017. **93**(February): p. 307–315.
 - 15 Akbay, D. and R. Altındağ, *Reliability and evaluation of point load index values obtained from different testing devices*. *The Southern African Institute of Mining and Metallurgy*, 2020. **120**(3): p. 181–190.
 - 16 Al-Jassar, S.H. and A.B. Hawkins, *Geotechnical Properties of The Carboniferous Limestone of The Bristol Area The Influence of Petrography And Chemistry*. in *4th ISRM Congress*, Montreux, Switzerland, 1979. p. 3–14.
 - 17 Çobanoğlu, I. and S.B. Çelik, *Estimation of uniaxial compressive strength from point load strength, Schmidt hardness and P-wave velocity*. *Bulletin of Engineering Geology and the Environment*, 2008. **67**(4): p. 491–498.
 - 18 Minaeian, B. and K. Ahangari, *Prediction of the uniaxial compressive strength and Brazilian tensile strength of weak conglomerate*. *International Journal of Geo-Engineering*, 2017. **8**(1): 19, p. 1–11.
 - 19 Ferentinou, M. and M. Fakir, *An ANN Approach for the Prediction of Uniaxial Compressive Strength, of Some Sedimentary and Igneous Rocks in Eastern KwaZulu-Natal*. *Procedia Engineering*, 2017. **191**: p. 1117–1125.
 - 20 Teymen, A., *Prediction of Basic Mechanical Properties of Tuffs Using Physical and Index Tests*. *Journal of Mining Science*, 2018. **54**(5): p. 721–733.
 - 21 Khajevand, R. and D. Fereidooni, *Utilization of the point load and block punch strengths to predict the mechanical properties of several rock samples using regression analysis methods*. *Innovative Infrastructure Solutions*, 2019. **4**: p. 15.
 - 22 Brook, N., *Size Correction for Point Load Testing*. *International Journal of Rock Mechanics and Mining Sciences & Geomechanics Abstracts*, 1980. **17**(2): p. 231–235.
 - 23 Abbs, A.F., *The Use of the Point Load Index in Weak Carbonate Rocks*. in *ASTM STP 883*, R. C. Chaney and K. R. Demars, Eds., American Society for Testing and Materials, Philadelphia, 1985. p. 413–421.
 - 24 Norbury, D.R., *The Point Load Test*. *Engineering Geology Special Publication*, 1986. **2**: pp. 326–329.
 - 25 Hawkins, A.B., *Aspects of rock strength*. *Bulletin of Engineering Geology and the Environment*, 1998. **57**(1): p. 17–30.
 - 26 Khanlari, G., B. Rafiei, and Y. Abdilor, *Evaluation of strength anisotropy and failure modes of laminated sandstones*. *Arabian Journal of Geosciences*, 2014. **8**: p. 3089–3102.
 - 27 Smith, H.J., *The Point Test for Weak Rock in Dredging Applications*. *International Journal of Rock Mechanics and Mining Sciences*, 1997. **34**(295): p. 3–4.
 - 28 Look, B.G. and S.G. Griffiths, *An Engineering Assessment of the Strength and Deformation Properties of Brisbane Rocks*. *Australian Geomechanics Journal*, 2001. **36**(3): p. 17–30.
 - 29 Quane, S.L. and J.K. Russell, *Ranking welding intensity in pyroclastic deposits*. *European Journal of Mineralogy*, 2003. **15**: p. 855–864.
 - 30 Basu, A. and A. Aydin, *Predicting uniaxial compressive strength by point load test: Significance of cone penetration*. *Rock Mechanics and Rock Engineering*, 2006. **39**(5): p. 483–490.
 - 31 Kabilan, N., M. Muttharam, and V. Elamathi, *Prediction of Unconfined Compressive Strength for Jointed Rocks Using Point Load Index Based on Joint Asperity Angle*. *Geotechnical and Geological Engineering*, 2017. **35**: p. 2625–2636.
 - 32 Ren, F., H. Liu, R. He, G. Li, and Y. Liu, *Point load test of half-cylinder core using the numerical model and laboratory tests: Size suggestion and correlation with cylinder core*. *Advances in Civil Engineering*, 2018. **2018**(Special Issue): p. 1–11.
 - 33 Mesutoğlu M., İ. Özkan, *Büyük ölçekli kömür arınında gerçekleştirilen schmidt sertlik indeksi ve nokta yükleme dayanımı deney sonuçlarının değerlendirilmesi*. *Konya Journal of Engineering Sciences*, 2019. **7**: p. 681–695.
 - 34 Guevara-Lopez F., R. Jimenez, P. Gardoni, P. Asem, *Probabilistic prediction of intact rock strength using point load tests using a Bayesian formulation*. *Georisk*, 2020. **14**(3): p. 206–215.
 - 35 Jamshidi A., Y. Abdi, and R. Sarikhani, *Prediction of Brittleness Indices of Sandstones Using a Novel Physico-Mechanical Parameter*. *Geotechnical and Geological Engineering* 2020. **38**: p. 1–9.
 - 36 Şahin M., R. Ulusay, and H. Karakul, *Point Load Strength Index of Half-Cut Core Specimens and Correlation with Uniaxial Compressive Strength*. *Rock Mechanics and Rock Engineering*, 2020. **53**: p 3745–3760.
 - 37 TSE, *TS EN 1936, Natural stone test methods - Determination of real density and apparent density and of total and open porosity*. 2010, Ankara, Türkiye: TSE.
 - 38 TSE, *TS EN 13755, Natural stone test methods - Determination of water absorption at atmospheric pressure*. 2014, Ankara, Türkiye: TSE.
 - 39 TSE, *TS EN 14579, Natural stone test methods - Determination of sound speed propagation*. 2006, Ankara, Türkiye: TSE.
 - 40 TSE, *TS EN 14157, Natural stone - Determination of the abrasion resistance*. 2017, Ankara, Türkiye: TSE.
 - 41 TSE, *TS EN 1926, Natural stone test methods - Determination of uniaxial compressive strength*. 2013, Ankara, Türkiye: TSE.
 - 42 ISRM, *The complete suggested methods for rock characterization, testing and monitoring: 1974–2006*. 2007, London, UK: Springer.
 - 43 TSE, *TS EN 12372, Natural stone test methods - Determination of flexural strength under concentrated load*. 2013, Ankara, Türkiye: TSE.
 - 44 TSE, *TS EN 13161, Natural stone test methods -*

Determination of flexural strength under constant moment.
2014, Ankara, Türkiye: TSE.

- 45 ISRM, *Suggested Method for Determining Point Load Strength.* in ISRM, U. R. and H. J.A., Eds., 1985, London, UK: Springer, p. 53–60.
- 46 Mavko, G., T. Mukerji, and J. Dvorkin, *The Rock Physics Handbook.* 2009, Cambridge, UK: Cambridge University Press.

**Research Article**

Prediction of cutting temperature in carbide cutting tool using finite element method

Mercy Ozakpolor ^a , Cyril Aliyegbenoma ^{b,*}  and Dikson David Olodu ^{a,b} 

^aDepartment of Production Engineering, Faculty of Engineering, University of Benin, Benin City, Edo State, Nigeria

^bDepartment of Mechanical Engineering, Faculty of Engineering, Benson Idahosa University, Benin City, Edo State, Nigeria

ARTICLE INFO*Article history:*

Received 14 January 2021

Revised 04 July 2021

Accepted 03 August 2021

Keywords:

Natural stone

Point load index

Rock characterization

Test device

ABSTRACT

This study demonstrated the effectiveness of the finite element method in predicting the cutting temperature in carbide inserted cutting tool. A three-factor Box-Behnken design, making seventeen cutting tests of a cylindrical mild steel bar with 200 mm length by von mises diameter was employed to study the numerical and the experimental predictions. The data obtained from the tool tests was compared and statistically analyzed using the reliability plots. On comparison, both the experimental and finite element method (FEM) analysis by ANSYS® readings were in close agreements, with the minimum and maximum error of 0.010% and 0.895%, respectively. In conclusion, the research clearly shows that ANSYS® is a very efficient expert tool for modeling and predicting the cutting temperature of carbide insert cutting tool in dry turning operation using mild steel.

1. Introduction

Machining process like the metal cutting operation is a plastic deformation process that has been found to generate more heat than the simple manual tools due to the sliding friction of the chip on the rake face. The heat generated during the cutting operation brings about a rise in the temperature of the tool, chip and the work-piece. As the temperature increases, it adversely impairs the cutting tool, chips and weakens the mechanical properties of the machined surface. The magnitude of the cutting temperature depends on quite a number of factors like the tool geometry parameters, cutting conditions (wet or dry), type of material of the cutting tool/work piece and the process parameters [1]. However, the major effect of the increased cutting temperature in Von Mises stress, which inevitably is induce on the cutting tool due to high strains. The produced Von Mises stresses are the major cause of tool fracture, fatigue and failure; a situation resulting from loses of bindings within the crystals of the tool materials [2]. This makes the prediction of the tool's temperature an important undertaking, as it will optimally adjust the various cutting parameters before-hand for an improved

machinability. Ostafieu et al. [3] examined tool heat transfer in orthogonal metal cutting under steady state. The iterative procedure was used to determine the temperature distributions on the cutting tool. Thereafter, the heat flux model with its conditions was analyzed. Their results showed agreement with the experimental results; meaning that the chosen heat flux model was appropriate. Grzesik [4] studied the influence of the tool-work interface temperature when machining AISI 1045 and AISI 304. The researcher employed the use of a standard K-type thermocouple to measure the interface temperature of the work piece. Dewes et al. [5] developed a temperature prediction model which they applied under transient conditions. It was done by a fixed-point iteration process in quasi-steady energy partitioning to improve on Stephen's model. Chaudhary et al. [6] addressed the tribology in metal cutting in treating the thermal issues, they developed an analytical model that was used to determine the temperature distributions in the chip, the tool and the work piece material using the combined effect of two heat sources, namely; the nature of the apparent heat partition in the shear plane and the variable heat partition at the chip-tool interface. The researchers were

* Corresponding author. Tel.: +23-470-318-45015.

E-mail addresses: othuke2477@gmail.com (M. Ozakpolor), cyril.aliyegbenoma@eng.uniben.edu (C. Aliyegbenoma), dolodu@biu.edu.ng (D.D. Olodu)

ORCID: 0000-0002-7625-0087 (M. Ozakpolor), 0000-0003-0056-7763 (C. Aliyegbenoma), 0000-0003-3383-2543 (D.D. Olodu)

DOI: 10.35860/iarej.859488

© 2021, The Author(s). This article is licensed under the CC BY-NC 4.0 International License (<https://creativecommons.org/licenses/by-nc/4.0/>).

able to justify the empirical model using a wide range of pellet numbers available in the experimental data obtained from literature. Miller et al. [7] carried out a study on cutting tool temperature measurement using a new experimental technique known as modern digital infrared imaging technique. This device was able to overcome many problems associated with past experimental techniques during orthogonal machining operations. The device was effective as it successfully displaced the temperature distributions on the cutting tool. Abhang and Hameedullah [8] carried out a study on EN-31 steel alloy with tungsten carbide insert using the tool-work thermocouple technique to research the tool-chip interface temperature. Their results showed agreement with the shaw's non-dimensional model. In addition, the work was able to ascertain that increasing cutting speed, feed rate and depth of cut can bring about increase in the cutting temperature of the tool. Ranc et al. [9] also studied temperature prediction in orthogonal cutting of Al/SiCp composites with a k-20 carbide cutting tool using a thermocouple. This was to measure the temperature along the cutting tool edge at various cutting speeds and depths of cut while the feed rate was kept constant. The temperature distributions at the cutting edge, shear zone and the interface region were estimated from the analysis of the steady state heat transfer carried out by the researchers. Nasr et al. [10] confirmed that when they studied the turning process during metal cutting. They agreed on the fact that the metal cutting process is the biggest part of the manufacturing sector which in turn represents the biggest energy consumers in the world. Their results showed that the cutting temperature increases with increase in the spindle speed, feed rate and depth of cut.

This study focused on expert modeling and prediction of cutting temperature in carbide insert cutting tool using finite element method (ANSYS).

2. Materials and Methods

2.1 Workpiece Material

The workpiece material that is used in the cutting tool test was a cylindrical bar mild steel (American Iron and Steel Institute, AISI 1010). This choice is the result of sustainability in a wide variety of automotive applications such as axles and spline shafts [11]. The mild steel (workpiece) was first planed to a uniform dimension of 200 mm in length and 44 mm in diameter, respectively.

2.2 Tool material

The tool material used in this study is a triangular and removable coated carbide insert P(10). In this study, it was selected since it performs better than the uncoated carbide tool when turning steel. Thomas et al. [12] founded that it can reduce tendency to built up edges, less heat generation

and increase tool life thanks to reduced friction, fewer thermal cracks and most importantly the wear pattern which is recognized easily by the yellow tin layer [13].

2.3 Experimental Method

The Box Behnken Design (BBD) The 3 factors Box Behnken Design BBD is a response surface design that is suitable for exploiting quadratic response surfaces, thereby helping to generate a second-degree polynomial model that is used for optimising the process. It is also advantageous for three factors taken at different levels because it requires fewer numbers of runs but for four or more factors this advantage disappears. Hence it has been adopted for this study because it was used to determine the process relationship between the independent variable (spindle speed, federate and depth of cut) and dependent variable (Cutting temperature which is ordinary difficult with direct straight line experimental method. Some other characteristics of BBD are good lack of fit detection, suitability for blocking, minimum number of treatments. combinations, good graphical analysis through simple data patterns, very cost effective, good distribution of variance of the produced response(s) through the design region and internal estimate of error. It was developed using the design expert (software). While the experimental runs is determined by the number of the input parameters using Equation (1) below:

$$N = K^2 + K + C_p \quad (1)$$

where N = number of experimental runs, K= Factors number which is 3 in this case, Cp= number of replications at the centre point which is 5 in this case.

In this study, the experimental cutting test included the dry cutting of a cylindrical mild steel bar is 200 mm length by 44 mm diameter by using the industrial Lathe machine. For the machining operation, carbide inserts single-point cutting tool was used. The three-factors BBD of experiment was adopted. The parameters of cutting that are the feed rate, depth of cut and the spindle speed are shown in Table 1. 7th experiment were performed as given in Table 1. For the cutting tool tests, The 2060 Electronic numerical controlled (ENC) model lathe situated at Prototype Engineering Development Institute (PEDI), Ilesa, Osun state, Nigeria was used.

Interpretation and evaluation of result is expressed in this stage. Seventeen experiments were conducted for the cutting temperatures in carbide insert tools while machining AISI 1010 mild steel under dry condition. The cutting tool tests were based on the three factors Box-Behnken design generated by the Design Expert. During, the experimental test, the K-type digital multi- meter thermometer was used to measure the tool's temperature.

The carbide inserts cutting tool test was conducted based on the three factors Box Behnken's experimental

design on a 2060 CNC industrial lathe under dry condition using cylindrical mild steel of 200 mm long. Before the experiments, the work piece was first plain for uniform diameter of 44 mm in the university of Benin Production laboratory.

The plain work piece was then taken to the lathe for machining where it was supported between the three chucks of the rotating center of the tail stock while the carbide inserts cutting tool was mounted on the righthand tool holder. And at different times, the cutting tool was automatically fed based on the selected values and levels of the cutting parameters. The researcher's application of the three factors Box Behnken Design is to determine the optimum values of the cutting parameters that will enable effective functioning of the cutting tool when using mild steel. The cutting parameters were chosen at different levels of spindle speed ranging from 200-600 rpm and federate from 0.05-1.5 mm/rev.

The configuration is based on the experimental designed matrix of seventeen runs was used. The tool work piece thermocouple (k-type digital thermocouple GM 1312) was used to measure the cutting temperature of the cutting tool. During the experiment three readings were taken at every 5 minutes and their average was adopted measured data so as to minimize experimental error. And after each single test the carbide tool was replaced, this was to eliminates the defects of temperature and possible tool wear on the tool and responses.

2.4 Numerical Method

The finite element method (FEM) which is an expert tool was used for simulating the behavior of the cutting tool during machining. Furthermore, commercial FEM software such as ANSYS® was used to analyze finite element problem in three steps namely: preprocessing, solution and post processing according to Etin-osa and Achebo [14].

Governing equation and bounding conditions of heat transfer:

The governing equation for temperature variation in the carbide insert cutting tool is derived from energy conservation and fourier law as showed below; Energy in-Energy out +Energy generation=Energy stored.

Table 1. Cutting parameters and corresponding levels [15]

Tools Type		Cemented Carbide inserts		
Workpiece materials		Mild Steel		
Cutting parameters	Symbols/ Units	Low (-1)	Medium (0)	High (+1)
cutting speed	n, rpm	200	400	600
Feed rate	f, mm/rev	0.05	0.1	0.15
Depth of cut	d, mm,	0.5	1.0	1.5

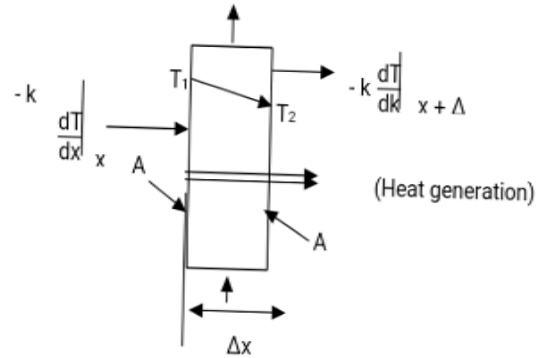


Figure 1. Control volume showing energy inflow and outflow by conduction through the carbide insert cutting tool.

From Figure 1, the basic description of the process is using the first law in control volume form (steady flow energy equation as given in Equation (2) below:

$$Qx = -K \left(\frac{dT}{dx} \right) x \tag{2}$$

Taking the limit as dx approaches zero, we have:

$$\frac{dQ(x)}{dx} = 0 \tag{3}$$

or

$$\frac{d}{dx} \left(KA \frac{dT}{dx} \right) = 0 \tag{4}$$

Equation (4) is the temperature field for quasi-one dimensional steady state heat transfer. Where K is constant, Equation (4) reduces to

$$\frac{d}{dx} \left(A \frac{dT}{dx} \right) = 0 \tag{5}$$

The term $\frac{dT}{dx}$ is called the gradient, which is the slope of the temperature curve with length x.

The temperature conditions for the cutting tool from Equation (4) where A is constant is:

$$\frac{d^2T}{dx^2} = 0 \tag{6}$$

When Equation (5) is integrated, it becomes:

$$\frac{dT}{dx} = 0 \tag{7}$$

and

$$T = cx + d \tag{8}$$

Equation (8) is the expression for the temperature field where c and d are constants of integration. For second order equation such as Equation (6), 2-boundary conditions are needed to determine c and d. One of such set of boundary conditions can be specification by the temperatures at both sides of the tool as:

$$T_0 = T_1 \text{ and } T_L = T_2$$

or

$$T = T_1 \text{ at } x = 0 \tag{9}$$

$$T = T_2 \text{ at } x = L \tag{10}$$

so $T_1=d$, $T_2=cL +d$. Therefore,

$$T = \frac{T_1 - T_2}{L} x + T_2 \tag{11}$$

When surface temperature is specified, $T \Big|_{x=0} = T_s$.

Therefore, the Fourier equation for steady conduction in a limiting case where Δx tends zero for the cutting tool is written in differential form. This includes the geometrical properties defining of the problem, the element connectivity (mesh the model), the element types to be used, the material properties of the elements, the physical constraints (boundary conditions) and the loadings. Figure 2 shows the basic model of the carbide single point cutting tool. The AutoCAD Inventor was used for the design and exported into ANSYS for the temperature analysis [15].

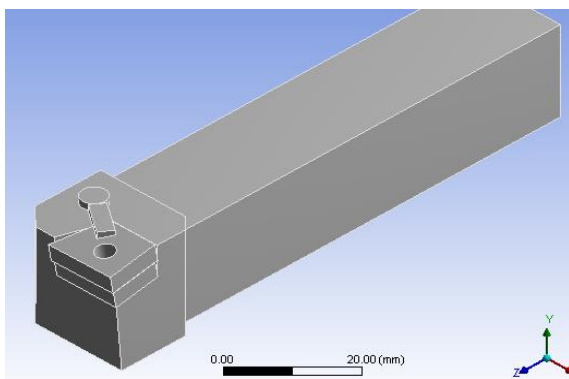


Figure 2. Carbide Insert Single Point Cutting Tool

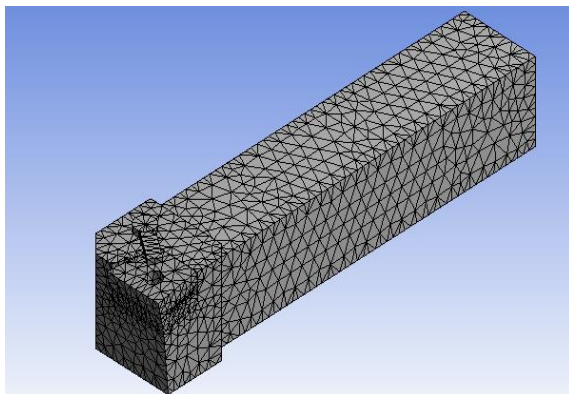


Figure 3. Meshing of Carbide Tool

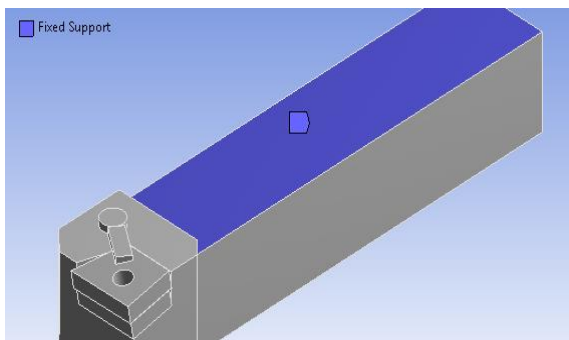


Figure 4. Fixed Support

Table 2. The coded and actual levels for the box-behnken experimental design

Process parameters	Symbols	Coded and Actual Levels		
		-1	0	+1
Spindle speed (rpm)	X ₁	200	400	600
Feed rate (mm/rev)	X ₂	0.05	0.10	0.15
Depth of cut (mm)	X ₃	0.5	1.0	1.5

After the geometry modelling using AutoCAD, the geometry was exported to ANSYS® tool. The surface mesh for the specimen is shown in Figure 3. The fine was selected as the center relevance at the detail mesh section. 46407 and 28437 were the numbers of nodes and elements, respectively. They were generated for the meshed cutting tool. Finally, the analysis of the settings was carried out, where the boundary conditions such as applied force, fixed support, pressure etc. are specified. The fixed support for the cutting tool is shown in Figure 4, the top and bottom part are movement restricted. To find the induced temperature on the cutting tool, the values of the spindle speed, feed rate and depth of cut as given in Table 2 were attributed to tool of ANSYS®.

Solution:

In this step, the features like numerical integration, equation solving and matrix manipulation are performed automatically by the tool of software. The governing algebraic equation in matrix form, computation of the unknown values of the primary field and assembling was automatically done. The details of the discretization of the solution domain carried out for the FEM analysis and thus used by the expert system for the generation of the results are 46407 and 28437 for the nodes and the elements, respectively. The analysis was performed with the same design matrix at varying spindle speed, feed rate and depth of cut for seventeen different runs. The cutting tool was modeled using inventor 2019 and simulated using the commercial FE-ANSYS 16.0 expert, a finite element based software. The effect of the cutting temperature on the cutting tool is characterized with their maximum value at the fixed end of the tool in the FEM distributions field of this study and was then adopted in prediction of the concerned response simply to validate the experimental results.

3. Results

3.1 Results Obtained from the Experiment

Table 2 shows the coded and the actual levels for the Box-Behnken experimental design, while Tables 3 and 4 shows the experimental and numerical results obtained for carbide insert tool. Table 5 shows the experimental, FEM predicted and absolute percentage error for carbide cutting temperature.

Table 3. Experimental data for carbide tool while machining mild steel

Experimental runs	Spindle speed (rpm)	Feed rate (mm/rev)	Depth of cut (mm)	Average cutting temperature °C
1	200	0.15	1.00	141.10
2	400	0.05	1.50	161.11
3	600	0.10	1.50	340.60
4	400	0.10	0.50	72.10
5	600	0.05	1.00	154.40
6	400	0.05	0.50	74.90
7	600	0.10	0.50	135.00
8	600	0.15	1.00	311.60
9	400	0.10	1.00	177.79
10	200	0.05	1.00	80.00
11	400	0.15	1.50	330.52
12	400	0.10	1.00	177.79
13	400	0.10	1.00	177.77
14	400	0.10	1.00	177.79
15	400	0.10	1.00	177.78
16	400	0.15	0.50	130.00
17	200	0.10	1.50	152.99

Table 4. FEM Predicted results for carbide cutting tool

Run No.	Spindle speed, n (rpm)	Feed rate, f (mm/rev)	Depth of cut, ap (mm)	FEM Predicted cutting temperature, T (°C)
1	200	0.15	1.0	142.22
2	400	0.05	1.5	162.73
3	600	0.10	1.5	342.33
4	200	0.10	0.5	72.658
5	600	0.05	1.0	155.02
6	400	0.05	0.5	75.576
7	600	0.10	0.5	135.44
8	600	0.15	1.0	312.41
9	400	0.10	1.0	178.57
10	200	0.05	1.0	80.351
11	400	0.15	1.5	330.00
12	400	0.10	1.0	178.57
13	400	0.10	1.0	178.57
14	400	0.10	1.0	178.57
15	400	0.10	1.0	178.57
16	400	0.15	0.5	131.33
17	200	0.10	1.5	153.97

Figure 5 and 6 shows the prediction of carbide cutting temperature using FEM while Figure 7 shows the reliability plots showing comparison between experimental and predicted carbide cutting temperature.

3.2 Discussion of Results

Table 2 was used by the selected design Expert 7.0 version to generate the randomized design matrix for the experimental and numerical study. The experimental matrix consists of three independent variables namely; spindle speed (rpm), feed rate (mm/rev) and depth of cut

(mm). The response for this study is the cutting temperature. The data in Table 3 above shows that as spindle speed of machining mild steel with carbide tool increased from 200rpm to 600rpm while other input parameters are kept constant, the tool's cutting temperature increased from 72.10°C to 340.60°C. This is because the spindle speed determines the movement of the cutting tool; therefore, its variation causes a rise in the tool's temperature. This was found to be in line with past researchers like Grzesik et al. and Ozel and Altan [4, 16] who stated that increased in cutting speed and feed rate brought about increased in cutting zone temperature when they machined AISI 1045 and AISI 304 with carbide insert tool. Figure 5 shows the prediction that was obtained for carbide cutting temperature at varying process parameters using the finite element expert system. From Figure 5, the result shows that the predicted carbide cutting temperature is 142.22°C when a spindle speed of 200rpm, feed rate of 0.15mm/rev and depth of cut of 1.0mm were applied. Figure 6 shows the prediction that was obtained for carbide cutting temperature at varying process parameters using the finite element expert system. From Figure 6 the result shows that the predicted carbide cutting temperature is 162.73°C when a spindle speed of 400rpm, feed rate of 0.05mm/rev and depth of cut of 1.5mm were applied. The same predictive approach was used for experiment numbers 7-17. Table 4 shows the result of the FEM predicted values for carbide cutting tool while machining mild steel. From the result obtained, it can be deduced that as the spindle speed increased from 200rpm to 600rpm, there was an increased in the tool's cutting temperature from 142.22 °C to 342.33 °C.

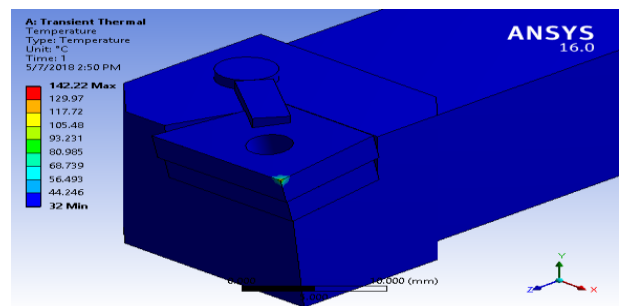


Figure 5. Prediction of carbide cutting temperature Using FEM

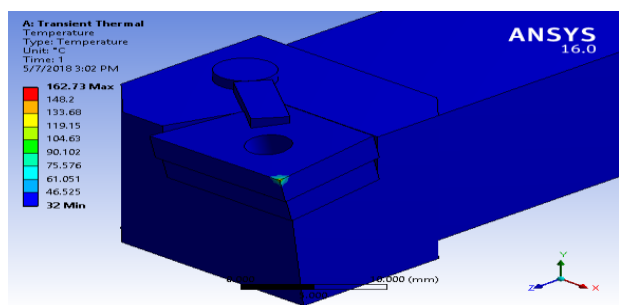


Figure 6. Prediction of carbide cutting temperature using FEM

Table 5. The experimental, FEM predicted and absolute percentag error for carbide cutting temperature

Run No.	Cutting temperatures (°C) Experimental (E)	Cutting temperatures (°C) FEM Predicted (P)	Absolute percentage error (%)
1	141.10	142.22	0.02381
2	161.11	162.73	0.01006
3	340.60	342.33	0.50793
4	72.10	72.658	0.76283
5	154.40	155.02	0.40155
6	74.90	75.576	0.89453
7	135.00	135.44	0.32593
8	311.60	312.41	0.25995
9	177.79	178.57	0.43872
10	80.00	80.351	0.43750
11	330.52	330.00	0.15733
12	177.79	178.57	0.43872
13	177.77	178.57	0.43876
14	177.79	178.57	0.43872
15	177.78	178.57	0.44437
16	130.00	131.33	0.01023
17	152.99	153.97	0.69980

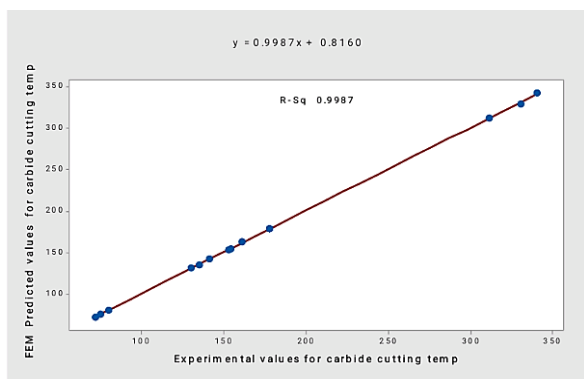


Figure 7. Reliability plots showing comparison between experimental and predicted carbide cutting temperature

It was also observed, that the increase in depth of cut from 0.5 mm to 1.5 mm generated a corresponding increase in the tool's cutting temperature from 72.658°C to 330.99°C. The same applied to the feed rate as it is increased from 0.5mm/rev to 0.1mm/rev, the tool's tip response also increased from 162.73°C to 342.33°C. Hence, it is suggested that the cutting parameters (n, f and ap) should be controlled in such a way as to have the optimum cutting temperature, as this will guarantee minimum tool wear and prolonged tool life for a better machining economy. This is also in line with the work of Elbestawi et al. [17]. The predicted result of Table 5 when compared with the experimental result shows a mean absolute error of 0.3936%. This value is small and below the maximum error of 10% recommended by Lazoglu and Altintas [2]; Olodu [18], respectively. Hence, the value is satisfactory and show good predictability of the model and its adequacy to predict the carbide cutting temperature.

The carbide prediction inserted cutting tool cutting temperature when machining mild steel using dry orthogonal cutting process was executed by using the finite element method and experiment. This is to know-how accurate the FEM can predict the temperature on the tool. Finally, a comparison between the FEM and experiment was performed as presented in Table 5. It can be seen that both experimental and FEM (ANSYS®) reading were in close agreements, with the minimum and the maximum errors as 0.010 and 0.895, respectively in this table. From the FEM closeness pattern of the experiment (in Figure 7), it shows clearly that ANSYS® is a very useful predicting tool, that can be used for a cutting tool temperature simulation analysis.

4. Conclusion

In this study, an approach using FEM for predicting carbide insert cutting temperature has been successfully and effectively demonstrated. Based on the results and discussions presented in the preceding sections, the following conclusions have been drawn;

- All the three selected process parameters (spindle speed, feed rate and depth of cut) have significant effects on the tools' cutting temperature. However, the spindle speed has the most significant influence, followed by the depth of cut and then the feed rate. So, when a lower cutting temperature is desired for longer tool performance, the values of the process parameters should be set at considerably low levels.
- The experimental test shows that the chip formations are continuous type at lower process parameters.
- The FEA results show that the maximum cutting temperature is at the top of the cutting tool, which is the cause of tool failure.

Therefore, from the obtained results, it has been shown that the FEM predictions of the tool's temperature can improve the cutting tool service life as well as the machined components integrity. Therefore, the metal cutting industries should endeavor to use FEM simulated means like the ANSYS®, to predict their tool's cutting temperature for a specified cutting process, in order to prolong the service life of the cutting tools and to avoid exceedance of their yield points; a cause which leads to tool failure and wear when machining mild steel with carbide inserts cutting tools.

Declaration

The authors declared no potential conflicts of interest with respect to the research, authorship, and/or publication of this article. The authors also declared that this article is original, was prepared in accordance with international publication and research ethics, and ethical committee permission or any special permission is not required.

Author Contributions

M. Ozakpolor developed the methodology and performed the analysis. C. Aliyegbenoma assisted in data collection, and D.D. Olodu improved the study.

References

- Dautzenberg, J.H., Jasper, S.P.F.C and Taminiou, D. A., *The Work Piece Material in Machining*. International Journal of Advanced Manufacturing Technology, 1999. **15** (6): p. 383-386.
- Lazoglu, L. and Altintas, Y., *Prediction of Tool Chip Temperature in Continuous and Interrupted Machining*. International Journal of Machine Tools and Manufacture, 2002. **42**: p. 1011-1022.
- Ostafiev, V., Kharkevich A., Weinert, K. and Ostafiev S., *Tool Heat Transfer in Orthogonal Metal Cutting*. Journal of Manufacturing Science and Engineering, 1999. **121**: p. 541-549.
- Grzesik, W., *Experimental Investigation of the Cutting Temperature when Turning with Coated Indexable Inserts*. International Journal of Machine Tools and Manufacture, 1999. **39**: p. 355-369.
- Dewes, R.C., Chua, K.S and Newton P.G., *Temperature Measurement when High Speed Machining Hardened Mould/Die Steel*. Journal of Materials Processing Technology, 1999. **92-93**: p. 293-301.
- Chaudhary, S. K. and Bartarya, G., *Role of Temperature and Surface Finish in Predicting Tool Wear using Neural Network and Design of Experiment*. International Journal of Machine Tools and Manufacture, 2003. **43**: p. 747-753.
- Miller, M.R., Mulholland, G. and Anderson, C., *Experimental Cutting Tool Temperature Distributions*. Journal of Manufacturing Science and Engineering, 2003. **125**: p. 667-673.
- Abhang, L.B. and Hameedullah, M., *Chip-Tool Interface Temperatures Prediction Model for Turning Process*. International Engineering Science and Technology, 2010. **2**: p. 382-393.
- Ranc, N., Pina, V., Sutter, G. And Philippon, S., *Temperature Measurement by Visible Pyrometry: Orthogonal Cutting Application*. Journal of Heat Transfer, 2004. **126**: p. 931-936.
- Nasr, M. N. A, Balbaa, M. and Elgamal, H., *Modeling Machining-Induced Residual Stresses after Laser-Assisted Turning of Steels*. Advanced Materials Research, 2014. **96**: p. 622- 627.
- Aberg, E. and Green, R.E. Machinery's Handbook 25th Edition Industrial Press Inc. New York, 1996.
- Thomas, M., Beauchamp, Y., Youssef, Y.A., Masounave, J., (1997). *An Experimental Design for Surface Roughness and Built-up Edge Formation in Lathe Dry Turning*. International Journal of Quality Science, 1997. **2**(3), p. 167-180.
- Harinath G., et al., *Experimental Investigations and effects of Cutting Variables on MRR and Tool Wear for AISI 52 Tool Steel*. Proceedings of Materials Science, 2014. **5**: p. 1398-140.
- Etin-osa, C. E. and Achebo, J. I., *Analysis of Optimum Butt Welded Joint for Mild Steel Components Using FEM (ANSYS)*. American Journal of Naval Architecture and Marine Engineering, 2017. **2**(3): p. 61-70.
- Ozakpolor, M., Achebo, J.I., and Ogbeide, S.E., *Expert Modelling And Prediction of Von Mises Stresses In Carbide Insert Cutting Tool Using Fem (Ansys)"* Global Scientific Journals, 2019. **7**(1): p. 397-402.
- Ozel, T. and Altan, T., *Determination of Work Piece Flow Stress and Friction at the Chip-Tools Contact for High-Speed Cutting*. International Journal of Machine Tools and Manufacture, 2000. **40**(1): p. 133-152.
- Elbestawi, M. A., El-Wardeny, T.L. and Mohammed, E., *Cutting Temperature of Ceramic Tools in High Speed Machining of Difficult to Cut Raw Materials*. International Journal of Machine Tools and Manufacture, 1996. **36**(5): 611-634.
- Olodu, D. D., *Optimization and Analysis of Cutting Tool Geometrical Parameters using Taguchi Method*. Journal of Applied Science Environmental Management, 2018. **22**(3): p. 346-349.



Research Article

Determination of mechanical performance of glass fiber reinforced and elastomer filled polyamide 6 composites

Hüseyin ÜNAL^a  and Kemal ERMIŞ^{b,*} 

^a Sakarya University of Applied Science, Faculty of Technology, Dept. of Metallurgical and Materials Engineering, Sakarya, 54187, Turkey

^b Sakarya University of Applied Science, Faculty of Technology, Dept. of Mechanical Engineering, Sakarya, 54187, Turkey

ARTICLE INFO

Article history:

Received 08 May 2021

Revised 07 August 2021

Accepted 10 September 2021

Keywords:

Glass fiber
Mechanical properties
Polyamide
Rubber
SEBS

ABSTRACT

In this study, the mechanical performances of neat Polyamide 6 (PA6) polymer, 20wt.% glass fiber reinforced PA6, and 8% SEBS elastomer with 20% glass fiber reinforced PA6 composite were investigated. Composite materials were first produced in the form of granules by using a twin-screw extruder. Later, mechanical test samples were molded, in accordance with the American Society of Testing Materials (ASTM) standards, using an injection molding technique. Mechanical parameters such as tensile strength, tensile modulus, elongation at break, impact strength, flexural strength, and flexural modulus were determined by tensile, impact, and bending tests. With the addition of 20wt.% glass fiber reinforcement to the PA6 polymer matrix, properties such as tensile strength, tensile modulus, flexural strength, and flexural modulus increased, while properties such as elongation at break and impact strength decreased. For the 20% glass fiber reinforced PA6 composite with 8% SEBS rubber additive, while the impact strength increased by 177%, other mechanical values decreased. The fractured surface microstructure images of the samples obtained from the tensile tests were examined using a scanning electron microscope.

1. Introduction

Polymer materials have become one of the indispensable materials of our daily life and continue to replace traditional materials such as metallic materials, ceramics, and glass. Polymers have advantages such as lightness, chemical resistance, transparency, easy processability, ease of construction, colorability, and corrosion resistance, as well as disadvantages such as low strength, low-temperature resistance, scratch ability, and low resistance to UV rays. In order to reduce the disadvantages of polymers, many different additives can be used. These can be strength-enhancing additives such as glass fiber, carbon fiber, aramid fiber, and natural fibers, as well as mineral fiber-based additives such as glass beads, kaolin, talc, wollastonite, glass sphere, barium sulfate, and mica. In addition, some elastomer-based materials can be added to increase the impact toughness of polymer materials. Engineering polymers are preferred especially in industrial applications where strength,

temperature, and rigidity resistance are required. Polyamide polymers are also among the most widely used plastics in the engineering plastics group. Among the most widely used polyamide varieties in the industry are PA6, PA66, PA46, and cestamide polymers. Polyamide (PA) polymers are widely used in industrial applications due to their advantageous properties such as low friction coefficient, good wear resistance, high strength, ease of processing, and high melting temperature, however, they have a high cost and show fragility in multi-axial load situations [1]. Polyamide 6 and PA66 polymers are better than all other polyamide types with regards to properties such as hardness, high strength, and heat resistance. While the density of PA6 varies between 1.12-1.14 g/cm³, the melting point is approximately 225 °C and the glass transition temperature is between 50-54 °C [2].

In order to combine the properties of various polymer materials in a single material, polymers that are compatible

* Corresponding author. Tel.: +90-264-616-0288; Fax: +90-264-616-0014.
E-mail addresses unal@subu.edu.tr (H. Ünal), ermis@subu.edu.tr (K. Ermiş)
ORCID: 0000-0003-0521-6647 (H. Ünal), 0000-0003-3110-2731 (K. Ermiş)
DOI: 10.35860/iarej.934740

© 2021, The Author(s). This article is licensed under the CC BY-NC 4.0 International License (<https://creativecommons.org/licenses/by-nc/4.0/>).

with each other are mixed and polymer mixtures are obtained. Polymer mixes are extensively utilized in a variety of sectors for the creation of novel materials that combine the unique characteristics of each component and may be achieved by a simple physical blending process. Due to its cheap production cost, this material class is an economically viable choice for a range of applications [3, 4]. The impact resistance of plastics is vital in many industrial applications [5]. PA's impact strength must be increased before it can be utilized in some engineering or packaging applications. Reinforcing PA using glass fiber [6-9] and other polymers such as elastomers [1, 10] and thermoplastics has been attempted to enhance its impact strength. As a reactive compatibilizer, styrene-ethylene-butadiene-styrene (SEBS) rubber [11–15] has been utilized in PA6 blends. Compatible mixes had greater hardness values and a higher degree of crystallinity [16].

Oshinski et al. [14, 17] examined the mechanical characteristics of PA6 and PA66 polymers using varied ratios of SEBS and SEBS-g-MA compatibilizers. As a result of their research, they discovered that adding SEBS and SEBS-g-MA rubbers to PA6 polymer enhanced the izod impact strength and percent elongation at break values of the polymer combination while decreasing the elasticity modulus and yield strength values. The inclusion of 20% SEBS-g-MA elastomer resulted in the maximum impact strength. This was explained as a result of the SEBS-g-MA's low molecular weight and ability to bind effectively with the PA6 and PA66 major matrix polymers. The soft rubber phase reduced the elastic modulus and yield strength values of the polymer combination, but enhanced the percent elongation and impact strength values. Xianwei et al. [18] examined the mechanical characteristics of PA6/ABS/g-SEBS polymer blends for application in the automotive and electronics sectors, including tensile and yield strength, modulus of elasticity, notched impact strength, and percent elongation at break. In their study, they investigated the effect of a g-SEBS compatibilizer on a PA6/ABS polymer mixture. As a result of their studies, they observed that the yield strength values of the g-SEBS compatibilizer added PA6/ABS polymer mixture decreased, while the izod impact strength and % elongation at break values increased significantly. They attributed this to the high toughening properties of the g-SEBS-based elastomer phase and its ability to adhere well to the polymer blend. Carvalho et al. [19] investigated the mechanical and thermal properties of a PA6 polymer and SEBS rubber mixture using a SEBS-g-MA coupling agent. They set the ratio of the PA6/SEBS mixture (50:50) and added the SEBS-g-MA compatibility agent at rates of 5, 7.5 and 15 phr to the mixture. As a result of their studies, they observed that the tensile strength, hardness and melting temperature values and % elongation values of the mixture increased with the addition of SEBS-g-MA.

Glass fiber is typically made by mechanically pulling molten glass through a tiny aperture and is composed largely of silicon dioxide and metallic oxide modifying components. Because of their inexpensive cost and good corrosion resistance, they are frequently utilized.

This experimental study was carried out for applications that require consideration of the impact and toughness properties, as well as the strength properties, of 20% short glass fiber reinforced polyamide polymer composites [19-24], which is widely used in sectors such as automobile, electrical, electronics, textiles in the industry.

In this study, the mechanical performances of neat PA6 polymer, 20% glass fiber reinforced PA6, and 8% SEBS elastomer with 20% glass fiber reinforced PA6 composite were investigated. Mechanical tests such as tensile, impact and bending tests were carried out and properties such as tensile strength, elasticity modulus in tensile, elongation at break, impact strength, bending strength, and elastic modulus in bending were determined. The broken surface microstructure images of the samples obtained from the tensile test were examined using scanning electron microscopy.

2. Experimental Study

2.1 Materials

Polyamide 6 polymer, which is the main matrix material used in the experiments, was obtained from DomoPolimer with the trade code Domamid. The glass fiber used as the strength enhancer, was a PA2 coded obtained in compliance with polyamide from the Cam Elyaf Sanayi company. The average diameter of the glass fiber was 11 μm and its length was 4.5 mm. Styrene-ethylene-butylene-styrene rubber triblock copolymer grafted with 1.84% maleic anhydride acid coded Kraton FG 1901 from Kraton Polymers Company was used as the thermoplastic elastomer to act as the toughening material.

2.1 Composite preparation

The PA6-CE-SEBS composite was produced in granule form in a model MC75 Japanese-made industrial twin-screw compound machine. Extruder barrel heater temperatures were adjusted between 210-250 $^{\circ}\text{C}$. The produced PA6-GFR-SEBS composite granules were first kept at room temperature for 24 hours and then dried in a tray at 80 $^{\circ}\text{C}$ for 4 hours. Then, the test specimens were molded using the injection molding technique. Injection barrel heater temperatures were adjusted between 220-245 $^{\circ}\text{C}$. Mechanical test specimens were printed in an injection mold manufactured in accordance with standards. The injection pressure was set to 180 bar.

Tensile test specimens were prepared according to ASTM D638 standard, impact test specimens according to ASTM D256, and flexure test specimens according to

ASTM D790 standard. Tensile and flexure experiments were carried out in Zwick Z020 tensile tester at a tensile speed of 10 mm/min. Impact tests were also carried out with the Zwick brand Izod impact device. The experiments were carried out in a conditioned laboratory environment at room temperature and 50% humidity. Each test sample was repeated at least 3 times and the mean values were used in the graphs.

The working plan for the production of PA6-GFR-SEBS composite is given schematically in Figure 1.

The compositions of the produced PA6-GFR-SEBS polymer composite and the injection and extrusion process conditions are given in Table 1. The image of the tensile, impact and bending test specimens produced by injection according to the standards, used in the experiments is given in Figure 2.

3. Results and Discussion

Figure 3 shows the change of tensile strength of injection molded neat PA6 polymer, 20% glass fiber reinforced PA6, and 8% SEBS elastomer added with 20% glass fiber PA6 composites.

As shown in Figure 3, the tensile strength of the neat PA6 polymer was determined to be 74.36 MPa, while the tensile strength of the 20% glass fiber reinforced PA6 composite was 133.28 MPa and the tensile strength of 8%SEBS elastomer and 20% glass fiber added to the PA6 composite was 119.11 MPa. When 20% glass fiber was added to the PA6 polymer, its tensile strength increased by 79.2% compared to the neat PA6 polymer.

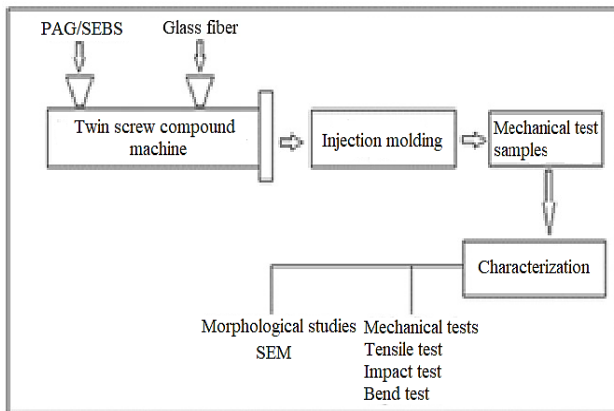


Figure 1. Schematic representation of the working plan for PA6-GFR-SEBS composite production

Table 1. Compositions and process conditions of PA6-GFR-SEBS polymer composite

No	PA6 (by weight)	Glass fiber (by weight)	SEBS elastomer (by weight)	Process conditions
1	100	-	-	Twin-screw extruder heater temperature range: 210-250 °C
2	80	20	-	Injection heater temperature range: 220-245 °C
3	72	20	8	

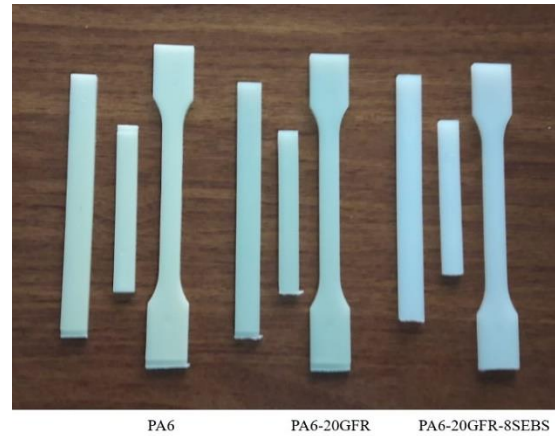


Figure 2. Image of tensile, impact and bending test samples produced by injection molding method

Its tensile strength increased by 60.1% compared to the neat PA6 polymer. However, with the addition of SEBS elastomer, a decrease of 14.17% was observed in tensile strength compared to 20% glass fiber PA6 composite.

The change in the elongation values at break of the neat PA6 and the PA6 composites, the 20% glass fiber reinforced PA6 and the 8%SEBS elastomer and 20% glass fiber reinforced PA6, are given in Figure 4.

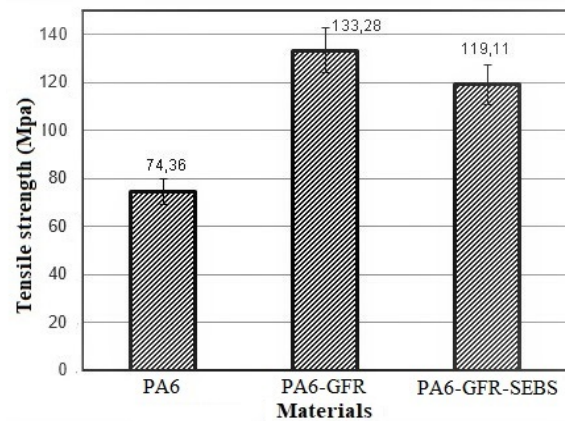


Figure 3. Tensile strength of PA6 polymer, 20% glass fiber PA6, 20% glass fiber reinforced PA6 with 8% SEBS elastomer composites

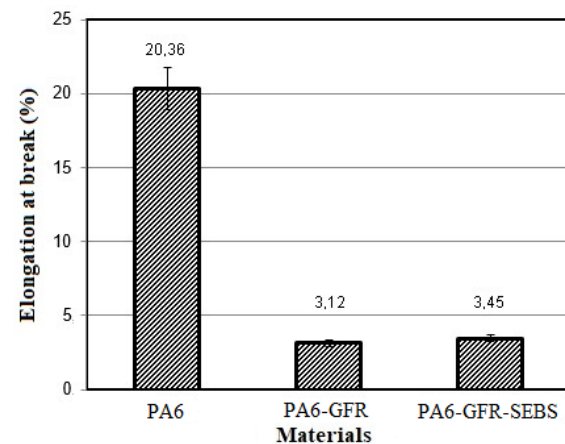


Figure 4. The change in the % elongation values at break of the PA6 polymer and the PA6-20%GFR and PA6-20%GFR-8%SEBS composites

As it is clearly seen in Figure 4, the % elongation value of the neat PA6 polymer at break was determined as 20.36%. When the main matrix material was reinforced with 20% glass fiber by weight, the elongation value at break of the PA6 composite was 3.12%, and similarly, the elongation value at break was 3.45% for the 8% SEBS elastomer and 20% glass fiber added PA6. For the 20% glass fiber reinforced PA6 composite, the elongation value at break was 84.6% lower compared to the neat PA6 polymer. It was also determined that when the PA6 main matrix material was reinforced with 8% SEBS elastomer and 20% glass fiber, the elongation value of the composite at break was 83% lower compared to the neat PA6 polymer.

Figure 5 shows the variation of the modulus of elasticity in the tensile strength tests for the polyamide 6 polymer and the PA6-20%GFR and PA6-20%GFR-8%SEBS composites according to the materials produced. As indicated in the figure, the elastic modulus obtained in the tensile test for the non-additive polyamide 6 polymer main matrix was determined as 2792 MPa. When 20% glass fiber was added to the PA6 polymer, the elastic modulus of the composite was determined to be 7237 MPa and the elastic modulus of the 8% SEBS elastomer and 20% glass fiber added polyamide 6 composite was determined to be 5492 MPa. With 20% glass fiber reinforcement to the polymer main matrix, the elastic modulus of the composite was observed to increase by 159% compared to the neat polyamide 6 polymer.

Similarly, when the polyamide 6 polymer was reinforced with 8% SEBS elastomer and 20% glass fiber, the elastic modulus of the composite was observed to increase by 96.7% compared to the neat PA6 polymer. However, with the addition of 8% SEBS rubber, the elastic modulus value of PA6-20%GFR-8%SEBS composite decreased by 24% compared to the 20% glass fiber PA6 composite. The reason for the increase in the elastic modulus of the composite is because the glass fibers were used as a strength enhancer. Glass fibers added to the polymer generally play a role in increasing the rigidity, mechanical properties, and hardness of the polymer. Styrene-ethylene-butylene-styrene elastomer is in the rubber phase and is added to thermoplastic polymers to increase the toughness of the hard polymers. SEBS elastomer was added to the composite to reduce hard, brittle, and rigid structure of the PA6 polymer composite with 20% glass fiber, and to reduce its brittleness by increasing its toughness in the area of use. SEBS disperses homogeneously in the polymer matrix, absorbing any impact to the material, increasing impact toughness and elongation at break (see Figures 6 and 4, respectively), but also causes a decrease in tensile strength values and stiffness (see Figures 3 and 5). SEBS-g-MA compatibilization agent has a low modulus of elasticity

and causes a decrease in the stiffness of the composite material. Similar results were observed in previous studies in the literature [11, 14, 16-19].

The variation of the Izod impact strength values of PA6 polymer and the PA6-20%GFR and the PA6-20%GFR-8%SEBS composites is given in Figure 6. As seen in the figure, the izod impact strength of the neat PA6 polymer was determined to be 17 kJ/m² on average.

With 20% GFR reinforcement to the polyamide 6 matrix, the Izod impact strength of the PA6-20GFR composite was determined to be 10.6 kJ/m². In addition, with 8% SEBS rubber and 20% glass fiber reinforcement by weight, the Izod impact strength of PA6-20%GFR-8%SEBS composite was determined as 29.4 kJ/m². With 20% glass fiber reinforcement to the PA6 polymer main matrix, the impact strength of the PA6-20%GFR composite was reduced by approximately 37.6% compared to the neat PA6 polymer. Likewise, when 20% glass fiber and SEBS rubber reinforcement were made to the PA6 matrix, the impact strength of PA6-20%GFR-8%SEBS composite increased by approximately 73% and 177%, respectively, compared to the impact strength values of the PA6 polymer and the PA6-%GFR composite.

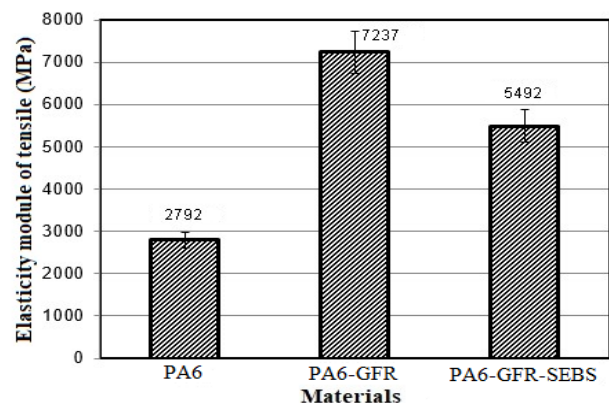


Figure 5. The change of elastic modulus of tensile strength of PA6 polymer and PA6-20%GFR and PA6-20%GFR-8%SEBS composites.

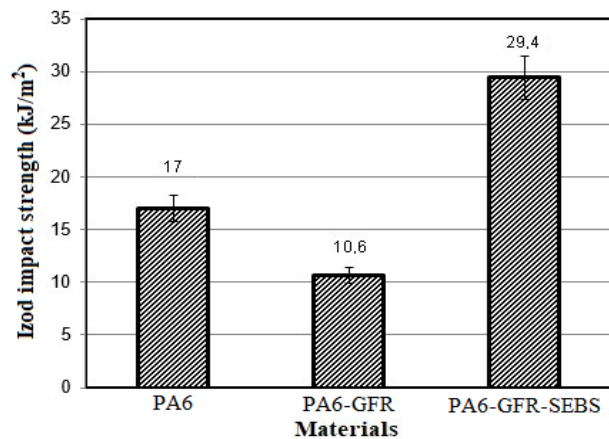


Figure 6. The variation of Izod impact strengths of neat PA6 polymer and PA6-20%GFR and PA6-20%GFR-8%SEBS composites.

Impact strength decreased with the addition of glass fiber but increased with the addition of the SEBS rubber. By adding SEBS rubber to the 20% glass fiber reinforced PA6 polymer composite, the composite became tough. Rubber phase SEBS provided the hardening factor. The results obtained are in accordance with previous studies in the literature [11, 14-18, 25, 26].

Figure 7 shows the change of flexural strength values of the PA6 polymer and the PA6-20%GFR and PA6-20%GFR-8%SEBS composites used in the experiments.

As it is clearly observed in the figure, the flexural strength of the PA6 polymer was determined as 76.62 MPa, while the flexural strength of the PA6-20%GFR composite was 137.2 MPa and the flexural strength of the PA6-20%GFR-8%SEBS composite was determined as 108.11 MPa. With 20% glass fiber reinforcement to the polymer main matrix, the flexural strength of the PA6-20%GFR composite by 79% compared to the bending strength of the neat PA6 polymer. Similarly, when 20% glass fiber and SEBS rubber reinforcement was made to the polymer main matrix, the flexural strength of the PA6-20%GFR-8%SEBS composite was found to increase by 41% compared to the neat PA6 polymer. However, with the addition of 8%SEBS rubber, the flexural strength of the PA6-20%GFR-8%SEBS composite was reduced by 37.9% compared to the flexural strength of the PA6-20%GFR composite.

The variation of the modulus of elasticity of the neat PA6 polymer, PA6-20%GFR, and PA6-20%GFR-8%SEBS composites in bending is given in Figure 8.

As it is clearly seen in the figure, the elastic modulus of the polyamide 6 main matrix in bending was determined as 1483 MPa, the elastic modulus of the composite with 20% glass fiber reinforcement in the polyamide main matrix was 3820 MPa and the elastic modulus of the 8% SEBS elastomer and 20% glass fiber reinforced PA6 composite in bending was determined as 2623.7 MPa. With 20% glass fiber reinforcement to the main matrix, the elastic modulus of the PA6-20%GFR composite in bending increased by 107.2% compared to the neat PA6 polymer. Similarly, when 20% glass fiber and SEBS rubber reinforcement was made to the polymer main matrix, the elastic modulus of the PA6-20%GFR-8%SEBS composite in bending increased by 42.3% compared to the neat PA6 polymer. However, with the addition of 8% SEBS rubber, the elastic modulus of the PA6-20%GFR-8%SEBS composite in bending decreased by 45.5% compared to the elastic modulus of PA6-20%GFR composite. The reason for the composite's elastic modulus increasing in bending is the same as the reason for the composite's elastic modulus increasing in tension. In other words, glass fibers added to the polymer increase the bending strength, rigidity, and hardness of the composite.

The addition of SEBS rubber also causes toughening of the polymer composite (see Figures 7 and 8, respectively).

The fracture surface scanning electron microscope images obtained after the tensile test of the neat PA6 polymer, and the PA6-20%GFR, and PA6-20%GFR-8%SEBS (10 μm view and 100 μm view) composites are given in Figure 9 (a, b, c, d).

It can be seen from the fractured surface microstructure images of the non-additive polyamide 6 polymer that the main matrix has elasticity and the elongated and white parts on the fracture surface are plastic deformation (See Figure 9 (a).) In Figure 9 (b), the fracture surface image of the PA6-20%GFR composite is given. It was determined that the short glass fibers are homogeneously distributed within the main matrix and the fracture surface is smooth and brittle. In Figure 9 (c), the fracture surface image of the PA6-20%GFR-8%SEBS composite is given and the microstructure images show that the glass fibers are generally homogeneously distributed in the matrix material. At the same time, the elongation of the main matrix after the applied force, despite the 20% glass fiber reinforcement, shows that the SEBS rubber in its composition makes the composite elastic.

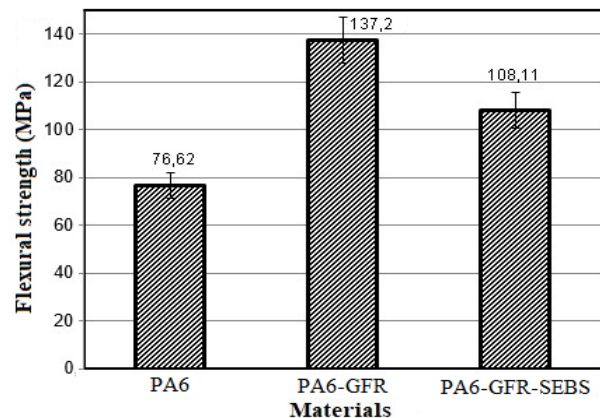


Figure 7. The variation of Izod impact strengths of the neat PA6 polymer and PA6-20%GFR and PA6-20%GFR-8%SEBS composites

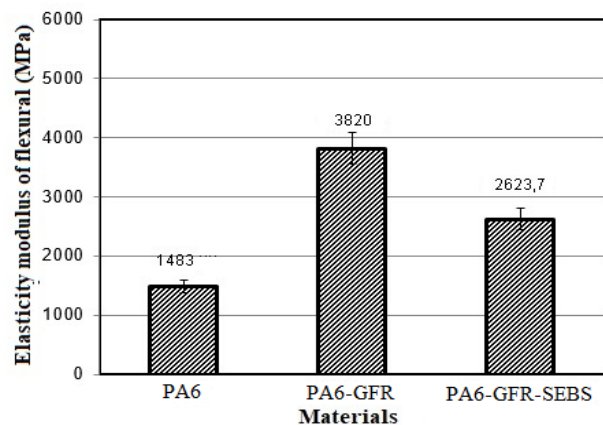
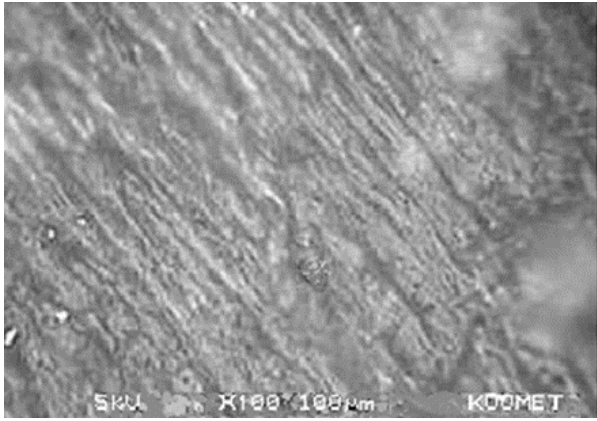
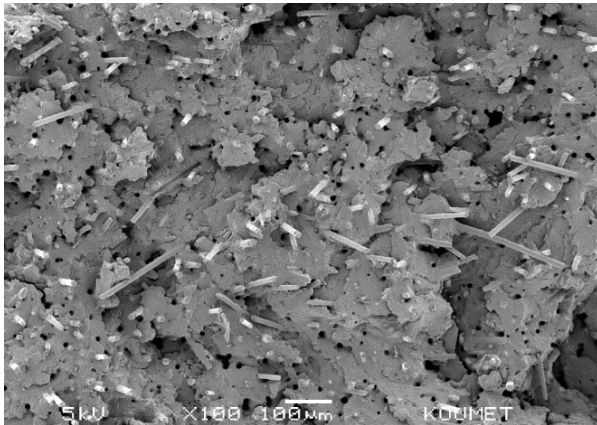


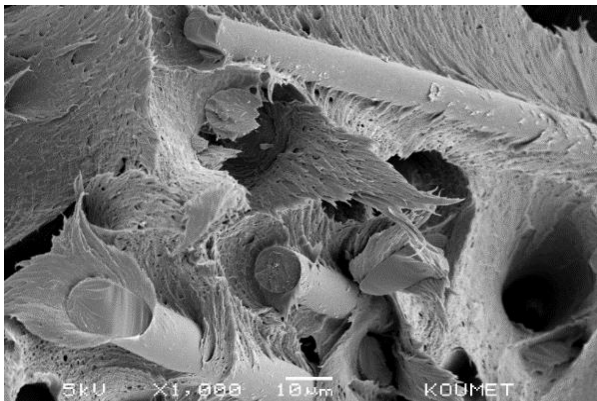
Figure 8. The variation of the modulus of elasticity in bending of the neat PA6 polymer and the PA6-20%GFR and PA6-20%GFR-8%SEBS composites



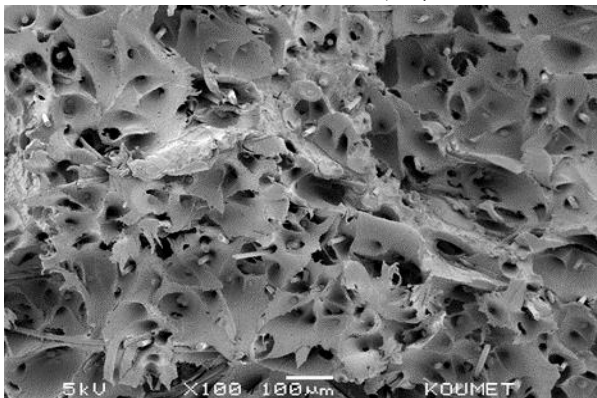
a) PA6



b) PA6-%20GFR



c) PA6-%20GFR-%8SEBS (10 µm view)



d) PA6-%20GFR-%8SEBS (100 µm view)

Figure 9. PA6, PA6-20% GFR, and PA6-20%GFR-8% SEBS SEM images

Meanwhile, it is observed that short glass fibers, which act as strength enhancers, are well bonded to the main matrix body and the fiber/matrix interface bond is good (See 9 (c and d)).

4. Conclusions

As a result of the experimental study, the following mechanical and microstructural test results were obtained.

- With the short glass fiber reinforcement added to the PA6 polymer main matrix, the tensile strength, elasticity modulus in tensile strength, flexural strength, and elastic modulus in bending of the composite material increased. It was determined that the 20% glass fiber reinforcement composite added to the main matrix increased the tensile strength, elasticity modulus in tensile, flexural strength, elastic modulus in bending by approximately 79.2%, 159%, 79%, and 107.2%, respectively.
- With the short glass fiber reinforcement added to the PA6 polymer main matrix, the % elongation at break and decrease in Izod impact strength values of the composite material were detected. Again, it was determined that 20% glass fiber reinforcement added to the polymer matrix reduced the elongation and Izod impact strength values of the composite by approximately 84.6% and 37.6%, respectively.
- The 8% SEBS rubber added to the PA6-20%GFR composite caused a significant increase in the Izod impact strength of the composite material. Compared to the PA6-20%GFR composite, the impact strength of the PA6-20%GFR-8%SEBS composite was greater by approximately 177%.
- The 8% SEBS rubber added to the PA6-20%GFR composite caused a decrease in the tensile strength, elasticity modulus in tensile, bending strength, and elasticity modulus in bending of the composite material. It was determined that the addition of 8% SEBS elastomer added to the main matrix decreased the tensile strength, elasticity modulus in tensile strength, flexural strength, and elastic modulus in bending by 14.17%, 24%, 37.9%, and 45.5%, respectively.
- In industrial applications where toughness, as well as strength, is required, it may be recommended to consider the values obtained from the PA6-20%GFR-8%SEBS composite.

Declaration

The authors declared no potential conflicts of interest with respect to the research, authorship, and/or publication of this article. The authors also declared that this article is original, was prepared in accordance with the international publication, and any special permission is not required.

Author Contributions

H. Ünal developed the methodology and experimental study. K. Ermiş supervised and prepare the manuscript.

Nomenclature

ASTM : American Society of Testing Materials
 GFR : Glass fiber
 PA6 : Polyamide
 SEBS : Styrene-ethylene-butadiene-styrene
 SEM : Scanning electron microscope
 P : Power

References

- Bai, S.L., G.T. Wang, J.M. Hiver, and C. G'Sell *Microstructures and mechanical properties of polypropylene/polyamide 6/polyethylene-octene elastomer blends*, Polymer, 2004. **45**: p. 3063–3071.
- Kaştan, A., Y. Yalçın, H. Ünal, and Ş. Talaş, *PA6/YYPE /Nanokil Kompozitlerin Mekanik Özelliklerinin İncelenmesi*, AKÜ FEMÜBİD, 2015. **15**: p. 9–20 (in Turkish).
- Folkes, M.J., and P.S. Hope, *Polymer Blends and Alloys*. Polymer Blends and Alloys. 1993, Netherlands: Springer.
- Utracki, L.A., and C.A. Wilkie, *Polymer Blends Handbook*. 2014, Netherlands: Springer.
- Brydson, T.J.A. *Brydson's Plastics Materials*. 2017, Eighth Edi. Gilbert M, editor. Cambridge: Elsevier Ltd.
- Doğan N.F. and A. Erklığ, *On the effect of nano particle inclusion in fiber reinforced composite tensile and flexural behavior*, International Advanced Researches and Engineering Journal, 2018. **2**(3): p. 240-244.
- Aras S. and N. Tarakçioğlu, *Experimental investigation of the effect of compression pressure on mechanical properties in glass fiber reinforced organic material-based brake pads production*, International Advanced Researches and Engineering Journal, 2019. **3**(2): p. 11-115.
- Li H., Y. Wang, C. Zhang, and B. Zhang, *Effects of thermal histories on interfacial properties of carbon fiber/polyamide 6 composites: Thickness, modulus, adhesion and shear strength*, Composites Part A: Applied Science and Manufacturing, 2016. **85**: p. 31–39.
- Luo H., G. Xiong, C. Ma, D. Li, and Y. Wan, *Preparation and performance of long carbon fiber reinforced polyamide 6 composites injection-molded from core/shell structured pellets*, Materials and Design, 2014. **64**: p. 294–300.
- Matei E., M. Rapa, A. A. Andras, A. M. Predescu, C. Pantilimon, A. Pica, and C. Predescu, *Recycled Polypropylene Improved with Thermoplastic Elastomers*, International Journal of Polymer Science, 2017. **2017**: 7525923, p. 1-10.
- Ishigami A., S. Nishitsuji, T. Kurose, and H. Ito, *Evaluation of toughness and failure mode of PA6/mSEBS/PS ternary blends with an oil-extended viscoelastic controlled interface*, Polymer, 2019. **177**: p. 57–64.
- Lee C. H., Y. M. Lee, H. K. Choi, S. Horiuchi, and T. Kitano, *Effect of a functional triblock elastomer on morphology in polyamide 6/polycarbonate blend*, Polymer, 1999. **40**: p. 6321–6377.
- Jeon I., M. Lee, S. W. Lee, and J. Y. Jho, *Morphology and Mechanical Properties of Polyketone/Polycarbonate Blends Compatibilized with SEBS and Polyamide*, Macromolecular Research, 2019. **27**: p. 827–832.
- Oshinski A.J., H. Keskkula, and D. R. Paul, *Rubber toughening of polyamides with functionalized block copolymers: 1. Nylon-6*, Polymer, 1992. **33**(2): p. 268–283.
- Mengual A., D. Juárez, R. Balart, and S. Ferrándiz, *PE-g-MA, PP-g-MA and SEBS-g-MA compatibilizers used in material blends*, Procedia Manufacturing, 2017. **13**: p. 321–326.
- De Carvalho A. P. A., and A. S. da Sirqueira, *Effect of compatibilization in situ on PA/SEBS blends*, 2016. **26**: p. 123–128.
- Oshinski A.J., H. Keskkula, and D. R. Paul, *Rubber toughening of polyamides with functionalized block copolymers: 2. Nylon-6.6*, Polymer, 1992. **33**(2): p. 284–293
- Xianwei S., and X. Xu-Ming, *Creating super-tough and strong PA6/ABS blends using multi-phase compatibilizers*, Chinese Chemical letters, 2019. **30**(1): p. 149–152.
- Njuguna J., Z. Mouti, and K. Westwood, *Toughening mechanisms for glass fiber-reinforced polyamide composites*. Chapter 8. Editors; Q., Qin, and J. Ye. *Toughening Mechanisms in Composite Materials*. 2015, UK: Woodhead Publishing Series. p. 211–232.
- Thomason J. L., *Glass fibre sizing: A review*. Composites Part A: Applied Science and Manufacturing, 2019. **127**: 105619. p. 1-24.
- Zhuang R. C, T. Burghardt, R. Plonka, J. W. Liu, and E. Mäder, *Affecting glass fibre surfaces and composite properties by two stage sizing application*. Express Polymer Letters, 2010. **4**: p. 798–808.
- Xu M., J. Lu, Y. Qiao, L. Wei, T. Liu, P. C. Lee, L. Zhao, and C. B. Park, *Toughening mechanism of long chain branched polyamide 6*, Materials and Design, 2020. **196**: 109173, p. 1-8.
- Guo K., D. Wang, G. Zhang, J. Song, T. Wu, and J. Qu, *Effect of series explosion effects on the fiber length, fiber dispersion and structure properties in glass fiber reinforced polyamide 66*, Polymers for Advanced Technologies, 2021. **32**: p. 505–13.
- Xiao Y., X. Mu, B. Wang, W. Hu, J. Wang, F. Zhou, C. Ma, Y., and L. Song, *A novel phosphorous-containing polymeric compatibilizer: Effective reinforcement and flame retardancy in glass fiber reinforced polyamide 6 composites*, Composites Part B: Engineering, 2021. **205**: 108536, p. 1-9
- Kawada J., M. Kitou, M. Mouri, T. Mitsuoka, T. Araki, C. Lee, T. Ario, O. Kitou, and A. Usuki, *Morphology controlled PA11 bio-alloys with excellent impact strength*, ACS Sustainable Chemistry & Engineering, **2016**. **4**: p. 2158–2164.
- Kawada J., M. Kitou, M. Mouri, Y. Kato, Y. Katagiri, M. Matsushita, T. Ario, O. Kitou, and A. Usuki, *Super impact absorbing bio-alloys from inedible plants*, Green Chemistry. 2017. **19**: p. 4503–4508.



Research Article

The production of open cell Ni-foam using KBr as spacer and oxidation shield via powder metallurgy technique

Mustafa Güven Gök ^a 

^aHakkari University, Engineering Faculty, Materials Science and Eng. Department, Turkey

ARTICLE INFO

Article history:

Received 01 June 2021

Revised 03 September 2021

Accepted 16 September 2021

Keywords:

High porosity

Molten salt shield

Nickel foam

Potassium bromide

Powder metallurgy

ABSTRACT

Metallic materials having a porosity of 70% or more are generally referred as highly porous metals. In this study, highly porous pure nickel materials were produced by powder metallurgy route. In the production process, potassium bromide was used both as a space-holder phase and as an oxidation shield. In the method, firstly, nickel and potassium bromide powders were mixed according to the desired void ratio. The obtained nickel-potassium bromide powders were pressed in a hydraulic press and turned into pellets (diameter: 13mm). Then, these pellets were pressed again in a wider mold (diameter: 21mm) so that all surfaces were covered with potassium bromide, and the encapsulation process was carried out. These capsules were embedded in potassium bromide in an alumina crucible for sintering. The sintering process was carried out in an open atmosphere at 1050 °C for 60 minutes. After the sintering process, the crucibles were kept in water to dissolve the crystallized potassium bromide around and inside the sample. Density, macrostructure, microstructure and EDS analyzes were performed on the samples. It was observed that open cell pores (58.3 - 78.1% vol) with diameters varying between 5 and 500 μm, which are homogeneously distributed in nickel, have been successfully obtained. In addition, it was proved that nickel foam materials can be produced in different sizes and designs.

1. Introduction

With the development of technology, the need for lighter and stronger metals is increasing. Also, in some applications, such as high temperature filters or fuel cells, it is desirable for the metal to have a high surface area. Therefore, metallic foams gain importance. Terms such as metal foam and porous metal have the same meaning. Metal foams are cellular structures in the form of solid metal that contain many voids or pores within their volume. In this way, very light (low density) and strong metallic construction materials, filter materials, heat exchangers, solid oxide fuel cells and materials having vibration and/or impact absorbing properties can be produced [1-6]. There are two types of metal foams, open-cell (containing interconnected voids) and closed-cell [1, 7, 8]. The open-celled one of these appeals to many areas such as filters, heat exchangers, fuel cells, etc.

On the other hand, porous Nickel (Ni) foam materials are used in many high-tech applications due to their functional properties (good electrical and thermal

conductivity, high specific surface area, sound absorption and gas-liquid permeability). Examples of these applications are heterogeneous catalysis systems, high temperature filters, heat exchangers and solid oxide fuel cells [5, 9, 10]. Different methods such as powder metallurgy (PM), casting, infiltration casting and electrodeposition can be used in the production of porous Ni. Among these, the PM method is advantageous compared to others in terms of being suitable for open-cell foam production, allowing precise dimensional tolerances and high purity production [11-14]. In addition, it is possible to good control the volume fraction, geometry and size of the pores by the PM method. However, as in other high-temperature manufacturing methods, one of the biggest problem in PM is the oxidation of the metallic material to be produced due to the high temperature of the sintering process [15-18]. In order to prevent this, "vacuum", "inert gas (argon etc)" or "reducing gas" atmospheres, which are called protective atmospheres, must be created in the sintering furnace during production, and this increases the production cost.

* Corresponding author. Tel.: +90-438-211-0893 (1494); Fax: +90-438-212-1211.

E-mail addresses: m.guvengok@hakkari.edu.tr (M.G. Gök)

ORCID: 0000-0002-5959-0549 (M.G. Gök)

DOI: 10.35860/iarej.946611

© 2021, The Author(s). This article is licensed under the CC BY-NC 4.0 International License (<https://creativecommons.org/licenses/by-nc/4.0/>).

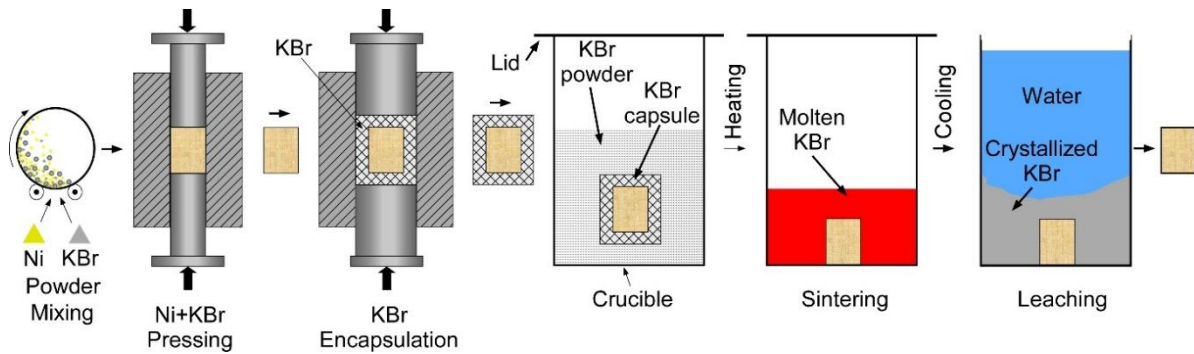


Figure 1. Schematic summary of the production process.

According to a method discovered recently (2019) to solve this problem in the PM method, it has been proven that the oxidation of Titanium metal sintered in potassium bromide (KBr) salt is not more than materials sintered in inert atmosphere [19]. Thus, a significant reduction in production costs is possible. The article by Dash et al. [19], published in the "Nature", was reported on scientific news websites such as The American Ceramic Society with the headline of "No more inert atmospheres—Molten salt synthesis prevents oxidation of materials in air" [20]. Briefly, the researchers carried out the encapsulation process by pressing the pelleted Titanium (Ti) powder into the KBr salt. It is reported that thanks to this encapsulation, KBr becomes gas-tight at room temperature and prevents contact of metal pellets with the atmosphere and oxidation during sintering up to its melting temperature of 734 °C. Then, the encapsulated pellets were placed in an alumina crucible containing KBr powder (salt bed), and filled the remaining part of the crucible with KBr powder. After the sintering process, water was used to dissolve the salt which passed from the liquid phase to the solid phase with cooling, and this water was evaporated to obtain KBr again (recycling) [19]. It was reported that 1.02 kg of KBr can be dissolved in 1 liter of water at 100°C [21]. Therefore, KBr can be used repeatedly. In another study by Roy et al. [22], Ti_2AlN and V_2AlC (MAX phase) ceramics were sintered between 900 – 1100 °C using PM method in KBrCl-NaCl salt environment. As a result, they proved that when molten salt is used instead of inert gas atmosphere or vacuum, oxidation does not occur in the sintered samples and the productions take place in an economical way. Therefore, in both studies [19, 22], it is stated that sintering in KBr environment is ecologically positive, sustainable, energy and cost efficient and can be used in industrial applications.

The use of salts such as sodium chloride (NaCl), carbamide (CH_4N_2O) and ammonium bicarbonate (NH_4HCO_3) as space holders in the production of porous metals is seen in the studies in the literature [1, 5, 10, 23]. In addition, Noor et al. used KBr as a space holder in the production of porous Ti foams and obtained porosity values ranging from 16 to 31% [24]. However, there is no

study in the literature regarding the use of KBr as both space holder and oxidation shield in porous Ni production.

The aim of this study can be defined as the production of highly porous Ni foams by PM method using KBr salt powder as both a space holder and an oxidation protective shield to reduce production costs. As a result of the studies, Ni foams having open porosity up to 78.1% were produced by creating voids in the Ni owing to the water-soluble feature of KBr. Moreover, thanks to KBr molten salt shielded synthesis, Ni metal was sintered without using a protective atmosphere.

2. Materials and Methods

2.1 Mixing, Pressing, Sintering and Leaching

The methods followed in the production process were made as described below and summarized schematically in Figure 1.

- First of all, Nickel (powder size 2 μm , purity 99.5%, manufacturer: Molchem) and Potassium Bromide (KBr, purity: 99.5%, manufacturer: EduKim) powders were weighed on precision balance (RADWAG AS220.R2) to contain more than 70% KBr by volume. The stereo microscope image showing the morphology and size of the KBr powder were given in Figure 2.
- The weighed powders were poured into the mixing bowl without binder and mixed dry in a horizontal mechanical mixer using zirconia balls (ball to powder ratio, 1:2) at 250 rpm for 2 hours.
- The prepared powder mixtures were placed in a metal mold ($\varnothing = 12$ mm) and cold pressed in a hydraulic press with a pressure of 200 MPa. Thus, Ni+KBr pellets were obtained (see Figure 3 (a)) without any binder.

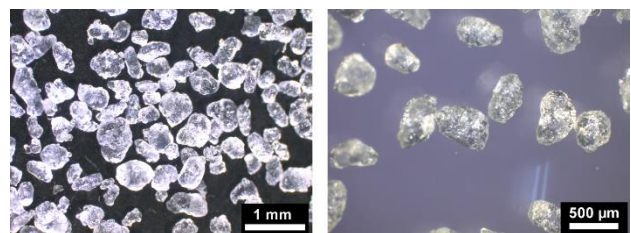


Figure 2. Stereo microscope images of KBr salt powder at different magnifications (average grain size 500 μm).

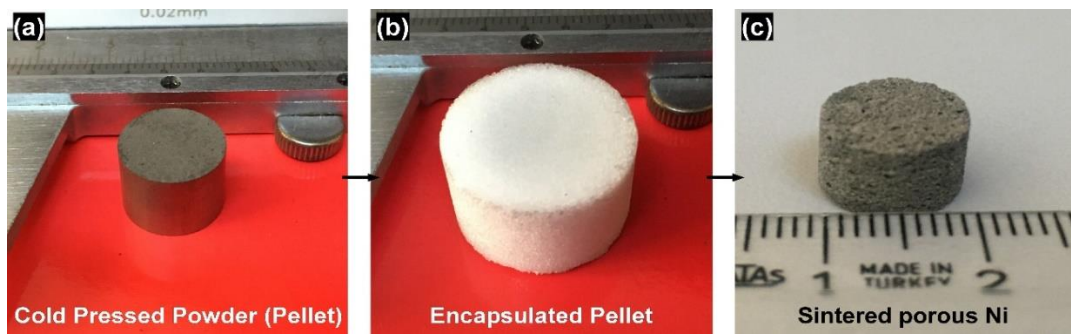


Figure 3. Image of cold pressed Ni+KBr pellet (a), KBr encapsulated pellet (b) and sintered porous Ni foam (c).

- The cold pressed powder pellets were placed in a larger diameter ($\varnothing = 21$ mm) metal mold containing KBr powder and pressed again under 200 MPa pressure after adding KBr powder to remaining part of the mold. Thus, the Ni+KBr pellets were completely encapsulated with the KBr and made ready for sintering (see Figure 3 (b)).
- Alumina crucibles were used for the sintering process. First of all, a salt bed was formed by adding KBr powder to the floor of the crucibles, and encapsulated pellets were placed on these beds. Then the inside of the crucibles was completely filled with KBr powder (exceeding the size of the pellets). Another alumina was left on the alumina crucibles as a lid (without any compression, gasketing, etc.).
- These crucibles were placed in the sintering furnace (Protherm-muffle furnace) and sintered for 60 minutes at a sintering temperature of 1050 °C (heating rate 5 °C/min) in normal atmosphere (without using any additional protective gas, vacuum etc.).
- The cooling process was carried out in the furnace. After cooling, the crucibles were soaked in hot water to dissolve KBr, which both crystallized in the crucible and dispersed in Nickel. Thus, sintered Nickel samples in porous (foam) structure were obtained (see Figure 3 (c)).

2.2 Characterizations

Density, macrostructure and microstructure (with optical

microscope and scanning electron microscope) analyzes of the produced samples were performed. The density of the porous nickel foams was calculated by measuring the mass and the volume from their physical dimensions. A stereo microscope (Leica) was used for optical microstructure examinations. In addition, TESCAN VEGA3 Thermionic Emission Scanning Electron Microscope (SEM) and Energy Dispersion Spectrometer (EDS - Oxford/Inca) were used for detailed microstructure studies and elemental distribution analysis, respectively.

3. Results and Discussions

3.1 Macrostructure and Density Analysis

In Figure 4, a macrostructural photograph of Ni foams having different porosity and designs was given. It was determined that the samples could be produced in different porosity ratios.

In addition, the manufacturability of Ni foams with different designs was also tested and produced successfully. As seen in Figure 4, it was possible to produce designs such as inner part hollow outer part porous (ring shaped) which is the preferred geometry in many filter applications, inner part dense outer part porous used in some cathode applications where both strength and excess surface area are desired and outer part dense inner part porous for some insulation and heat exchanger applications.

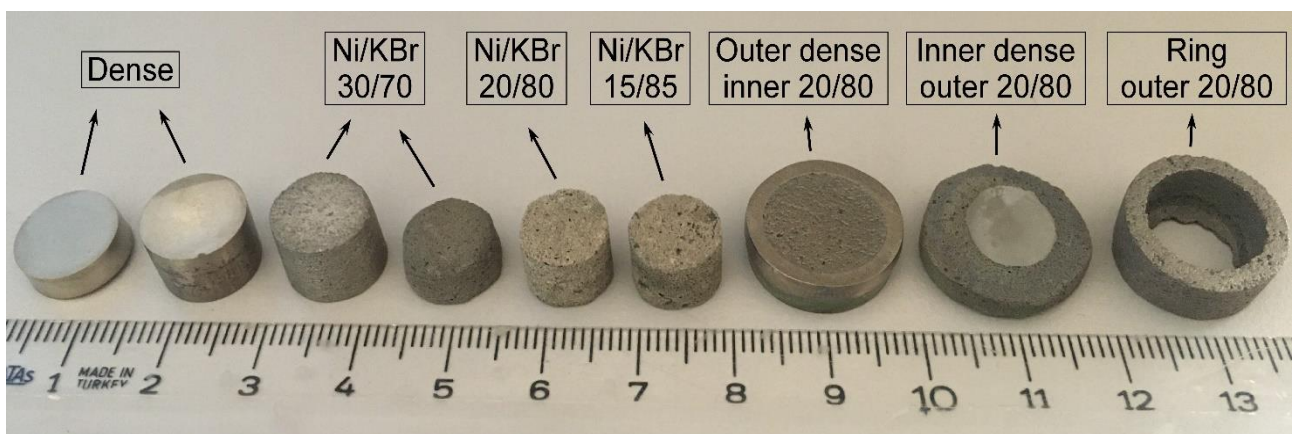


Figure 4. Macro view of Ni foams with different porosity and designs

On the other hand, it was determined that there is an upper limit in terms of porosity value in the production of Ni foam by powder metallurgy method using KBr. The production of foams with a KBr ratio greater than 85% was not possible with this method. As seen in Figure 5, a concave bending occurred from the center of the cylinder bases of the samples that were tried to be produced with the KBr ratios between 85% and 90%. Above 90% KBr, sintering did not occur and the samples were fragmented into particles. Because the excess KBr in the composition prevented Ni powder particles from coming into contact with each other and neck formation during sintering. Therefore, diffusion did not occur.

As seen in Table 1, the production of Ni foams having open porosity up to 78.09% by volume was achieved. Amount of closed porosity increased with decreasing KBr ratio. This was an expected result. Because as the amount of KBr decreased, the nickel particles covered the KBr particles like a cell wall. This caused the KBr space holders to be trapped inside the Ni cell. The relative density value of the dense Nickel sample without KBr was measured as approximately 95%. Therefore, it was possible to achieve a density reduction of approximately 82% by means of porous nickel foams.

3.2 Analysis by Optical Microscopy

Images of porous Ni foams produced by powder metallurgy method in KBr medium, obtained from stereo optical microscope, were given in Figure 6 (a-f). When Figure 6 (a and b) was examined, it was observed that the porosities were homogeneously distributed in the samples with a Ni/KBr ratio of 20/80. In Figure 6 (c and d), the microstructures of the samples at higher magnification were given. The porosities had an interconnected (open-cell) morphology. It was concluded that Ni and KBr powders were successfully mixed during the powder preparation process, since the porosities were homogeneously dispersed

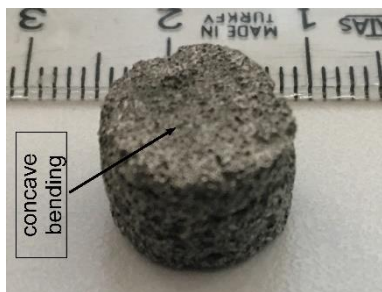


Figure 5. Macro view of the concave bending from the center of the surface that occurs in samples containing more than 85% KBr.

Table 1. Density and porosity values of Ni foam.

Ni/KBr (vol %)	Density (g/cm ³)	Closed porosity (vol %)	Open porosity (vol %)
30/70	2.99	11.66	58,34
20/80	2.03	9.09	70.91
15/85	1.52	6.91	78.09

Figure 6 (e) shows the image of the sintered sample without KBr encapsulation, while Figure 6 (f) demonstrates the sintered sample with KBr encapsulation. Accordingly, as a result of not performing the KBr encapsulation process, an oxidation layer of approximately 330 μm thickness formed on the outer surfaces of the sample. This oxidation (NiO) layer was seen in green (Figure 6 (e)).

On the other hand, as seen in Figure 6 (f), no oxidation layer was found on the surface of porous Ni foam sintered after KBr encapsulation. This indicated that encapsulation with KBr prevented oxidation of the metal sample as in an inert or vacuum atmosphere. Dash et al. [19] reported that a capsule wall thickness of 4 mm and pressure of 200 MPa would be sufficient for KBr to act as a gas-tight capsule. In this study, since the thickness of the KBr capsule for Ni foams was at least 4 mm, the Ni foam samples were protected from oxidation by encapsulation during sintering up to 734 $^{\circ}\text{C}$, the melting temperature of KBr. When the KBr melted at about 734 $^{\circ}\text{C}$ and went into the liquid phase, the Ni foam samples sank to the bottom of the KBr liquid in the crucible. Thus, the Ni foam samples were protected from oxidation by encapsulation until the transition of KBr to the liquid phase, and after the liquid phase, they sank into the the KBr liquid and did not come into contact with the atmosphere (oxygen).

3.3 Microstructural Analysis by SEM

Scanning electron microscope (SEM) images of Ni foams with 70.9% open porosity at different magnifications were presented in Figure 7 (a-d).

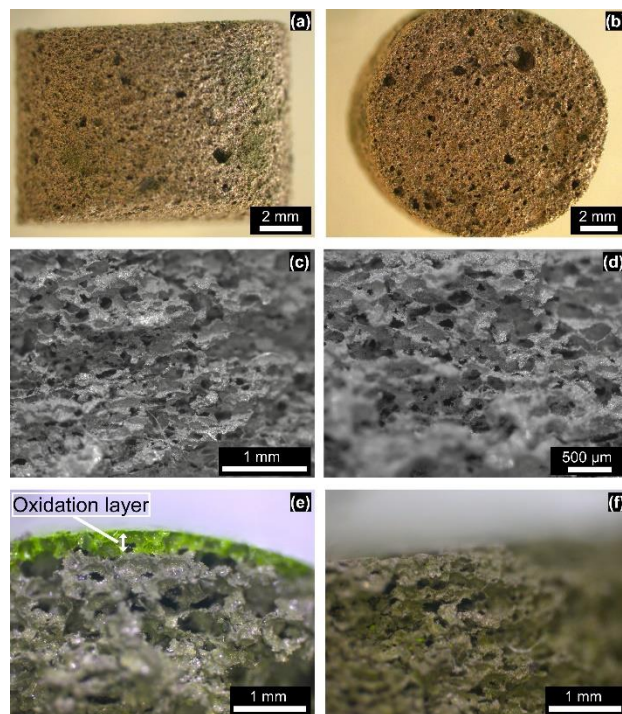


Figure 6. Images of Ni foam samples taken from stereo optical microscope, (a and b) general view, (c and d) morphology of porosities, (e and f) the effect of encapsulation with KBr on oxidation.

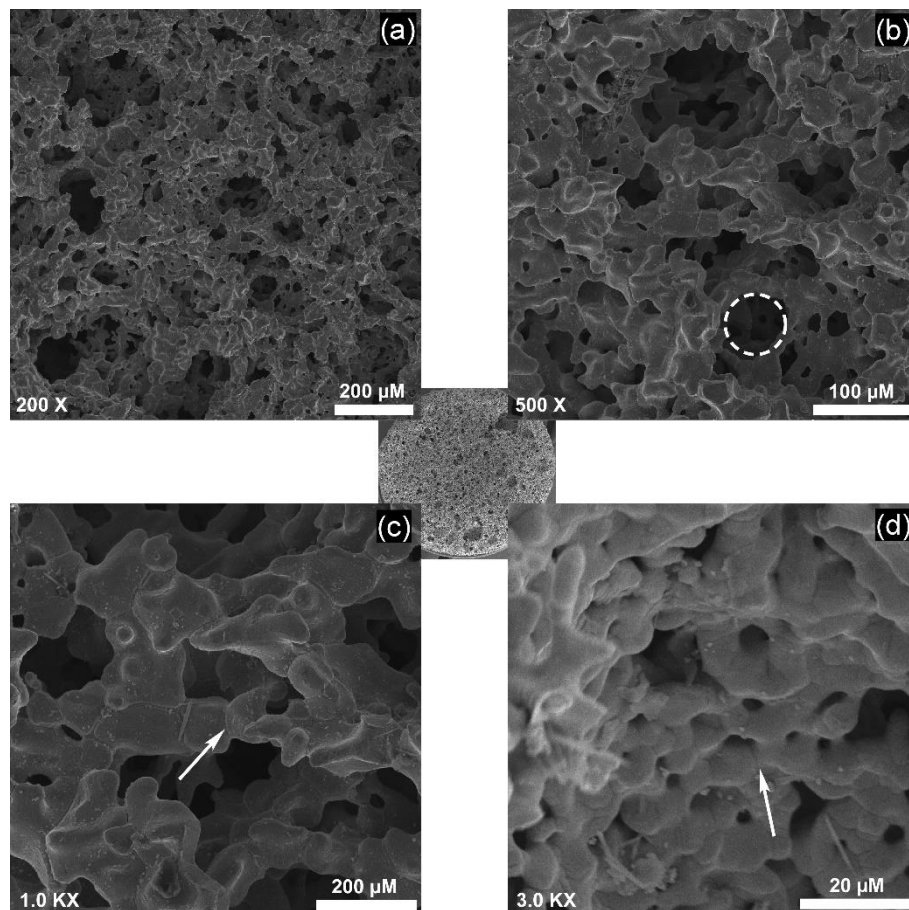


Figure 7. Microstructural images of porous Ni foam sample taken at different magnifications by SEM. (a) 200X, (b) 500X, (c) 1000X and (d) 3000X.

As can be seen from the images, the samples contained interconnected (open) porosities and the porosities were homogeneously distributed in the microstructure. The diameters of the porosities ranged from about 5 μm to 500 μm . Accordingly, it was understood that powder preparation and sintering parameters were appropriate. When the interfaces between Ni powder particles were examined (shown by arrows in Figure 7 (c and d)), it could be said that the neck characteristic of sintering formed between the particles, and both bonding and growth occurred through diffusion from these neck regions. Therefore, the sintering process with powder metallurgy route was successful and the powder particles formed a strong bond with each other. On the other hand, some small pores having diameter less than 5 μm were present in the microstructure, as clearly seen in Figure 8 (d). It was thought that this situation took place due to the crunch of the KBr space holders during pressing. The same situation was reported by Wang at al [25], who used NaCl as space holder for Cu foam production.

Figure 8 showed the results of the energy dispersive x-ray spectroscopy (EDS) analysis made from three different points of the Ni foam sample surface and the points where the point analysis was made. In the spectra obtained from the EDS analysis, the presence of any element other than Nickel was not found. According to these results, it has been

understood that Nickel foams can be produced successfully in KBr environment without oxidation.

4. Conclusions

In this study, highly porous Ni foams having open porosities were produced by using KBr as both space-holder and oxidation shield. Also, the manufacturability of Ni foams with different designs was tried. With this method, it was possible to produce Ni foam materials in different designs (with inner dense outer porous, inner porous outer dense, ring shaped, etc.). There was an upper limit for the porosity ratio in Ni foam production with this method. In the experiments, it was observed that a concave bending occurred on the surfaces of the samples with a KBr ratio above 85%. The sintering process was not successful in the samples containing 90% or more KBr by volume. It was observed that the porosities were in interconnected (open) morphology and homogeneously distributed in the structure. In addition, porosity diameters ranged from 5 to 500 μm . While an oxidation layer was formed on the surface of the samples sintered without KBr encapsulation, it did not form on the encapsulated samples. In this way, the samples were protected from oxidation during sintering thanks to KBr molten salt.

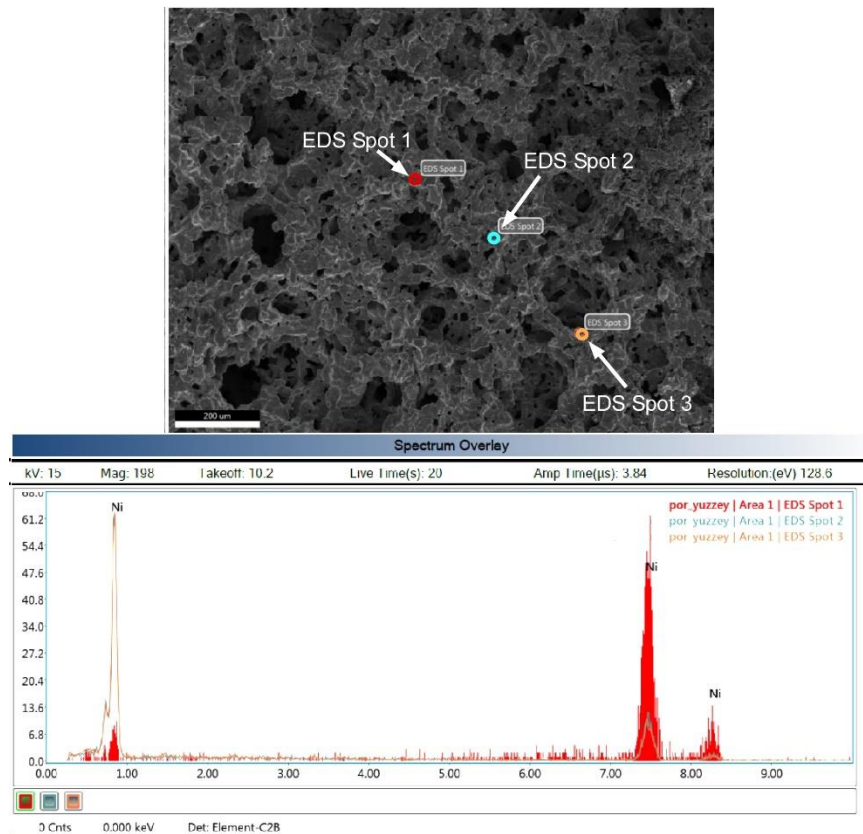


Figure 8. EDS analysis points and EDS spectra.

Declaration

The author declared no potential conflicts of interest with respect to the research, authorship, and/or publication of this article. The author also declared that this article is original, was prepared in accordance with international publication and research ethics, and ethical committee permission or any special permission is not required.

Author Contributions

Mustafa Guven Gok is responsible for all section of the study.

Acknowledgment

This work was supported by the Hakkari University Scientific Research Projects Unit (project number: FM20BAP9).

References

- Kennedy, A., *Porous Metals and Metal Foams Made from Powders*. 2012, in Powder Metallurgy: ed. Kondoh, K., IntechOpen. p. 31–46.
- García-Moreno, F., *Commercial applications of metal foams: Their properties and production*. Materials, 2016. **9**(2): p. 1-27.
- Patel, P., Bhingole, P.P., Makwana, D., *Manufacturing, characterization and applications of lightweight metallic foams for structural applications: Review*. Materials Today Proceedings, 2018. **5**(9): p. 20391–20402.
- Gibson, L.J., *Metallic Foams: Structure, Properties, and Applications*. 2001, in Mechanics for a New Millennium: ed. Aref, H., Phillips, J., Springer. p. 57–74.
- Unver, I., Gulsoy, H.O., Aydemir, B., *Ni-625 superalloy foam processed by powder space-holder technique*. Journal of Materials Engineering and Performance, 2013. **22**(12): p. 3735–3741.
- Güven, Ş.Y., *Toz Metalurjisi ve Metalik Köpükler*. SDÜ Teknik Bilimler Dergisi, 2011. **1**(2): p. 22–28.
- Oriňák, A., Oriňáková, R., Králová, Z.O., Turoňová, A.M., Kupková, M., Hrubovčáková, M., et al., *Sintered metallic foams for biodegradable bone replacement materials*. Journal of Porous Materials, 2014. **21**(2): p. 131–140.
- Kulshreshtha, A., Dhakad, S.K., *Preparation of metal foam by different methods: A review*. Materials Today Proceedings, 2019. **26**(2): p. 1784–1790.
- Mohamed, A.A., Abdel-Karim, R.M., Zohdy, K.M., El-Raghy, S.M., *Electrocatalytic activities of macro- Porous nickel electrode for hydrogen evolution reaction in alkaline media*. Egyptian Journal of Chemistry, 2019. **62**(4): p. 1065–1078.
- Gnedovets, A.G., Zelenskii, V.A., Ankudinov, A.B., Alymov, M.I., *Hierarchically Structured, Highly Porous Nickel Synthesized in Sintering–Evaporation Process from a Metal Nanopowder and a Space Holder*. Doklady Chemistry, 2019. **484**(2): p. 64–67.
- Ternero, F., Caballero, E.S., Astacio, R., Cintas, J., Montes, J.M., *Nickel porous compacts obtained by medium-frequency electrical resistance sintering*. Materials, 2020. **13**(9): p. 1–15.
- Tracey, V.A., *Sintering of Porous Nickel*. Powder Metallurgy, 1983. **26**(2): p. 89–92.
- Abdullah, Z., Razali, R., Subuki, I., Omar, M.A., Ismail, M.H., *An Overview of Powder Metallurgy (PM) Method for*

Porous Nickel Titanium Shape Memory Alloy (SMA). Advanced Materials Research, 2016. **1133**, p. 269–274.

14. Mohamed, L.Z., Ghanem, W.A., El Kady, O.A., Lotfy, M.M., Ahmed, H.A., Elrefaie, F.A., *Oxidation characteristics of porous-nickel prepared by powder metallurgy and cast-nickel at 1273 K in air for total oxidation time of 100 h*. Journal of Advanced Research, 2017. **8**(6): p. 717–729.
15. Taniş, N.A., Hakan, G., Bülent, B., *Effect of Cu addition on microstructure and mechanical properties of NiTi based shape memory alloy*. International Advanced Researches and Engineering Journal, 2018. **02**(01): p. 20–26.
16. Gül, B., Gezici, L.U., Ayvaz, M., Çavdar, U., *The comparative study of conventional and ultra-high frequency induction sintering behavior of pure aluminum*. International Advanced Researches and Engineering Journal, 2020. **4**(3): p. 173–179.
17. Nayar, H.S., *Sintering Atmospheres*. 2015, in Powder Metallurgy: ed. Samal, P., Newkirk, J., ASM International. p. 237–246.
18. Gök, M.G., *Spark Plasma Sintering of Nano Silicon Carbide Reinforced Alumina Ceramic Composites*, European Mechanical Science, 2021. **5**(2), p. 64-70.
19. Dash, A., Vaßen, R., Guillon, O., Gonzalez-julian, J., *Molten salt shielded synthesis of oxidation prone materials in air*. Nature Materials, 2019. **18**, p. 465-468.
20. Mcdonald, L., *No more inert atmospheres—Molten salt synthesis prevents oxidation of materials in air*, 2019. [cited May 30, 2021]; Available from: <https://ceramics.org/ceramic-tech-today/manufacturing/no-more-inert-atmospheres-molten-salt-synthesis-prevents-oxidation-of-materials-in-air>.
21. Pinho, S.P., Macedo, E.A., *Experimental measurement and modelling of KBr solubility in water, methanol, ethanol, and its binary mixed solvents at different temperatures*. The Journal of Chemical Thermodynamics, 2002. **34**(3): p. 337–360.
22. Roy, C., Banerjee, P., Bhattacharyya, S., *Molten salt shielded synthesis (MS3) of Ti2AlN and V2AlC MAX phase powders in open air*. Journal of the European Ceramic Society, 2020. **40**(3): p. 923–329.
doi: <https://doi.org/10.1016/j.jeurceramsoc.2019.10.020>.
23. Moradi, M.R., Moloodi, A., Habibolahzadeh, A., *Fabrication of Nano-composite Al-B4C Foam via Powder Metallurgy-Space Holder Technique*. Procedia Materials Science, 2015. **11**(2000): p. 553–559.
24. Mat Noor, Fazimah, et al., *Potassium Bromide as Space Holder for Titanium Foam Preparation*, Applied Mechanics and Materials, 2014. **465**(466): p. 922–926.
25. Wang, Q.Z., Cui, C.X., Liu, S.J., Zhao, L.C., *Open-celled porous Cu prepared by replication of NaCl space-holders*. Materials Science and Engineering: A., 2010. **527**(4): p. 1275–1278.



Research Article

Knockdown factors for cylindrical shells caused by torsional Mode-I type geometric imperfections under axial compression

Ibrahim Kocabaş^{a,*}  and *Haluk Yılmaz*^a 

^aVocational School of Transportation, Eskişehir Technical University, Eskişehir, Turkey

ARTICLE INFO

Article history:

Received 05 March 2021

Revised 21 May 2021

Accepted 01 June 2021

Keywords:

Axial compression
Cylindrical shell
Finite element method
Geometric imperfection
Knockdown factor

ABSTRACT

Geometrical imperfection, which is generally a result of manufacturing process and service conditions, plays a crucial role in load-bearing capacity of shell structures. This study presents a numerical study on knockdown factors of cylindrical shells as a result of torsional Mode-I type of geometric imperfections under compressive loads. The deformation patterns obtained from liner bifurcation analysis (LBA) for torsional Mode-I shape are used as a source of geometric imperfection. Then, geometrically nonlinear buckling analysis with imperfect model (GNIA) is incorporated with LBA in ANSYS Workbench to obtain limit loads of imperfect structures. A parametric study is thus performed to investigate the influence of imperfection depth on the load-bearing capacity considering a wide range of cylindrical shell configurations. Local and global buckling characteristics of the imperfect shells are examined and knockdown factors are characterized by three distinct regions as a basis of normalized imperfection depth. For a large number of shell configurations, a scattering of knockdown factors against normalized imperfection depth is given with mathematical expressions evolving lower and upper bounds. These expressions provide the minimum and maximum values of knockdown factors for a given imperfection depth, which can be treated as a design tool to ensure safety of the shell structure.

1. Introduction

Cylindrical shells are major structural elements that are widely used in most industries such as, storage tanks, silos, launch-vehicle systems, pressure hulls and other engineering applications. This kind of structures is mostly subjected to compressive loadings due to weight of the structural components in which they are connected. Cylindrical shell structures especially undergo local or global buckling failure as a result of axial compression. For this reason, prediction of buckling load plays an important role in the design stage of cylindrical shells. If it occurs, this type of failure mode tends to rapid and complete destruction of the shell structure. For a perfect cylindrical shell structure (without any imperfection), the critical buckling stress is expressed by Equation 1 [1].

$$\sigma_{cr} = \frac{E}{\sqrt{3(1-\mu^2)}} \frac{t}{R} \quad (1)$$

where E is Young's modulus, μ is Poisson's ratio, t is wall thickness and R is cylinder radius. Load-bearing capacity

of a shell structures is quite sensitive to geometric imperfections even though they are very small. A geometric imperfection can be described as the deviations of geometric features from the ideal cylindrical shape. Generally, the pattern of a geometric imperfection in the shell is a result of utilized manufacturing process and interactions of the components in the construction [2]. These imperfections cause drastic variation of the actual buckling load in comparison with that of the perfect (ideal) shell structure [3]. Donnell [4] and Flügge [5] are the first studies to develop non-linear formulations taking into account large-scale initial geometric imperfections to evaluate actual buckling loads of imperfect structures. Later, Koiter [6] proposed an analytical method to obtain scatterings of the experimental geometric imperfection trends. However, the buckling loads are very sensitive to the form and type of geometric imperfections. There are various forms of geometric imperfections of shell structures, for example, out of roundness, local dimple, eccentricity, sinusoidal wave-type deviations, etc. Each has a characteristic influence on the buckling load of

* Corresponding author. Tel.: +90 222 224 13 91; Fax: +90 222 224 13 92.

E-mail addresses: ibrahimkocabas@eskisehir.edu.tr (I. Kocabaş), halukyilmaz@eskisehir.edu.tr (H. Yılmaz)

ORCID: 0000-0003-0600-2034 (I. Kocabaş), 0000-0002-6750-3708 (H. Yılmaz)

DOI: 10.35860/iarej.891791

© 2021, The Author(s). This article is licensed under the CC BY-NC 4.0 International License (<https://creativecommons.org/licenses/by-nc/4.0/>).

cylindrical shell structures. Many forms of geometric imperfections on the shell buckling have been studied in references [7-9].

The knockdown factor referred to as KDF, the ratio of the buckling load of an imperfect cylindrical shell to the predicted buckling load of an ideal cylinder obtained from Equation 1 ($F_{cr}=2\pi R t \sigma_{cr}$) is commonly used to characterize influence of the geometric imperfections on the load-bearing capacity of the shell structure. According to a series of test results, an empirical design guideline was proposed by NASA [10] which provides lower-bound KDFs for the design of cylindrical shells as shown in Equation 2. This guideline is very conservative and resulting cylindrical shells would be so redundant and inefficient, thereby affecting the payloads for these structures [10].

$$KDF = 1 - 0.92 \left(1 - e^{-\frac{\sqrt{R/t}}{16}} \right) \quad (2)$$

For axially compressed cylindrical shell with initial geometric imperfection, Evkin and Lykhachova [11] implemented an energy barrier method to estimate buckling load and knockdown factors considering elasto-plastic buckling case. They conducted a parametric analysis of the structure and derived a formula for design buckling load which splits up the zone of the high sensitivity of the shell to imperfections [11]. Initial geometric imperfections caused by different mode shapes under axial compression is studied by Kim [12] to develop practical design equations and charts predicting buckling strength of cylindrical shells and tanks. Among the shell structures, cylindrical shells are a standard structure (membrane stress dominant by nature of the structure form) which are quite sensitive to imperfections. For this reason, more robust KDF's for the design of shells are a primary factor for efficient construction. Several important studies in the literature, concerning the initial geometric imperfection for axially compressed cylindrical shells, are: (i) robust KDF's for the design of cylindrical shells [13], (ii) experimental and numerical campaign on low KDF's [14], (iii) improved KDF's for composite cylindrical shells with geometric imperfections [15], and (iv) buckling of quasi-perfect cylindrical shell under axial compression [16].

Type of loading is a factor that affects the geometric imperfection of the shell structure as well as the geometrical characteristics of imperfections. Combined loadings lead to more complex buckling responses in terms of geometrically imperfect structures. To increase the load-bearing capacity and avoid the stress-failure before reaching the critical load, Mahdy et al. [17] investigated buckling and stress-competitive failure analysis of composite cylindrical shells under axial compression and torsion. Similarly, the buckling behaviour of imperfect cylindrical shells subjected to torsion examined by Zhang and Han [18] using a singular perturbation technique.

However, most of the studies in the available literature focus on a limited range of geometric imperfection patterns. The influence of the geometric imperfections caused by the torsional interactions on the buckling load of cylindrical shells under axial compression remains still unclear.

This study presents lower and upper bound of knockdown factors for the geometrically imperfect cylindrical shells under axial compression. Torsional Mode-I type deformation patterns are considered as a geometric imperfection. The influence of deformation patterns and imperfection depths is examined at various cylindrical shell configurations. In the available literature, no study concerning torsional Mode-I type of geometric imperfections has been found for axially compressed cylindrical shells. In this way, this study is expected to be have a contribution to fill this gap in the literature.

2. Material and Method

2.1 Shell Geometry

The geometry of a cylindrical shell structure is schematically illustrated in Figure 1. There are three independent geometric parameters in the construction of a cylindrical shell which are denoted as shell length L , wall thickness t and cylinder radius R . A reference cylindrical coordinate system is presented in Figure 1 at which r , θ and z denote radial, circumferential and vertical directions, respectively. Schematic illustration of a torsional Mode-I type of geometric imperfection is shown in Figure 1b, where Δw denotes the level of imperfection depth. Since the maximum value of the imperfection depth is critical in buckling behaviour, Δw is selected as an imperfection parameter.

For general knockdown factor (KDF) evaluations, it is useful to consider normalized shell parameters. Therefore, dimensionless parameters, such as radius-to-thickness ratio R/t , ratio of the imperfection depth to the wall thickness $\Delta w/t$, and length-to-radius ratio L/R are used for KDF evaluation. To reveal influence of each normalized parameter on knockdown factors (KDF's), a parametric study is performed in two stages as can be seen in Table 1.

Table 1. Shell configurations for the parametric study.

Stage I			Stage II		
R/t	$\Delta w/t$	L/R	R/t	$\Delta w/t$	L/R
100	0.1	2	100	0.1	2
200	0.2			0.2	3
400	⋮			⋮	4
800	1			1	5
1600	1.2			1.2	6
	1.5			1.5	
	2			2	
	3			3	

*Factorial design methodology is considered and total number of tested configurations is $5 \times 14 \times 1 + 1 \times 14 \times 5 = 140$.

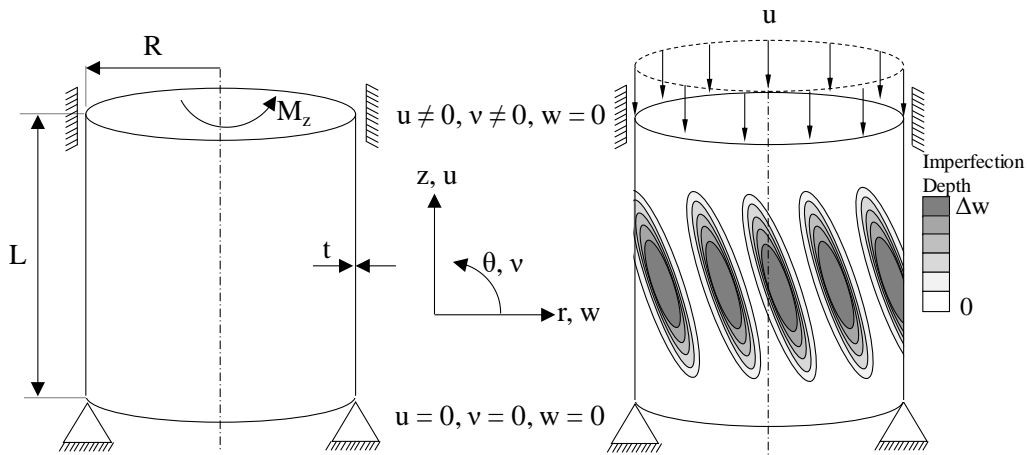


Figure 1. Cylindrical shell geometry with boundary conditions and dimensions a) perfect shell structure under the action of a torsional moment M_z , b) axially compressed imperfect structure with the torsional Mode-I type of geometric imperfection.

In Stage I, the influence of R/t and $\Delta w/t$ on KDF is systematically investigated at $L/R=2$ taking $R=100$ mm. In the second stage, a similar procedure is applied at a constant $R/t=100$ to understand the influence of L/R on the imperfection sensitivity.

2.2 Numerical Analysis

Details of the finite element model, boundary conditions and numerical analysis are presented in this section. A numerical model is constructed in ANSYS Workbench package program. Figure 1 displays the boundary conditions employed in the numerical model. Bottom end of the shell model is clamped and the top of the shell is free to move in u and v direction, and displacement u is applied progressively

until the buckling occurrence as shown in Figure 1. The numerical analysis takes nonlinear geometry and imperfection referred to GNIA (geometrically nonlinear elastic analysis with imperfection included) into account in this study. An elastic material model is considered ($E=200$ GPa and $\mu=0.3$ where E and μ are Young’s modulus and Poisson’s ratio, respectively) since the elastic buckling behaviour of the shells is investigated. Shell181, four-node quadrilateral shell element with large displacement capability, is selected for the numerical analysis. For the analysis of shell structures, the ideal element size is suggested to be $0.5\sqrt{Rt}$ [13] for the numerical analysis. For this reason, a variable element size according to the above formula is considered for each shell configuration.

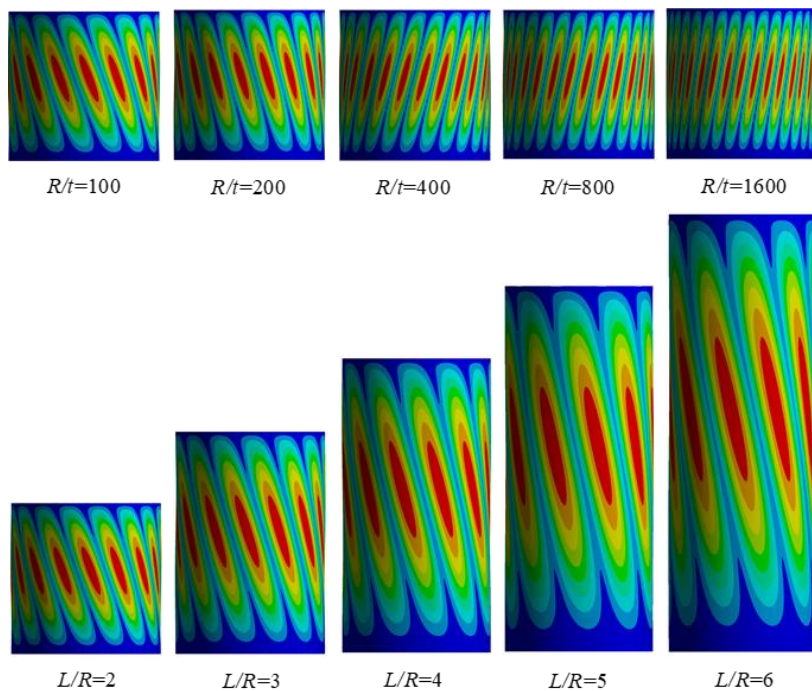


Figure 2. Torsional Mode-I deformation patterns as a source of geometric imperfection for the cylindrical shells at different geometry configurations.

2.3 Characteristics of geometric imperfection

There are different types of initial geometric imperfections as a result of service conditions and manufacturing processes of the cylindrical shells. One of them is the localized geometric imperfection with a certain orientation which is circumferentially distributed over the cylindrical shell surface, as shown in Figure 1 as a result of torsional pre-loadings. If a cylindrical shell is subjected to a torsional moment of M_z due to service conditions, a typical Mode-I deformation pattern forms. This fairly produces a geometric imperfection in the shell structure. It may cause a loss in the load-bearing capacity of the cylindrical shell under axial compression in service conditions. To investigate this phenomena, deformation patterns of the shells should be retrieved after applying a torsional moment of M_z to create an imperfect structure to be tested for axial compression. The deformation pattern of a particular mode shape is obtained by performing a linear elastic bifurcation analysis, LBA, (eigenvalue analysis). This kind of analysis is carried out on a perfect model without taking into account the imperfections. To extract and use the torsional Mode-I deformation pattern of each cylinder configuration as a geometric imperfection, linear buckling analysis is conducted and obtained results are presented in Figure 2. As can be seen, the mode shapes vary depending on the shell parameters R/t and L/R . In the linear buckling analysis, the maximum depth of imperfection Δw is adjusted to 1 mm. Therefore, a scaling factor on the deformed shell is used to obtain desired $\Delta w/t$ values. After this step, the deformed cylindrical shells (imperfect shells) are subjected to axial compression until the buckling occurrence. A flowchart for determining the buckling load of an imperfect shell configuration is described in Figure 3. KDF of each configuration is calculated considering the ratio of the

buckling load of imperfect cylindrical shells to the perfect (ideal) case ($F_{cr} = 2\pi R t \sigma_{cr}$).

3. Results and Discussion

The results of the numerical analysis of the cylindrical shell configurations are presented to investigate knockdown factors (KDF's) of geometrically imperfect structures. Equilibrium path (load-axial displacement curve) is an important tool to indicate the general buckling behaviour of an imperfect shell structure. For this reason, the load-axial deformation curve of a selected configuration, where $R/t=100$, $L/R=2$ and $\Delta w/t=0.9$, is plotted in Figure 4 for the assessment of general buckling behaviour. As can be seen, there are several critical points (A, B, C, D and E) on the equilibrium curve which represents local buckling, non-linear collapse and post-buckling stages of the imperfect cylindrical shell. Additionally, formation of buckles and corresponded deformation patterns at each critical points are shown in Figure 4. The results show that local buckling occurs as a first failure mode (Point A) and shortly afterwards second local buckling mode observed (Point B), then it results in a non-linear collapse (Point C) with a buckling load equals to about 310 kN. At the first local buckling instant, torsional deformation strips are still visible and shortly afterwards the mode shape turns into a different shape, which has circumferentially localized dimples over the shell surface, as seen in Figure 4 (picture for point B). After this point, the mode shape does not radically change during the non-linear collapse and post-buckling stages (see points D and E). However, the depth of the dimples increases and the number of dimples is prone to decrease during the loading history. It is noteworthy that the initial torsional deformation pattern disappears in axial compression, which is replaced by localized dimples.

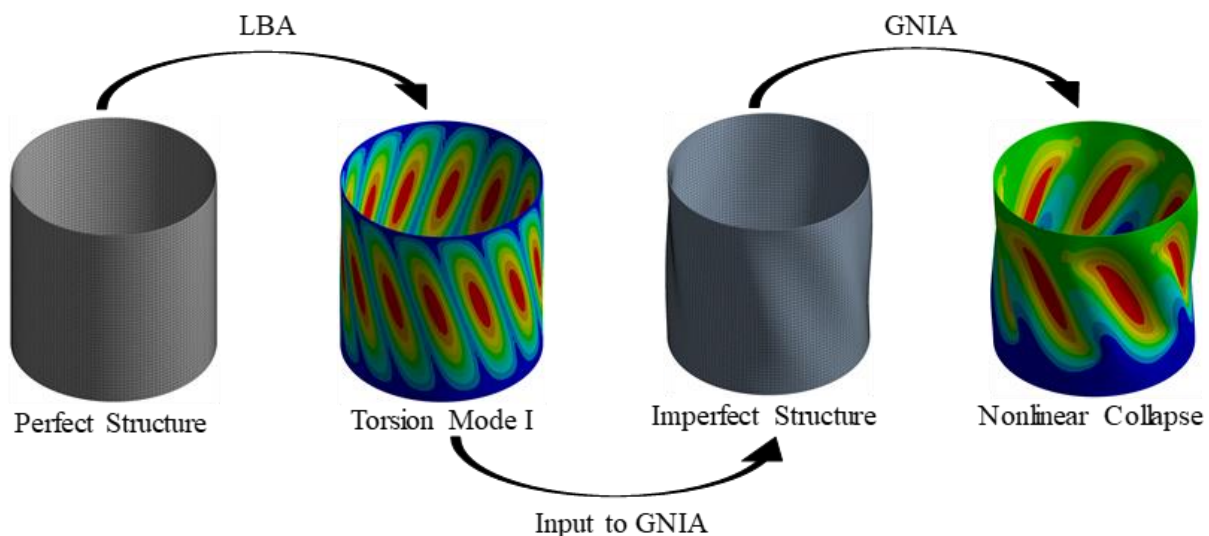


Figure 3. Flowchart of the non-linear buckling analysis of an imperfect cylindrical shell structure under axial compression. At the first step, LBA is applied to obtain torsional Mode-I type geometric imperfection. Secondly, the imperfect structure (deformed shape) exported to GNIA buckling analysis using a scale factor for the arrangement of imperfection depth Δw . At the last step, axial compression is applied to the imperfect shells until the global buckling occurrence.

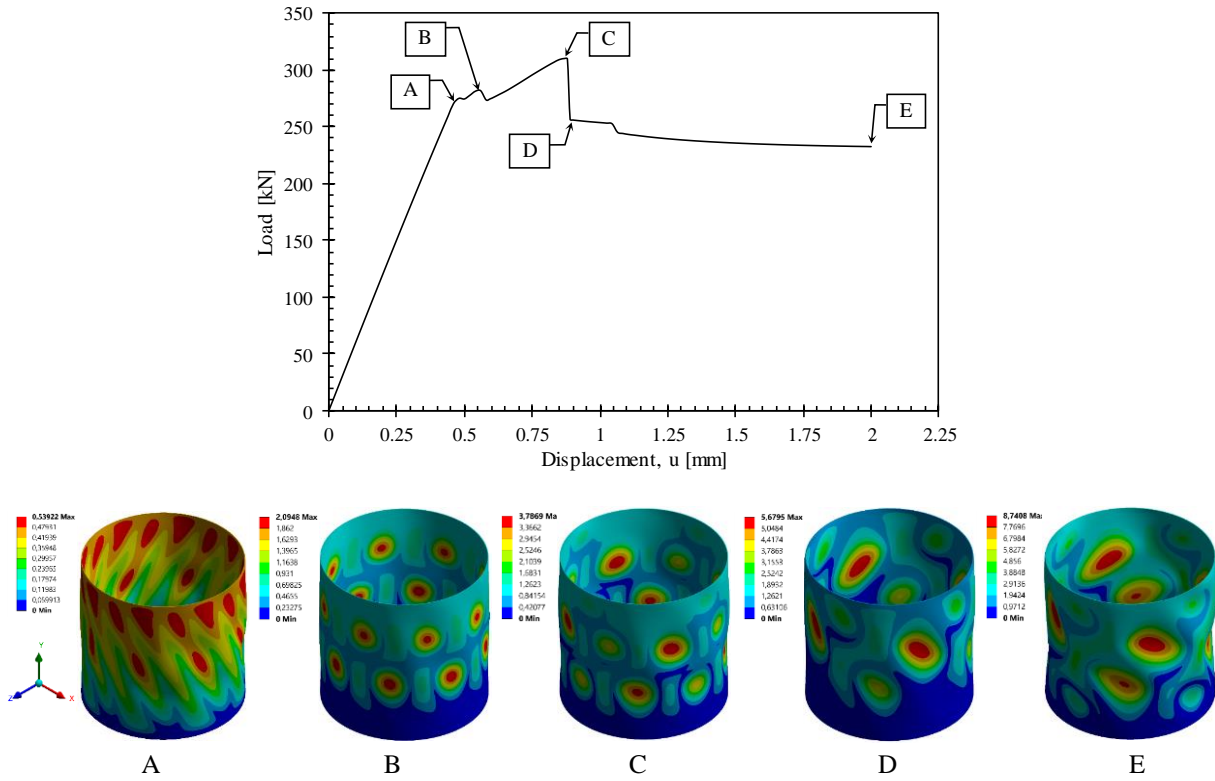


Figure 4. Load-displacement diagram of the imperfect shell with the critical buckling stages.

Change of KDF concerning $\Delta w/t$ is plotted in Figure 5 to evaluate the role of $\Delta w/t$ on the load-bearing capacity of geometrically imperfect cylindrical shells. To perform this task, a shell configuration for which R/t and L/R equal to 100 and 4 is selected, respectively. It is more convenient to divide KDF curve into three distinct regions (Region I, II and III). In Region I, it is seen that even very small $\Delta w/t$ values cause a reduction of about 40% in load-bearing capacity ($KDF \approx 0.6$) of the cylinder. This is because cylindrical shells are a standard structure (membrane stress dominant) and are quite sensitive to imperfections. However, no additional change in KDF is observed until the next region since the imperfection depth does not reach a threshold value to induce extra bending stress in the shell structure.

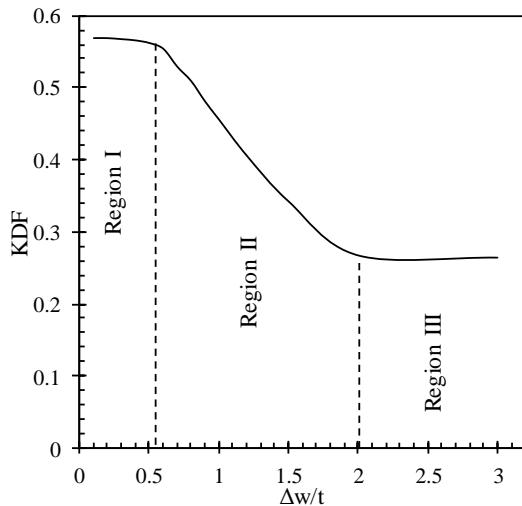


Figure 5. KDF vs $\Delta w/t$ diagram

On the other hand, KDF drops drastically up to Region III due to additional bending effects of the $\Delta w/t$ values. For this reason, Region II at which $\Delta w/t$ varies between 0.6 and 2 may be called a critical interval in terms of torsional Mode-I type imperfection sensitivity (see Figure 5). Beyond this region, KDF reaches a stability region in which no further changes are observed.

Knockdown factor is a multivariate function of whole set of shell parameters such as, R/t , L/R and $\Delta w/t$. However, it is a quite challenging task to produce exact solutions of KDF as a function of the aforementioned shell parameters due to stochastic nature of geometric imperfections. For this reason, it is more practical to demonstrate a scattering of the KDF values for the whole set of shell families, as depicted in Figure 6. In this way, the variation of KDF at a certain shell configuration can be represented depending on the $\Delta w/t$ values. In terms of design perspective, it is more useful to give lower and upper bound equations to evaluate the maximum and minimum KDF values at a particular $\Delta w/t$. Furthermore, it provides an interval for the KDF values to make sure that the shell structure with torsional Mode-I type of geometric imperfection is safe under the action of axial compression. The lower bound may be expressed with a preliminary exponential function, which is found using a trial error approach considering various form of mathematical functions, as the following:

$$(KDF)_{LB} = Ae^{-B\sqrt{\Delta w/t}} \tag{3}$$

Similarly, the upper bound may be expressed with a preliminary power function:

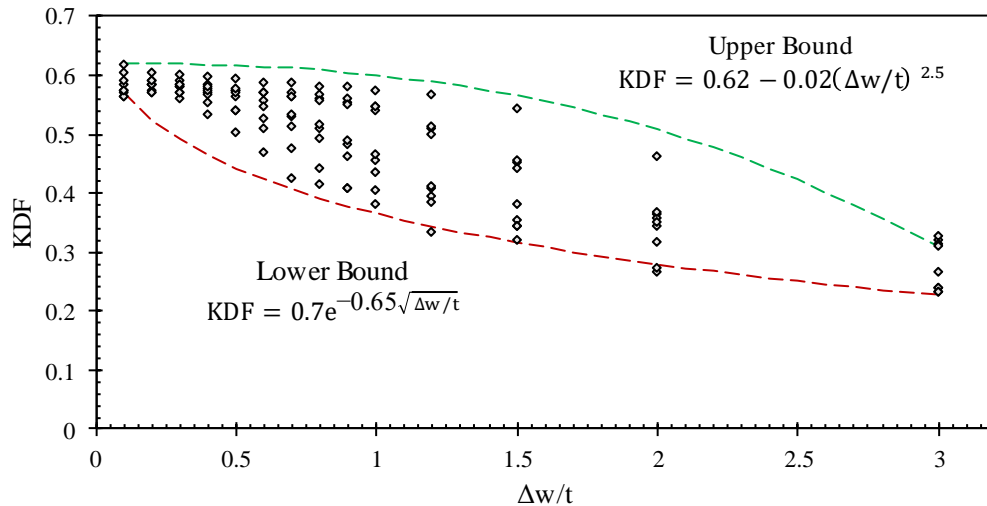


Figure 6. Scattering of the KDF values for the whole set of shell configurations

$$(KDF)_{UB} = C - D(\Delta w/t)^n \quad (4)$$

where A , B , C , D and n are positive real numbers. In this case, proposed expressions give more accurate trend of lower and upper bounds than polynomial or linear functions. Eqs. 3 and 4 predict the limit values of KDF's at a random cylindrical shell configuration regardless of R/t and L/R . The coefficients A , B , C , D and n are estimated using Least Square Method as 0.7, 0.65, 0.62, 0.02 and 2.5, respectively.

4. Conclusions

The current study investigates the influence of torsional Mode-I type of geometric imperfections on the load-bearing capacity of cylindrical shells under axial compression. A parametric study is performed covering a wide range of cylindrical shell configurations. Knockdown factors (KDF's) caused by the geometric imperfections are examined and relevant deformation patterns are illustrated. The results obtained from the current study are highlighted as the followings:

- It is concluded that even an inconsiderable amount of geometric imperfection depth may cause nearly 40% reduction in the load-bearing capacity of the cylindrical shells having a torsional Mode-I type of geometric imperfection.
- It is seen that KDF slightly increases with the increasing values of R/t and L/R . This is an indication of lower imperfection sensitivity to higher values of both R/t and L/R .
- The influence of $\Delta w/t$ on the knockdown factor (KDF) can be characterized by three distinct regions: The first region is accepted to be a plateau indicating the threshold value of $\Delta w/t$ for additional decrement of KDF. The second region is the critical range of the $\Delta w/t$ values. No considerable change in KDF is achieved in the last region.

- The KDF values emerge a stochastic distribution (no visible correlation with the shell parameters) and it is difficult to establish an efficient relationship. However, Eqs. 3 and 4 are proposed to estimate a local minima and maxima of KDF's stochastic distribution as a function of $\Delta w/t$.

Declaration

The authors declared no potential conflicts of interest with respect to the research, authorship, and/or publication of this article. The authors also declared that this article is original, was prepared in accordance with international publication and research ethics, and ethical committee permission or any special permission is not required.

Author Contributions

İ. Kocabaş and H. Yılmaz conceived the study together. İ. Kocabaş supervised the research, analysed the data and drafted / finalized the paper. H. Yılmaz conducted the numerical analysis, contributed to the data analysis, proposals of equations and revised the paper.

Acknowledgement

The authors are greatly thankful to Eskişehir Technical University, Turkey for providing the facilities in developing the paper.

References

1. *Buckling of Steel Shells European Design Recommendations*, ECCS, 2008. ISBN: 978-92-9147-116-4.
2. de Paor, C., K. Cronin, J.P. Gleeson and D. Kelliher, *Statistical characterisation and modelling of random geometric imperfections in cylindrical shells*, Thin-Walled Structures, 2012. **58**: p. 9-17.
3. Kepple, J., M. Herath, G. Pearce, G. Prusty, R. Thomson, and R. Degenhardt, *Improved stochastic methods for modelling imperfections for buckling analysis of composite*

- cylindrical shells*, Engineering Structures, 2015. **100**: p. 385-398.
4. Donnell, L.H., *A new theory for the buckling of thin cylinders under axial compression and bending*, ASME Transactions of the American Society of Mechanical Engineers, 1934. **56**(12): p. 795-806.
 5. Flügge, W., *Die stabilität der kreiszylinderschale*, Ingenieur-Archiv, 1932. **3**: p. 463-506.
 6. Koiter, W.T., *A translation of the stability of elastic equilibrium*. 1970, USA: Stanford University, Department of Aeronautics & Astronautics.
 7. Teng, J.G., X. Lin, J.M. Rotter, and X.L. Ding, *Analysis of geometric imperfections in full-scale welded steel silos*, Engineering Structures, 2005. **27**(6): p. 938-950.
 8. Rotter, J.M., R. Coleman, X.L. Ding, and J.G. Teng, *The Measurement of Imperfections in Cylindrical Silos for Buckling Strength Assessment*, 4th International Conference on Bulk Materials: Storage, Handling and Transportation, 1992, Wollongong, N.S.W., p. 473-479.
 9. Zhang, D., Z. Chen, Y. Li, P. Jiao, H. Ma, P. Ge, and Y. Gu, *Lower-bound axial buckling load prediction for isotropic cylindrical shells using probabilistic random perturbation load approach*, Thin-Walled Structures, 2020. **155**: p. 106925.
 10. Peterson, J.P., P. Seide, and V.I. Weingarten, *Buckling of Thin-Walled Circular Cylinders*, Technical Report, 1968. NASA SP-8007.
 11. Evkin, A., and O. Lykhachova, *Energy barrier method for estimation of design buckling load of axially compressed elasto-plastic cylindrical shells*, Thin-Walled Structures, 2021. **161**: p. 107454.
 12. Kim, S.E. and C.S. Kim, *Buckling strength of the cylindrical shell and tank subjected to axially compressive loads*, Thin-Walled Structures, 2002. **40**(4): p. 329-353.
 13. Wagner, H. N. R., C. Hühne, S. Niemann, K. Tian, B. Wang, and P. Hao, *Robust knockdown factors for the design of cylindrical shells under axial compression: Analysis and modeling of stiffened and unstiffened cylinders*, Thin-Walled Structures, 2018. **127**: p. 629-645.
 14. Wagner, H. N. R., C. Hühne, and M. Janssen, *Buckling of cylindrical shells under axial compression with loading imperfections: An experimental and numerical campaign on low knockdown factors*, Thin-Walled Structures, 2020. **151**: p. 106764.
 15. Wang, B., X. Ma, P. Hao, Y. Sun, K. Tian, G. Li, K. Zhang, L. Jiang, and J. Guo, *Improved knockdown factors for composite cylindrical shells with delamination and geometric imperfections*, Composites Part B, 2019. **163**: p. 314-323.
 16. Wang, B., Z. Shiyang, H. Peng, B. Xiangju, D. Kaifan, C. Bingquan, M. Xiangtao, and C.J. Yuh, *Buckling of quasi-perfect cylindrical shell under axial compression: A combined experimental and numerical investigation*, International Journal of Solids Structures, 2018. **130**(131): p. 232-247.
 17. Mahdy, W.M., L. Zhao, F. Liu, R. Pian, H. Wang, and J. Zhang, *Buckling and stress-competitive failure analyses of composite laminated cylindrical shell under axial compression and torsional loads*, Composite Structures, 2021. **255**: p. 112977.
 18. Zhang, X., and Q. Han, *Buckling and postbuckling behaviors of imperfect cylindrical shells subjected to torsion*, Thin-Walled Structures, 2007. **45**(12): p. 1035-1043.

**Research Article****Harmonic response analysis of elliptically curved thin plates**Oğuzhan Daş^a ^aDokuz Eylul University, Department of Motor Vehicles and Transportation Technologies, Izmir, 35700, Turkey**ARTICLE INFO***Article history:*

Received 27 July 2021

Revised 19 September 2021

Accepted 07 October 2021

Keywords:

Elliptically curved plates

Finite element analysis

Harmonic response

ABSTRACT

In this study, harmonic response analysis of isotropic elliptically curved thin plate structures has been conducted. The structure has been excited by a harmonic load, whose maximum magnitude is 100 N. The structure has been considered under fixed from both straight edges boundary conditions. The effect of the elliptical geometry on the harmonic response of the structure in terms of the critical frequency region, phase angle, stress, and displacement has been examined. For this purpose, the vertex to co-vertex ratio has been varied from 3 to 4 by 0.1 intervals. All analyses have been performed via ANSYS Workbench by employing the Mode Superposition Method. The results indicated that the elliptical geometry has a significant impact on the harmonic response of elliptically curved thin plate structures.

1. Introduction

The vibration behavior of a structure is a significant research field in which researchers conducted various studies to understand the effects of damage [1-3], geometry [4-6], material [7-9], and other parameters [10-17] on this concept. Related to vibrational behavior, the harmonic response is another essential concept for understanding a steady-state response of a structure under sinusoidal loads. The principal interest of the harmonic response analysis is the resonance frequency region since excessive vibrations, stress, displacement, and noise occurs near or at that region. Some studies that cover vibration analysis including the harmonic response of various structures have been briefly presented as follows. Kiral examined the harmonic response of laminated composite beams under various boundary conditions and considering different stacking sequences [18]. Ramesha et al. performed a modal analysis and harmonic response analysis of free-free and ball bearing constrained crankshaft considering 0 -5000 Hz excitation frequency range [19]. Yu et al. conducted both modal and harmonic response analysis of some key components of a ditch device [20]. Zhang et al. employed a harmonic analysis for coupled plate structures by considering the dynamic stiffness method [21]. Jiaqiang et al. measured the harmonic response of a solar dish power generation system

considering the wind-induced vibration [22]. Çeçen and Aktaş performed both modal and harmonic response analyses of carbon fiber laminate reinforced concrete railway sleepers [23]. Rahmani and Moslemi Petrucci examined the nonlinear vibrations and dynamic response of self-excitation of a cantilever nanocomposite tube, which contains flowing fluid. They employed Galerkin Method and Euler-Bernoulli Beam Theory to solve the corresponding Ordinary Differential Equations to evaluate the behavior of the structure [24]. Cruceanu and Sorohan employed the Finite Element Analysis to evaluate the harmonic response of a railway wheelset [25]. Zeng et al. investigated the vibration response characteristics of a cracked rotating compressor blade using the Finite Element Analysis. They measured the impact of the aerodynamic force, angular acceleration, and crack properties on the vibrational characteristics of the compressor blade [26]. Jena et al. performed a dynamic response analysis for fractionally damped beam structures under external loads. They employed Homotopy Analysis Method to evaluate the vibrational response of the beam structure [27]. Gawryluk et al. measured the dynamic response of a composite beam, which rotates at a constant speed due to harmonic excitation. For this purpose, they used the Finite Element Method and an experimental setup [28]. Son et al. performed a shock and harmonic response

* Corresponding author. Tel.: +90-232-632-1248 (139).

E-mail addresses: oguzhan.das@deu.edu.tr (O. Daş)

ORCID: 0000-0001-7623-9278 (O. Daş)

DOI: 10.35860/iarej.975247

© 2021, The Author(s). This article is licensed under the CC BY-NC 4.0 International License (<https://creativecommons.org/licenses/by-nc/4.0/>).

analysis for unmanned aerial vehicle's nose landing gear having air damper. They built a dynamic model which comprises a main mass and a wheel mass that are linked to each other by U-shaped landing gear. They evaluated the harmonic response of the system by considering the ratio between the displacement amplitude and the amplitude of the base excitation [29]. Kumar and Sarangi used the Finite Element Method to conduct the harmonic response analysis for carbon nanotube-reinforced functionally graded beam structure. For this purpose, they considered X, Δ, and O type functionally graded carbon nanotube beam structures modelled in ANSYS [30]. Praharaj and Datta investigated the dynamic behavior of thin plate structures subjected to a moving load and resting on a fractional viscoelastic foundation. They examined the effects of the foundation parameters, fractional-order derivative, acceleration, and velocity of the subjected moving load on the dynamic response of the structure [31]. Abed and Majeed measured the impact of the boundary conditions on the harmonic response of cross-ply and angle-ply composites having different materials and thicknesses [32]. Aghazadeh investigated the dynamics of fluid conveying axially functionally graded pipes. For this purpose, a higher-order shear deformation theory is employed to satisfy zero-shear conditions to obtain realistic results [33]. Liu et al. examined the dynamic response of curvilinearly stiffened plates by employing the Finite Element Method. They measured the influence of the temperature on the dynamic behavior of the isotropic structure [34]. Alavi and Eipakchi evaluated the dynamic response of viscoelastic annular sector plates subjected to asymmetric impulsive and harmonic transverse force. They used Hamilton's principle to derive the equation of the motion by considering the first-order shear deformation theory [35]. Heydarpour et al. developed a differential quadrature method based on the Heaviside function and a non-uniform rational B-spline-based multi-time integration scheme to examine the nonlinear dynamic response of laminated composite cylindrical shells. They measured the impacts of the geometrical properties, impulse loading types, time durations, loading location, and the number of layers on the nonlinear dynamic response of the structure [36]. Yulin et al. investigated the dynamic response of a three-beam system having intermediate elastic connections, under mass-spring, and subjected to a moving load. For this purpose, they employed the Finite Sine-Fourier Transform to obtain the dynamic ordinary differential equations, which are solved to evaluate the dynamic response of the structure [37]. Eyvazian et al. investigated the dynamics of nanocomposite cylindrical shells subjected to a moving harmonic load. For this purpose, they employed the first-order shear deformation theory in accordance with the nonlocal strain gradient theory to obtain the equations of

motion of the cylindrical nanoshell resting on an elastic foundation [38]. Oke and Khulief performed a dynamic response analysis for fluid conveying composite pipes whose inner wall has a surface discontinuity. For this purpose, they employed Hamilton's principle and wavelet-based Finite Element Method [39].

Elliptically curved plate structures are employed in various engineering fields such as aerospace, automotive, ships, etc. Therefore, investigating the harmonic response of elliptical plates considering their geometry can provide significant knowledge to these fields. To the best of the author's knowledge, although numerous studies address the harmonic response of various structures, the harmonic response of elliptically curved structures has not been covered. Besides, the effect of the structure's geometry on the harmonic response has not been measured in the literature.

In this study, the harmonic response of the isotropic elliptically curved thin plates has been investigated. Besides, the effect of the structure's geometry on the harmonic response has been examined by varying the co-vertex – vertex ratio. For these purposes, the structures have been modeled via the commercial finite element software ANSYS [40]. The co-vertex – vertex ratio values have been ranged from 3 to 4 by 0.1 intervals. The harmonic response analyses have been conducted by considering a sinusoidal load, which alternates between 0-100N. The damping ratio has been chosen as $\xi=0.02$ [18]. The analysis results have been interpreted by considering the variation of the resonance frequency, maximum stress, and deformation at the resonance frequency. The contributions of the study can be expressed as follows:

- Investigating the free vibration and harmonic response characteristics of an elliptically curved thin plate structure.
- Examining the effect of the structural dimensions on the first two natural frequencies of the elliptically curved thin plate structure.
- Measuring the impact of the co-vertex – vertex ratio of the elliptically curved plate on the phase angle and critical frequency value where excessive vibrations occur.
- Measuring the impact of the co-vertex – vertex ratio of the elliptically curved plate on the maximum response and maximum stress occurred due to the subjected harmonic load.

2. Harmonic Response Analysis

The harmonic response analysis has been evaluated considering the governing equation of motion of the system, which is

$$M\{\ddot{q}\} + \dot{C}\{\dot{q}\} + K\{q\} = \{F\} \quad (1)$$

where M , C , and K are the mass, damping, and stiffness

matrix respectively. $\{q\}$ represents the generalized displacement vector including in-plane and out-of-plane displacements [41] and F is the harmonic (sinusoidal) force which can be written in complex notation as:

$$F = F_{max} e^{j\alpha} e^{j\omega t} \quad (2)$$

where ω and α is the excitation frequency and the phase angle of the applied force, respectively. The response of a system is also harmonic, which can be defined as:

$$y = y_{max} e^{j\eta} e^{j\omega t} \quad (3)$$

where η is the phase angle of the response. It can be concluded from the Equations (2) and (3) the phase angles of the load and response can be different, while the frequencies should be the same. Note that the phase shift of the force may exist if multiple loads are applied in different phase angles. Besides, the displacement phase shift may be present in the existence of damping or applied forces. [42] The mass, damping, and stiffness matrices can be evaluated by employing the Classical Plate Theory. The corresponding mathematical expressions and considered assumptions can be found in any textbook [41].

The solution of the governing equation given in Equation 1 in the presence of harmonic loads is:

$$(-\omega^2 M + j\omega C + K)\{y\} = \{F\} \quad (4)$$

Following the brief harmonic response theory given above, the harmonic response analysis of elliptically curved thin plates has been conducted via ANSYS Workbench 18.2 software. For this purpose, a number of 1000 SHELL181 elements have been considered since the SHELL181 element satisfies the assumptions and required degrees of freedom for a thin structure [41]. As seen from Figure 1, the structure has fixed from both straight edges. A distributed harmonic force with 100 N maximum magnitude and 0° phase angle has been applied. To measure the effects of the structural geometry on the harmonic response, the ratio of the vertex-co-vertex (R_c) has been increased from 3 to 4 by considering 0.1 intervals. The thickness of the structure is remained constant everywhere and is taken as 1.5 mm. As seen from Figure 2, other geometrical parameters have been considered as independent and constant values. Table 1 presents the considered material properties [41] of the structure to perform harmonic analysis. Before proceeding with the harmonic response analysis, the first two natural frequency values of all structures have been evaluated by performing a free vibration analysis. The results have been evaluated by considering the 0-1500 Hz frequency range to include the second natural frequency values (see Table 2) of all considered structures.

As the solution method, the Mode Superposition Method has been considered since it uses the eigenvectors of the free vibration problem providing accurate results and costs less time when compared with the Full Method [41].

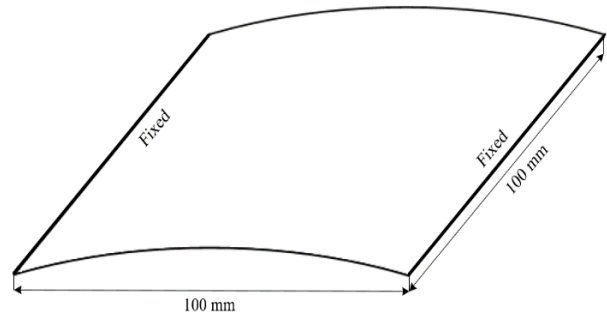


Figure 1. Elliptically curved thin plate

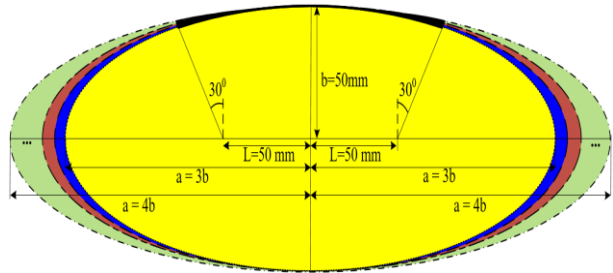


Figure 2. Dimensions of the elliptically curved plate structure

Table 1. Material properties of the elliptically curved thin plate

Property	Symbol	Value
Modulus of Elasticity (GPa)	E	200
Shear Modulus (GPa)	G	76.9
Density (kg/m^3)	ρ	7850
Poisson's Ratio	ν	0.3

Afterward, the frequency response and the corresponding phase angle responses have been evaluated for each structure to determine the most critical frequency and corresponding phase angle values for the structure. By using these critical values, the maximum stress and displacement have been obtained. The evaluated results have been interpreted with respect to the change in the R_c .

3. Numerical Results

Table 2 gives the variation of the first two natural frequencies of the elliptically curved structure with respect to changes in respect to the ratio of the vertex to co-vertex (R_c) of the structure.

It is seen from Table 2 that the first two natural frequencies decrease as the R_c value increases. Besides the numerical difference between the first and the second natural frequencies becomes smaller for higher R_c values. Such differences take place due to the difference in the stiffness characteristics of the elliptically curved structure.

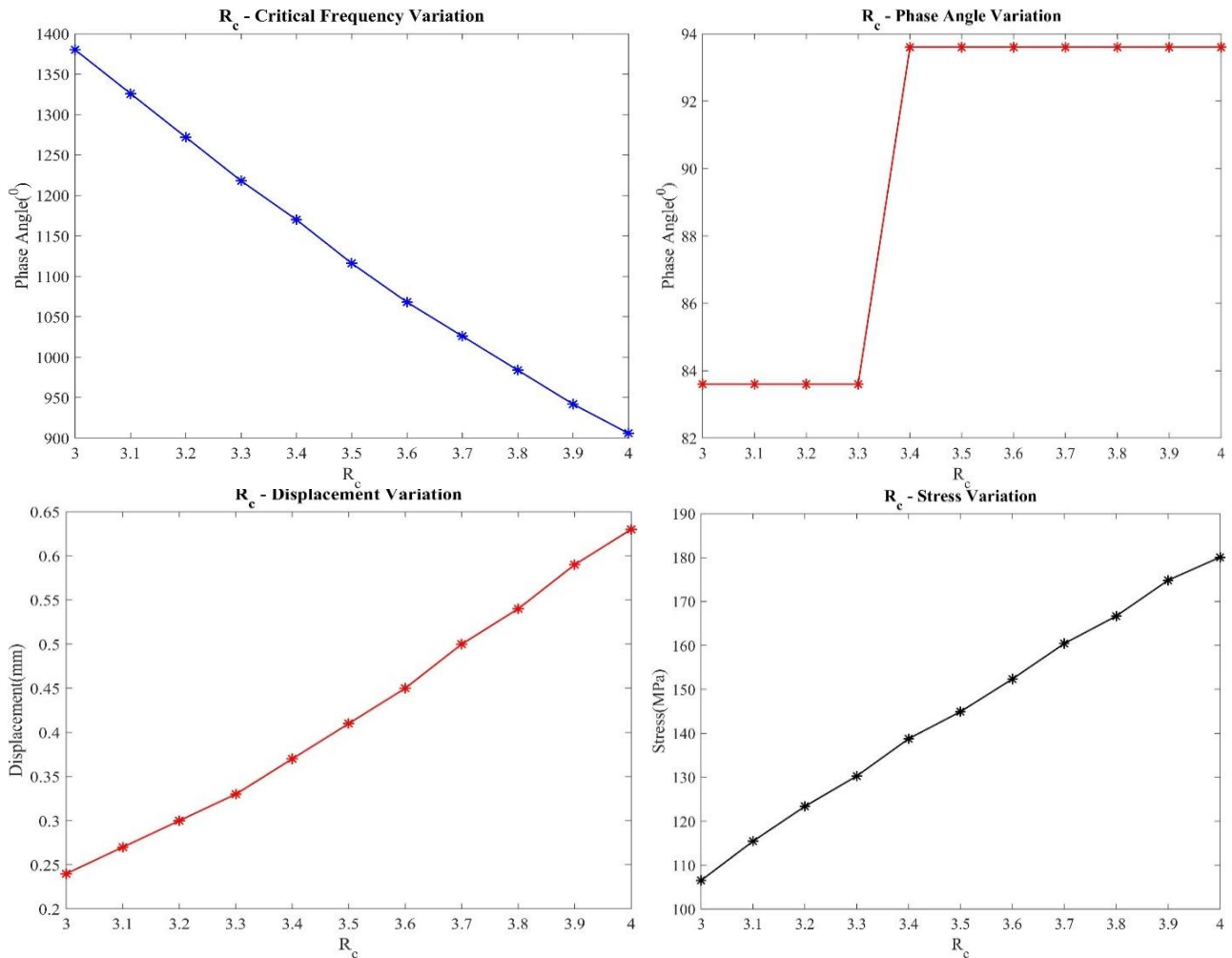


Figure 3. Variation of the fundamental frequency, phase angle, stress, and displacement with respect to R_c

Table 2. The variation of the first two natural frequencies of elliptically curved thin plate structures with respect to R_c

R_c	3.0	3.1	3.2	3.3
Freq.1 (Hz)	977.35	973.02	968.97	965.19
Freq.2 (Hz)	1380.90	1328.20	1274.70	1221.50
R_c	3.4	3.5	3.6	3.7
Freq.1 (Hz)	961.67	958.39	955.06	952.21
Freq.2 (Hz)	1169.40	1119.10	1070.90	1025.20
R_c	3.8	3.9	4.0	
Freq.1 (Hz)	949.54	941.61	903.63	
Freq.2(Hz)	982.12	947.04	977.31	

Figure 3 gives the variation of the critical frequency, phase angle, stress, and displacement responses of elliptically curved thin plate structure with respect to R_c values. It is seen from Figure 3 that the critical frequency of the elliptically curved structure decreases as the R_c value increases. Besides, the critical frequency has been evaluated close to the second natural frequency for R_c values ranged between 3-3.8. However, it approximates the fundamental frequency for $R_c=3.9$ and 4.

As seen from Figure 3 that the difference in the critical frequency is almost linear. Since the damping ratio has been considered as $\xi=0.02$, a difference in phase angle has

occurred. The phase angle has been evaluated as 83.6° for 3-3.3 R_c values, while it has been obtained as 93.6° for the remained R_c values. In other words, the maximum response occurred at the critical frequency value takes place slightly earlier than the fundamental or the second frequency for R_c values lower than and equal to 3.3 when compared with those frequencies for R_c values bigger than 3.3.

It can be interpreted that the phase angle is not affected considerably by the co-vertex – vertex ratio since the difference is small.

Figures 4 and 5 show the bode diagram of the displacement-frequency response and the phase difference between the response and the applied force for $R_c=3$ and 4 respectively. It is seen that the critical response for the structure with $R_c=3$ has been obtained for the frequency region close to the second natural frequency. On the other hand, the region becomes closer to the fundamental frequency for the structure having $R_c=4$ ratio. As also seen in Figure 3, the phase angle of the structure having $R_c=3$ ratio is smaller than those of the structure with $R_c=4$.

The maximum stress and displacement values have been evaluated for the excitation frequency equal to the fundamental frequency.

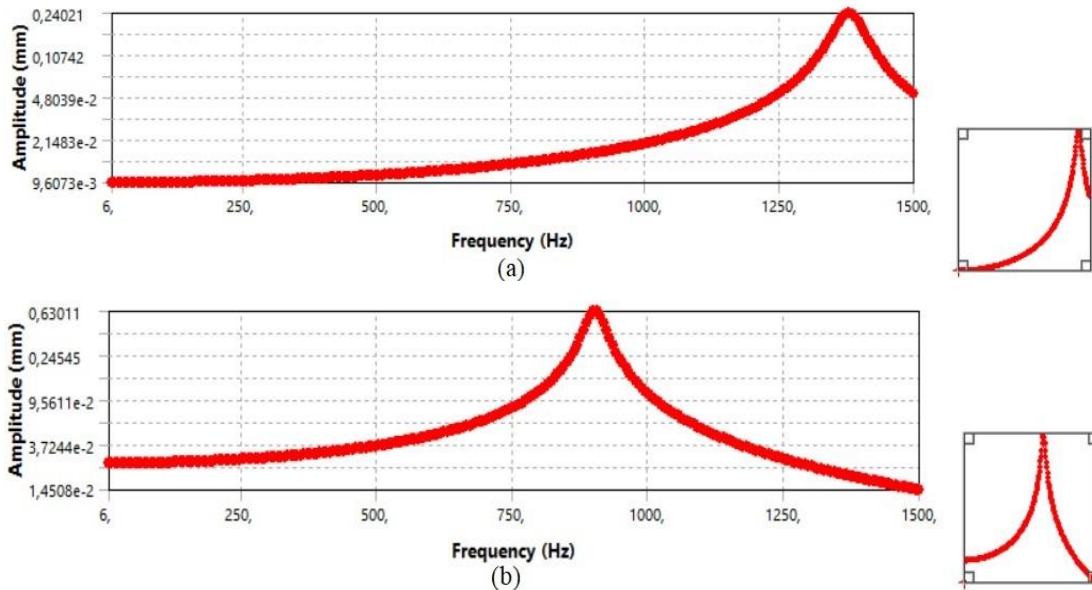


Figure 4. The displacement-frequency bode diagram of the elliptically curved thin plate having (a) $R_c=3$ and (b) $R_c=4$ ratio

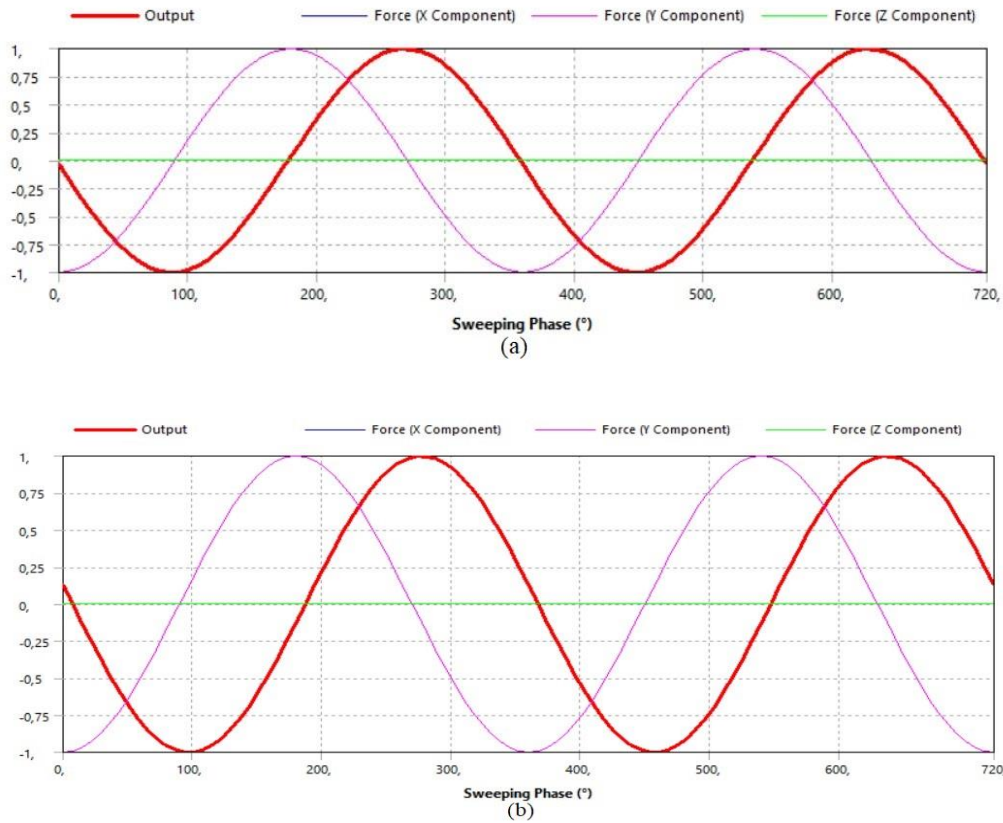


Figure 5. The phase shift between the response and applied force of the elliptically curved thin plate having (a) $R_c=3$ and (b) $R_c=4$ ratio

The damping ratio has been taken as $\xi=0.02$ [18] to prevent the structure from resonance in which failure may occur due to excessive displacement response. As seen in Figure 3, the maximum stress increases as the R_c increases. Similarly, the maximum displacement increases up to 2.5 times as the R_c value reaches 4 from 3. Both displacement and stress values vary almost in a linear form in accordance with the co-vertex – vertex ratio. The

maximum stress value is obtained for $R_c=4$ as 180.07 MPa while the minimum stress is obtained for $R_c=3$ 106.54 MPa. The maximum displacement value is observed for $R_c=4$ as 0.64 mm whereas the minimum displacement is evaluated for $R_c=3$ as 0.24 mm.

As seen in Figures 6 and 7, the maximum displacement and stress locations are the same for both $R_c=3$ and 4. On the other hand, the displacement and stress distributions

vary. It is seen from Figures 6 and 7 that at the most critical frequency, a wider area has been stressed and displaced for the structure with $R_c=4$ ratio when compared with that of having $R_c=3$ ratio. The behavior of the structure shown in Figure 6 also represents the second mode shape for $R_c=3$ and the first mode shape for $R_c=4$. Therefore, it can be concluded that the maximum stress and displacement occurred in the region where the highest displacements have been observed in the relevant mode shape.

Considering the stress and displacement regions shown in Figures 6 and 7, it is seen that both displacement and stress values in locations close to the fixed edge differ for structures with $R_c=3$ and $R_c=4$. It is seen that these values are higher for the structure having $R_c=3$ than that of $R_c=4$. A similar interpretation can be made for the width of the displacement and stress regions. As seen from Figures 6 and 7 the displacement and stress regions of the structure having $R_c=3$ ratio are narrower than these of the structure having $R_c=4$ ratio regardless of the magnitude of the stress and displacement. Therefore, it can be concluded that the

difference in co-vertex – vertex ratio does not only affect the maximum stress and displacement values, but also the distribution of the stress and displacement along with the structure.

4. Conclusions

In this study, harmonic response analysis of elliptically curved thin plate structure has been conducted. The effect of the vertex to co-vertex ratio on the harmonic response has been examined considering the critical frequency region, phase angle, stress, and displacement. All analyses have been conducted by considering the Mode Superposition Method. According to the results of the study, the following conclusions can be drawn.

- The first two natural frequencies of elliptically curved thin plate structures decrease as the vertex to the co-vertex ratio (R_c) increases. Besides, the numerical difference between those two frequencies become smaller as the R_c value increases.

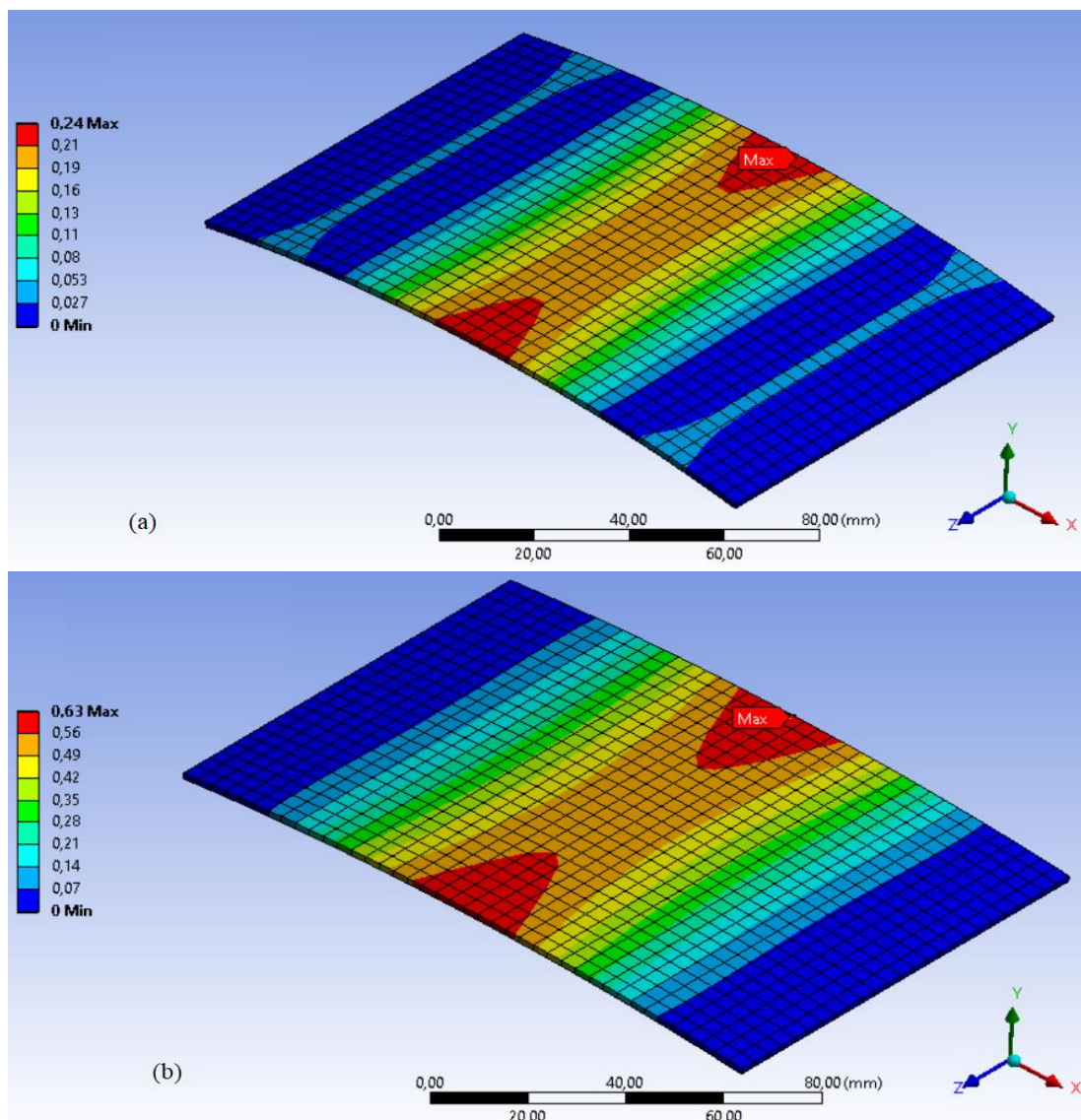


Figure 6. Critical displacement response of the elliptically curved thin plate having (a) $R_c=3$ and (b) $R_c=4$ ratio

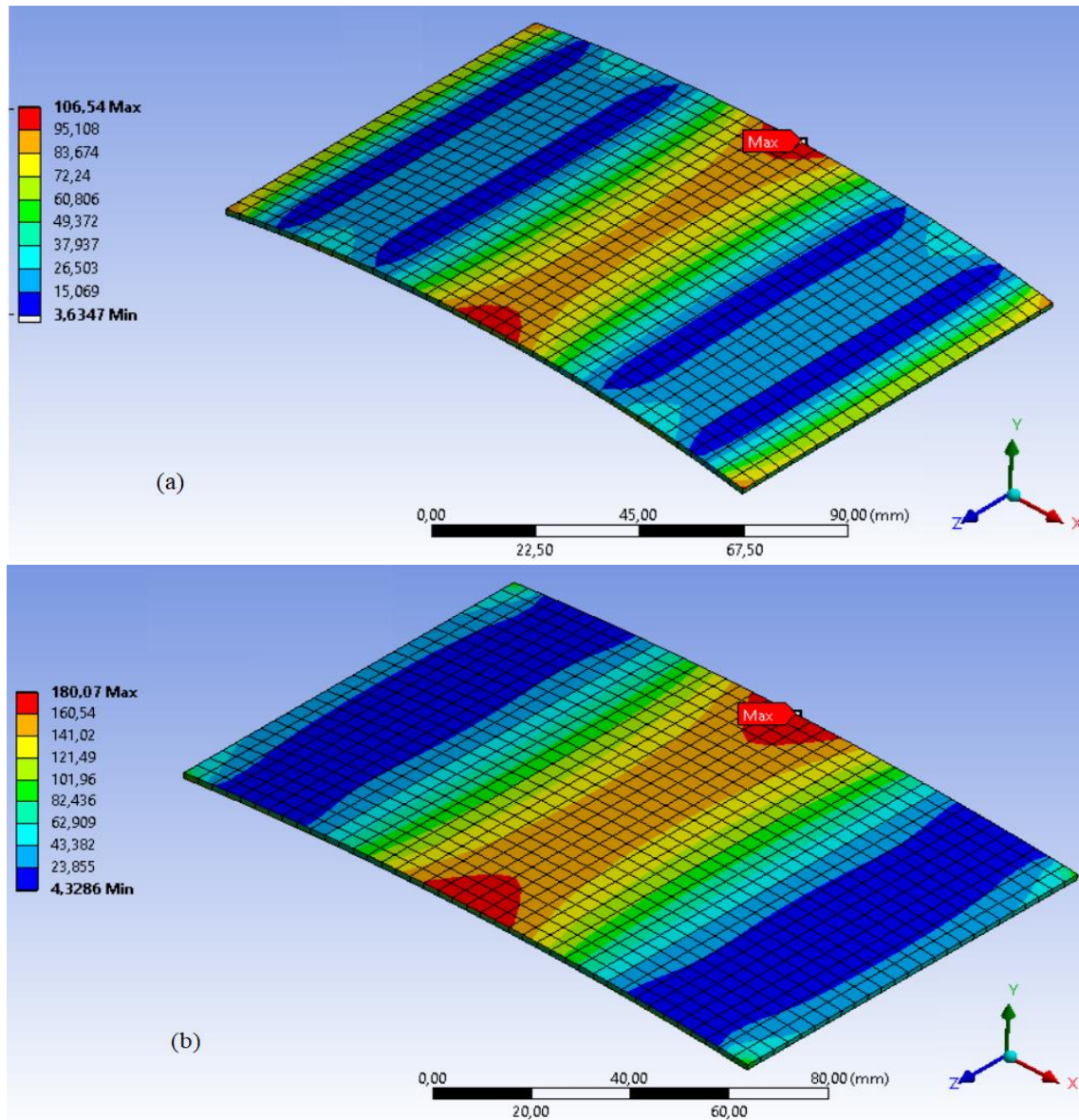


Figure 7. Critical stress distribution of the elliptically curved thin plate having (a) $R_c=3$ and (b) $R_c=4$ ratio

- The critical frequency, which causes the highest stress and displacement values, decreases as the R_c ratio increases. Besides, the critical frequency region approximates the second natural frequency for $R_c=3$ -3.8 values whereas it approaches the fundamental frequency for $R_c=3.9$ and 4.0.
- The phase angle increases from 83.6 to 93.6 for R_c values higher than 3.3
- The maximum stress increases with respect to the increment in R_c values. Likewise, the maximum displacement increases up to 2.5 times as the R_c value increases from 3 to 4.
- The maximum stress and displacement are located in the region where the highest displacement of the relevant mode shapes has been observed.
- The numerical results indicate that the variation of the maximum stress, maximum displacement, and the natural frequency values are almost in a linear form in accordance with the co-vertex – vertex ratio. On the other hand, although it seems that the phase angle changes abruptly as the co-vertex – vertex ratio reaches 3.4, the difference is considerably small. Therefore, it can be concluded that the phase angle is not affected significantly by the change in the co-vertex – vertex ratio.
- It is concluded that the co-vertex – vertex ratio also affects the stress and displacement regions of the structure. The stress and displacement values that occurred near the fixed edges are evaluated higher for the structure having $R_c=3$ than that of $R_c=4$. Besides, the stress and displacement regions of the structure having $R_c=3$ ratio are narrower than those of the structure having $R_c=4$ ratio regardless of both displacement and stress values.
- The future works may comprise the impacts of the characteristics of the curvature and dimensions of the

structure on the harmonic response of curved structures. Besides, the effects of the fiber orientation on the response of the structure may be examined by taking the plate structure as a composite one.

Declaration

The author declared no potential conflicts of interest with respect to the research, authorship, and/or publication of this article. The author also declared that this article is original, was prepared in accordance with international publication and research ethics, and ethical committee permission or any special permission is not required.

Author Contributions

Oğuzhan Daş: Conceptualization and management of the study, data collection and analysis, interpretation of results, writing the draft and final version of the manuscript.

References

1. Minh, P.P., Do, T. V., Duc, D. H., and Duc, D. N, *The stability of cracked rectangular plate with variable thickness using phase field method*. Thin-Walled Structures, 2018. **129**: p. 157-165.
2. Gonenli, C., and Das, O., *Effect of crack location on buckling and dynamic stability in plate frame structures*. Journal of the Brazilian Society of Mechanical Sciences and Engineering, 2021. **43**: 311.
3. Marjanović, M., and Vuskanović, D., *Layerwise solution of free vibrations and buckling of laminated and sandwich plates with embedded delaminations*. Composite Structures, 2014. **108**: p.9-20.
4. Javed, S., Viswanathan, K. K., Nurul Izyan, M. D., Aziz, Z. A., and Lee, J. H., *Free vibration of cross-ply laminated plates based on higher-order shear deformation theory*. Steel and Composite Structures, 2018. **26**(4): p.473-484.
5. Das, O., Ozturk, H., and Gonenli, C., *Finite element vibration analysis of laminated composite parabolic thick plate frames*. Steel and Composite Structures, 2020. **35**(1): p.43-59.
6. Hongwei, G., Hong, Z., and Xiaoying, Z., *Numerical manifold method for vibration analysis of Kirchhoff's plates of arbitrary geometry*. Applied Mathematical Modelling, 2019. **66**: p.695-727.
7. Belarbi, M., Tati, A., Ounis, H., and Khechai, A., *On the free vibration analysis of laminated composite and sandwich plates: A layerwise finite element formulation*. Latin American Journal of Solids and Structures, 2017. **14**(12): p.2265-2290.
8. Vaghepour, H., and Arvin, H., *Nonlinear free vibration analysis of pre-actuated isotropic piezoelectric cantilever nano-beams*. Microsystem Technologies, 2019. **25**: p.4097-4110.
9. Kaddar, M., Kaci, A., Bousahla, A. A., Tounsi, A., Bourada, F., Tounsi, A., Beida, E. A. A., Al-Osta, M. A., *A study on the structural behaviour of functionally graded porous plates on elastic foundation using a new quasi-3D model: Bending and free vibration analysis*. Computers and Concrete, 2020. **25**(1): p. 37-57.
10. Malekzadeh, K., and Sayyidmousavi, A., *Free vibration analysis of sandwich plates with a uniformly distributed attached mass, flexible core and different boundary conditions*. Journal of Sandwich Structures and Materials, 2010. **12**(6): p.709-732.
11. Demirtas, S., and Ozturk, H., *Effective mode shapes of multi-storey frames subjected to moving train loads*. Coupled Systems Mechanics, 2020. **9**(4): p.311-323.
12. Vinyas, M., *A higher-order free vibration analysis of carbon nanotube-reinforced magneto-electro-elastic plates using finite element methods*. Composites Part B: Engineering, 2021. **158**: p.286-301.
13. Safarpour, M., Rahimi, A. R., and Alibeigloo, A., *Static and free vibration analysis of graphene platelets reinforced composite truncated conical shell, cylindrical shell, and annular plate using theory of elasticity and DQM*. Mechanics Based Design of Structures and Machines, 2020. **48**(4): p.496-524.
14. Rahimi, A., Alibeigloo, A., and Safarpour M., *Three-dimensional static and free vibration analysis of graphene platelet reinforced porous composite cylindrical shell*. Journal of Vibration and Control, 2020. **26**(19-20): p.1627-1645.
15. Sahla, M., Saidi, H., Draiche, K., Bousahla, A. A., Bourada, F., Tounsi, A., *Free vibration analysis of angle-ply laminated composite and soft core sandwich plates*. Steel and Composite Structures, 2019. **33**(5): p.663-679.
16. Yan, Y., Liu, B., Xing, Y., Carrera, E., and Pagani, A., *Free vibration analysis of variable stiffness composite laminated beams and plates by novel hierarchical differential quadrature finite elements*. Composite Structures, 2021. **274**: 114364.
17. Bidgoli, E. M. R., and Arefi, M., *Free vibration analysis of micro plate reinforced with functionally graded nanoplatelets based on modified strain-gradient formulation*. Journal of Sandwich Structures and Materials, 2021. **23**(2), p.436-472.
18. Kıral, Z., *Harmonic response analysis of symmetric laminated composite beams with different boundary conditions*. Science and Engineering of Composite Materials, 2014. **21**(4): p.559-569.
19. Ramesha, C. M., Abhijith, K. G., Singh, A., Raj, A., and Naik, C. S., *Modal analysis and harmonic response analysis of a crankshaft*. International Journal of Emerging Technology and Advanced Engineering, 2015. **5**(6): 323-327.
20. Yu, Y., Zhang, S., Li, H., Wang, X., and Tiang, Y., *Modal and harmonic response analysis of key components of ditch device based on ANSYS*. Procedia Engineering, 2017. **174**: p.956-964.
21. Zhang, C., Jin, G., Ye, T., and Zhang, Y., *Harmonic response analysis of coupled plate structures using the dynamic stiffness method*. Thin-Walled Structures, 2018. **127**: p.402-415.
22. Jiaqiang, E., Liu, G., Liu, T., Zhang, Z., Zuo, H., Hu, W., and Wei, K., *Harmonic response analysis of a large dish solar thermal power generation system with wind-induced vibration*. Solar Energy, 2019. **181**: p.116-129.
23. Çeçen, F., and Aktaş, B., *Modal and harmonic response analysis of new CFRP laminate reinforced concrete railway sleepers*. Engineering Failure Analysis, 2021. **127**: 105471.
24. Rahmani, M., and Moslemi Petruđi, A., *Nonlinear vibration and dynamic response of nano composite conical tube by conveying fluid flow*. International Advanced Researches

- and Engineering Journal, 2020. **4**(3): p.180-190.
25. Cruceanu, I. C., and Sorohan, S., *Determination of the harmonic response of a railway wheelset using the finite element analysis method*. Procedia Manufacturing, 2020. **46**: p.173-179.
 26. Zeng, J., Chen, K., Ma, H., Duan, T., and Wen, B., *Vibration response analysis of a cracked rotating compressor blade during run-up process*. Mechanical Systems and Signal Processing, 2019. **118**: p.568-583.
 27. Jena, R. M., Chakravety, S., and Jena, S. K., *Dynamic response analysis of fractionally damped beams subjected to external loads using homotopy analysis method*. Journal of Applied and Computational Mechanics, 2019. **5**(2); p.355-366.
 28. Gawryluk, J., Mitura, A., and Teter, A., *Dynamic response of a composite beam rotating at constant speed caused by harmonic excitation with MFC actuator*. Composite Structures, 2019. **210**: p. 657-662.
 29. Son, L., Surya, M., Bur, M., Ubaidillah, U., and Dhelika, R., *Shock and harmonic response analysis of UAV nose landing gear system with air damper*. Cogent Engineering, 2021. **8**(1): 1905231.
 30. Kumar, M., and Sarangi, S. K., *Harmonic response of carbon nanotube reinforced functionally graded beam by finite element method*. Materials Today: Proceedings, 2021. **44**(6): p.4531-4536.
 31. Praharaj, R. K., and Datta, N., *Dynamic response of plates resting on a fractional viscoelastic foundation and subjected to a moving load*. Mechanics Based Design of Structures and Machines, 2020. p. 1-16.
 32. Abed, Z. A. K., and Majeed, W. I., *Effect of boundary conditions on harmonic response of laminated plates*. Composite Materials and Engineering, 2020. **2**(2): p.125-140.
 33. Aghazadeh, R., *Dynamics of axially functionally graded pipes conveying fluid using a higher order shear deformation theory*. International Advanced Researches and Engineering Journal, 2021. **5**(2): p.209-217.
 34. Liu, J., Fei, Q., Wu, S., Zhang, D., and Jiang, D., *Dynamic response of curvilinearly stiffened plates under thermal environment*. Journal of Mechanical Science and Technology, 2021. **35**: p.2359-2367.
 35. Alavi, S. H., and Eipakchi, H., *An analytical approach for dynamic response of viscoelastic annular sector plates*. Mechanics of Advanced Materials and Structures, 2021. p. 1-17.
 36. Heydarpour, Y., Mohammadzaheri, M., Ghodsi, M., Soltani, P., Al-Jahwari, F., Bahadur, I., and Al-Amri, B., *A coupled DQ-Heaviside-NURBS approach to investigate nonlinear dynamic response of GRE cylindrical shells under impulse loads*. Thin-Walled Structures, 2021, **165**: 107958.
 37. Yulin, F., Lizhong, J., and Zhou, W., *Dynamic response of a three-beam system with intermediate elastic connections under a moving load/mass-spring*. Earthquake Engineering and Vibration, 2020, **19**(2): p.377-395.
 38. Eyvazian, A., Shahsavari, D., and Karami, B., *On the dynamic of graphene reinforced nanocomposite cylindrical shells subjected to a moving harmonic load*. International Journal of Engineering Science, **154**: 103339.
 39. Oke, W. A., and Khulief, Y. A., *Dynamic response analysis of composite pipes conveying fluid in the presence of internal wall thinning*. Journal of Engineering Mechanics, 2020, **146**(10): 04020118.
 40. Ansys® Training Manual [cited 2021 21 July], Available from: http://www.eng.lbl.gov/~als/FEA/ANSYS_V9_INFO/Workbench_Simulation_9.0_Intro_3rd_Edition/ppt/AWS90_C h10_Harmonic.ppt.
 41. Petyt, M., *Introduction to Finite Element Vibration Analysis*. 2010, USA: New York.
 42. Ansys® Workbench, Release 18.2, Harmonic Response Analysis.



Research Article

Explicit dynamics finite element analyses of asymmetrical roll bending process

Tuncay Kamaş^{a,*}  and Müfit Sarıkaya^a 

^aAkyapak Makina A.Ş Research and Development Center. Hasanağa Osb Mah. Hosab Sanayi Cad. No:62 Nilüfer / Bursa, Türkiye

ARTICLE INFO

Article history:

Received 24 May 2021

Revised 10 September 2021

Accepted 14 October 2021

Keywords:

Elliptically curved plates

Finite element analysis

Harmonic response

ABSTRACT

In this article, results obtained from a preliminary study that contains a set of explicit dynamics finite element analyses of a metal plate bending process are presented through 3D asymmetrical three roller models. ANSYS Ls-Dyna explicit dynamics finite element (ED-FEA) preprocessor and solver were used to carry out dynamic simulations. Explicit dynamics of a low-velocity process such as the roll-bending of a metal plate is a computationally expensive method. Since plastic deformation occurs on the plate in addition to elastic flexure to eventually possess a circular geometry, the plate material is considered a non-linear material. In this particular study, an aluminum plate was modeled with the Bilinear Kinematic Hardening model including plasticity parameters such as the tangent modulus. A very significant parameter called the mass scaling factor was taken into account to be able to define a specific time-step that was used to determine the computation time interval and the total temporal cost. However, exaggerated reduction of the computation time results in unphysical consequences. The results were presented before and after redesigning the lower and side rolls having a convex geometry and the peripheral velocity of upper roll rotation was decreased to minimize the distortion that occurred on the pre-bent side walls of the aluminum plate.

1. Introduction

In energy and civil engineering fields, the metal pipe industry plays a significant role and via this industry, large-diameter circular pipes can be produced with a single weld bead. The pipelines are required to flawlessly convey liquid or gas without any leakage to a long distance thanks to new technological developments on plate bending process in recent decades. Three roll pyramids [1,2] and asymmetric machines [3–5] and four roll machines [6,7] have been developed to bend plates into cylinders, tanks, and pipes. Pipe, tank, or any large-sized cylindrical metal product manufacturers commonly choose four roll plate bending machines (Figure 2) because they have better efficiency compared to three roller machines. Four roll plate bending machines can have different operation modes to be able to carry out versatile functions with two independent side rolls that can be swung upward and downward and be pivoted by a wing to be suitably located for pre-bending and bending processes.

In the literature, many outstanding theoretical and experimental researches [2,8–13] have been performed to develop analytical and empirical models as well as FEA

models regarding three-roller and four-roller machines. Gandhi and Raval [2] discussed three analytical concepts for pyramid type three-roller bending process and proposed an empirical model to estimate the top roller position explicitly as a function of desired (final) radius of curvature for three-roller bending considering the contact point shift at the bottom roller plate interfaces. Tailor et-al [11] investigated the effects of top roller and of rolling speed on bending quality by using an explicit dynamic FEA model in Hypermesh/Ls-Dyna. The four roll plate bending procedures in one pass using one of the side rolls without pre-bending have been modeled more widely asymmetric-three roller models [3,5]. Gavrilesco et al. [14,15] attempted to analytically and numerically model a pyramid three roll bending process. They utilized a 2-D model in a commonly known commercial FEA software, LS-DYNA, alike many other metal-forming researchers [4,16], in the ANSYS Workbench Graphical User Interface (GUI). They also developed an analytical model to predict the vertical displacement of the inner roller to obtain the desired curvature by using geometrical and deformation compatibilities. In addition, they developed

* Corresponding author. Tel.: +90 224 280 75 00; Fax: +90 (224) 280 75 01.
E-mail addresses: tkamas@akyapak.com (T. Kamas), ms@akyapak.com (M. Sarıkaya)
ORCID: 0000-0002-4623-5732 (T. Kamas), 0000-0002-0413-6146 (M. Sarıkaya)
DOI: 10.35860/iarej.934544

© 2021, The Author(s). This article is licensed under the CC BY-NC 4.0 International License (<https://creativecommons.org/licenses/by-nc/4.0/>).

another mathematical procedure to estimate the bending force. For validation, they compared analytical model results with FEA results. Authors attempted to estimate the vertical displacement versus inner radii of the plate and versus the bending forces. In the beginning of the parametric study conducted with S235JR and S275JR steel materials at various thicknesses and the inner roller at various vertical displacements, they did not have a precise predictive model, however, the loop in the algorithm using the regression models increased the precision further in each iteration.

Fu et-al [10] developed analytical model serving for investigating the three-roll bending forming process including spring-back effects of WELDOX900 material and developed an analytical and FEA models well agreed with the experiments. They developed created 3-D FEA models to bend a plate into a semi-circular workpiece. They also presented another mathematical formula for the vertical displacement of the inner roller with unloaded radius after spring-back [17]. The spring-back radius and angle were also calculated in that study. They studied different three-roll bending machine models that had rollers with different sizes in ABAQUS software which was confirmed to be an optimum tool by experiments.

Feng & Champlaud [4] created both analytical and dynamic numerical models of an asymmetric three-roll bending process by using ANSYS/LS-DYNA [18], which is a commercial finite element analysis (FEA) software, and they analyzed the explicit FEA results by comparing them with experimental results.

Taking the heat into account, Quan et al. [16,19] conducted a set of thermo-mechanical FEA analyses through 3D explicit dynamic models by using ANSYS/LS-Dyna. They first discussed an analytical model developed by Salem [3,20] previously by including elastic deformation, elastic-perfectly plastic and elastoplastic deformation zones [16].

In the literature, the research studies related to ED-FEA models have mostly considered cylindrical rollers and flat plates to study the roller bending process [21,22]. Even though different roller geometries such as concave and convex shapes are commonly applied at a certain level in bending machine designs to compensate the cylinders' deflections that affect the final curvature of a plate being bent, there is still a lack of investigation in terms of the effect of the convex geometric design of the rollers and a bending plate with special geometry. Any ED-FEA study including discussions related to the rolling speed and the mass scaling factor and conducted to investigate the effect of time step size has not been encountered in the literature even though such studies are as significant as a convergence study widely conducted while investigating the effects of the element sizes on the results.

In the ED-FEA models to simulate the rolling process, the rollers are always defined with SHELL elements and a rigid material whereas the plate is defined with SHELL elements and number of integration points through the thickness of the plate. The material of the sheet is defined as a non-linear material with an elasto-plastic behavior with isotropic hardening [14].

2. Roll Bending Process

As can be seen in Figure 1 and Figure 2, operation principles of three-roller and four-roller bending machines have essential differences. As schematically shown in Figure 1, the inner roller only moves up and down and it is idle (that is, it is not driven by a motor), while the outer rollers are driven to rotate but they are stagnant (that is, they do not move upward or downward). By displacement of the inner roller toward the plate, it moves down to the point where the pinch pressure applied to the bending plate was set at a certain pressure [5]. As graphically shown in Figure 2, the difference in four-roller bending machines is not only the number of rollers but also the motion of the outer (side) rollers. Initially, the side rollers are located as symmetric in the design even though they can pivot by swing independent from each other by means of a part called wing. Hence, the side rollers can apply the required force and moments onto the plate [7,21].

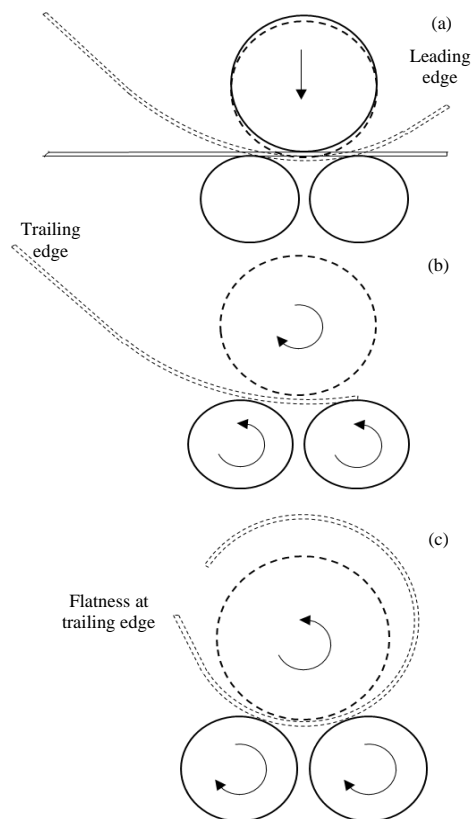


Figure 1. Schematic illustration of the steps of bending in a symmetric three roll quick rolling machine: (a) static bending (b) reverse pre-bending (c) forward bending

Four roll plate bending machines (Figure 3) that have higher efficiency compared to three roller machines are more commonly chosen by metal pipe manufacturers since they can have different operation modes to be able to carry out versatile functions. In another word, a four roll plate bending machine has two independent side rolls that can be moved upward and downward to be located for pre-bending and continuous bending processes in one pass from right to left or vice-versus. Thus, a fully circular geometry can be eventually obtained in different curvature sizes as desired (sequences 2 and 4 in Figure 2).

Hua et al [23–25]. conducted an elaborate study by developing a theoretical definition of the four-roll bending process comprehending the complete bending mechanism. Lin & Hua defined the sequences of bending as shown in Figure 2. The steady continuous roll-bending mode (sequences 4-6, Figure 2) is implemented to accomplish fully circular curvature in a certain diameter for the major portion of the part. The edge bending mode consisting of two sub-modes, edge pre-bending mode (sequence 2, Figure 2) and edge continuous roll-bending mode (sequence 3, Figure 2), has the function used to reduce the length of flat leading and trailing edges.

Springback concept and its analytical estimation in a metal forming [26] for its compensation in practice in die industry is of paramount importance in general as well as in the metal plate bending through both three-roller and four roller bending machines in particular. Springback can be defined as the elastically driven change of shape that occurs after deforming a plate at loading stage and then the plate tends to return to its original shape at unloading stage [21] and it partially returns due to the elasto-plastic deformation [5].

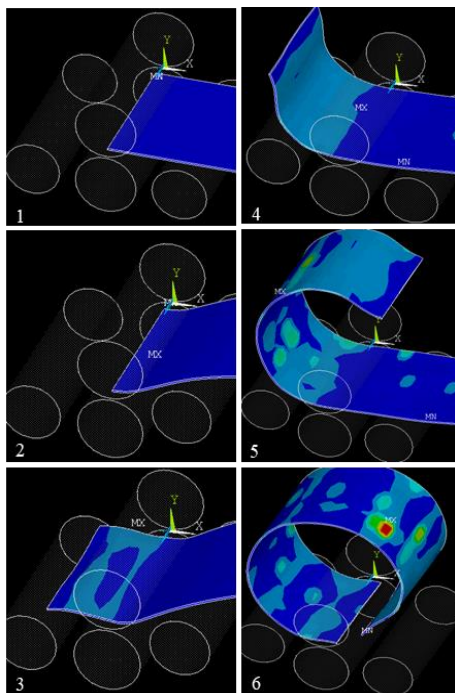


Figure 2. Sequence of four roll plate bending

3. Material and Methods

This study aims at developing a 3-D theoretical model using a non-linear explicit dynamics finite element model for a bending procedure of a metal plate with special geometry in a four roll bending machine (Figure 3). The FEA model is defined in detail so that it can be used for more generic cases of the continuous metal plate bending process. LS-DYNA solver in ANSYS Mechanical APDL (ANSYS Parametric Design Language) was employed as an explicit dynamic preprocessor for the generation of the two models including cylindrical as well as convex rollers. They were processed by Ls-Dyna solver engine and post-processor for analyses of the simulation results. In addition, since the discussion of the mass scaling factor, which significantly effects results as well as the computation cost, seems necessary and it should be included in any explicit dynamics model, this study takes into account the discussion of the peripheral velocity and mass scaling effects.

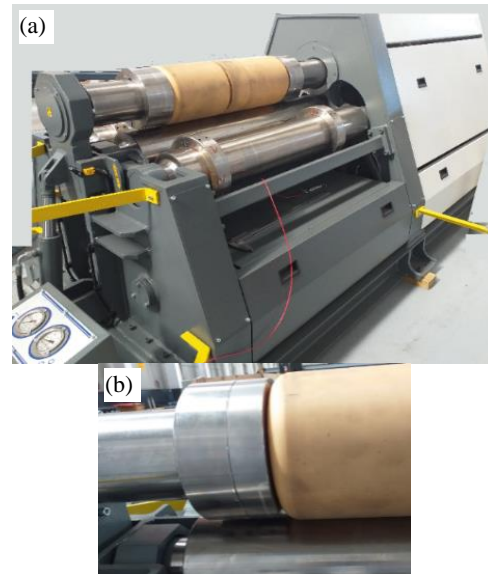


Figure 3. a) Four roll bending machine and b) the specific geometry of the top roller with channels

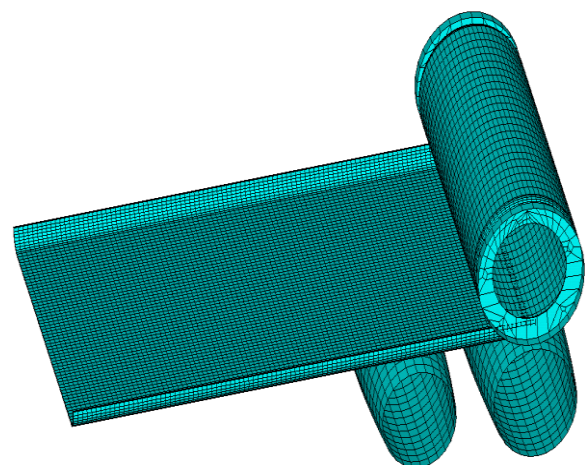


Figure 4. 3D meshed FEA model of asymmetric three roll bender for continuous bending of a plate

In the explicit non-linear dynamics FEA model, two different models were first generated in a commercial 3-D solid modeling software and then they were respectively imported into the ANSYS Mechanical APDL environment as step files in order to further generate the finite element models by defining; element types, mesh sizes, materials, contacts between the parts and motions with constraints.

Element types were defined as SOLID 164 for the Aluminum plate and SHELL 163 for the rollers' outer surfaces as listed in Table 1. After the solid model is imported into ANSYS, the model consists of areas and does not have volume. Before setting the SOLID 164 element type to the volumes and meshing them as illustrated in Figure 4, it is needed to convert areas that compose the plate into volumes and combine the generated volumes through the VGLUE command. Since shell element can be appointed to the areas, no conversion of the areas of the rollers is required to set the SHELL 163 to the certain roller areas.

Plate material is modeled by elasto-plastic Bilinear Kinematic Hardening model (Figure 5) through using the mechanical properties given in Table 2. To include the Bauschinger effect, it is assumed by the plasticity material model that the total stress range is equal to twice the yield stress. This model was chosen for the aluminum material since it met Von Mises yield criteria including the most metals. The tangent modulus is not able to take a value less than zero or its value cannot be greater than the value of elastic modulus [18]. The material properties were obtained from the tensile test data of the Al-552-H32 isotropic material depicted as the stress-strain graphic in Figure 5.

The three-roller materials were modeled as rigid steel materials as shown in Table 1, and their mechanical properties, as well as the transitional and rotational constraints, are presented in Table 2.

Contacts between each roller and the plate are defined as the general surface to surface contact with 0.3 static and dynamic friction coefficients. The real constant values for the shear factor and the number of integration points through the thickness of shell element of 1 mm are assumed to be 0.83 (5/6) and 5 respectively.

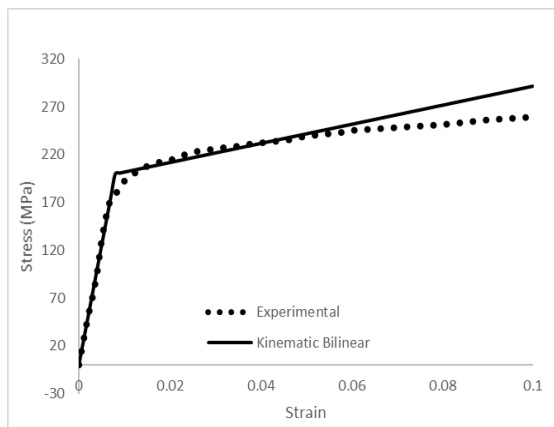


Figure 5. Kinematic Bilinear model and experimental Stress strain relation of Al-552-H32 material of the plate

Table 1 Material and element information for the parts of the model

Part	Mater.	Elem. type	Model 1: Elem. #	Model 2: Elem. #
1	Al	SOLID 164	15200	11400
2	Steel	SHELL 163	624	676
3	Steel	SHELL 163	728	780
4	Steel	SHELL 163	3193	3825

To bend the plate at desired diameter, the side roller is required to move upward at a certain distance and a certain speed. For this study, the coordinate of its final stop is (60.8; 15.49) in mm along y and z directions. The velocity of the side roller is supposed to be 10 mm/s. The duration of the transitional motion of the side roll from its velocity is defined as follows:

$$v_{sRoll} = 10 \text{ mm/s} \quad (1)$$

$$\tan \alpha = \frac{60.8}{15.49} \quad (2)$$

$$\alpha = 75.7^\circ \quad (3)$$

$$v_z = -10 \cos \alpha = -2.4699 \text{ m/s} \quad (4)$$

$$v_y = -10 \sin \alpha = 9.69 \text{ m/s} \quad (5)$$

$$t = \frac{y}{|v_y|} = \frac{60.8}{9.69} = 6.27 \text{ s} \quad (6)$$

or

$$t = \frac{z}{|v_z|} = \frac{15.49}{2.4699} = 6.27 \text{ s} \quad (7)$$

The angular velocity of the upper roll rotation ω_{TRoll} is determined as 0.72 rad/s (equals to 5000 mm/min of its peripheral velocity, v_{TRoll}) for the first set of the FEA simulations. The relation between the ω_{TRoll} and v_{TRoll} is as the following algebraic procedure;

$$v_{TRoll} = 5000 \text{ mm/min} \quad (8)$$

$$n = \frac{v_{TRoll}}{\pi D} = \frac{5000 \text{ mm/min}}{\pi \cdot 230 \text{ mm}} = 6.92 \text{ rpm} \quad (9)$$

$$\omega = \frac{2\pi n}{60} = 0.72 \text{ rad/s} \quad (10)$$

3.1 FEA Model with Cylindrical Rollers

In the first model, as shown in Figure 6, the bottom roller and the side roller are defined as cylinders with diameters of $\varnothing 210$ mm and $\varnothing 190$ mm, respectively. The top roller is $\varnothing 230$ mm cylinder and has channels with a certain depth on its two ends for insertion of the side walls of the aluminum plate as depicted in Figure 6. The thickness of the aluminum plate was chosen as 3.175 mm, the width from outer surface of the side wall to that of the other side wall as 635 mm, and the length as 1000 mm. In this research, we aim at finding out a suitable design for the four roll bending machine and set a proper rotation velocity of the upper roll to achieve bending without any failure. It is a challenging task to accomplish the

bendability with a neat final circular geometry due to the pre-bent side walls of the aluminum plate.

3.2 FEA Model with Convex Rollers

Although it was not possible to eliminate the material failure that occurred during the beginning of the bending process, to minimize it, the design of the bottom and the side rolls was changed to convex geometry as shown in Figure 7.

The diameters of the bottom pinch roll were defined as Ø180-Ø210 mm and that of the side roll as Ø160-Ø190 mm. The top roll design remained the same.

The computation time and accuracy of the results should be optimized by conducting a convergence study. Conducting explicit dynamic analyses is costly in terms of computation time in order to obtain accurate results.

Is-Dyna solver is the best-fit and the most convenient software for such analyses. For a low-velocity metal forming process done through ED-FEA, the computation time and the results are affected by the time step size. To be able to minimize the computation cost, the element size can be set by the Mesh Tool assigning to a specific size for critical edges or zones usually relatively smaller in comparison to non-critical ones. Another effective method is mass scaling. The use of mass scaling, as explained in detail in the Appendix section, can be very helpful, especially in the low-velocity simulations such as that of roll-bending of a plate. It is useful in situations in which more intensively meshing of an area of interest is needed.

First, a 3-D FEA model including cylindrical rollers was created and a pre-bending simulation with top roller not being rotated was conducted only to validate the model by comparing it with the experimental results. In the FEA model, the mass scaling was assigned as 4×10^{-6} . The element sizes along the width and the length of the plate were chosen to be 25mm; however, the element size along the thickness – that is critical to simulate the bending phenomenon – was chosen to be much smaller (5 elements along the thickness of 3.175 mm) in comparison to other dimensions of the plate.

4. Result and Discussion

4.1 Influence of Side Walls of the Plate

As seen in Figure 9(a), the aluminum plate experiences various deformation forms at different time spots as the plate is being bent. The nodal deformation list in Y

direction along the rear edge of the plate was extracted as csv data file and plotted in Excel. The results are also illustrated in 2-D graphics in terms of the nodal deformation of the rear edge of the plate in mm as shown in Figure 9 (b). The deformation of the plate becomes concave and then takes a convex form similar to the experimental result as shown in Figure 10. The distortion has occurred only on one side wall in both FEA (Figure 11) and experimental results (Figure 10). These conclude that the FEA model very closely predicts the reality of the bending phenomena of an aluminum fender by a four-roll bending machine. Therefore, the low-velocity non-linear explicit FEA model could be considered for different parameters in a future parametric study.

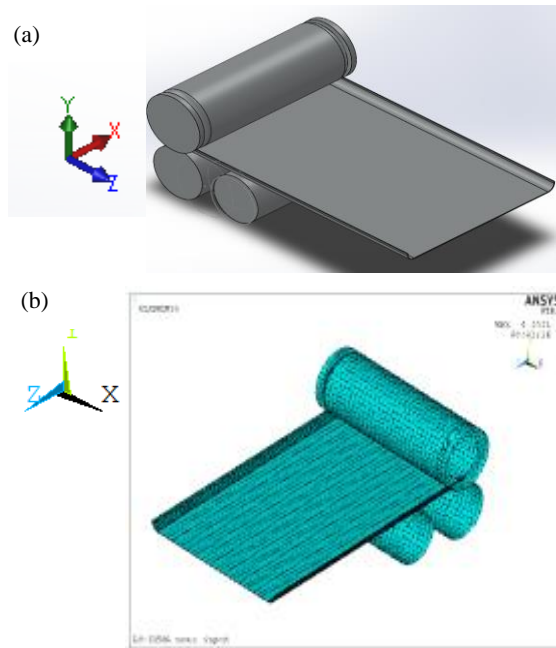


Figure 6. Three-dimensional a) solid model and b) meshed model of asymmetric three roll bending

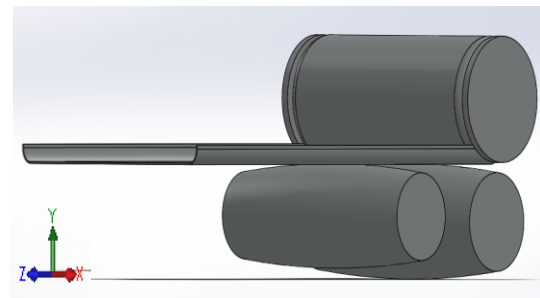


Figure 7. Three-dimensional solid model of asymmetric three roll bender with convex side and bottom roller

Table 2. Material models of the aluminum plate and the rollers

Material	Model	Density (kg/mm ³)	Young's Modulus (MPa)	Poisson Ratio	Yield Stress (MPa)	Tangent Modulus (MPa)	Translational Constraint	Rotational Constraint
Alum. Plate	Bilinear Kinem.	2.68×10^{-6}	70300	0.33	193	750		
Side roll	Rigid	7.8×10^{-6}	210000	0.3			X Disp.	All Rot.
Bottom roll	Rigid	7.8×10^{-6}	210000	0.3			All Disp.	All Rot.
Top roll	Rigid	7.8×10^{-6}	210000	0.3			All Disp.	All Rot.

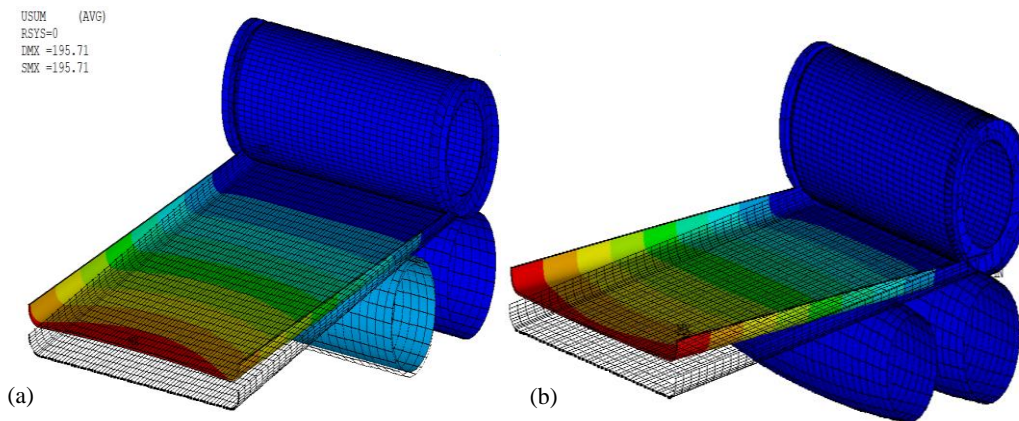


Figure 8. Demonstration of two models with a) cylindrical rollers and b) convex side and bottom rollers

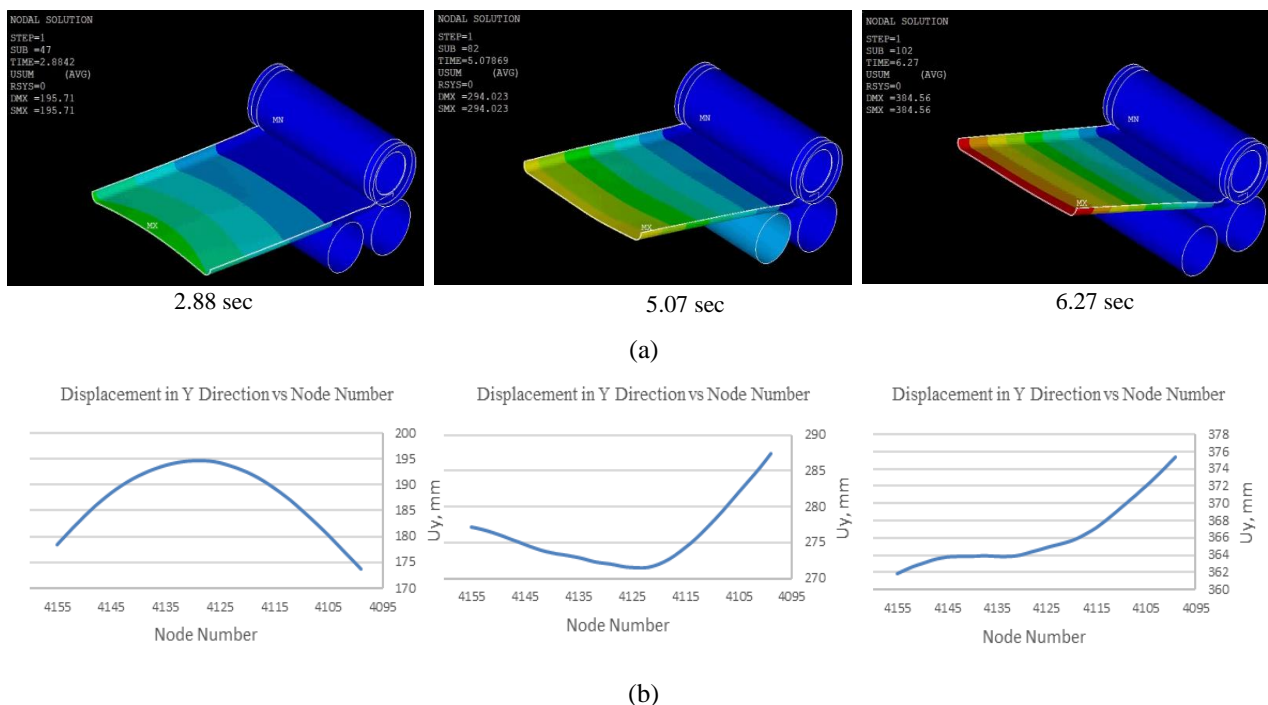


Figure 9. Demonstration of the deformation results from the cylindrical roller model in a) contour plots and b) 2-D plots of the displacements along the nodes of the rear edge of the aluminum plate at different time spot

4.2 Influence of Top Roller Rotation Speed During Bending

The design of the bottom and side roller geometries was changed to convex. The new design was tried in another FEA simulation to avoid the experimental cost with regards to a lot of scraps. Because the previous FEA model in Ls-Dyna accomplished to predict the experimental results obtained from the cylindrical rollers, another FEA simulation was conducted with the 3D model involving convex rollers. In this simulation, the top roller was rotated with the peripheral velocity of 5000 mm/min (angular velocity of 0.72 rad/s) and the mass scaling factor was doubled in a way to be 8×10^{-6} for the sake of reducing the computational cost in half. Although the bottom and side roller geometry were changed to convex with the sizes

given in the previous section, the top roller design was not changed.

4.3 Influence of convex rollers during pre-bending

Since the distortion still seemed too much, the rotation speed was presumed as the reason and the rotational speed of the top roller was reduced to 0.18 rad/s, the element size along the length and the width of the plate was reduced to 10 mm, and the rest of the model remained the same. The design change of the bottom and side rollers and the reduction of the top roller speed did not work out as expected. The distortion could be neither avoided nor reduced as the plate being bent by a four roller plate bending machine as can be seen in Figure 12. Therefore, a completely different methodology could be studied in the future to accomplish the bending of a fender with two side walls.



Figure 10. Demonstration of the experimental deformation results

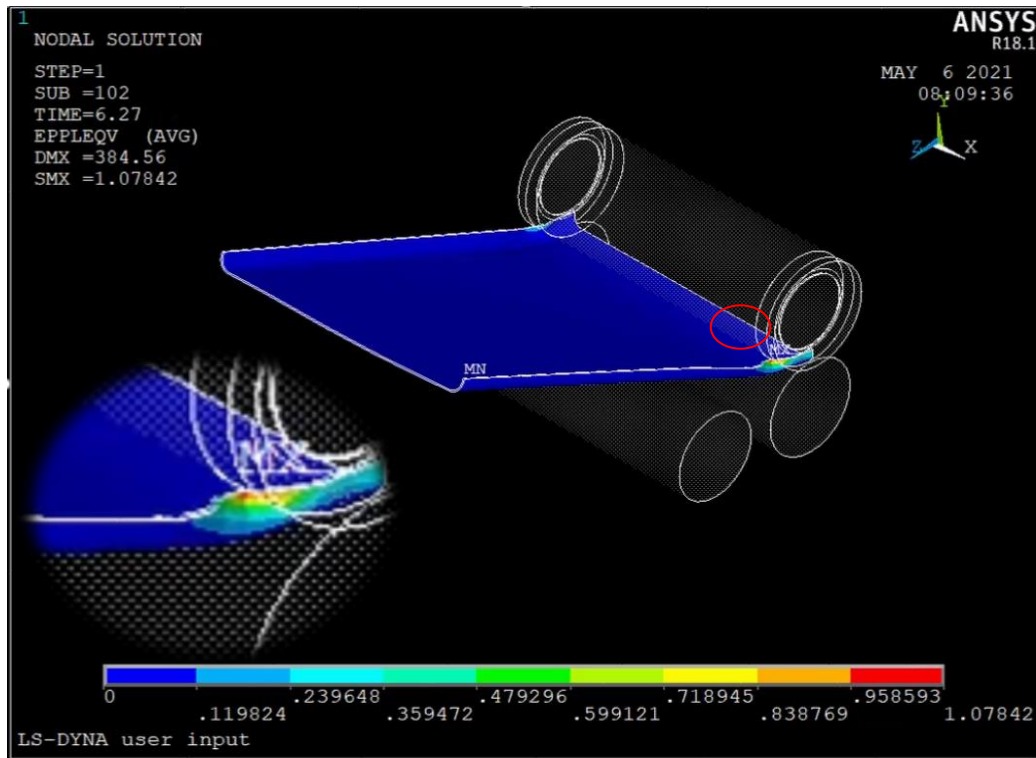


Figure 11. Demonstration of the Von-Mises Equivalent stress results from the cylindrical roller model in contour graphs

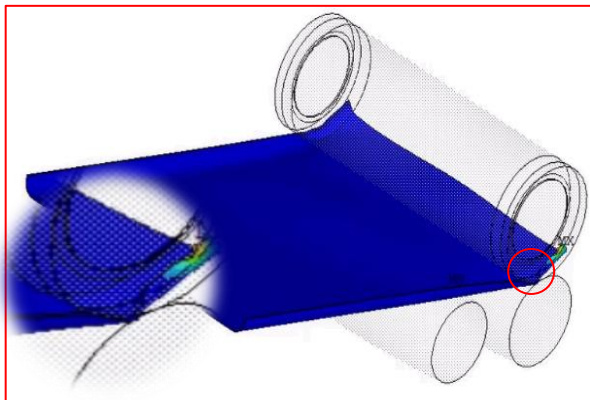


Figure 12. FEA results in terms of distortion of the side wall of the plate during bending

5. Conclusions

In this study, the explicit dynamics FEA model was created with two different 3-D models including cylindrical and convex geometries of bottom and side

rollers. The FEA model was first validated with the experimental results. Since resembling deformation results was obtained, the FEA model with different parameters such as geometry, element size, mass scaling factor, and rotational speed was created in Ls-Dyna and simulated for different cases to avoid experimental trial and error costs such as scraps, labor, and time. In this study, the importance of the mass scaling factor to minimize computational cost was also discussed. It is used to increase the time step of the explicit dynamics simulation; however, one needs to pay attention that too much reduction of the simulation time results in unphysical consequences.

Unfortunately, the design change and speed reduction did not work out as not to avoid the distortion. Nevertheless, the results obtained in this study may shed light on a possible future study to be conducted on bending an aluminum fender with sidewalls such as two-step

forming process involving roll bending and then roll forming or vice-versus.

For the researchers in the metal-forming field, this study also aimed to present a comprehensive explanation for an explicit dynamics FEA simulation of roll-bending of a plate and creation of a 3-D model with the significant parameters such as mass scaling and element size used to control for optimization between the prediction accuracy and the computational cost. In a simple static structural analysis, a convergence analysis with regards to the element size might be sufficient to optimize an FEA model, however, once a highly costly non-linear dynamic analysis is considered, the time step must be also taken into account more carefully to attain physical and accurate results

Declaration

The author(s) declared no potential conflicts of interest with respect to the research, authorship, and/or publication of this article. The author(s) also declared that this article is original, was prepared in accordance with international publication and research ethics, and ethical committee permission or any special permission is not required.

Author Contributions

F. Author performed the analysis and developed the methodology. S. Author supervised and improved the 3-D model.

Nomenclature

α	: The angle of transitional motion of the side roller
c	: The sonic velocity
E	: Young's (Elasticity) Modulus
ρ	: The material density
n	: The rotation count per minute
ν	: Poisson's ratio
Δt	: The time step size
t	: The time
v_{Sroll}	: The transitional velocity of the side roller
v_{TRoll}	: The peripheral velocity of the top roller
ω	: The angular velocity

References

- Zeng, J., Z. Liu, and H. Champlaud, *FEM dynamic simulation and analysis of the roll-bending process for forming a conical tube*, Journal of Materials Processing Technology, 2008. **198**: p. 330–343.
- Gandhi, A.H. and H.K. Raval, *Analytical and empirical modeling of top roller position for three-roller cylindrical bending of plates and its experimental verification*, Journal of Materials Processing Technology, 2008. **197**: p. 268–278.
- Salem, J., H. Champlaud, Z. Feng, and T.M. Dao, *Experimental analysis of an asymmetrical three-roll bending process*, International Journal of Advanced Manufacturing Technology, 2016. **83**: p. 1823–1833.
- Feng, Z. and H. Champlaud, *Modeling and simulation of asymmetrical three-roll bending process*, Simulation Modelling Practice and Theory, 2011. **19**: p. 1913–1917.
- Shinkin, V.N., *Asymmetric three-roller sheet-bending systems in steel-pipe production*, Steel in Translation, 2017. **47**: p. 235–240.
- Wang, Y., X. Zhu, Q. Wang, and X. Cui, *Research on multi-roll roll forming process of thick plate*, International Journal of Advanced Manufacturing Technology, 2019. **102**: p. 17–26.
- Wu, K., Y. Sun, C. Cao, C. Zhou, Q. Liu, and X. Chang, *On Simulation Analysis of Plate Forming and Deformation Compensation Technology of the side roll for Four-roll Plate Bending Machine*, Procedia Engineering, 2017. **207**: p. 1617–1622.
- Hua, M., K. Baines, and D.H. Sansome, *Design and Performance Considerations of the Continuous Four-roll Bender: A Precision Machine for the Roller Bending of Plates*, Progress in Precision Engineering, 1991. p. 277–289.
- Chudasama, M.K. and H.K. Raval, *Bending force prediction for dynamic roll-bending during 3-roller conical bending process*, Journal of Manufacturing Processes, 2014. **16**: p. 284–295.
- Fu, Z., X. Tian, W. Chen and B. Hu, *Analytical modeling and numerical simulation for three-roll bending forming of sheet metal*, Int J Adv Manuf Technol, 2013. p. 1639–1647.
- Taylor, V.K., A.H. Gandhi, R.D. Moliya and H.K. Raval, *Finite Element Analysis of Deformed Geometry in Three Roller Plate Bending Process*, in: International Manufacturing Science and Engineering Conference MSEC2008, Evanston, IL, USA, 2018. p. 1–8.
- Zhigulev, G.P., M.N. Skripalenk, V.A. Fadeev, and M.M. Skripalenko, *Modeling of Deformation Zone during Plate Stock Molding in Three-Roll Plate Bending Machine*, Metallurgist, 2020. **64**: p. 348–355.
- Amiolemhen, P.E. and J.K. Abiegbe, *Design and Fabrication of a Three - Rolls Plate Bending Machine*, Innovative Systems Design and Engineering, 2019. **10**: p. 31–41.
- Boazu, I., D. and F. Stan, *Estimating of bending force and curvature of the bending plate in a three-roller bending system using finite element simulation and analytical modeling*, Materials, 2021. **14**: p 1–16.
- Gavrilescu, I. and D. Boazu, *Simulation of Roll Bending with Three Rollers Pyramid System Using FEM*, 2017. p. 21–28.
- Tran, Q.H., H. Champlaud, Z. Feng, and T.M. Dao, *Analysis of the asymmetrical roll bending process through dynamic FE simulations and experimental study*, International Journal of Advanced Manufacturing Technolog, 2014. **75**: p. 1233–1244.
- Burchitz, I., *Springback: improvement of its predictability: Literature study report*, 2005. p. 49–62.
- ANSYS/LS-DYNA Help, (2018).
- Quan, T.H., H. Champlaud, Z. Feng, J. Salem, D.T. My, *Heat-assisted roll-bending process dynamic simulation*, International Journal of Modelling and Simulation, 2013. **33**: p. 54–62.
- Salem, J., ©Tous droits réservés, Jamel Salem, 2012.
- G. Yu, J. Zhao, C. Xu, *Development of a symmetrical four-roller bending process*, International Journal of Advanced Manufacturing Technology, 2019. **104**: p. 4049–4061.
- Quan, T.H., H. Champlaud, Z. Feng, and D. Thien-My,

Dynamic analysis of a workpiece deformation in the roll bending process by FEM simulation, 24th European Modeling and Simulation Symposium, EMSS 2012. p. 477–482.

23. Lin, Y.H. and M. Hua, *Influence of strain hardening on continuous plate roll-bending process*, International Journal of Non-Linear Mechanics, 2000. **35**: p. 883–896.
24. Hua, M., I.M. Cole, K. Baines, and K.P. Rao, *A formulation for determining the single-pass mechanics of the continuous four-roll thin plate bending process*, Journal of Materials Processing Technology, 1997. **67**: p. 189–194.
25. Hua, M., K. Baines, and I.M. Cole, *Continuous four-roll plate bending: A production process for the manufacture of single seamed tubes of large and medium diameters*, International Journal of Machine Tools and Manufacture. 1999. **39**: p. 905–935.
26. Wagoner, R.H., J.F. Wang, M. Li, and T. Ohio, *Springback*, 2006. p. 1–23.

Appendix

The Mass Scaling increases the required time step by increasing the mass of the minimum sized elements. In conditions where the low velocity analysis type is conducted, the mass scaling is better to be switched on, and in the Hourglass effect, the type 6 can be chosen for the low-velocity analyses. For explicit time integration, the minimum time step-size depends on the minimum element length (l_{\min}) and the sonic speed (c). Note that, in the model, the smallest element size controls the minimum time step size (Δt_{\min}) for a given set of material properties. In addition, for a certain mesh, the minimum time step size varies based on the sonic speed that is a function of material properties:

$$\Delta t_{\min} = \frac{l_{\min}}{c} \quad (\text{A1})$$

$$c = \sqrt{\frac{E}{(1-\nu^2)\rho}} \quad (\text{A2})$$

where ν is the Poisson's ratio, E is the Young's modulus, and ρ is the density.

In the ANSYS LS-DYNA software, the minimum time step size can be controlled through including mass scaling into the analysis process. To be able to reduce the temporal cost, the mass scaling criterion must be used when the time-step calculated by the software is too minimal. In conditions where the mass scaling is specified, element density is set to reach a pre-defined time step size Δt_{sp} with the following equation:

$$\rho_i = \frac{\Delta t_{sp}^2 E}{l_i^2 (1-\nu^2)} \quad (\text{A3})$$



Research Article

Analysis of Spatio-temporal rainfall trends and rainfall variability in Botswana between 1958 and 2019

Hüseyin Gökçekuş^a , Youssef Kassem^{a, b} and Lorato Precious Mphinyane^{a, *}

^aDepartment of Civil Engineering, Civil and Environmental Engineering Faculty, Near East University, 99138 Nicosia, Cyprus

^bDepartment of Mechanical Engineering, Engineering Faculty, Near East University, 99138 Nicosia, Cyprus

ARTICLE INFO

Article history:

Received 31 March 2021

Revised 18 August 2021

Accepted 06 October 2021

Keywords:

Botswana

Climate change

Mann Kendall test

PCI

Rainfall variability

Spatio-temporal

ABSTRACT

Environments with a climatic characteristic of semi-aridity exhibit high rainfall variability, increasing significantly as the climate changes. In this study, rainfall concentration and Spatio-temporal trends in annual and seasonal (November to March) rainfall in Botswana were analyzed. The satellite data (1958-2019) is obtained from the Southern African Science Service Centre for Climate Change and Adaptive Land Management and the Climate Toolbox. The Mann–Kendall trend test (MK), autocorrelation function (ACF), relative percentage change (RPC), precipitation concentration index (PCI), and Theil–Sen's slope estimator (β) methods were adopted for data analysis. The regions include Gaborone, Maun, Francistown, Serowe, Kasane, Tsabong, Ghanzi, and Pandamatenga. The results indicated that the magnitude of change of the significant downward trends in the annual rainfall was found to be -1.11 mm/year at Maun, -1.62 mm/year at Ghanzi, -0.33 mm/year at Pandamatenga, and -0.25 mm/year at Tsabong. The magnitude of change of the significant downward trends in the seasonal rainfall was between -0.60 mm/year at Pandamatenga and -0.19 mm/year at Tsabong. All these regions, except Ghanzi, experienced a downward trend in the rainfall distribution. This is owing to the synoptic characteristic of the below-average geopotential heights over Ghanzi. Which might exacerbate the formation of convective systems, leading to a positive rainfall trend at Ghanzi. The annual calculated PCI values are divided into three classes; $PCI > 10 \leq 15$, $PCI > 16 \leq 20$, and $PCI > 20$. The Mann-Kendall analysis of the PCI values indicates that all the regions experienced a downward rainfall trend, implying that it is heading toward a uniform to a moderate distribution. There were distinct patterns that emerged from the Pandamatenga region, indicating a strongly irregular distribution. The regions of Kasane, Maun and Francistown, demonstrated moderate to an irregular distribution. For Gaborone and Francistown, results showed occurrences of a moderate to strongly irregular distribution.

1. Introduction

The variability of rainfall in Southern Africa has undergone significant changes, particularly in recent decades, since the late 1960s, increasing inter-annual variability. In particular, droughts are now affecting different regions worldwide and are becoming more intense [1]. The rainfall patterns are spread and distributed across these regions. With this, there seems to be a link to El Niño Southern Oscillation (ENSO) [2]. The Southern African Development Community (SADC) countries experienced almost close to severe droughts in the 1980s to 1990s. From 2015 – 2016, Botswana experienced water scarcity because of extremely low rainfall seasons [3]. Nevertheless, rainfall and

temperature patterns analysis are often used to track climate change intensity and size [4–6]. Evaporation rates have been increasing in staggering amounts, one of the most significant influences of climate variability, causing similar increases in extreme rainfall [7].

Like most Southern African nations, Botswana undergoes extremely volatile rainfall patterns, contributing to droughts [8]. Droughts in southern Africa appear to occur after an El Niño incident in the rainy season from December to March [9]. Impacts of rainfall variability, causing droughts, have generally increased because of the lack of rainfall and at increased degrees of temperatures. Thereby increases the stresses on evapotranspiration rates [10, 11]. Semiarid

* Corresponding author. Tel.: +90-392-223-6464.

E-mail addresses: huseyin.gokcekus@neu.edu.tr (H. Gökçekuş), youssef.kassem@neu.edu.tr (Y. Kassem), mphinyanelorato@icloud.com (L. P. Mphinyane)

ORCID: 0000-0001-5793-4937 (H. Gökçekuş), 0000-0002-1451-5457 (Y. Kassem), 0000-0003-0575-8710 (L. P. Mphinyane)

DOI: 10.35860/iaiej.906557

© 2021, The Author(s). This article is licensed under the CC BY-NC 4.0 International License (<https://creativecommons.org/licenses/by-nc/4.0/>).

climates are a climate over a region that receives rainfall potentially below evapotranspiration. These climates are determined by one of the widely used climate systems, the Köppen Climate Classification. Group B is Dry climates. That is where most countries in the southern part of Africa fall. It is necessary to have up-to-date information regarding climate patterns and climate changes. It will be essential for future predictions, planning, management, and water resources sustainability [10–12].

Botswana is a landlocked country situated on the African plateau. It is a deserted area with 582,000 km² and inhabitants reaching 2,3 million people [15]. The seasonal rainfall occurs from November to March. The country experiences dry spells of two to four days, where no rainfall falls in particular regions (Table 1) [16]. In the early summer to late summer, there are increases in westerly thermal waves that move across Botswana edges, causing increases in the isolated showers of rainfall experienced in Botswana [17]. The mean annual rainfall is 412.19mm, from 1901 to 2016 [18].

Mphale et al. [19], It showed analyses of a period of 30 years of annual rainfall for Botswana from 1971 to 2000. Their studies noted that Botswana's yearly rainfall decreased significantly in its hard veldt region, values being -1.097, -0.029, -0.407, and -1.327 mm/year. While Batisani et al. [20] used a 31-year-long dataset, researchers looked at yearly rainfall trends in Botswana's sand and hard veldt areas. From 1975 to 2005, annual rainfall data confirmed the same patterns throughout the country. Besides, Kenabatho et al. [21] attempted to analyze rainfall and temperature changes at four anchor climates, and they concluded that Between 1926 and 2011. They explained that if the current trend continues, average annual rainfalls will be reduced by around 30 mm by 2050. However, Da Silva [22] and Lazaro et al. [23] observed two significantly contrasting results in both of their studies.

The variability of rainfall is likely to rise as Botswana continues to dry. Climate change estimates from the (Intergovernmental Panel on Climate Change) predict a 30 to 40 percent decline in rainfall from 2080 to 2099, with the most significant drops occurring during the already dry winter season. Over time, research has shown a decrease in the patterns of mean temperatures and annual amounts of rainfall in Africa, respectively. Predictions state that these increments will surpass 4 degrees Celsius around the ending of the 21st century [5, 31].

Several studies have been undertaken to probe into climate variability by analyzing rainfall and temperature trends, both on a regional and a global scale. Groleau et al. [25] undertook a study from 60 stations where they utilized data that consist of January and February daily rainfall and the bootstrap-based Mann-Kendall and Sen's slope estimator. Meanwhile, in India, Da Silva [18] researched the annual and seasonal total rainfall, which occurred over 33 years from 1976 to

2008. They employed the non-parametric Mann–Kendall, Z, and Sen's Slope methods. From 1935 through 1992, they used monthly, seasonal, and yearly statistics. Muhire et al. [26] stations in Rwanda used linear regression analysis.

Similarly, Recha et al. [27] used annual and seasonal rainfall alongside the Mann-Kendall trend analysis and Sen's slope estimator from Kenya. Moreover, Che Ros et al. [28] performed an in-depth study in Malaysia, analyzing the daily and monthly rainfall trends from 1940 to 2010. Again, Nenwiini et al. [29] in South African areas, yearly and seasonal rainfall were similarly examined using the Mann-Kendall trend analysis and Sen's slope estimator. The annual rainfall analysis from 1940 to 2015 in Benin was reported by Ahokpossi [30], which showed that trends can be affected by the selected statistical trend test. For instance, the MK variance correction with complete autocorrelation showed significant trends in the number of stations studied by Wang et al. [31]. Meanwhile, Elzopy et al. [32] analyzed annual, seasonal, and monthly time scales, from 1901-2015, using the Modified MK trend test; seasonality index (SI), PCI, the rainfall departure analysis (RDA) and rainfall anomaly index (RAI) in Ethiopian areas. Arragaw and Woldeamlak [24], also worked on the spatiotemporal variability and trends in rainfall and temperature in the central highlands of Ethiopia from 1983-2013.

From the recent studies that have been performed in the last year, Sezen et al. [33] and Tokgoz et al. [34] performed an analysis of the annual and seasonal rainfall from 1960 to 2015 using the Mann-Kendall trend analysis and Sen's slope estimator in Turkey's various regions. Also, Harmse et al. [35] analyzed the monthly rainfall data for 30 years, from 1989 to 2018. Rahardjo et al. [36], analyzed daily rainfall data from 1982 to 2011 using Slope stability analysis in Singapore. Ibrahim et al. [7] performed a study on the time scales covering monthly, annual, and seasonal periods of 1970–2016 in Nigeria. Wang et al. [31] used the innovation trend analysis on the yearly and Seasonal data from 1961 to 2018 in China (Table 6).

The methodologies used in this study are not suited for data with periodicities such as seasonal data only. For the method to be effective, recently developed software that can analyze seasonal data was employed in this study. Another disadvantage of the methodology is that; more negative results will be produced for shorter datasets hence why rainfall data was used for a more extended period.

This study aims to to carry out a long term (62 years) rainfall trend analysis in Botswana using MK trend test applied on PCI values, (β), ACF and RPC analysis applied in the towns of Gaborone, Maun, Francistown, Serowe, Kasane, Tsabong, Ghanzi, and Pandamatenga, since there are few works reported on rainfall trend analysis in Botswana. This is also the most recent study done which covers more regions of Botswana when compared to previous works on rainfall trend analysis. The method employed in this study covers

long term periods with different procedures different from other reported works [16, 37–39]. The results explain the analysis of rainfall trends and rainfall variability that can be used to understand the current rainfall trends and make future predictions showing the impacts of climate change.

2. Materials and Methods

2.1 Data used

The annual and seasonal (November to March) satellite rainfall data that is used in this paper is from the Southern African Science Service Centre for Climate Change and Adaptive Land Management (SASSCAL) and the Climate Toolbox, which was developed by members of the Applied Climate Science Lab (ACSL) at the University of California Merced and the UW Hydro group at the University of Washington. The selected regions for the study and all the satellite data coverage of annual and seasonal was for 62 years (Table 2). The seasonal data is the wet months, which is from November all through to March. This is when the country receives the most rain, especially in January and February.

2.2 Data Analysis

The Precipitation Concentration Index (PCI), Mann–Kendall trend test, Theil–Sen's slope estimator (β), Autocorrelation Function (ACF) and relative percentage change (RPC) methods were adopted for data analysis. These tests were performed using the R software, a programming language and a free software environment for statistical computing and data analysis.

2.3 Precipitation concentration index (PCI)

Oliver created the Precipitation Concentration Index (PCI) in 1980 to measure rainfall concentration and erosivity [40]. PCI was computed on an annual and seasonal basis for each grid point in this investigation using Equations (1) and (2).

$$PCI_{\text{annual}} = \frac{\sum_{i=1}^{12} P^2}{\left(\sum_{i=1}^{12} P_i\right)^2} * 100 \quad (1)$$

$$PCI_{\text{seasonal}} = \frac{\sum_{i=1}^3 P^2}{\left(\sum_{i=1}^3 P_i\right)^2} * 25 \quad (2)$$

Table 1. Recording period and location of all the regions

Region	Location		Period
	Latitude	Longitude	
Gaborone	-22.3755	26.7367	1958-2019
Francistown	-24.6720	25.9128	1958-2019
Serowe	-22.3627	26.7437	1958-2019
Kasane	-17.7931	25.1671	1958-2019
Maun	-19.9862	23.4258	1958-2019
Pandamatenga	-17.9389	25.2507	1958-2019
Ghanzi	-21.6830	21.6830	1958-2019
Tsabong	-26.0025	22.4081	1958-2019

2.4 The Serial Correlation Effect

The MK trend analysis is described to be a non-parametric approach that is applied to discover significant trends in times series datasets that are hydrological and meteorological without using predefined parameters. It is a straightforward and robust analysis that can handle undefined parameters as well as values that are below the detection limit [12, 41, 42]. There is a need to analyze and understand meteorological weather patterns across a region [38–41]. To use the Mann Kendall analysis to investigate the dataset, it is necessary to check if there is a significant correlation coefficient or not. This was carried out because the Mann Kendall test requires that a time series dataset has to be serially independent. If the serial correlation is present, this can affect the time series dataset, leading to the rejection of the null hypothesis, which makes the Mann Kendall ineffective [31]. The autocorrelation coefficient is required to be calculated to identify any existence of a significant autocorrelation within the time series.

2.5 Trend Analysis on Yearly PCI values

A trend test was performed on the yearly PCI value to see if it was trending toward a very erratic or uniform precipitation distribution. To determine any rise or reduction in rainfall, the annual and seasonal rainfall data were examined using the trend test. The Mann Kendall test allows researchers to assess if rainfall rises or decreases in the selected locations. The Mann Kendall trend test, with critical values of = 0.01, 0.05, and 0.1, differentiates the importance of upward and downward precipitation distribution. The Mann Kendall;

$$S = \sum_{k=1}^{n-1} \sum_{j=k+1}^{n-1} \text{sign}(x_j - x_k) \quad (3)$$

Where;

$$\text{sign}(x_j - x_k) = \begin{cases} 1 & \text{if } (x_j - x_k) > 0 \\ 0 & \text{if } (x_j - x_k) = 0 \\ -1 & \text{if } (x_j - x_k) < 0 \end{cases} \quad (4)$$

$$\text{VAR}(S) = \frac{n(n-1)(2n+5) - \sum_{i=1}^m ti(ti-1)(2ti+5)}{18} \quad (5)$$

Janni et al. [45] says that a positive z value indicates an increasing trend as well as statistical significance. A negative z value, on the other hand, indicates a downward tendency. The test statistic Z was then computed using Equations (4) and (5) from the following equation:

$$Z = \begin{cases} 1 \frac{S-1}{\sqrt{\text{VAR}(S)}} & \text{if } S > 0 \\ 0 & \text{if } S = 0 \\ -1 \frac{S+1}{\sqrt{\text{VAR}(S)}} & \text{if } S < 0 \end{cases} \quad (6)$$

2.6 Magnitude of change of the rainfall trend (β)

Sen devised a non-parametric technique to assess the magnitude of change (per unit time) in the Theil-Sen slope estimator [46]. To understand the magnitude of change of the trend, alongside these non-parametric tests, Theil's Sen Slope estimator was utilized to understand better what the patterns were alluding to, either a downward or an upward trend.

$$\beta = \text{median} \left(\frac{x_j - x_k}{j - k} \right) \forall k < j \tag{7}$$

2.7 Relative percentage change

Equation (8), where n is the length of the trend cycle (years), x is the absolute average value of the time series defined and the Theil-Sen median estimator, and n is the length of the trend period, applied to calculate the RPC of monthly and yearly rainfall. This method was employ by [47], [48], and [7] in a similar study.

$$\text{RPC} = \left(\frac{n\beta}{\bar{x}} \right) 100 \tag{8}$$

3. Results and Discussion

3.1 Precipitation concentration index (PCI)

The PCI values for the study regions of Gaborone, Maun, Francistown, Serowe, Kasane, Tsabong, Ghanzi, and Pandamatenga were estimated to be within 3 and 43 (Table 2), which suggests the distribution of rainfall ranges from low precipitation concentration to a strongly irregular distribution (Table 3). The estimation for all 8 regions was from 1958-2019. The Pandamatenga region indicated the highest values of PCI compared to other regions. The precipitation concentration index in Pandamatenga gears toward a strongly irregular distribution, which means high precipitation concentration than in most regions in the country, as indicated with PCI values between 3 and 43. It is also indicated in the average rainfall that is experienced in this region. Kasane, Maun and Francistown's regions indicated the frequency count for the PCI which revealed that rainfall distribution is moderate, irregular, and strongly irregular. While, the PCI values of Gaborone and Francistown are within the range 9 and 43, having occurrences of a moderate to strongly irregular distribution of rainfall throughout the country. The lowest PCI values were recorded in the Tsabong and Ghanzi regions. As would be expected, these regions' mean annual total rainfall is the lowest in Botswana.

3.2 The serial Autocorrelation test performed on rainfall data

The serial autocorrelation analysis were performed on all the annual rainfall data of the regions to show the rainfall trend. The figures (Figures 2, 3, 4, and 5) for Pandamatenga, Serowe, Kasane, and Tsabong represent all the study regions.

These results showed that the autocorrelation present is insignificant because most of the vertical spikes resulting from the Autocorrelation function are shown to be compressed between the dotted horizontal lines, suggesting that the rainfall data tested are insignificant. Therefore, the Mann Kendall trend test can be carried out without any corrections to the data.

Table 2. Study stations showing PCI frequency count.

Region	PCI≤1	PCI>10≤1	PCI>16≤2	PCI>2
Gaborone	0	9	10	43
Francistown	0	5	18	39
Serowe	0	4	39	19
Kasane	0	6	23	33
Maun	0	15	30	17
Pandamatenga	0	9	18	35
Ghanzi	0	3	18	41
Tsabong	0	4	20	38

Table 3. Classes of PCI values adapted from Oliver (1980)

PCI values	Distribution of precipitation
PCI≤10	Uniform precipitation distribution (low precipitation concentration)
11-15	Moderate precipitation concentration
16-20	Irregular distribution
PCI>20	Strongly irregular distribution (high precipitation concentration)

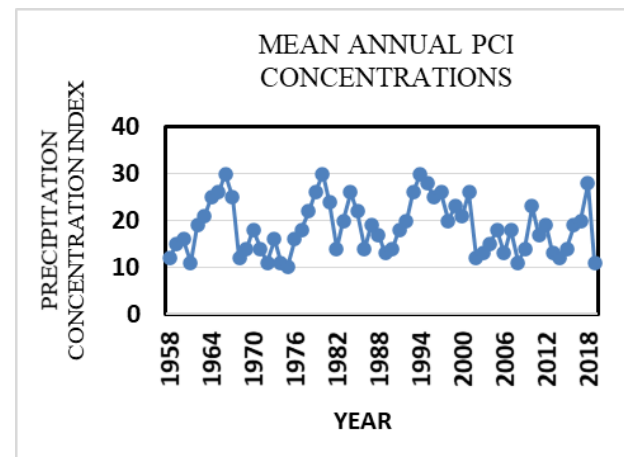


Figure 1. Mean annual PCI concentrations

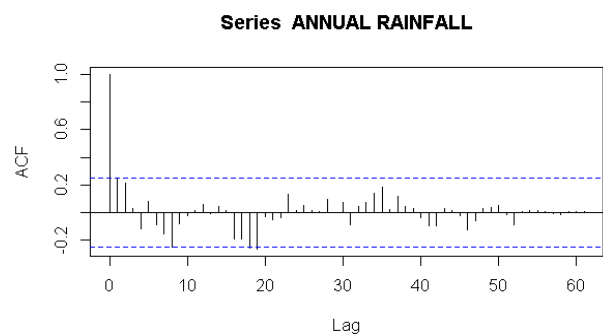


Figure 2. The serial autocorrelation analysis of annual rainfall data, Tsabong

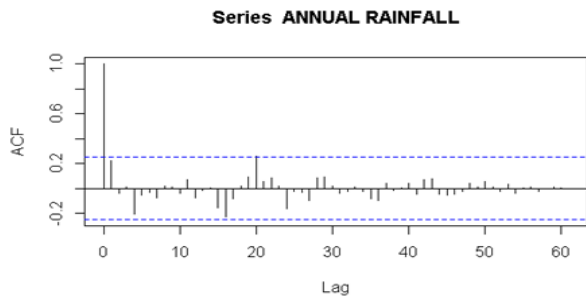


Figure 3. The serial autocorrelation analysis of annual rainfall data, Serowe

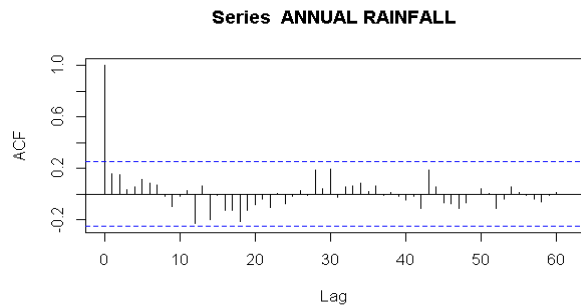


Figure 4. The serial autocorrelation analysis of annual rainfall data, Pandamatenga

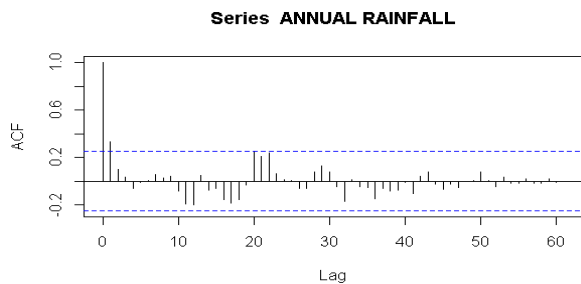


Figure 5. The serial autocorrelation analysis of annual rainfall data, Kasane

3.3 Annual trends in rainfall

On yearly rainfall data from 1958 to 2019, the Mann Kendall trend test was used to examine the precipitation concentration index trend. The Mann Kendall trend test (Table 4) show that the p-values of Gaborone, Francistown, Serowe, and Kasane are greater than the α values suggesting that there is an insignificant trend that indicates an insignificant trend in the rainfall of these regions. Maun, Ghanzi, Pandamatenga and Tsabong's results had a p-value of 0.079, 0.0023, 0.029 and 0.058, respectively,

which is less than the α values. These figures demonstrate that all of these areas are seeing a significant decreasing trend. The findings of the Z-values show a downward trend in all locations.

3.4 Seasonal trends in rainfall

The precipitation concentration index for the seasonal period was analyzed with the Mann Kendall test for all the study regions. The PCI trends for the wet months (Table 5). It shows that the p-values of Gaborone, Francistown, Serowe, Maun, and Ghanzi are more significant than the α values. This suggests an insignificant trend, indicating an insignificant downward trend in Gaborone and Serowe's rainfall. This indicates that rainfall is changing from a regular to an erratic pattern.

Moreover, an insignificant upward trend at Francistown, Maun and Ghanzi was experienced. However, for Pandamatenga and Tsabong, there was a significant upward trend. The test statistic, Z-value, reveals a negative trend for Gaborone, Serowe, Kasane, Pandamatenga and Tsabong. In Gaborone, there exists significance at $\alpha=0.01$.

3.5 Relative Percentage Change analysis performed on annual rainfall data

The RPC in annual rainfall data (Table 4 and 5) indicated that most of the areas that were studied have a negative RPC. The decrease of annual rainfall with the highest percentage change was 0.24% for the region of Ghanzi. While, there was an increase in seasonal rainfall that was experienced (Table 5) at Francistown, Maun and Tsabong at 0.03%, 0.04% and 0.04%, respectively.

3.4 The magnitude of change of annual and seasonal rainfall trends

The analysis of the annual precipitation concentration index (Table 4) using the Theil-Sen slope estimator (β) indicated that the regions of Gaborone, Francistown, Serowe, and Kasane experienced a magnitude of change of the rainfall trend of -1.36 mm/year, -0.16 mm/year, -0.22 mm/year, and -0.50 mm/year, respectively and for all these, there was an insignificant downward trend of rainfall, while the regions of Maun, Ghanzi, Pandamatenga, and Tsabong experienced a magnitude of change of -1.11 mm/year, -1.62 mm/year, -0.33 mm/year and -0.25 mm/year.

Table 4. Annual PCI trends, relative percentage change(% Δ)

Region	Z-Value	p-value	β	\bar{x} (mm)	% Δ
Gaborone	-1.422	0.145	-1.361	452.65	-0.186
Francistown	-0.207	0.836	-0.167	450.27	-0.023
Maun	-0.280	0.080*	-1.115	440.76	-0.157
Ghanzi	-1.634	0.0023***	-1.615	406.69	-0.246
Pandamatenga	-0.268	0.029*	-0.336	652.09	-0.032
Serowe	-0.392	0.695	-0.224	418.03	-0.033
Kasane	-0.504	0.614	-0.500	613.95	-0.051
Tsabong	-0.442	0.058*	-0.253	306.31	-0.051

*** Significant trend at $\alpha=0.01$, * Significant trend at $\alpha=0.05$, * Significant trend at $\alpha=0.1$

Table 5. Seasonal PCI trends, RPC (%Δ)

Region	Z-Value	p-value	β	\bar{x} (mm)	%Δ
Gaborone	-1.0691	0.135*	-0.920	380.06	-0.150
Francistown	0.2734	0.785	0.237	404.85	0.036
Serowe	-0.2794	0.780	-0.200	370.18	-0.033
Kasane	-0.7168	0.474	-0.750	573.69	-0.081
Maun	0.06682	0.947	1.652	406.85	0.041
Pandamatenga	-0.5528	0.040**	-0.600	626.36	-0.059
Ghanzi	0.8686	0.385	1.038	370.01	0.173
Tsabong	-0.23084	0.017***	-0.190	261.10	-0.045

*** Significant trend at $\alpha=0.01$, ** Significant trend at $\alpha=0.05$, * Significant trend at $\alpha=0.1$

The result indicated that there was a significant trend present in Maun, Ghanzi, Pandamatenga and Tsabong. All these regions, except Ghanzi, experienced a downward trend in the rainfall distribution. This is due to the synoptic characteristic of below-average geopotential heights over Ghanzi, which might exacerbate the formation of convective systems, leading to a positive rainfall trend at Ghanzi. [19]. The analysis of the seasonal precipitation concentration index indicated that the regions of Gaborone, Francistown, Serowe, Kasane, Maun and Ghanzi experienced a magnitude of change of -0.92mm/year, -0.24 mm/year, -0.20 mm/year, -0.75 mm/year, 1.65mm/year and -1.04 mm/year, respectively and for all these, there was an insignificant downward trend, except the region of Ghanzi, which experienced an insignificant downward trend in the rainfall distribution. Moreover, the regions of Pandamatenga and Tsabong experienced a magnitude of change of a significant downward trend of -0.60 mm/year and -0.19 mm/year.

In the region of Pandamatenga, the minimum amount of rain received was 341mm in 1965, while the maximum amount was 1122mm in the year 1958, and the average rainfall received in a year was 589mm. Pandamatenga is one of the regions that receive a significant amount of rain during the rainy season. Still, as indicated, it is experiencing insignificant declines in the amount of rainfall (Figure 6).

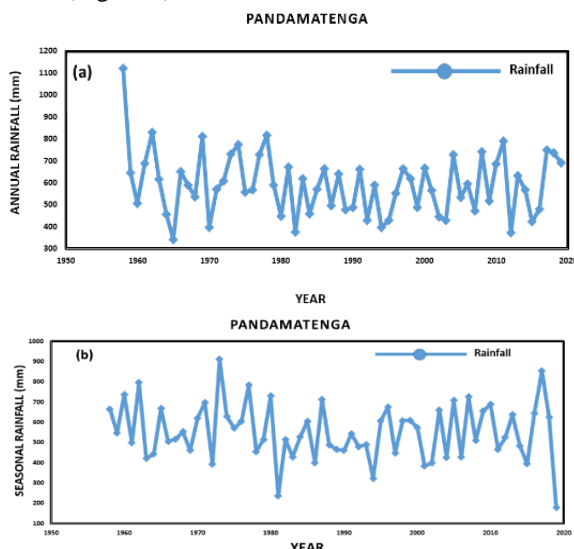


Figure 6. Pandamatenga trend (a) Annual rainfall, (b) Seasonal rainfall

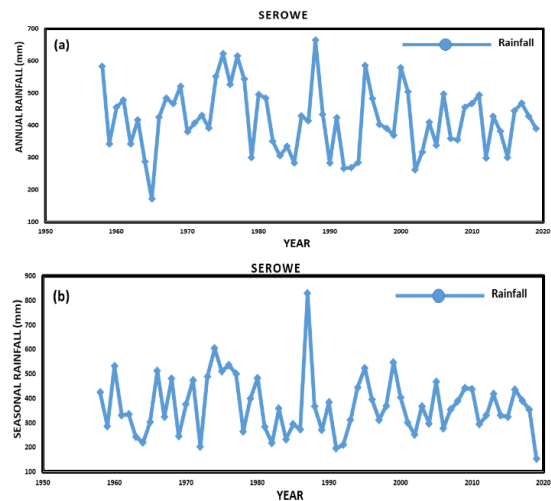


Figure 7. Serowe trend (a) Annual rainfall, (b) Seasonal rainfall

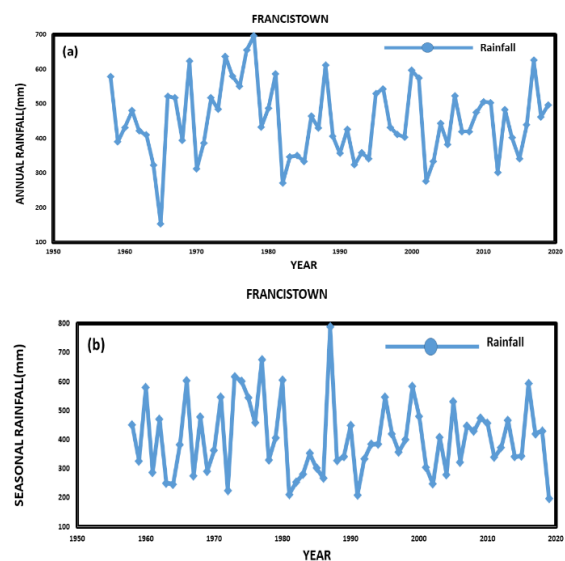


Figure 8. Francistown trend (a) annual rainfall, (b) seasonal rainfall

In the region of Serowe, the minimum amount of rain that was received was 172 mm in the year 1965, while the maximum amount was 665 mm in the year 1988. The average rainfall was 418mm (Figure 7). Although insignificant, there is a decline annually and seasonally in Serowe.

The minimum amount of rain received in the Francistown region was 153 mm in 1965. The maximum amount was 697mm in 1978, and the average rainfall

received in a year was 450 mm. Francistown gets a significant amount of rain annually and is the second-highest inhabited location. It is Botswana's second capital city.

In the region of Maun, the minimum amount of rainfall that was received was 235 mm in the year 1965, while the maximum amount was 792 mm in the year 1974. The average rainfall received in a year was 440mm. Maun gets a significant amount of rain annually and has similar climatic characteristics to Pandamatenga.

In the region of Serowe, the minimum amount of rain that was received was 172 mm in the year 1965, while the maximum amount was 665 mm in the year 1988. The average rainfall received in a year was 418mm. Serowe gets a significant amount of rain annually compared to its neighbouring regions.

4. Conclusion

The analysis of spatio-temporal rainfall trends and rainfall variability in Botswana demonstrated a decrease in rainfall across the regions of Botswana. The annual rainfall

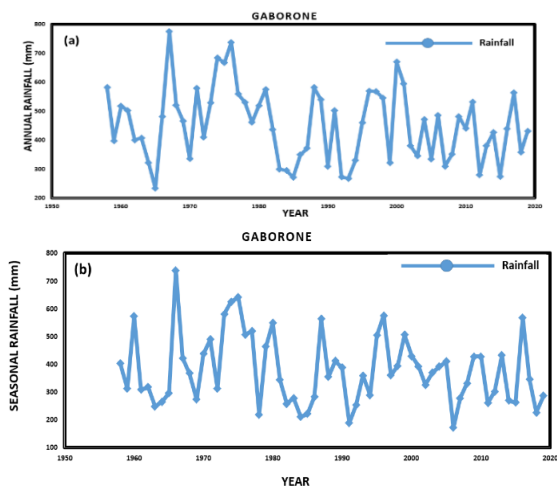


Figure 9. Gaborone trend (a) annual rainfall, (b) seasonal rainfall

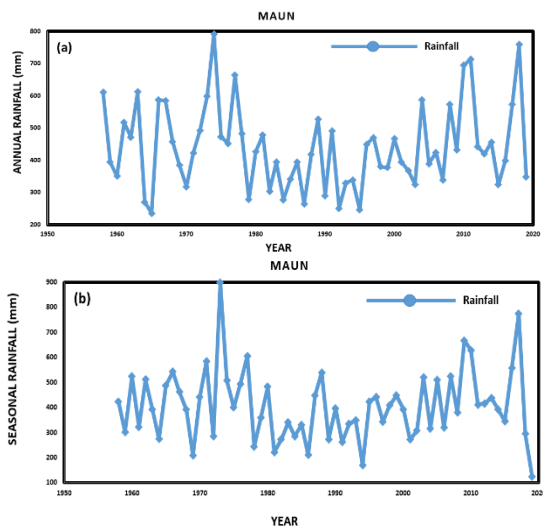


Figure 10. Maun trend (a) annual rainfall, (b) seasonal rainfall

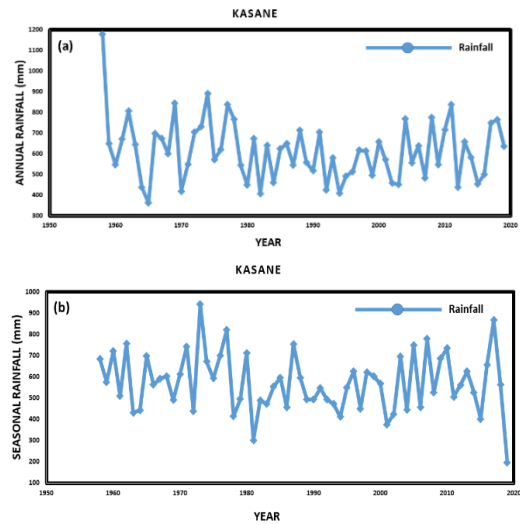


Figure 11. Kasane trend (a) annual rainfall, (b) seasonal rainfall trend

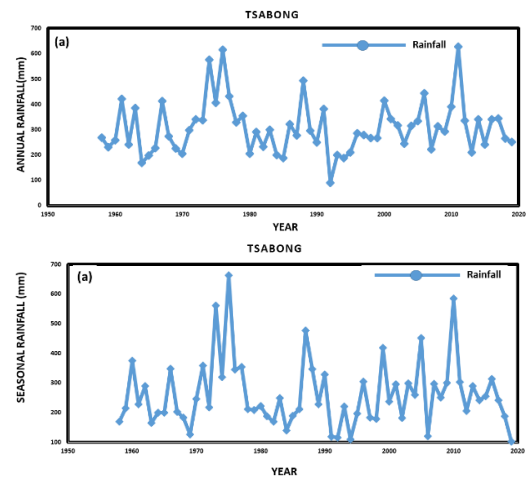


Figure 12. Tsabong trend (a) annual rainfall, (b) seasonal rainfall

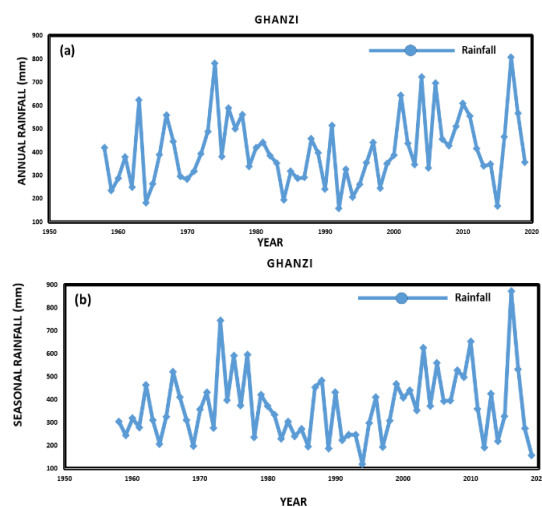


Figure 13. Ghanzi trend (a) annual rainfall, (b) seasonal rainfall experienced a magnitude of change that has a significant downward trend of -1.11 mm/year at Maun, -1.62 mm/year at Ghanzi, -0.33 mm/year at Pandamatenga -0.25 mm/year at Tsabong.

Table 6. Comparison of other related studies with this study

Country	Regions	Period	Method	PCI	RPC	Ref.
Nigeria	Bida, Jos, Yola, Yelwa, Minna, Bauchi, Kaduna, Maiduguri, Kano, Gusau, Sokoto, Nguru, Katsina	1970-2016	PCI, MK trend test, Sen Slope Estimator, RPC	11-15, 16-20, and PCI > 20	Varying changes from the different regions	[7]
India	Andrah Pradesh	1981-2010	PCI, Linear Regression Analysis, Descriptive Statistics	> 16	-	[49]
Iran	Iran	1961-2010	MK trend test, Sequential MK test, Homogeneity Test	< 10	-	[50]
Turkey	Euphrates-Tigris Basin	1987-2011	MK trend test, Sen Slope	-	-	[51]
China	Jiangxi Province	1960-2008	PCI, MK trend test	> 16	-	[52]
Botswana	Maun, Ghanzi, Tsabong, Tshane	1971-2000	MK trend test	-	-	[19]
Botswana	Francistown, Ghanzi, Kasane, Lobatse, Maun, Molepolole, Serowe, Tsabong	1975-2005	Thom Test, MK trend test	-	-	[20]
Botswana	Ghanzi, Maun, Serowe, Tsabong	1975-2005	Descriptive Statistics, MK trend test	-	-	[37]
Botswana	Francistown, Gaborone, Mahalapye, Maun, Ghanzi, Shakawe, Tsabong, Tshane	1965-2008	Intervention Analysis, Correlation Analysis, GLM model	-	-	[21]
Botswana	Gaborone, Francistown, Serowe, Kasane, Maun, Pandamatenga Ghanzi, Tsabong	1958-2019	PCI, MK trend test, RPC, Sen Slope Estimator,	PCI>10≤15, PCI>16≤20 and >20	Varying changes from the different regions	This Study

While the annual rainfall with insignificant downward trends have a magnitude of change which was found to be -1.36 mm/year at Gaborone, -0.16 mm/year at Francistown, -0.22 mm/year at Serowe -0.50 mm/year at Kasane, respectively. The seasonal rainfall with significant downward trends have a magnitude of change that was between -0.60 mm/year at Pandamatenga and -0.19 mm/year at Tsabong. While the seasonal rainfall with insignificant downward trends have a magnitude of change that was between -0.92mm/year at Gaborone, -0.24 mm/year at Francistown, -0.20 mm/year at Serowe, -0.75 mm/year at Kasane, 1.65mm/year at Maun and -1.04 mm/year at Ghanzi respectively. All these regions, except Ghanzi, experienced a downward trend in the rainfall distribution. This is owing to the synoptic characteristic of below-average geopotential heights over Ghanzi, which might enhance the formation of convective systems, leading to a positive rainfall trend at Ghanzi. The Mann-Kendall trend test (MK), autocorrelation function (ACF), relative percentage change (RPC), precipitation concentration index (PCI), and Theil-Sen's slope estimator (β) methods were adopted for data analysis in eight regions of Botswana (Figure 6,7,8,9,10,11,12, and 13).

These findings indicate that Botswana is already impacted by climate change due to the reduction in yearly rainfall amounts, meaning that significant problems are likely to arise because Botswana is water-scarce and heavily depends on groundwater, causing economic and industrial imbalance. Drier conditions signify more considerable variability in the amount of rain that the country is currently receiving.

Declaration

The authors declared no potential conflicts of interest with respect to the research, authorship, and/or publication of this article. The authors also declared that this article is original, was prepared in accordance with international publication and research ethics, and ethical committee permission or any special permission is not required.

Author Contributions

H. Gökçekuş, supervised and developed the work, Y. Kassem, supervised and improved the improved manuscript. L.P. Mphinyane developed methodology, performed analysis, developed and improved manuscript.

Nomenclature

SASSCAL : Southern African Science Service Centre for Climate Change and Adaptive Land Management

ACSL : Applied Climate Science Lab

UW : University of Washington

GEV : General Extreme Value

UN : United Nations

UNFCC : United Nations Framework Convention On Climate Change

DWA : Department of Water Affairs

IWMI : International Water Management Institute.

WUC : Water Utilities Corporation

CSO : Central Statistics Office

DMS : Department of Meteorological Services

ENSO : El-Nino Southern Oscillation

SADC : Southern African Development Community

WBG : World Bank Group

CV : Coefficient of Variation

MIN : Minimum

MAX : Maximum

G	: Skewness Coefficient
STAT	: Statistics
GEN	: General
PDF	: Probability Distribution Function
Mm	: Millimeter
MK	: Mann Kendall
PCI	: Precipitation concentration index
RAI	: Rainfall anomaly index
SI	: Seasonality index
DAR	: Departure analysis of rainfall

References

- Fauchereau N., Trzaska S., Rouault M., Richard Y., *Rainfall variability and changes in Southern Africa during the 20th century in the global warming context*. Natural Hazards, 2003. **29**(2): p. 139-154.
- Marumbwa FM, Cho MA, Chirwa PW, *Analysis of spatio-temporal rainfall trends across southern African biomes between 1981 and 2016*. Physics and Chemistry of the Earth, 2019. **114**(August): p. 102808.
- Archer ERM, Landman WA, Tadross MA, et al., *Understanding the evolution of the 2014–2016 summer rainfall seasons in southern Africa: Key lessons*. Climate Risk Management, 2017. **16**: p. 22-28.
- Solomon, S., D. Qin, M. Manning, Z. Chen, M. Marquis, K.B. Averyt MT and HLM, *IPCC, 2007: Climate Change 2007: The Physical Science Basis. Contribution of Working Group I to the Fourth Assessment Report of the Intergovernmental Panel on Climate Change.*; 2007.
- Pachauri RK, Meyer LA, *IPCC, 2014: Climate Change 2014: Synthesis Report. Contribution of Working Groups I, II and III to the Fifth Assessment Report of the Intergovernmental Panel on Climate Change*. Published online 2014: p. 151.
- Ghosh S, Mujumdar PP, *Climate change impact assessment: Uncertainty modeling with imprecise probability*. Journal of Geophysical Research Atmospheres, 2009. **114**(18).
- Ibrahim I, Usman MT, Abdulkadir A, Emigilati MA, *Analysis of Rainfall Distribution, Temporal Trends, and Rates of Change in the Savannah Zones of Nigeria*. Atmosphere - Ocean, 2020. **58**(5): p. 351-360.
- Cook C, Reason CJC, Hewitson BC, *Wet and dry spells within particularly wet and dry summers in the South African summer rainfall region*. Climate Research, 2004. **26**(1): p. 17-31.
- Vuille M, Bradley RS, Healy R, et al., *Modeling $\delta 18O$ in precipitation over the tropical Americas: 2. Simulation of the stable isotope signal in Andean ice cores*. Journal of Geophysical Research: Atmospheres, 2003. **108**(6).
- Ahmadalipour A, Moradkhani H, Demirel MC, *A comparative assessment of projected meteorological and hydrological droughts: Elucidating the role of temperature*. Journal of Hydrology, 2017. **553**: p. 785-797.
- Duboviy O, Ghazaryan G, González J, Graw V, Löw F, Schreier J, *Drought hazard in Kazakhstan in 2000–2016: a remote sensing perspective*. Environmental Monitoring and Assessment, 2019. **191**(8).
- Oguntunde PG, Abiodun BJ, Lischeid G, *Rainfall trends in Nigeria, 1901-2000*. Journal of Hydrology, 2011. **411**(3-4): p. 207-218.
- Cannarozzo M, Noto L V., Viola F, *Spatial distribution of rainfall trends in Sicily (1921-2000)*. Physics and Chemistry of the Earth, 2006. **31**(18): p. 1201-1211.
- Ogunrinde AT, Oguntunde PG, Akinwumiju AS, Fasinmirin JT, *Analysis of recent changes in rainfall and drought indices in Nigeria, 1981–2015*. Hydrological Sciences Journal, 2019. **64**(14): p. 1755-1768.
- Botswana Environment Statistics: Climate Digest*. 2019. [cited 2021 01 February]; Available from: <https://www.statsbots.org/bw/sites/default/files/publication/s/Climate%20Digest%20%202019.pdf>.
- Adedoyin J. A. and Mphale K., *Climate Variability: Its Impacts and Mechanism Within The Kalahari Transect of Southern Africa*. in Mali Symposium on Applied Sciences. Bamako: p. 120-135.
- Matarira CH, Jury MR, *Contrasting meteorological structure of intra-seasonal wet and dry spells in Zimbabwe*. International Journal of Climatology, 1992. **12**(2): p. 165-176.
- Worldbank, *Climate Change Knowledge Portal*. [cited 2021 10 February]; Available from: <https://climateknowledgeportal.worldbank.org/country/botswana/climate-data-historical>
- Mphale KM, Dash SK, Adedoyin A, Panda SK, *Rainfall regime changes and trends in Botswana Kalahari Transect's late summer precipitation*. Theoretical and Applied Climatology, 2014. **116**(1-2): p. 75-91.
- Batisani N, Yarnal B, *Rainfall variability and trends in semi-arid Botswana: Implications for climate change adaptation policy*. Applied Geography, 2010. **30**(4): p. 483-489.
- Kenabatho PK, Parida BP, Moalafhi DB, *The value of large-scale climate variables in climate change assessment: The case of Botswana's rainfall*. Physics and Chemistry of the Earth, 2012. **50-52**: p. 64-71.
- Da Silva VDPR, *On climate variability in Northeast of Brazil*. Journal of Arid Environments, 2004. **58**(4): p. 575-596.
- Lázaro R, Rodrigo FS, Gutiérrez L, Domingo F, Puigdefábregas J, *Analysis of a 30-year rainfall record (1967-1997) in semi-arid SE Spain for implications on vegetation*. Journal of Arid Environments, 2001. **48**(3): p. 373-395.
- Alemayehu A, Bewket W, *Local spatiotemporal variability and trends in rainfall and temperature in the central highlands of Ethiopia*. Geografiska Annaler, Series A: Physical Geography, 2017. **99**(2): p. 85-101.
- Groleau A, Maillhot A, Talbot G, *Trend analysis of winter rainfall over southern Québec and New Brunswick (Canada)*. Atmosphere - Ocean, 2007. **45**(3): p. 153-162.
- Muhire I, Ahmed F, *Spatiotemporal trends in mean temperatures and aridity index over Rwanda*. Theoretical and Applied Climatology, 2016. **123**(1-2): p. 399-414.
- Recha JW, Mati BM, Nyasimi M, Kimeli PK, Kinyangi JM, Radeny M, *Changing rainfall patterns and farmers' adaptation through soil water management practices in semi-arid eastern Kenya*. Arid Land Research and Management, 2016. **30**(3): p. 229-238.
- Che Ros F, Tosaka H, Sidek LM, Basri H, *Homogeneity and trends in long-term rainfall data, Kelantan River Basin, Malaysia*. International Journal of River Basin Management, 2016. **14**(2): p. 151-163.
- Nenwiini S, Kabanda TA, *Trends and Variability Assessment of Rainfall in Vhembe South Africa*. Journal of Human Ecology, 2013. **42**(2): p. 171-176.
- Ahokpossi Y, *Analysis of the rainfall variability and change*

- in the Republic of Benin (West Africa). *Hydrological Sciences Journal*, 2018. **63**(15-16): p. 2097-2123.
31. Wang Y, Xu Y, Tabari H, et al., *Innovative trend analysis of annual and seasonal rainfall in the Yangtze River Delta, eastern China*. *Atmospheric Research*, 2020. **231**(37): p. 104673.
 32. Elzopy KA, Chaturvedi AK, Chandran KM, Gopinath G, Naveena K, Surendran U, *Trend analysis of long-term rainfall and temperature data for Ethiopia*. *South African Geographical Journal*, 2021. **103**(03): p. 381-394.
 33. Sezen C, Partal T, *Wavelet combined innovative trend analysis for precipitation data in the Euphrates-Tigris basin, Turkey*. *Hydrological Sciences Journal*, 2020. **65**(11): p. 1909-1927.
 34. TOKGÖZ S, PARTAL T, *Trend Analysis with Innovative Sen and Mann-Kendall methods of Annual Precipitation and Temperature data in the Black Sea Region*. *Journal of the Institute of Science and Technology*, 2020. **10**(2): p. 1107-1118.
 35. Harmse CJ, Du Toit JCO, Swanepoel A, Gerber HJ, *Trend analysis of long-term rainfall data in the Upper Karoo of South Africa*. *Transactions of the Royal Society of South Africa*, 2021. **76**(1): p. 1-12.
 36. Rahardjo H, Nistor MM, Gofar N, Satyanaga A, Xiaosheng Q, Chui Yee SI, *Spatial distribution, variation and trend of five-day antecedent rainfall in Singapore*. *Georisk*, 2020. **14**(3): p. 177-191.
 37. Byakatonda J, Parida BP, Moalafhi DB, Kenabatho PK, *Analysis of long term drought severity characteristics and trends across semiarid Botswana using two drought indices*. *Atmospheric Research*, 2018. **213**(March): p. 492-508.
 38. Tsheko R, *Rainfall reliability, drought and flood vulnerability in Botswana*. *Water SA*, 2003. **29**(4): p. 389-392.
 39. Byakatonda J, Parida BP, Kenabatho PK, Moalafhi DB, *Prediction of onset and cessation of austral summer rainfall and dry spell frequency analysis in semiarid Botswana*. *Theoretical and Applied Climatology*, 2019. **135**(1-2): p. 101-117.
 40. Michiels P, Gabriels D, Hartmann R, *Using the seasonal and temporal Precipitation concentration index for characterizing the monthly rainfall distribution in Spain*. *Catena*, 1992. **19**(1): p. 43-58.
 41. Mondal A, Khare D, Kundu S, *Spatial and temporal analysis of rainfall and temperature trend of India*. *Theoretical and Applied Climatology*, 2015. **122**(1-2): p. 143-158.
 42. He Y, Ye J, Yang X, *Analysis of the spatio-temporal patterns of dry and wet conditions in the Huai River Basin using the standardized precipitation index*. *Atmospheric Research*, 2015. **166**: p. 120-128.
 43. Oguntunde PG, Lischeid G, Abiodun BJ, Dietrich O, *Analysis of long-term dry and wet conditions over Nigeria*. *International Journal of Climatology*, 2017. **37**(9): p. 3577-3586.
 44. Wang X, Huang G, Liu J, *Journal of geophysical research*. *Nature*, 1955. **175**(4449): p. 238.
 45. Janni W, Nitz U, Rack BK, et al., *Pooled analysis of two randomized phase III trials (PlanB/SuccessC) comparing six cycles of docetaxel and cyclophosphamide to sequential anthracycline taxane chemotherapy in patients with intermediate and high risk HER2-negative early breast cancer (n=5,9)*. *Journal of Clinical Oncology*, 2018. **36**(15_suppl): p. 522-522.
 46. PK. S, *Estimates of the regression coefficient based on Kendall's tau*. *Journal of the American statistical association*, 1968. **63**(324): p. 1379-1389.
 47. Tabari H, Somee BS, Zadeh MR, *Testing for long-term trends in climatic variables in Iran*. *Atmospheric Research*, 2011. **100**(1): p. 132-140.
 48. Tabari H, Hosseinzadeh Talae P, *Moisture index for Iran: Spatial and temporal analyses*. *Global and Planetary Change*, 2013. **100**: p. 11-19.
 49. Valli M, Sree KS, Krishna IVM, *Analysis of Precipitation Concentration Index and Rainfall Prediction in various Agro-Climatic Zones of Andhra Pradesh, India*. 2013. **2**(5): p. 53-61.
 50. Araghi A, Mousavi-Baygi M, Adamowski J, *Detection of trends in days with extreme temperatures in Iran from 1961 to 2010*. *Theoretical and Applied Climatology*, 2016. **125**(1-2): p. 213-225.
 51. Ay M, Karaca ÖF, Yildiz AK, *Comparison of Mann-Kendall and Sen's innovative trend tests on measured monthly flows series of some streams in Euphrates-Tigris Basin*. *Keywords. Erciyes Üniversitesi Fen Bilimleri Enstitüsü Dergisi*, 2018. **34**(1): p. 78-86.
 52. Huang J, Sun S, Zhang J, *Detection of trends in precipitation during 1960-2008 in Jiangxi province, southeast China*. *Theoretical and Applied Climatology*, 2013. **114**(1-2): p. 237-251.

**Research Article**

Investigation of proper material selection for rainwater harvesting in squares having higher urban heat island effect potential: KBU Social Life Center example

Sibel Temizkan ^a  and Merve Tuna Kayılı ^{b,*} 

^aKarabuk University, Institute of Graduate Sciences, Karabük, 78050, Turkey

^bKarabuk University, Department of Architecture, Safranbolu, 78600, Turkey

ARTICLE INFO*Article history:*

Received 26 June 2021

Revised 14 October 2021

Accepted 10 November 2021

Keywords:

Material selection

Rainwater harvesting,

Urban heat island,

Urban top cover

ABSTRACT

With the revolution in industrialization, the gas amount emitted into the atmosphere grew, causing global warming and climate change. This developing shift has a detrimental impact on natural resources and hastens their decline. Water is one of the natural resources that has been impacted. Water scarcity is becoming a problem due to causes known to be urbanization, population increase and climate change. With regards to sustainable architecture, rainwater collection from buildings for its efficient use, application of simple water treatment processes and its reuse are considered to be among the precautions that may be taken in order to save water. In addition to playing a role in reducing water resources, urbanization has another detrimental characteristic, such as creating heat islands with highly impermeable surfaces. Top cover designs that promote green spaces and minimize heat island impacts are the most effective way for minimizing the detrimental effects that heat islands have on outdoor thermal comfort in urban settings. Therefore, a top cover was proposed in this study for mitigating the effect of heat island observed in KBU Social Life Center square that may be characterized as a vast heat island within the campus, as well as to bring it in feature of collecting rainwater in its immense area. Materials to be used in the proposed top cover as well as the factors affecting the selection of material were determined in terms of efficiency in rainwater collection and the mitigation of urban heat island effect. A considerably optimum material that can be used in the cover was determined by one of the multi-criteria decision-making methods known to be PROMETHEE method. As a consequence of its pricing, roof efficiency, and albedo coefficient qualities, the polycarbonate panel material has been chosen as the most acceptable material to be used for the suggested top cover.

1. Introduction

With the rapid increase in world population and industrialization, the limited natural resources are either being destroyed or wasted day by day. Since the first day of industrialization, intense competition in the industry has caused the wheels to spin and the machines to be operated faster, which increased the need for fossil fuels each passing day. Based on this consumption and production spiral, these economic activities have caused global warming by accelerating the emission of CO₂ gas. Therefore, the natural life cycle has changed as a result of increasing, changing, and developing human activities. On the other hand, by affecting the natural resources

negatively, this change causes them to reduce and eventually deplete. One of the natural resources used up the most is water resources [1-3].

In addition to meeting the basic needs of people, water also plays an important role as a source of development in areas such as energy generation, industry, tourism, transport, and agriculture. However, each passing year, new countries are added to the list of water-scarce countries. Although Turkey does not take place on that list, it does not have sufficient water resources either. In Turkey, 73% of the water resources are used in irrigation, 16% in urban consumption, and 11% in industries [4, 5]. With its usable water amount of 1500m³ per person, it is among the countries approaching physical water scarcity.

* Corresponding author. Tel.: +90-370-418-8582; Fax: +90-370-418-8330.

E-mail addresses: sibelakmunarli@gmail.com (S. Temizkan), mervetunakayili@karabuk.edu.tr (M. Tuna Kayılı)

ORCID: 0000-0003-1755-1290 (S. Temizkan), 0000-0002-3803-8229 (M. Tuna Kayılı)

DOI: 10.35860/iarej.957829

© 2021, The Author(s). This article is licensed under the CC BY-NC 4.0 International License (<https://creativecommons.org/licenses/by-nc/4.0/>).

In case of an increase in the country's population to 100 million, it is predicted that the amount of usable water per person will decrease to 1100m³ [4, 5].

According to the World Population Prospects Report published by the UN Department of Economic and Social Affairs in 2017, the world population has reached 7.6 billion. The world population is expected to reach 8.6 billion by 2030, 9.8 billion by 2050, and 11.2 billion by the end of the century. This increase means that the world population will increase by 2.2 billion from 2017 to 2050 [4]. The rise in world population affects water resources in two ways. The first one is the decrease in the rate of water per person and the faster consumption of water resources, and the second one is the inability to ensure the continuity of water resources due to the widespread urbanization emerging to meet the housing needs of the increasing population [3- 5].

In addition to the water scarcity caused by the increase in urbanization, water-impermeable areas form urban heat islands, which in turn causes increasing temperatures in urban areas. The urban heat island (UHI) effect is defined as increased night temperature in urban areas caused by heat absorption on pavement and concrete surfaces due to anthropogenic climate change and reduced cooling by evaporation [6, 7]. Urban life quality is highly affected by harsh climatic conditions and high temperatures, and UHI's have adverse consequences that cause unsuitable temperature conditions, health problems, and diseases. Rising temperatures directly affect the energy consumed for cooling buildings and pose a greater risk of disease and eventually death [8-12] by transforming the city center and squares into thermally uncomfortable areas especially in summer [13]. Therefore, to mitigate the effects of UHI, it is essential to take into account environmental protection policies while planning and designing the cities [14-16].

Accordingly, the city centers face higher temperatures in urban areas. Factors, such as thermo-optical properties and albedo values of building materials resulting from the physical structure of the city, increasing in surface roughness, visual limitations due to street width and building height, anthropogenic warming, air pollutants, and decrease in water and humidity, cause cities to exhibit different climatic characteristics compared to their surroundings. Roofs are the surfaces most exposed to sunlight in urban areas. Therefore, roof and cover designs and material selection to be made for these designs play an important role in mitigating the urban heat island effect [17-19].

Considering solutions for the water crisis and urban heat islands can ensure the determination of a standard solution for both problems. In this context, the idea of rainwater collection in urban cover designs offering an effective solution in urban heat island areas is essential in terms of mitigating the UHI effect in the urban area and in saving

rainwater by collecting it. The cover design and the covering material required to have the property of both eliminating the heat island effect and allowing efficient water collection has revealed the problem of covering material selection for a square with a high urban heat island effect. It is thought that a cover system to be designed with an optimum and appropriate material for these properties will mitigate the heat island in the square; thus, an efficient water collection will be able to be achieved. In this study, the square of Karabük University Social Life Center (SLC) serving a large number of users was chosen as the sample study area. The aim was to collect rainwater in the square having a heat island effect with higher efficiency. The materials to be used in the proposed urban cover design for the square were determined by taking into account their properties that were based on rainwater collection efficiency. The mitigation of the heat island effect was targeted, and it was aimed to select the optimum material by using the multi-criteria decision-making (MCDM) method. Furthermore, the annual volume of rainwater that could be obtained using the cover system was determined for the SLC Square.

Since any study using both the MCDM method and material selection at a time in a cover system design for rainwater harvesting as well as reducing the heat island effect was not encountered in the literature review, this can be shown as the original aspect of this study. In addition, this study is the first of its kind in terms of that it was applied to the Social Life center designed as a common use area within a public university campus and also it proposes a top cover system reducing the heat island effect by harvesting rainwater. These features of this study are expected to guide the architects, landscape architects, and decision-makers in the selection of materials for top cover design.

In the studies planned to be conducted in the future, the form of the top cover, different roofing materials to be proposed, and the determination of suggestions for effective rainwater harvesting and mitigating the urban heat island effect will contribute to the literature on this subject.

2. Material and Method

2.1 Case Study and Climate Data

Karabük University Social Life Center (SLC) located in the Demir Çelik Campus was established on an area of 8957m², and its total construction area is 1320 m². The roof area of the center planned for the rain harvesting is 1500m² and it has been designed as a flat walkable terrace roof with reinforced concrete floor. The square area belonging to the center is 5136m² and it is covered with marble. The square part also constitutes the roof of the SLC dining hall located on the ground floor (Figure 1) [20].

The climate type effective in Karabük is mainly seen in the Black Sea coastal belt of the Marmara Region and the north-facing parts and the mountains of the region. There is not much temperature difference between the summer and winter seasons. While the summer months are relatively calm, the winter months are warm in the coastal area but cold and snowy in the higher regions. Since there is precipitation in almost all seasons, there is usually no water shortage. The natural vegetation in higher areas comprises coniferous forests that grow in humid and cold conditions, while it is composed of moist broad-leaf forests in the coastal areas [21]. The average temperatures of January, the coldest month, and July, the warmest month are 4.2°C and 22.1°C, respectively, and the annual average temperature is 13°C [22]. Karabük is located inside the seaside, where the climate characteristics of the Western Black Sea region are only partially observed, and it is not able to benefit sufficiently from the humid air of the Black Sea. Although it has the characteristic features of the terrestrial climate, dry summers and cold winter temperatures are not observed as much as in the Central Anatolia region. Coniferous forests are seen in the inner parts, while broad-leaved forests are seen in the coastal areas [21].

The average annual precipitation in Karabük is 542 mm. Most rainfall is seen in the spring and winter months. Although Karabük receives rain every season due to the Black Sea climate, there are short-term droughts in July and August. Therefore, precipitation is relatively less during these months than in others. The share of summer precipitation in the annual total is 19.4% [22]. The precipitation data of the years between 1980 and 2018 obtained from the station information database of the Karabük Province Meteorological Department were analyzed in the SPSS 22 statistical package program, and standard deviations for years, seasons, and months were calculated accordingly. Based on the results, the deviation rate was found to be ± 7.62 liters considering the annual data. In line with these results, it was concluded that the average precipitation data of the last five years would be sufficient for calculations.

Monthly average precipitation data for the previous five years is given in Table 1. In accordance with the data obtained from the Karabük Meteorology Department, the average amount of precipitation for five years is observed to be 542 mm/year. The highest precipitation occurs in June with an average of 76.5 mm/year [20].

2.2 Material Selection

Various criteria come to the forefront while determining the most appropriate coating material alternatives for the top cover to be carried by the steel space frame system. These criteria can be shown as the price of materials, roof efficiency coefficient, albedo value, thermal conductivity, intrinsic heat, and emissivity [24, 25]. Based on the studies conducted so



Figure 1. Karabük University Social Life Center [23]

far, the materials that can be recommended as top cover materials can be listed as follows [26]: Glass, Membrane, Aluminum, PVC coating, PTFE coating, Polycarbonate panel, Shingle coating, Galvanized sheet. The materials that can be used in the top cover recommended for Karabük University SLC square and their properties are given in Table 2.

2.3 Multi-Criteria Decision Method and PROMETHEE

To make accurate strategic decisions and selections, MCDM (Multi-Criteria Decision Making) methods enable decision-makers to solve various methods. Thus, by evaluating the determined alternatives in the best possible way, the most appropriate decision can be made. When it is required to make a selection among determined choices, multi-criteria decision-making methods are used to make the right decision. These methods are as follows [27, 28]:

- Basic Methods: Weighted Sum and Weighted Product Methods
- Valuable Combined Criteria Methods: AHP, TOPSIS, Gray Relation Method, Fuzzy TOPSIS
- Outranking Methods: Classified as ELECTRE and PROMETHEE (Preference Ranking Organization Method for Enrichment of Evaluations).

AHP: The AHP method is one of the most widely used MCDM methods in the literature. In the AHP method, the hierarchical structure of complex units, pairwise comparison, many criteria, eigenvector and consistency coefficient are used in the creation of weight coefficients. Among the usage areas of AHP, there are topics such as planning, choosing the best alternative, resource allocations, troubleshooting, and optimization [28, 29].

TOPSIS: With this method, among multi-criteria decisions, which one is the closest to the positive ideal solution and the farthest from the negative ideal solution can be evaluated. It has application opportunities in many areas such as risk and performance evaluation of enterprises in multi-purpose inventory planning [30].

Gray Relation Method: The GIA method is one of the widely used MCDM methods and has been developed for the analysis of relationships in cases of uncertainty caused by incomplete data or incomplete information [33].

Table 1. Monthly average precipitation data of Karabük province [22]

Year/Month	1	2	3	4	5	6	7	8	9	10	11	12	Total
2014	48.2	7.0	27.9	80.7	81.7	110.7	24.3	16.7	105.7	108.1	18.5	80.9	710.4
2015	45.2	26.1	42.5	32.8	18.1	111.6	0.4	6.7	40.0	52.3	60.8	62.3	498.8
2016	77.2	64.4	21.2	50.9	116.8	12.6	4.1	3.2	41.9	5.6	29.4	60.4	487.7
2017	30.6	29.0	26.7	37.6	45.1	79.5	23.4	26.4	2.0	75.3	70.1	44.4	490.1
2018	27.9	23.6	120.5	8.6	43.5	68.1	66.8	4.1	20.5	56.8	39.9	44.0	524.3
Average (mm/year)	45.8	30.0	47.7	42.1	61	76.5	23.8	11.4	42	59.6	43.7	58.4	542

Table 2. Materials that can be used in cover and their properties [31, 32]

Materials	Unit Price	Roof Efficiency Coefficient	Albedo	Thermal Conductivity (W/(m*K))	Specific Heat (J/kg °C)	Emissivity
Glass (10mm)	1500	0.9	0.7	1.0000	0.7530	0.84
Membrane	311	0.9	0.76	0.1380	2.0920	0.95
Aluminum	445	0.85	0.75	230.0000	0.8970	0.20
PVC	400	0.9	0.83	0.1670	1.6740	0.95
PTFE	622	0.9	0.69	5.5600	1.0040	0.95
Polycarbonate panel	29.8	0.9	0.86	0.1920	1.6740	0.95
Shingle	24	0.9	0.21	0.1200	1.2600	0.85
Galvanized sheet	19.3	0.85	0.4	53.0000	0.4800	0.4

Fuzzy TOPSIS: In the TOPSIS method, an index called positive – similarity to the ideal solution and negative – distance to the ideal solution is defined. As a result of this definition, the technique selects an option that is the most similar to the ideal answer. [34].

ELECTRE: The ELECTRE method is one of the MCDM methods, which is a technique that can interpret problems that dominate numerical calculations by converting them to verbal situations [35]. The ELECTRE method is a systematic analysis that compares all possible pairs of different alternatives regarding the criteria and reveals the values of alternatives based on these criteria [36]. Various criteria affect the selection at the decision stage, and the importance of these criteria relative to each other will lead the decision-maker to the most appropriate alternative. However, choosing the best among the alternatives is complicated. Each alternative may have different advantages over the other. Because it is pretty difficult to find exact solutions to such problems, some criteria are minimized while others are maximized. In such cases, PROMETHEE is a highly functional decision-making and ranking method that will make the closest optimum selection suitable for the purpose [37]. The PROMETHEE method, one of the most effective and frequently used methods in problem-solving today, has been developed based on the drawbacks of current preference methods in the literature [38]. Accordingly, the method evaluates the alternatives required for the decision-making problem based on determined preference functions and determines partial and complete preferences with the

paired comparison technique. In the literature, there are many studies conducted in different fields by using the PROMETHEE method [39-50]. In this context, in this study, the PROMETHEE method was chosen to rank the coating material to be used in the cover proposed based on the properties given in Chapter 2 and eventually to select the optimum material. The Best Worst Method (BWM) was used to calculate the weights of the criteria used in the PROMETHEE method. In the context of this method, a survey was conducted on experts and academicians working in the material sector in Turkey to determine the importance weights of the main parameters in material selection. The reason for choosing experts and academicians in this study was to reach more realistic data by taking both theoretical and practical opinions. However, since it was impossible to get the population due to time and cost constraints, data were collected using snowball sampling, which is among non-random sampling methods. 104 online questionnaire forms were collected from experts and academicians. 12 out of the 104 forms were excluded as they were incomplete and inaccurate. Therefore, the total number of questionnaires included in the analysis was 92. Analyses were done using the SPSS software. The results of the frequency analysis regarding the answers given by the participants, including experts and academicians, in determining the importance weights of the criteria are shown in Table 3.

After obtaining the survey data, the multi-criteria decision problem was defined and the criteria were weighted using the excel file created by Rezaei [51, 52].

Table 3. The degree of importance given to criteria by participants [31, 32]

Job		Price	Roof efficiency	Albedo	Emissivity	Specific heat	Thermal conductivity
Expert	Average	7	8.02	7.67	8.02	7.55	8.17
	N	40	40	40	40	40	40
	Std. deviation	1.98	1.60	1.80	1.56	1.48	0.98
Academician	Average	7.11	7.78	8.01	7.84	7.28	8.03
	N	52	52	52	52	52	52
	Std. deviation	1.95	1.60	1.14	1.05	1.57	1.58
Total	Average	7.06	7.89	7.86	7.92	7.40	8.09
	N	92	92	92	92	92	92
	Std. deviation	1.96	1.59	1.46	1.29	1.53	1.35

Table 4. Averages and criterion weights calculated using the BWM method

Criteria	Average	Weighting by means (%)	Weighting with the Best Worst Method (BWM)
Price	7.06	15.28	0.142
Roof efficiency coefficient	7.89	17.07	0.142
Albedo value	7.86	17	0.142
Thermal conductivity coefficient	8.09	17.50	0.285
Specific heat	7.40	16.01	0.142
Emissivity	7.92	17.14	0.142
Total	46.22	100	1

Table 5. Roof coefficients according to roofing material

Roof Material	Roof Coefficient
Concrete	0.70
Metal-Tile-Marble (glazed tiles)-Glass-Membrane-PVC-PTFE-Polycarbonate panel-Shingle	0.90
Aluminum-Galvanized sheet	0.80

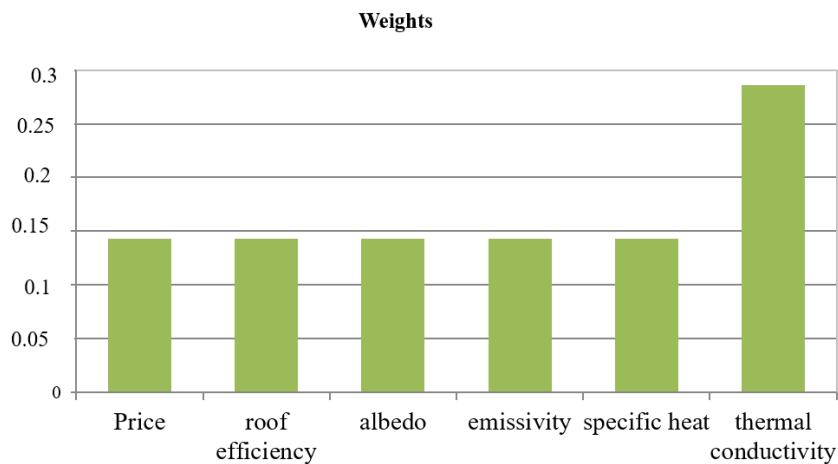


Figure 2. Graphical representation of the criteria weights

There are two most commonly used versions of BWM known as linear [52] and nonlinear [52]. In this study, the excel file based on linear BWM was used for weighting criteria. In this file, five steps that must be taken to construct and solve the problem are explained and formulated. Different pages (C=3, C=4,...) are given for problems with other criteria [53]. In the first step, the number of decision criteria is determined depending on the issue. In this study, the solution was attained using C=6. In the second step, the

best (e.g., the most desirable, the most important) and the worst (e.g., the least desirable, the least important) criteria are determined according to the decision made by the decision-maker. In this context, the best criterion was found to be “thermal conductivity”, whereas the worst criterion was determined to be “price”. In the third and fourth steps, the preference of the decision-maker for “the best criterion over all other criteria” and “all other criteria against the worst criterion” is specified by selecting a number between 1 and

9 from the drop-down box [54,55]. In the last step, the weighting results are calculated using the solver in the data tab in Table 4, and then the weights are graphically depicted in Figure 2.

While weighting the material parameters during material selection, the weight of thermal conductivity criteria was determined as 0.28, whereas the weights of other parameters were determined as 0.14. Linear function type was preferred for the price parameter, while V-type was preferred for different criteria. In this study, it was found that the values for all criteria except the price criterion were very close to each other, thus even minor differences were important. Therefore, although the preference was done considering the decision points with values above the average, values below this average were not desired to be neglected as well. While minimum values were preferred for unit price, thermal conductivity and intrinsic heat criteria, maximum values were preferred for roof efficiency coefficient, albedo, and emissivity criteria.

2.4 Calculation of Rainwater Harvesting

In determining the amount of water to be obtained in rainwater harvesting, information such as roof coefficient, filter efficiency coefficient, precipitation amount of the location and the collection area for the harvesting process are needed.

Roof coefficient: It is a coefficient determined based on the rainwater collection capacity of the collection area. This coefficient varies depending on the covering material used on the roof, as shown in Table 5.

Filter efficiency coefficient: It is the efficiency coefficient of the first filter to be used for separating the rainwater obtained from the roof from visible solid materials. This coefficient is determined based on the loss of a certain amount of rainwater while being filtered and is specified as 0.9 according to the DIN1989 standard.

Rainwater collection area: It is the roof area of the building where rainwater is intended to be harvested.

Precipitation amount: It is the average annual precipitation amount determined by the Directorate General of Meteorology.

Using the above-mentioned definitions, the amount of rainwater harvesting in the building was calculated according to the Equation 1 below.

$$\sum W = A \times M \times \alpha \times \beta \quad (1)$$

in where;

$\sum W$: Total rainwater harvesting (m³)

A: Rainwater collection area (m²)

M: Precipitation amount (mm/m²)

α : Roof coefficient (0.8)

β : Filter efficiency coefficient (0.9)

3. Results

In this study, decision matrices, including alternative

materials and criteria, were created first. The criteria to be used in selecting the optimum material for rainwater harvesting were determined as unit price, roof efficiency coefficient, albedo value, thermal conductivity, intrinsic heat, and emissivity values. V-shape preference type functions were used for other linear criteria for the unit price. After creating decision matrices, the change functions were determined for all criteria. Then, the weight of each criterion was determined according to the experts' and academicians' opinions obtained through the questionnaire. Figure 3 shows the PROMETHEE I (partial ranking) results of the materials recommended for use in the top cover. Positive and negative values between +1 and -1 are calculated for each alternative measured during partial ranking. Whereas the positive value indicates the superiority of the discussed alternative over other options, the negative value indicates how weak the discussed alternative is when compared to other alternatives. The partial ranking analysis result of roofing materials shows that polycarbonate panels and PTFE materials have positive superiority values over other options. Similarly, it shows that aluminum has negative values compared to other alternatives and that this material is comparatively weak.

In Figure 4, the positive and negative superiority values of the materials have been shown graphically, which depicts which material is positive or negative in terms of which factor.

When the Network diagram seen in Figure 5 is examined, it is observed that the polycarbonate panel alternative is superior to other alternatives in terms of positive and negative superiority values. However, since both positive and negative superiority values of aluminum are lower than other alternatives, it is positioned as the worst alternative.

In PROMETHEE II, the ranking is made depending on the net superiority values found by subtracting the negative superiority values from the positive superiority values. The values between 0 and +1 are the first values to be preferred.

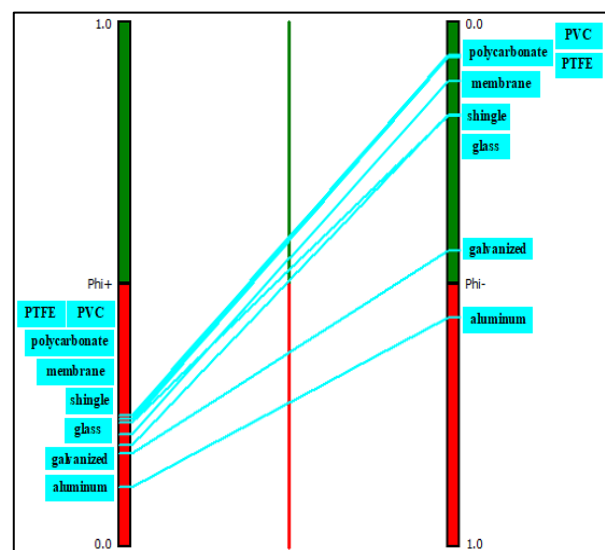


Figure 3. PROMETHEE I partial ranking for top cover material alternatives

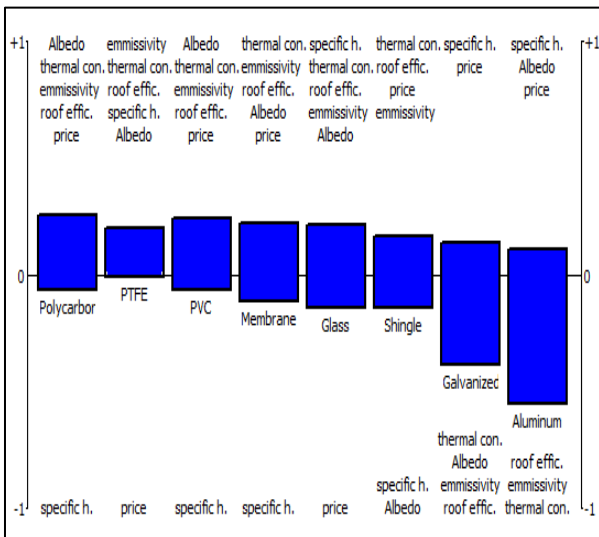


Figure 4. Superiority values for top cover coating material alternatives

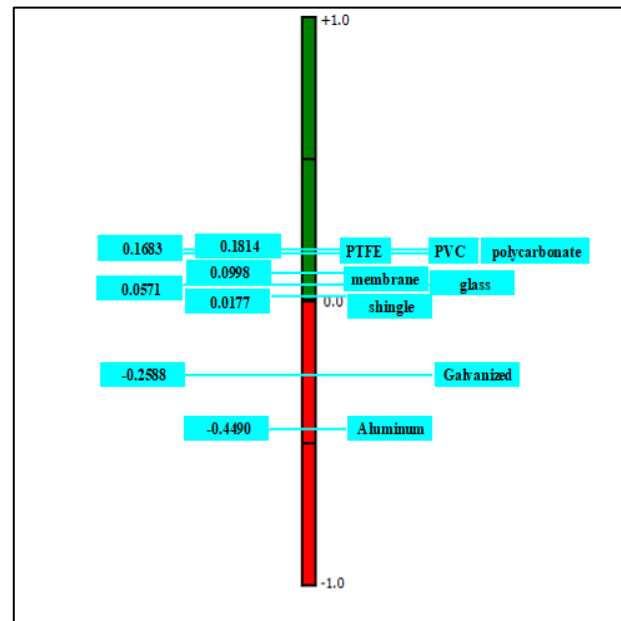


Figure 6. PROMETHEE II full ranking for top cover material alternatives

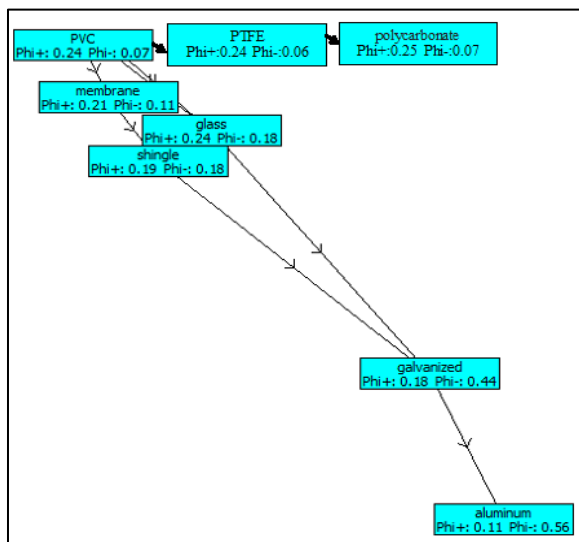


Figure 5. Network diagram for top cover coating material alternatives

With this ranking method, the most appropriate material is determined among the alternatives analyzed based on the selected criteria. According to the PROMETHEE II complete ranking result, with their positive net superiority values, polycarbonate panel (0.1836) and PTFE (0.1814) materials rank at the top among the preferences. In contrast, galvanized sheets (-0.2588) and aluminum (-0.4490) rank at the bottom with their negative net superiority values.

Table 6 contains the PROMETHEE Flow Table created based on the PROMETHEE II Complete Ranking result of the alternative materials included in the study. As a result of the study, while polycarbonate panel was the first roof material to be preferred with its net superiority value of 0.1836, aluminum coating material was the last to be preferred with its net superiority value of -0.4490. In addition, since the net superiority values of polycarbonate panels, PTFE coating, PVC coating, membrane and glass are found to be positive, respectively, according to the results of this analysis, these materials will be the first to be preferred.

3. Conclusions

As a result of the study conducted for the selection of the most appropriate coat material to be used in the top cover recommended for SLC Square that had a high urban heat island effect, both to mitigate the urban heat island effect and to establish an effective rainwater collection system, the most appropriate material was determined as polycarbonate panel considering the material properties and operating limits specified for this purpose.

According to the results of this analysis, glass is a material with a high albedo and roof effectiveness coefficient despite its high price. Membrane is one of the materials that can be preferred because it has a high coefficient of roof effectiveness, high albedo, and low thermal conductivity. Despite its high price, PVC is a material that can be preferred in terms of roof conductivity, albedo, and thermal conductivity values. Although PTFE is a preferable material in terms of roof effectiveness, value, and albedo, its price is quite high compared to others. Polycarbonate panel is a preferable material in terms of roof effectiveness coefficient, thermal conductivity, and albedo values, as well as price. Although shingle is an ideal material in terms of price and roof efficiency coefficient, its albedo value is quite low. Although aluminum is a material that can be preferred due to its high albedo and roof efficiency coefficient, it has a very high price and thermal conductivity. Although galvanized sheet is an ideal material in terms of price, roof efficiency, and thermal conductivity, its albedo value is the lowest among the selected materials. Accordingly, the most appropriate material was determined as a polycarbonate panel. Based on the result of the analysis and these properties, the material that should not be preferred was determined as an aluminum coating.

Table 6. Roof coefficients according to roofing material

PROMETHEE Flow Chart				
Rank	Material	Phi	Phi+	Phi-
1	Polycarbonate panel	0.1836	0.2500	0.0664
2	PTFE covering	0.1814	0.2443	0.0629
3	PVC covering	0.1683	0.2360	0.0677
4	Membrane	0.0998	0.2133	0.1136
5	Glass	0.0571	0.2375	0.1804
6	Shingle covering	0.0177	0.1939	0.1762
7	Galvanized sheet	-0.2588	0.1767	0.4354
8	Aluminium	-0.4490	0.1144	0.5634

In the current situation, the amount of rainwater to be harvested may decrease due to the temperature changes in the square, evaporation caused by the heat island effect, water losses caused by heavy pedestrian traffic, and water puddles and defects on the ground of the square area. The most effective way to prevent this loss is to collect the rainwater on the roof surface in a shorter time and send it to the storage tanks. In this sense, the amount of rainwater collected may increase or decrease depending on the properties of the materials selected on the roof. Therefore, the selection of roofing materials to be used in these covers is important. This study and the obtained results suggest the mitigation of urban heat islands and efficient rainwater harvesting for public spaces and squares in city centers.

In addition, the principle of resource conservation in the building, which stands out as the principle of sustainable architecture, can only gain effectiveness with the decisions made during the design phase. Therefore, it should be underlined that the rainwater collection systems need to be considered during the design phase of the building rather than being considered as structures that are integrated later on.

Declaration

The author(s) declared no potential conflicts of interest with respect to the research, authorship, and/or publication of this article. The author(s) also declared that this article is original, was prepared in accordance with international publication and research ethics, and ethical committee permission or any special permission is not required.

Author Contributions

S. Temizkan performed the analysis. M. Tuna Kayılı supervised and improved the study.

Acknowledgment

This study was derived from a master's thesis completed at the Institute of Graduate Sciences of Karabük University. This study was supported by project number FYL-2019-2077 of the Scientific Research Center of Karabük University, Turkey.

References

- Karahan, A., Gri suyun değerlendirilmesi. IX. Ulusal Tesisat Mühendisliği Kongresi, 2011. p. 1155-1164.
- Aküzüm, T., B. Çakmak and Z. Gökalp, *Türkiye'de su kaynakları yönetiminin değerlendirilmesi*. International Journal of Agricultural and Natural Sciences, 2010. **3**(1): p. 67-74 (in Turkish).
- Alpaslan, N., A. Tanik and D. Dölgen, *Türkiye'de su yönetimi sorunlar ve öneriler*. TÜSİAD, 2008. **9** (in Turkish).
- Bulut, S., and G. Şahin, *Pedagojik formasyon öğrencilerinin su tüketim davranışları ile su ayak izlerinin incelenmesi*. Akdeniz Üniversitesi Eğitim Fakültesi Dergisi, 2020. **3**(2), p. 53-70 (in Turkish).
- UNDP (United Nations Development Programme), *UNDP sustainable development goals 2030*, 2015. [cited 2020 7 Aug]; Available from: www.undp.org/content/undp/en/home/sustainable-development,
- Santamouris, M., *Energy and climate in the urban built environment*, Routledge, 2001. p. 145-159.
- Yılmaz, E. Y., and İ. T. D. Çiçek, *Ankara şehrinde ısı adası oluşumu*. Doctoral Dissertation, Ankara Üniversitesi SBE Coğrafya Anabilim Dalı, 2013 (in Turkish).
- Lin, T. P., A. Matzarakis and R. L. Hwang, *Shading effect on long-term outdoor thermal comfort*. Building and Environment, 2010. **45**(1): p. 213-221.
- Göçer, Ö., A. Ö. Torun and M. Bakoviç, *Kent dışı bir üniversite kampüsünün dış mekânlarında ısı konfor, kullanım ve mekân dizim analizi*. Gazi Üniversitesi Mühendislik Mimarlık Fakültesi Dergisi, 2018. **33**(3): p. 853-874 (in Turkish).
- Aghamolaei, R. and M. H. Shamsi, *Review of District-scale Energy Performance Analysis* 2018.
- Li, G., X. Zhang, P. A. Mirzaei, J. Zhang and Z. Zhao, *Urban heat island effect of a typical valley city in China: responds to the global warming and rapid urbanization*. Sustainable cities and society, 2018. **38**: p. 736-745.
- Mirzaei, P. A., *Recent challenges in modeling of urban heat island*. Sustainable cities and society, 2015. **19**, 200-206.
- Özeren, Ö. and M. T. Kayılı, *Designing public squares to optimize human outdoor thermal comfort: a case study in Safranbolu*. Journal of Awareness, 2021. **6**(1): p. 13-20.
- Mahmoud, A. H. A., *Analysis of the microclimatic and human comfort conditions in an urban park in hot and arid regions*. Building and environment, 2011. **46**(12): p. 2641-2656.

15. Chen, L and E. NG, Edward, *Outdoor thermal comfort and outdoor activities: A review of research in the past decade*. Cities, 2012. **29**(2): p. 118-125.
16. European Environmental Agency (EEA), *Urban adaptation to climate change in europe-challenges and opportunities for cities together with supportive national and european policies*, 2012. [cited 2020 11 Aug]; Available from: <http://www.eea.europa.eu/publications/urban-adaptation-to-climate-change>.
17. Akbari, H., S. Bretz, D. M. Kurn and J. Hanford, *Peak power and cooling energy savings of high-albedo roofs*. Energy and Buildings, 1997. **25**(2): p. 117-126.
18. Backenstow, D. E. and R. J. Gillenwater, *U.S. Patent No. 4,649,686*. Washington, DC: U.S. Patent and Trademark Office, 1987.
19. Yılmaz E. M., *Kurak İklimlerde içbükey çatı*, 2017. [cited 2020 6 Jun]; Available from: <https://www.konuttrend.com/mimari/kurak-iklimlere-icbukey-cati-h1242.html> (in Turkish).
20. Temizkan, S. and M. T. Kayılı, *Yağmur suyu toplama sistemlerinde optimum depolama yönteminin belirlenmesi: Karabük Üniversitesi Sosyal Yaşam Merkezi Örneği*. El-Cezeri Journal of Science and Engineering, 2020. **8**(1): p. 102-116 (in Turkish).
21. T.C. Tarım ve Orman Bakanlığı Karabük İl Tarım ve Orman Müdürlüğü, *Karabük hakkında*, 2020. [cited 2020 7 Mar.]; Available from: <https://karabuk.tarimorman.gov.tr/Menu/26/Karabuk-Hakkinda> (in Turkish).
22. T.C. Tarım ve Orman Bakanlığı Meteoroloji Genel Müdürlüğü, *Karabük ili aylık-yıllık yağış verileri*, Karabük Meteoroloji İl Müdürlüğü, 2019 (in Turkish).
23. Karabük Üniversitesi, *KBÜ 2019 yılı idari faaliyet raporu*, 2019. [cited 2020 11 Jun]; Available from: <https://strateji.karabuk.edu.tr/yuklenen/dosyalar/12634202030256.pdf> (in Turkish).
24. Okutan, A. E., *Çatı kaplama malzemesi seçim kriterlerinin belirlenmesi*, Master Thesis, İTÜ Fen Bilimleri Enstitüsü, 2007. p. 1-153 (in Turkish).
25. Bektaş, İ. and A. E. Dinçer, *Değişen iklim koşullarında çatı kaplama malzemelerinin verimliliğinin incelenmesi: Safranbolu Örneği*, Erciyes Üniversitesi Fen Bilimleri Enstitüsü Fen Bilimleri Dergisi, 2017. **33**(3): p. 35-53 (in Turkish).
26. Genç, E., *Çatı kaplama ürünlerinin seçiminde ürün bilgilerinin düzenlenmesi*, Master Thesis, YTÜ FBE Mimarlık ABD, 2011. p. 1-156 (in Turkish).
27. Hamurcu M. and T. Eren, *Transportation planning with analytic hierarchy process and goal programming*, International Advanced Researches and Engineering Journal, 2018. **02**(02): p. 92-97.
28. Tsou, C. S., *Multi-objective inventory planning using MOPSO and TOPSIS*. Expert Systems with Applications, 2008. **35**(1-2): p.136-142.
29. Chai, J., J. N. Liu and E. W. Ngai, *Application of decision-making techniques in supplier selection: A systematic review of literature*. Expert systems with applications, 2013. **40**(10): p. 3872-3885.
30. Wang, T. C. and H. D. Lee, *Developing a fuzzy TOPSIS approach based on subjective weights and objective weights*. Expert systems with applications, 2009. **36**(5): p. 8980-8985.
31. Autodesk Revit, Revit building information modelling, 2020.
32. Temizkan, S., *Kentsel ısı adası özelliği yüksek meydanlarda yağmur suyu hasadına yönelik uygun malzeme seçiminin araştırılması: KBÜ Sosyal Yaşam Merkezi örneği*, Master Thesis, Karabük Üniversitesi, FBE, 2020. p. 1-124 (in Turkish).
33. Senger, Ö. and Ö. K. Albayrak, *Gri İlişki Analizi yöntemi ile personel değerlendirme*. Uluslararası İktisadi ve İdari İncelemeler Dergisi, 2016. **17**: p. 235-258 (in Turkish).
34. Özdemir, A. İ. and N. Y. Seçme, *İki aşamalı stratejik tedarikçi seçiminin bulanık topsis yöntemi ile analizi*. Afyon Kocatepe Üniversitesi İktisadi ve İdari Bilimler Fakültesi Dergisi, 2009. **11**(2): p. 79-112 (in Turkish).
35. Çagil, G., *Küresel kriz sürecinde türk bankacılık sektörünün finansal performansının electre yöntemi ile analizi*. Maliye ve Finans Yazıları, 2008. **1**(93): p. 59-86 (in Turkish).
36. Türker, A., *Çok ölçütlü karar verme tekniklerinden "electre"*. Journal of the Faculty of Forestry Istanbul University, 1988. **38**(3): p. 72-87 (in Turkish).
37. Wang, J. J. and D. L. Yang, *Using a hybrid multi-criteria decision aid method for information systems outsourcing*. Computers & Operations Research, 2007. **34**(12): p. 3691-3700.
38. Genç, T., *PROMETHEE yöntemi ve GALA düzlemi*. Afyon Kocatepe Üniversitesi İktisadi ve İdari Bilimler Fakültesi Dergisi, 2013. **15**(1): p. 133-154 (in Turkish).
39. Balali, V., B. Zahraie, A. Hosseini and A. Roozbahani, *Selecting appropriate structural system: Application of PROMETHEE decision making method*. In 2010 Second International Conference on Engineering System Management and Applications. IEEE, 2010, p. 1-6.
40. Bottero, M., C. D'Alpaos and A. Oppio, *Multicriteria evaluation of urban regeneration processes: an application of PROMETHEE method in Northern Italy*. Advances in Operations Research, 2018. p. 1-12.
41. Hu, J. and Y. Jiang, *PROMETHEE method applied in the evaluation of urban air environmental quality*. Journal of University of Shanghai for Science and Technology, 2012. **4**: 318-322.
42. Pan, W.H. and J.Q. Li, *Application of AHP-PROMETHEE Method for Supplier Selection in Strategic Sourcing*. Operations Research and Management Science, 2009. **2** (008).
43. Bottero, M., F. Dell'Anna and M. Nappo, *Evaluating tangible and intangible aspects of cultural heritage: An application of the promethee method for the reuse project of the Ceva-Ormea railway*. In Seminar of the Italian Society of Property Evaluation and Investment Decision Springer, Cham, 2016. p. 285-295.
44. Lakićević, M. D. and B. M. Srđević, *Multiplicative version of Promethee method in assesment of parks in Novi Sad*. Zbornik Matice srpske za prirodne nauke, 2017. **132**: p. 79-86.
45. Vujosevic, M. L. and M. J. Popovic, *The comparison of the energy performance of hotel buildings using PROMETHEE decision-making method*. Thermal Science, 2016. **20**(1): p. 197-208.
46. Dražić, J., D., Dunjić, V. Mučenski and I. Peško, *Multi-criteria analysis of variation solutions for the pipeline route by applying the PROMETHEE method*. Tehnički vjesnik, 2016. **23**(2): p. 599-610.
47. Yan-ming, C. *Research on Evaluation of subcontractors of water project and Model established based on*

- PROMETHEE method*. Jilin Water Resources, 2015. **8**(4).
48. Dachowski, R. and K. Gałek, *Selection of the best method for underpinning foundations using the PROMETHEE II method*. Sustainability, 2020. **12**(5373): p. 1-9.
 49. Balali, V., A. Mottaghi, O. Shoghli and M. Golabchi, *Selection of appropriate material, construction technique, and structural system of bridges by use of multicriteria decision-making method*. Transportation research record, 2014. **2431**(1): p. 79-87.
 50. San Cristobal, J. R., *Critical path definition using multicriteria decision making: PROMETHEE method*. Journal of Management in Engineering, 2013. **29**(2): p.158-163.
 51. Rezaei, J., *Best-worst multi-criteria decision-making method*. Omega, 2015. **53**: p. 49-57.
 52. Rezaei, J., *Best-worst multi-criteria decision-making method: Some properties and a linear model*. Omega, 2016. **64**: p. 126-130.
 53. Kim, T., *Rainwater harvesting: the impact of residential-scale treatment and physicochemical conditions in the cistern on microbiological water quality*. Doctoral dissertation, The University of Texas at Austin, 2017. p . 1-144
 54. Lye, D. J., *Rooftop runoff as a source of contamination: A review*. Science of the total environment, 2009. **407**(21): p. 5429-5434.
 55. Alpaslan, N., A., Tanik and D. Dölgen, *Türkiye’de su yönetimi: Sorunlar ve öneriler*. TÜSİAD 2008. **09/469**: p. 1-216 (in Turkish).



Research Article

Investigating the construction parameters of deep mixing columns in silty soils

Yavuz Yenginar ^{a,*} , Ahmed A.M.M. Mobark ^b  and Murat Olgun ^b 

^a Necmettin Erbakan University, Engineering Faculty, Department of Civil Engineering, 42090, Konya, Turkey

^b Konya Technical University, Faculty of Engineering and Natural Sciences, Department of Civil Engineering, 42130, Konya, Turkey

ARTICLE INFO

Article history:

Received 05 August 2021

Revised 26 November 2021

Accepted 10 December 2021

Keywords:

Cement
Deep soil mixing
Fly ash
Silty soil
Superplasticizer
Taguchi method

ABSTRACT

In the present research, the optimum condition of the grout consisting of cement, fly ash, superplasticizer, and water was determined to produce the most durable and impermeable deep mixing columns (DMC) on silty soils. It is aimed to reduce the grout cost and environmental pollution by using high-rate fly ash in the grout. Superplasticizer additive was used to increase the flow consistency of grout consisting of high-rate fly ash. The design of the experiments was made using the 5-parameter and 4-level L16 orthogonal array table specific to the Taguchi method. Accordingly, the unconfined compression strength (q_u) and the permeability coefficient (k) of the soil-binder mixtures at the end of the 7- and 28-days curing time were determined. According to the test results, regression analyzes were performed and models with high reliability were created for q_u and k . As a result of optimization studies, to produce DMC having high strength and low permeability, grout content should be consisting of 14% cement, 14% fly ash (ratio of fly ash in the binder is 50%), 2.68% super plasticizer additive, and 0.95 water/binder ratio. The pozzolanic reactions in soil-binder samples with different grout contents were examined by SEM analysis.

1. Introduction

All over the world, especially in city centers, most of the stable soil had already been used. The construction site requires a stable area of appropriate soil properties since weak soils have to be improved before the construction work. One of the methods used for stabilizing soils is the deep mixing method (DMM), defined as the mixing process of cement, lime, slag, and other binders with soil. DMM improves the soil properties in terms of geotechnical concerns such as bearing capacity, hydraulic conductivity, settlement, and horizontal displacement.

The effects of cement and other binders on soil-cement slurry have been investigated by lots of researchers. The unconfined compression strength (UCS) of the deep mixing column depends on binder dosage, curing period, curing temperature, and natural soil water content [1]. Increasing cement dosage from 100 kg/m³ to 200 kg/m³ gives 10 times higher compression strength, and there is a linear relation between UCS and cement dosage [2].

Since cement production is expensive and causes environmental pollution, the binder replacement method with a natural or by-product material may be useful for many cement-based constructions works. A common by-

product material is fly ash generally used to create longer-lasting infrastructure in road constructions and embankments. Li et al. [3] found that the fly ash-soil samples had a strength between 940 kPa and 4300 kPa at the end of the 14-day cure period, whereas the soil alone had a strength of 317 kPa. Moreover, soil friction angles increased up to 2-3 times according to fly ash content. The optimum fly ash ratio for the mix was 60%. Since fly ash is a lightweight material, the higher percentage of fly ash decreases dry densities and increases optimum water content [4,5]. Increasing the amount of fly ash into soil reduces plasticity, hydraulic conductivity, and compressibility [6-9]. Although replacing cement with fly ash reduces cement cost and environmental pollution, fly ash additive materials have early strength problems but, the final compression strength is high [10]. Some minerals of silicon and aluminum in fly ash create a secondary reaction with the cement hydration products. Thus, the void ratio and permeability of the deep mixing column decreases. The UCS and elastic modulus of columns improved with increasing fly ash amount [11].

The injectability of the grouting mixture is important to obtain well-mixed columns. Although the higher water

* Corresponding author. Tel.: +90 507 857 9240.

E-mail addresses: yenginar@erbakan.edu.tr (Y. Yenginar), ahmeed696@yandex.com (A.A.M.M Mobark), molgun@ktun.edu.tr (M. Olgun)

ORCID: 0000-0002-6916-4068 (Y. Yenginar), 0000-0002-3989-641X (A.A.M.M Mobark), 0000-0001-7856-8227 (M. Olgun)

DOI: 10.35860/iaiej.978978

© 2021, The Author(s). This article is licensed under the CC BY-NC 4.0 International License (<https://creativecommons.org/licenses/by-nc/4.0/>).

content in the grouting mixture makes grouting easier, it reduces the strength of soil-cement samples. Therefore, to increase the strength, the water content has to be reduced. Since grouting mixtures are pumped into the soil at the field, higher fluidity and low viscosity are achieved by raising the water/cement ratio and adding chemical additives. In different studies, water/cement ratios were used as following; 0.5-2 [12], 0.6-2 [13], and 1-3 [14]. Adding chemical additives impacts the fluidity of cementitious material even for mixtures with very low water/cement ratios. Achieving higher strength requires lower water/cement ratios. However, lower water content results in low fluidity. Thus, chemical additives are used to maintain a higher fluidity value for that low water content. The addition of superplasticizers into grouting mixtures, more viscous grout at lower water/cement ratio [15,16], and more strength and less permeable soil-cement mixtures can be obtained.

Full factorial or partial factorial design can be performed when examining the effects of parameters that are effective on any process [17]. Full factorial design can be applied when the number of parameters studied is small. However, as the number of parameters and their levels increases, full factorial design becomes very laborious and time-consuming. The partial factorial design also has its downsides [18]. Genicci Taguchi developed a statistical method [19–22] to determine the relationship between the parameters that affect the process and the results by making a few experiments, observations, or analyzes as possible. This method is used in many different fields [23–27]. The basic methodology of the Taguchi method consists of four steps: (1) determining the parameters and their levels that affect the process, (2) choosing an appropriate orthogonal index table, (3) performing the experiments and analyzing the results, and (4) obtaining and verifying the optimum results.

The purpose of this research is to determine the optimum grout content to obtain the highest strength and the lowest permeability of the soil-binder mixture representing the deep mixing column. Grouting consists of different amounts of cement, fly ash, superplasticizer, and water/binder ratio mixed with the silty soil whose consistency changes semi-solid to liquid form and cured for 7 and 28 days. The design of the experiments (DOE) was performed using the Taguchi method, which is a statistical method. Experimental results were analyzed using a factorial design to find the optimum grout content. The optimum design is controlled by validation tests (unconfined compression and permeability tests) and SEM images.

2. Materials and Methods

2.1 Soil

The soil was obtained from the Doğanhisar district located

at Konya Province in Turkey. Liquid limit (w_L), plastic limit (w_p) and plasticity index (I_p) of soil determined as 31.3%, 18.1% and 13.2%, respectively. The soil is classified as ML according to USCS using Atterberg limits and grain size distribution curve given in Figure 1.

2.2 Grouting Materials

The grout consists of cement, fly ash, and superplasticizer. The main binder material in grout is Type I (42.5 R) Ordinary Portland Cement (OPC). Its chemical properties are given in Table 1. Since the fly ash gained strength over a long period, high early strength cement was used.

The fly ash was obtained from Aluminum Recovery Central in Seydişehir, Turkey. Fly ash is the petty binder material used to reduce cement costs inside the grout. The fly ash can be defined as high lime fly ash since its free lime content is 16.3% (Table 1). Most of its particles were in the silt size (84.2%) with light brown color.

The superplasticizer used in this study meets the requirements for water-reducing (Type A) and high range water-reducing (Type F) admixtures according to ASTM C 494/C 494M [28]. This additive maintains high plasticity in concrete for a longer time compared to traditional superplasticizers. In the plastic state, it extends slump retention, control set times, and minimizes bleeding water. On the other hand, in the hardened state, it provides higher earlier strength, increases ultimate compression strength, develops a higher modulus of elasticity, and decreases permeability.

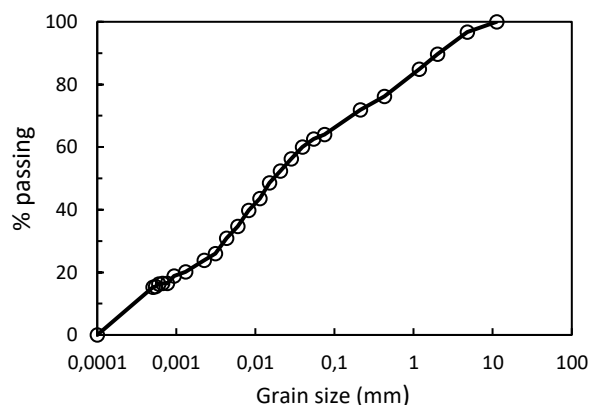


Figure 1. Grain size distribution curve of soil

Table 1. The chemical properties of cement and fly ash

Chemical composition (%)	Cement	Fly ash
SiO ₂	22.1	19.8
Al ₂ O ₃	5.3	8.1
Fe ₂ O ₃	2.2	6
CaO	63.7	28.3
MgO	2.4	1
SO ₃	3.1	18.2
Na ₂ O	0.12	0.1
K ₂ O	0.94	0.4
Free CaO	1.6	16.3
Loss on ignition	-	1.8

2.3 Design of Experiments (DOE)

Scientists systematically collect data and examine the relationship between input variables (factors) and output parameters (responses) that are effective on any process using the design of experiments (DOE) method. The Taguchi method is a robust DOE method used to optimize the parameters that affect the process. This method reduces the mean and variance of the process performance characteristics and allows obtaining high-quality analysis results with a few experiments. The first step in the Taguchi method is the selection of parameters and their levels.

In the present research, investigating parameters on column performance are amounts of cement, fly ash, superplasticizer, water/binder ratio in grout and water content of untreated soil. Parameters and their levels were given in Table 2. Taguchi’s standard L16 (5⁴) orthogonal array (OA), which consists of 5 factors and 4 levels, was used in the design of experiments (Table 3).

Unconfined compression strength (q_u) and permeability coefficient (k) values were used in the statistical analyzing process. In the first stage, Taguchi analysis was performed and S/N (signal-to-noise) ratios were obtained. S/N ratio refers to the distribution around the target value, and there are three categories for the performance characteristic: (1) larger the better, (2) smaller the better, and (3) nominal the better.

Table 2. Controllable factors and levels in Taguchi design

Levels	Parameters				
	C	F	A	w/b	w _n
1	3	0	0	0.9	20
2	7	5	1	1.1	24
3	11	10	2.5	1.3	28
4	15	15	4	1.5	32

Table 3. Design of experiment using Taguchi method (standard L16 orthogonal array)

Design No	Parameters and their levels				
	C	F	A	w/b	w _n
1	1	1	1	1	1
2	1	2	2	2	2
3	1	3	3	3	3
4	1	4	4	4	4
5	2	1	2	3	4
6	2	2	1	4	3
7	2	3	4	1	2
8	2	4	3	2	1
9	3	1	3	4	2
10	3	2	4	3	1
11	3	3	1	2	4
12	3	4	2	1	3
13	4	1	4	2	3
14	4	2	3	1	4
15	4	3	2	4	1
16	4	4	1	3	2

This study aims to manufacture a deep mixing column with high strength and low permeability. For this reason, S/N ratios were determined using Equation (1) of "larger the better" option for strength response and Equation (2) of "smaller the better" option for permeability response. In Taguchi analysis, the S/N ratio is used as the quality characteristic. Taguchi found that the mean and standard deviation are directly proportional to each other. This is the reason why the S/N ratio is used instead of the standard deviation. Each experiment was performed twice to reduce the effect of the uncontrollable factors. Statistical analyzes were made with Minitab software.

$$S/N = -10 \log_{10} \left(\frac{1}{n} \sum_{i=1}^n \frac{1}{Y_i^2} \right) \tag{1}$$

$$S/N = -10 \log_{10} \left(\frac{1}{n} \sum_{i=1}^n Y_i^2 \right) \tag{2}$$

where Y_i is the response (output) of the i-th experiment and n is the repetition number of response characteristics.

In the second stage, the desirability function approach was applied to optimize all parameter levels including the curing period of deep mixing samples. Derringer and Suich [29] initially developed the idea of the desirability function approach. In this approach, all responses are transformed into the same scale of undesirable desirability (individual desirability) [30]. There are 3 different desirability functions d_i(y_i) to obtain the response parameter y_i at the maximum, minimum, or target value. The individual desirability d_i(y_i) can be calculated to minimize a response using "smaller better" formulas in Equation (3) and maximize a response using "larger better" formulas in Equation (4) [29,31]. Then, the geometric mean of individual desirabilities using Equation (5) gives the overall desirability D.

$$d_i(y_i) = \begin{cases} 1 & , y_i(x) < T_i \\ \left(\frac{y_i(x) - U_i}{T_i - U_i} \right)^r & , T_i \leq y_i(x) \leq U_i \\ 0 & , y_i(x) > T_i \end{cases} \tag{3}$$

$$d_i(y_i) = \begin{cases} 0 & , y_i(x) < L_i \\ \left(\frac{y_i(x) - L_i}{T_i - L_i} \right)^r & , L_i \leq y_i(x) \leq T_i \\ 1 & , y_i(x) > T_i \end{cases} \tag{4}$$

$$D = (d_1(y_1) \times d_2(y_2) \times \dots \times d_m(y_m))^{1/m} \tag{5}$$

where x is the factors. L_i and U_i are lower and upper acceptable values of y_i, respectively, while T_i is target values desired for ith response, where L_i ≤ T_i ≤ U_i. r is used to determine the shape of d_i(y_i) and change between 0 and 1. m is the number of responses.

Desirability value changes between 0 and 1. A desirability value of 0 indicates that the predicted outcome value is outside of acceptable limits. A desirability value of 1 indicates that there is maximum agreement between factors

and results, that is, maximum performance has been achieved. [32]. In the desirability function approach, the curing period was added to the L16 design table as the sixth parameter with two levels (7 and 28 days). Hence the number of trial mixes was increased to 32. Then, regression analysis and multi-response optimization was performed using the desirability function approach in Minitab software. All of the statistical analyzes were carried out considering the 95% confidence interval.

2.4 Preparing and Curing Specimens

Before preparing the soil-binder mixtures, the soil was dried at 60° in the oven and sieved through a 2 mm opening sieve. For each design, the amount of cement and fly ash were determined as a percentage of dry soil and all were mixed in the dry state (the dry mixture). The total water content of the mixture includes grouting water and soil's natural water content. Grouting water is calculated by multiplying the water/binder ratio and dry binder amount. The amount of superplasticizer was determined as the percentage of a dry binder. Then, grouting water, water from soil's water content, and superplasticizer mixed (the liquid mixture). After that, the liquid mixture was added step by step to the dry mixture to obtain a homogeneous mixture. The mixing process was done by a mixer and continued for at least 10 minutes for each mixture. After that, the mixture was cast in PVC molds having 50 mm inner diameter. The height of molds used for UCS and permeability tests were 100 mm and 30 mm, respectively. Fresh mixtures of soil-binder samples cast in molds were left at room temperature for 5-6 hours to harden and then cured in the curing pool by sealing. The curing period of samples was 7 and 28 days.

3. Results and Discussion

3.1 Unconfined Compression Strength (UCS) Test

Unconfined compression strength tests were performed according to ASTM-D2166/D2166M [33]. The cylindrical soil-binder sample is loaded axially at an axial strain rate between 0.5 to 2%/min. The unconfined compression strength (q_u) of the deep soil mixing samples at 7 and 28 days of the curing period were determined at the end of the test (Table 4).

In the statistical analysis, the significance level of the parameters affecting the performance of the deep mixing samples can be understood from the magnitude of the delta value in the response table obtained for the S/N ratios (larger is better-maximizing strength) and rank of parameters on UCS. The UCS generally increases while increasing cement and fly ash amounts and curing period since S/N ratios increase for all parameter levels (Table 5). Cement is the first, and fly ash is the second effective parameter on UCS as they are the main component in the hydration reaction by which soil particles bind together and produce a high strength structure. During the cement hydration, calcium ions are

released then react with silica and alumina in soil. At the end of this process, pozzolanic products emerge and the strength increases. These pozzolanic products bind the clay particles together to form a new bonded, strong soil matrix [34]. The reactions between soil and calcium oxide (CaO) in cement and fly ash produce cementitious and pozzolanic gels such as C-S-H (calcium silicate hydrate gel) and C-A-S-H (calcium aluminate silicate hydrate gel). The increase in strength is related to the type and the number of possible reacting products. Therefore, the higher the content of calcium ions that exists in the binder, the higher strength is gained (Figure 2a).

The third efficient parameter on strength is the water content of the soil. Increasing its values maximizes UCS responses to a third level than the higher values of 28% water content of soil decreases UCS responses.

The water content of soil has little effect on the strength according to binders because the strength of samples primarily depends on the gel produced from the pozzolanic reactions. Therefore, the water content affects the strength indirectly by meeting the necessary moisture in the hydration reaction. The response of water content on strength depends on the water content needed for the applied binder contents. Each binder content has only one optimum water content. Fewer water contents lead to uncompleted hydration reaction and produce less gel causing a decrease in UCS. On the other hand, water amount over the optimum value cannot be absorbed during the hydration reaction. Therefore, it remains in the pores between soil particles causing larger voids at the microstructure. The optimum water content for mixing soil is the total water content by which the maximum strength is gained at a certain curing period [35]. The optimum water content was found by other researchers as the liquid limit of soil [36]. In this research, the optimum water content of soil-binder samples was 28% for silty soil since the liquid limit of the soil is 31%.

Table 4. Unconfined compression strength tests results for 7- and 28-days curing period

Design No	7 days		28 days	
	q_{u1} (kPa)	q_{u2} (kPa)	q_{u1} (kPa)	q_{u2} (kPa)
1	171	192	99	99
2	220	283	433	552
3	226	298	497	506
4	128	136	292	265
5	117	134	229	242
6	516	518	944	1041
7	834	967	1403	1061
8	1162	1079	1163	1695
9	303	274	513	521
10	777	942	1299	1342
11	743	760	1083	1319
12	1024	1281	1719	2083
13	1137	946	1161	966
14	1444	1337	1445	1337
15	1467	1917	1467	1917
16	2763	2460	2823	2459

Table 5. Response table for S/N ratios of UCS

Curing Period	Level	C	F	A	w/b	w _n
7 days	1	45.99	49.18	56.33	57.09	57.35
	2	54.08	55.96	53.95	56.72	56.16
	3	56.66	57.39	55.36	54.34	56.06
	4	64.03	58.24	55.13	52.61	51.19
	Delta	18.04	9.07	2.38	4.48	6.16
	Rank	1	2	5	4	3
28 days	1	49.17	50.54	57.47	57.54	57.50
	2	58.07	59.77	57.86	59.77	59.59
	3	60.96	60.49	58.56	58.07	60.01
	4	64.10	61.50	58.41	56.92	55.20
	Delta	14.94	10.96	1.09	2.85	4.82
	Rank	1	2	5	4	3

The effect of the water/binder ratio could be achieved according to the water content that had already been described above. It was concluded that the UCS decreases for both higher water content and higher water/binder ratios (Figure 2b).

The superplasticizer amount is the least effective parameter on UCS responses, but it was essential for the pumpability of binder grout consisting of high fly ash.

The regression equation established for the model created between UCS and design parameters was given in Equation (6) in coded units. Each parameter effect individually the UCS results and two- and three-parameter interactions were considered to increase the model quality. According to the statistical model, the values of R-sq., R-sq.(adj), and R-sq.(pred) were found 97.15%, 94.11%, and 93.04%, respectively. Concerning these very high regression qualities, the model created is accepted. Unconfined compression strength values of experimental results and predicted values according to regression analysis are given in Figure 3. There is a good conformity between the experimental and the predicted results: $q_{u, predicted} = 0.987q_{u, experimental}$. These results are confirmed with other researchers for the feasibility and robustness of the Taguchi method [37,38] and desirability function approach [31,39].

$$\begin{aligned}
 q^{0.5} = & -33.7 + 9.51C + 5.90F - 0.315A + 57.6(w/b) \\
 & - 0.911w_n + 0.124P - 0.583CF - 7.1C(w/b) \\
 & + 0.0014CP - 4.96F(w/b) + 0.0219FP \\
 & + 0.560CF(w/b) - 0.00151CFP
 \end{aligned}
 \tag{6}$$

3.2. Permeability test

Permeability tests were performed according to ASTM-D5084 [40]. After the soil-binder samples were placed into the cell of the triaxial compression test apparatus, the cell pressure and backpressure were applied as 500 kPa and 450 kPa, respectively. Experiments were repeated two times for each specimen. The permeability coefficient (k) of samples (Table 6) was calculated according to the following equation:

$$k = \frac{V \cdot L}{\Delta t \cdot A \cdot \Delta h}
 \tag{7}$$

where, V: volume of water leaking through the sample, L: specimen length, Δt: test duration, A: cross section area of specimen and Δh: head loss (height of water corresponds to back pressure since water pressure at outlet is zero).

In the S/N analysis, factors affecting the permeability coefficient (k) of the deep mixing samples are ranked as fly ash, cement, water/binder ratio, water content of the soil, and superplasticizer additive for 7 day-cured samples. At the end of the 28 days, the rank of parameters affecting k is water/binder ratio, water content of the soil, fly ash, superplasticizer additive, and cement (Table 7).

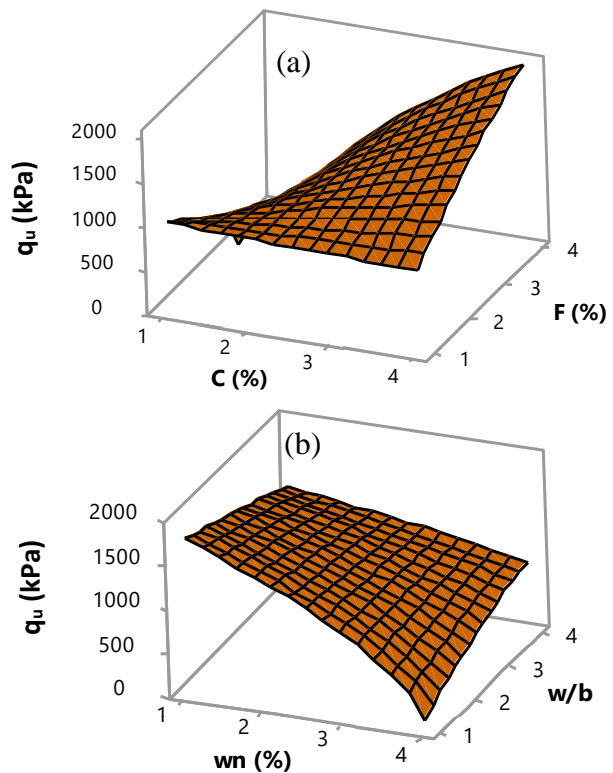


Figure 2. Surface plot of qu vs a) cement and fly ash, b) water content and water/binder ratio

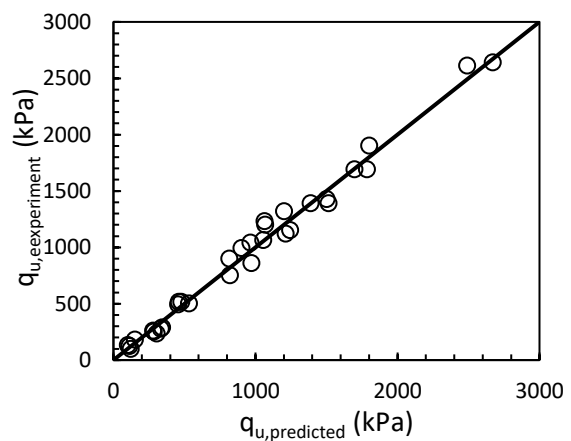


Figure 3. Unconfined compression strength values of experimental results and predicted values according to regression analysis

Permeability could change in different ways according to each parameter and its levels. Increasing cement content could affect permeability in two different ways. The first effect is decreasing permeability due to cement hydration because pozzolanic products bind the soil particles and decrease voids between them. The second effect is increasing the permeability by increasing the water amount in the sample, which causes more voids within the solid particles. According to their combined effects, the permeability could increase or decrease. As the permeability decreased from level 1 till level 2, the decrease in voids due to pozzolanic products was higher than the increase in voids due to the excess water amount. Between the 2nd and the 3rd levels of cement, the permeation increased massively because the increase in voids due to excess water was larger with respect to the decrease in voids due to pozzolanic products. Over the 3rd level of cement content, the permeability decreases again according to the increase in cement content. The decrease in voids due to pozzolanic products was larger than the increase in voids due to water excess. The fly ash amount also shows the same effects on permeability. Increasing fly ash content results in a decrease in permeability. Increasing fly ash content over the 2nd level up to the 3rd level resulted in a massive increase in permeability which means that the increase in voids due to water excess was very large with respect to the decrease in voids due to pozzolanic products. Finally, the increase in fly ash content from the 3rd up to the 4th level resulted in a little decrease in permeability with respect to the previous increase. In this period, the decrease in voids due to pozzolanic products was larger than the increase in voids due to water excess. The first two levels of the additive result in high permeability. On the other hand, the last two levels result in lower permeability. Therefore, the additive is accepted to be a permeability decreasing parameter. The water/binder ratio reduces the permeability until the third level. After that, the permeability starts to rise again while increasing the water/binder ratio over that level. For the water content, a similar effect was noticed as the permeability decreases while increasing water level till the second level. Then, it starts to rise again while increasing water over the second level till the fourth. In addition, the long curing periods result in lower permeability.

The regression equation is established for the model created between the coefficient of permeability and designing parameters as shown in Equation (8). This regression equation shows that the parameters have various effects on permeability. In addition, interactions of two and three parameters were included through the model for their high effects. According to the model, almost high regression quality ratios were found. The values of R-sq., R-sq.(adj), and R-sq.(pred) were obtained 96.41, 90.58, and 70.33, respectively. Concerning these high values, the model could be accepted. Permeability coefficient values of experimental results and predicted values according to regression analysis

are given in Figure 4. There is a good agreement between the experimental results and the predicted values:
 $k_{predicted} = 0.864k_{experimental}$

$$\begin{aligned}
 -k^{-0.5} = & 69.3 - 15.19C - 6.98F + 0.16A - 127.7(w/b) \\
 & + 1.305w_n + 0.14P + 0.914CF + 13.98C(w/b) \\
 & - 0.0151CP + 6.77F(w/b) + 0.0294FP \\
 & - 0.741CF(w/b) - 0.00500CFP
 \end{aligned} \tag{8}$$

3.3 Optimization

There are two types of optimizations; single response and multi-response optimizations. For single response optimizations, one optimal solution can be obtained. For multi-response optimizations, a set of optimal solutions would be found.

Table 6. Permeability tests results for 7- and 28-days curing period

Design No	7 days		28 days	
	k ₁ (x10 ⁻⁹) (m/s)	k ₂ (x10 ⁻⁹) (m/s)	k ₁ (x10 ⁻⁹) (m/s)	k ₂ (x10 ⁻⁹) (m/s)
1	1.790	1.730	2.230	2.200
2	0.479	0.301	0.813	0.674
3	2.370	2.180	1.040	1.180
4	1.400	0.951	7.370	7.060
5	1.550	1.320	0.753	0.673
6	0.417	0.393	2.890	2.680
7	6.260	6.280	1.040	1.040
8	1.360	1.320	1.820	1.780
9	1.500	1.440	0.937	0.956
10	1.780	1.790	0.778	0.793
11	23.10	22.80	2.760	2.680
12	14.60	12.70	1.110	1.010
13	0.500	0.500	0.618	0.604
14	2.110	2.120	1.040	1.050
15	10.70	10.70	13.30	12.60
16	2.010	2.070	0.937	0.942

Table 7. Response table for S/N ratios of k

Curing Period	Level	C	F	A	w/b	w _n
7 days	1	178.7	178.7	172.4	167.5	171.7
	2	176.6	181.1	170.4	176.1	175.7
	3	165.4	162.3	175.1	174.6	176
	4	173.2	171.8	175.9	175.6	170.4
	Delta	13.3	18.8	5.5	8.6	5.6
	Rank	2	1	5	3	4
28 days	1	174.4	180.2	174.0	178.0	172.0
	2	177.1	178.8	175.7	178.3	180.8
	3	178.3	172.0	178.5	181.2	178.5
	4	175.5	174.4	177.2	168.0	174.2
	Delta	3.9	8.2	4.5	13.1	8.9
	Rank	5	3	4	1	2

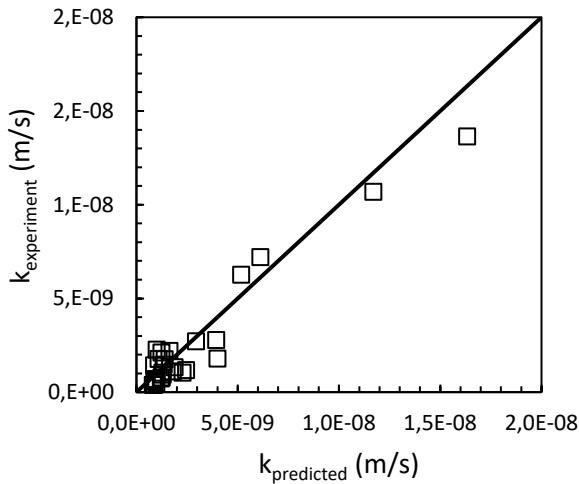


Figure 4. Permeability coefficient values of experimental results and predicted values according to regression analysis

In this study, two responses (q_u and k) were used because it was intended to construct the most durable and most impermeable deep mixing column. Therefore, optimum design parameters were obtained for maximizing q_u and minimizing k . The desirability function method was applied to find an optimal combination. The importance level of responses was chosen as 6 and 3 for q_u and k , respectively. The optimization plot of the two responses shows the parameter values of the optimal solutions (Figure 5). The vertical red lines represent the optimal values of parameters. The horizontal blue dashed lines represent the optimum response values ($q_u=2821.5326$ kPa and $k=8.82E-11$ m/s). The black curves represent the desirability on the vertical axis and the parameter values on the horizontal axis. The value of composite desirability is 0.9998. The optimal parameter

values are as followed; cement is 3.75 (14 %), fly ash is 3.80 (14 %), additive is 3.1212 (2.68 %), water/binder ratio is 1.25 (0.95), water content of untreated soil is 1.25 (21 %) and curing period is 2 (28 days). Cement and fly ash are responsible for producing gels to bind the soil particles and fill the voids between them. Therefore, the higher ratios of these two parameters can increase UCS and decrease the coefficient of permeability. According to these behaviors, higher values were chosen for binders in the present study as shown above. The optimum cement content is related to the stabilized soil type besides the requirements for the site [41]. Besides, different soils react differently to cementitious additives concerning the conditions of the site. They optimized the cement content for clay soil between 10%, 15%, and 20% of the dry weight of the clay. Replacing clay with fly ash in various ratios through 5, 10, 20, and 50% by dry weight of the total mixture, the load-bearing capacity of clay increase with the fly ash amount [42]. Yet fly ash contents from 20 to 50% didn't improve the load-bearing capacity. As a result, the optimum fly ash content was accepted as %20. For binders, generally, these optimum amounts could change concerning the site conditions and the stabilized soil type as mentioned before. The UCS values are related to the molding water content [13]. There is an optimum value for each cement content. Besides, UCS response for water/binder ratios between 0.6 and 2, the curves between UCS against water are similar to the compaction curves between dry density and water content. The difference in UCS values depends only on the bonds resulting from the water available.

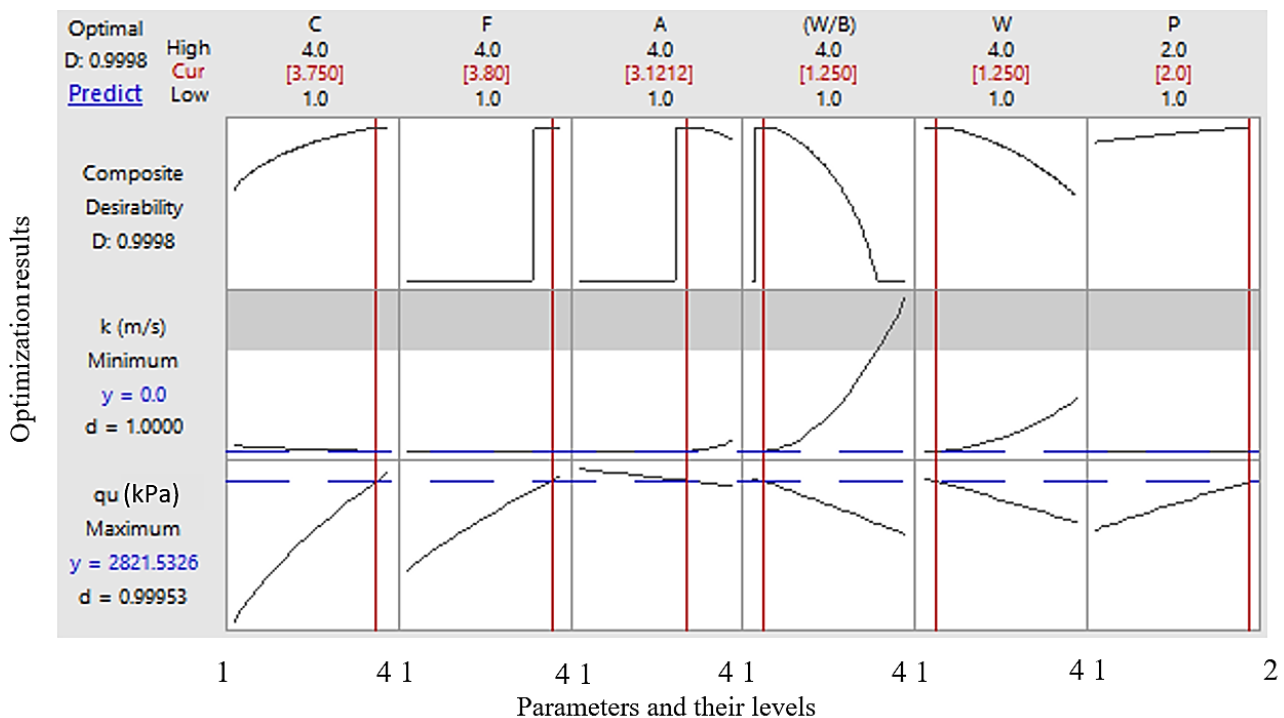


Figure 5. Optimization graphs for two responses

The addition of superplasticizers decreases yield value and plastic viscosity [43]. The arrangement of the particles within samples depends on the superplasticizer type. The w/c ratio has a significant effect on the performance of the superplasticizer because high w/c ratios decrease the performance of the superplasticizer. Superplasticizers can release water from the mixture. Therefore, more releases of water under higher dosages of superplasticizer could result in a great loss with the pozzolanic products and their gel causing more voids and less strength within the samples. This is why small dosages are applied generally like 1% by the weight of cementitious materials [16].

After selecting the optimal levels of each parameter, the last step is to predict and verify the values of the responses by using these optimal levels. For the unconfined compression strength, the error between experimental and predicted results was 3%, which means that the model is close to the real situation (Table 8). For the coefficient of permeability, the percentage of error was found a little bit higher as 13.5% which means that the developed model still includes some errors or another effective parameter should have been included in the developed model, or maybe there is an included parameter that misleads the prediction process.

3.4 Scanning Electron Microscopy (SEM) Analysis

Scanning electron microscope (SEM) analysis was performed to understand the microstructure of deep mixing samples. SEM images on untreated silty soil and soil-binder samples (design 9, design 11, and the optimum design) are given in Figure 6. The clear SEM images were obtained at 1000 magnifications. Untreated soil includes just minerals with voids caused by the irregularity of soil minerals (Figure 6a). In design 9, the microstructure of the soil-binder sample contains calcium silicate hydrate (C-S-H), calcium hydrate (C-H), and large voids (Figure 6b). The cement content of 11% produced C-S-H gels filling many voids and binding soil particles, however more voids were observed. In addition, many C-H particles were deposited on the surface of C-S-H gels as there weren't any fly ash particles. Therefore, the unconfined compression strength wasn't high enough. In design 9, the grains were accumulated separately leaving large voids. Such a structure could be classified as aggregated but deflocculated (FF associations).

In the microstructure of design 11, the formation of C-S-H gel, C-H, ettringite, and portlandite were observed (Figure 6c). By adding fly ash, the amount of C-S-H gels increases because of the reaction between C-H particles and fly ash.

Table 8. Experimental validation of the developed model with optimal parameters

Responses	Predicted	Experimental	Error
q_u (kPa)	2821.5	2737.1	3.0%
k (m/s)	8.82E-11	1.02E-10	13.5%

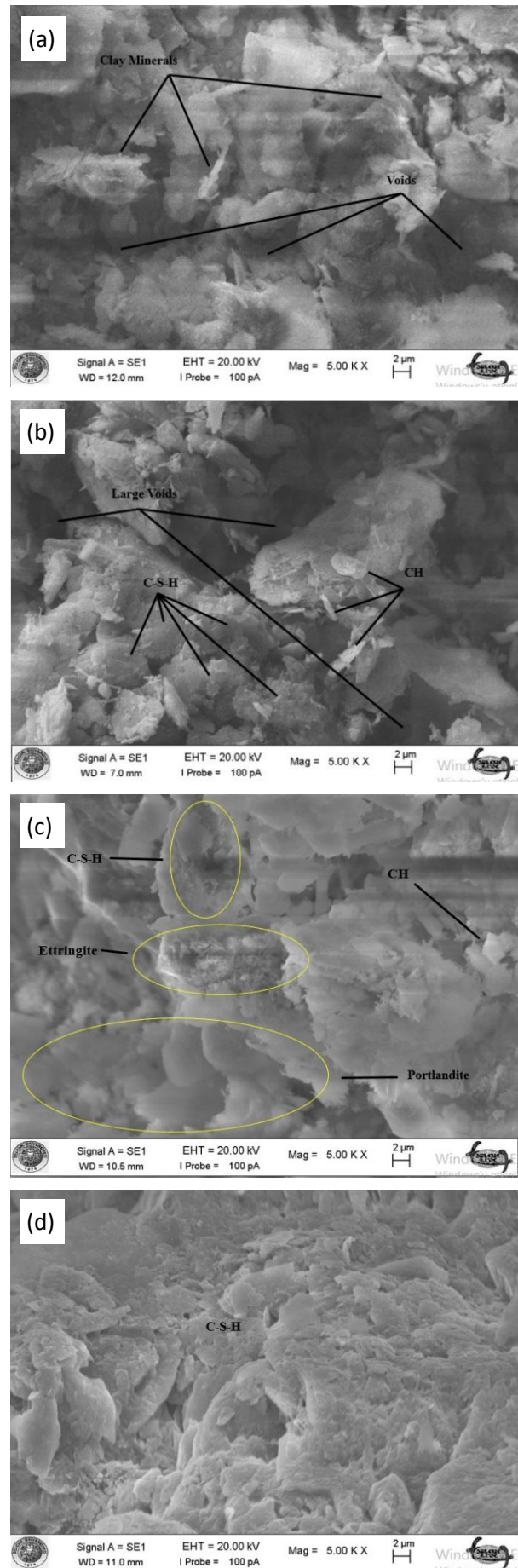


Figure 4. SEM images of a) untreated silty soil, b) design 9, c) design 11, and d) optimum design

Hence, fewer C-H particles were observed on the surface of C-S-H. Therefore, smaller voids and stronger bonds were obtained. Besides, ettringite between particles was very effective that high strength could be obtained. The formation of large portlandite particles was useful as it reduced the voids that existed within the microstructure because design 11 contains a continuous smooth face with fewer voids in between the particles. It could be classified as flocculated and aggregated (EE associations). In the microstructure of the optimum design, only C-S-H gel exists (Figure 6d). The aim of applying SEM analysis on the optimum design is to validate this model again for the formations at the microstructure. Almost all C-H particles were reacted with fly ash resulting in more C-S-H gels since the optimum content of fly ash was applied. Therefore, most of the voids were filled with C-S-H gels causing highly reduction in the permeability. Concerning the optimum design, all the particles are regularly connected, the surface has no roughness, and the particles are arranged in the same direction. Therefore, this structure could be classified as flocculated and aggregated (EE associations).

4. Conclusions

The effects of soil water content, cement, fly ash, superplasticizer contents, water/binder ratio, and curing period for soil-binder samples simulating deep mixing columns were studied by unconfined compression tests, permeability tests, and SEM analysis. Since there are so many parameters and levels to be researched, the design of the experiments was made according to the Taguchi method. The results were analyzed by S/N and regression analyzes, and then the optimization study was performed. While the amount of cement is effective in manufacturing durable columns, the amount of fly ash is effective in manufacturing impermeable columns. The increase in strength with cement content depends mainly on the cement hydration by which released calcium ions react with silica and alumina of the silty soil and form pozzolanic products. Increasing cement and fly ash content could affect the permeability in two different ways. The first effect is decreasing the permeability due to cement hydration because pozzolanic products bind the soil particles and decrease the void ratio. The second effect is increasing the permeability due to the higher water content causing more voids between particles. The first effect is more dominant for lower water/binder ratios and vice versa. The addition of superplasticizers decreases the flow consistency and the plastic viscosity. However, more dosages of superplasticizers could cause a great loss on forming the pozzolanic products.

In the optimum design of DMC having high strength and low permeability, grout content should be consisting of 14% cement, 14% fly ash, 2.68% superplasticizer additive, and 0.95 water/binder ratio. That is, 50% of the

total dry binder amount is fly ash. This result shows that in soil improvement works with deep soil mixing method, the use of cement is reduced by 50% by using fly ash to produce more durable and more impermeable columns. One more binder silo can be installed on the construction site and the grout can easily be prepared with cement and fly ash. In this case, it is necessary to use the superplasticizer additive as the fly ash will increase the density and flow consistency of the grout. The additive can also be added to the grouting water and then added to the grout mixture.

Declaration

The author(s) declared no potential conflicts of interest with respect to the research, authorship, and/or publication of this article. The author(s) also declared that this article is original, was prepared in accordance with international publication and research ethics, and ethical committee permission or any special permission is not required.

Author Contributions

The authors carried out the investigation and co-designed the planning of the experiments. Y. Yenginar contributed to obtaining and interpreting the experimental and statistical results, writing and editing the article. A.A.M.M. Mobark contributed to the experimentation, literature review and writing original draft of article. M. Olgun contributed to the interpretation of the results, writing review of the article.

Reference

1. Shrestha R. and A. Al-Tabbaa, *Development of predictive models for cement stabilized soils*. In: *Proceedings of the Fourth International Conference on Grouting and Deep Mixing*, 2012: New Orleans, Louisiana, United States. p. 221–231.
2. Dias D.R., G. Camarini, and M.G. Miguel, *Preliminary laboratory tests to study the increase of strength in samples of soft soils with cement, for treatments using Dry-Mix System*. In: *Proceedings of the Fourth International Conference on Grouting and Deep Mixing*, 2012: New Orleans, Louisiana, United States. p. 454–462.
3. Li L., F. Santos, Y. Li, P.E.W. Shao, Q. Zhao, and F. Amini, *Evaluation of fly ash and soil mixtures for use in highway embankments*. In: *Geo-Congress: State of the Art and Practice in Geotechnical Engineering*, 2012: Oakland, California, United States. p. 3672–3680.
4. Ranga S.K., *Geotechnical characterization of soft clay treated with a bottom and fly ash mixture*. In: *Geo-China: Innovative Technologies for Severe Weather and Climate Change*, 2016: Shandong, China. p. 118–125.
5. Akash P., K. Arvind, G. Deepak, and P. Pankaj, *Compaction and strength behavior of tire crumbles–fly ash mixed with clay*. *J. Mater. Civ. Eng.*, 2018. **30**(4): p. 1–9.
6. Show K., J. Tay, and A.T.C. Goh, *Reuse of incinerator fly ash in soft soil stabilization*. *J. Mater. Civ. Eng.*, 2003. **15**(4): p. 335–343.

7. Kumar B.R.P. and R.S. Sharma, *Effect of fly ash on engineering properties of expansive soils*. J. Geotech. Geoenviron. Eng., 2004. **130**(7): p. 764–767.
8. Senol A., E. Etminan, and C.G. Olgun, *Stabilization of clayey soils using fly ash and homopolymerpolypropylene*. In: *Geo-Congress: State of the Art and Practice in Geotechnical Engineering*, 2012: Oakland, California, United States. p. 3929–3938.
9. Amadi A.A., A.O. Eberemu, and K.J. Osinubi, *Strength consideration in the use of lateritic soil stabilized with fly ash as liners and covers in waste landfills*. In: *Geo-Congress: State of the Art and Practice in Geotechnical Engineering*, 2012: Oakland, California, United States. p. 3835–3844.
10. Akbulut S. and A. Sağlamer, *Evaluation of fly ash and clay in soil grouting*. In: *Grouting and Ground Treatment*, 2003: New Orleans, Louisiana, United States. p. 1192–1199.
11. Jongpradist P., N. Jumlongrach, Y. Sompote, and S. Chucheeprakul, *Influence of fly ash on unconfined compressive strength of cement-admixed clay at high water content*. J. Mater. Civ. Eng., 2010. **22**(1): p. 49–58.
12. Zhang C., J. Yang, X. Ou, J. Fu, Y. Xie, and X. Liang, *Clay dosage and water/cement ratio of clay-cement grout for optimal engineering performance*. Applied Clay Science, 2018. **163**(1): p. 312–318.
13. Ribeiro D., R. Néri, and R. Cardoso, *Influence of water content in the UCS of soil-cement mixtures for different cement dosages*. In: *Procedia Engineering*. Elsevier Ltd., 2016. **143**(1): p. 59–66.
14. Azadi M.R., A. Taghichian, and A. Taheri, *Optimization of cement-based grouts using chemical additives*. Journal of Rock Mechanics and Geotechnical Engineering, 2017. **9**(4): p. 623–637.
15. Zhang Q., J. Liu, J. Liu, F. Han, and W. Lin, *Effect of superplasticizers on apparent viscosity of cement-based material with a low water–binder ratio*. J. Mater. Civ. Eng., 2016. **28**(9): p. 1–7.
16. Shaikh F.U. and S.W.M. Supit, *Effects of superplasticizer types and mixing methods of nanoparticles on compressive strengths of cement pastes*. J. Mater. Civ. Eng., 2016. **28**(2): p. 1–7.
17. Aita C.A.G., I.C. Goss, T.S. Rosendo, M.D. Tier, A. Wiedenhöft, and A. Regulý, *Shear strength optimization for FSSW AA6060-T5 joints by Taguchi and full factorial design*. Journal of Materials Research and Technology, 2020. **9**(6): p. 16072–9.
18. Voelkel J.G., *Fractional factorial designs*. In: *Encyclopedia of Statistics in Quality and Reliability*. 2008, Chichester, U.K.: John Wiley & Sons, Ltd.
19. Taguchi G. and S. Konishi, *Taguchi methods orthogonal arrays and linear graphs: Tools for quality engineering*. 1987, Dearborn, Michigan: Amer Supplier Inst.
20. Taguchi G., E.A. Elsayed, and T.C. Hsiang, *Quality engineering in production systems*. 1989, New York, N.Y.: McGraw-Hill.
21. Taguchi G., *Introduction to quality engineering: Designing quality into products and processes*. 4th ed. 1988, Tokyo: Asian Productivity Organization.
22. Taguchi G., S. Chowdhury, and Y. Wu. *Taguchi's Quality Engineering Handbook*. 2004, Hoboken, NJ, USA: John Wiley & Sons, Inc.
23. Tan Ö., *Investigation of soil parameters affecting the stability of homogeneous slopes using the Taguchi method*. Eurasian Soil Science, 2006. **39**(11): p. 1248–1254.
24. Tan Ö., A.S. Zaimoglu, S. Hinislioglu, and S. Altun, *Taguchi approach for optimization of the bleeding on cement-based grouts*. Tunnelling and Underground Space Technology, 2005. **20**(2): p. 167–173.
25. Wasantha P.L.P. and P.G. Ranjith, *The Taguchi approach to the evaluation of the influence of different testing conditions on the mechanical properties of rock*. Environmental Earth Sciences, 2014. **72**(1): p. 79–89.
26. Zhang F., M. Wang, and M. Yang, *Successful application of the Taguchi method to simulated soil erosion experiments at the slope scale under various conditions*. CATENA, 2021. **196**:104835.
27. Özel S., E. Vural, and M. Binici, *Taguchi method for investigation of the effect of TBC coatings on Ni-Cr bond-coated diesel engine on exhaust gas emissions*. International Advanced Researches and Engineering Journal, 2020. **4**(1): p. 14–20.
28. ASTM C494/C494M–19, *Standard specification for chemical admixtures for concrete*. 2020, West Conshohocken, PA.
29. Derringer G. and R. Suich, *Simultaneous optimization of several response variables*. Journal of Quality Technology, 1980. **12**(4): p. 214–219.
30. Bouzid L., S. Berkani, M.A. Yallese, F. Girardin, and T. Mabrouki, *Estimation and optimization of flank wear and tool lifespan in finish turning of AISI 304 stainless steel using desirability function approach*. International Journal of Industrial Engineering Computations, 2018. **9**(1): p. 349–368.
31. Fitrianto A. and H. Midi, *Multi-response optimization via desirability function for the black liquor data*. Journal of Science and Technology, 2012. **4**(1): p. 91–101.
32. Sahoo A.K. and P.C. Mishra, *A response surface methodology and desirability approach for predictive modeling and optimization of cutting temperature in machining hardened steel*. International Journal of Industrial Engineering Computations, 2014. **5**(3): p. 407–416.
33. ASTM D2166-00, *Standard test method for unconfined compressive strength of cohesive soil*. 2000, West Conshohocken, PA.
34. Lorenzo G.A. and D.T. Bergado, *Fundamental characteristics of cement-admixed clay in deep mixing*. J. Mater. Civ. Eng., 2006. **18**(2): p. 161–174.
35. Bergado D.T. and G.A. Lorenzo, *Economical mixing method for cement deep mixing*. In: *Innovations in Grouting and Soil Improvement*, 2005: Austin, Texas, United States. p. 1–10.
36. Tastan E.O., T.B. Edil, C.H. Benson, and A.H. Aydilek, *Stabilization of organic soils with fly ash*. J. Geotech. Geoenviron. Eng., 2011. **137**(9): p. 819–833.
37. Uray E., Ö. Tan, S. Çarbaş, and İ.H. Erkan, *Metaheuristics-based pre-design guide for cantilever retaining walls*. Teknik Dergi, 2021. **32**(4): p. 10967–93.
38. Kate G.K., C.B. Nayak, and S.B. Thakare, *Optimization of sustainable high-strength–high-volume fly ash concrete with and without steel fiber using Taguchi method and multi-regression analysis*. Innovative Infrastructure Solutions, 2021. **6**(2): p. 1–18.
39. Şimşek B., Y.T. İç, E.H. Şimşek, *A full factorial design-based desirability function approach for optimization of properties of C 40/50 concrete class*. Mathematical and Computational Applications, 2013. **18**(3): p. 330–339.

40. ASTM D5084-16a. *Standard test methods for measurement of hydraulic conductivity of saturated porous materials using a flexible wall permeameter*. 2016, West Conshohocken, PA.
41. Fatahi B., D. Engelbert, S. Mujic, and H. Khabbaz, *Assessment of surcharging on strength and stiffness of cement treated clays*. In: *Proceedings of the Fourth International Conference on Grouting and Deep Mixing*, 2012: New Orleans, Louisiana, United States. p. 272–80.
42. Priyadarshee A., A. Kumar, D. Gupta, and P. Pushkarna, *Compaction and strength behavior of tire crumbles–fly ash mixed with clay*. *J. Mater. Civ. Eng.*, 2018. **30**(4):04018033 p. 1-9.
43. Faroug F., J. Szwabowski, and S. Wild, *Influence of superplasticizers on workability of concrete*. *J. Mater. Civ. Eng.*, 1999. **11**(2): p. 151-157.



Research Article

Dimensional optimization of two-phase flow boiling in microchannel heat sinks

Rahim Jafari ^{a,*} 

^a Department of Automotive Engineering, Atılım University, Kızılcaşar St., İncek, Gölbaşı, 06830, Ankara, Turkey

ARTICLE INFO

Article history:

Received 08 September 2021

Revised 28 November 2021

Accepted 10 December 2021

Keywords:

Electronics cooling

Microchannels

Mixture model

Optimization

Two-phase flow

ABSTRACT

The heat transfer coefficient (HTC) of microchannel heat sinks (MHS) is higher than common heat sinks due to higher area to volume ratio. Its value for two-phase flow boiling is much superior to single-phase flow. In addition, the two-phase flow boiling provides uniform wall temperature close to the coolant's saturation temperature in low vapor qualities. In the present study, a heat sink is optimized dimensionally after modeling of the boiling of R134a refrigerant in the microchannels. Firstly, mixture two-phase method along with the wall heat flux partitioning are utilized to introduce an applied thermal model to design MHSs. The heat sink mounted on the backside of an Intel core i7-900 desktop processor with dimensions of 19 mm×14.4 mm× 1 mm is numerically simulated to investigate the thermal performance. The HTC and the exit vapor quality are comparable with the available empirical correlations and first law of thermodynamics, respectively. Then the proposed model is developed to optimize the dimensions of the microchannels to design the heat sink with minimized wall temperature. Bound optimization by quadratic approximation (BOBYQA) method results in the optimized dimensions of the microchannels in the heat sink. Optimization of heat sink's geometry in terms of the dimensions of the microchannels at various boundary conditions will be practical as the unique application of the model.

1. Introduction

Dissipation of the generated excessive heat due to the increased power density is the major issue for compact integrated circuits. For instance, desktop PCs generated maximum heat flux of 108 W/cm² and maximum junction temperature of 85°C in 2016 [1Hata! Başvuru kaynağı bulunamadı.]. In addition, the average power density for specialty applications such as laser diode arrays raised over 1000 W/cm² [2,3]. The conventional cooling methods such as forced air cooling in combination with heat sinks has maximum HTC of 250 W/m²·°C [4]. Therefore, based on maximum junction temperature of 85°C and ambient temperature of 20°C, the dissipated heat flux typically limited to 20 W/cm² seems to be unsatisfactory to overcome this challenge.

MHS is an alternative method with a considerable and improved cooling capability for impacted electronic devices. HTC of MHSs is higher than common heat sinks due to higher area to volume ratio. Its value for two-phase flow boiling is much superior to single-phase flow. In addition, the two-phase flow boiling provides uniform wall

temperature close to the coolant's saturation temperature except the higher vapor qualities near to one.

Available experimental data and correlations in the literature with adjustable parameters could be used to design MHSs with boiling. However, the results will be controversial issue as the parameters of interests fall outside the range of physical parameters, which they were developed. For instance, the mean absolute error of HTC for the correlation (smooth surface) suggested by Jafari et al. [5] has the minimum difference with the correlation proposed by Lee and Mudawar [6] and Kim and Mudawar [7]. The reason may be that the cooling fluid is R134a, which is the same for the first two correlations.

In addition, there are many numerical studies in the literature carried out to simulate flow boiling in microchannels. Common methods in the literature are based on the tracking of the interface between the liquid and vapor phases. Level-set method [8,9], Volume of Fluid [10], phase-field method [11,12] and Arbitrary Lagrangian-Eulerian (ALE) method [13] are techniques which track the interface of two separated phases of vapor and liquid. In Lattice- Boltzmann method, phase

* Corresponding author. Tel.: +90-312-586-8761; Fax: +90-312-586-8090.

E-mail addresses: rahim.jafari@atilim.edu.tr (R. Jafari)

ORCID: 0000-0003-1155-3711 (R. Jafari)

DOI: 10.35860/iarej.992871

© 2021, The Author(s). This article is licensed under the CC BY-NC 4.0 International License (<https://creativecommons.org/licenses/by-nc/4.0/>).

separation occurs automatically and it is not necessary to track the interface [14]. It should be assumed that nucleation starts at a specified point like a tiny hot plate in a microchannel. All these methods have been employed to model different types of boiling flows as bubbly flow, slug flow, annular flow and film boiling in microchannels.

Türkakar and Okutucu-Özyurt optimized MHS mounted on Intel Core i7-900 Desktop Processor dimensionally for single phase [15] and two-phase flows [16]. Entropy generation analysis has been done to optimize the channels' dimensions.

Non-linear set of equations govern the two-phase flow. In addition, equations for interfacial discontinuity and mass transfer between the liquid and vapor phases make the model more complex. This way, local heat transfer and fluid flow properties such as the local HTC and temperatures, bubble hydrodynamics in microscale and hot spots are predictable.

On the other hand, while the foregoing numerical methods provide precise information about the hydrodynamics and heat transfer of boiling in microscale, they are mostly restricted to confined geometries as a few bubbles, two-dimensional geometry and some presumptions due to computational time and cost. Therefore, an alternative numerical method, which is computationally cheaper than the aforementioned methods is required to simulate an extensive domain of MHSs. In the other words, an alternative quick and inexpensive model is necessitated to design MHSs, which phase change occurs. Besides, optimization of heat sink's geometry and boundary conditions will be practicable as the unique application of the method.

In the present study, the mixture method is utilized to develop a model, which results desired outcomes of saturated R134a flow boiling in MHSs in terms of HTC and vapor quality. An optimization is performed to minimize the temperature of the walls employing the proposed numerical method.

2. Numerical Model

2.1 Mixture Two-phase Flow Model

Mixture models [17] follow the average phase concentration, volume fraction, instead of the interface explicitly. Furthermore, one single momentum equation is defined to solve the mixture velocity, and both phases share the same pressure field. Hence, considerably smaller numbers of variables are solved comparing the other multiphase models. In this way, a multiphase model is developed for a practical application in which comprises whole geometry with less assumption.

The momentum equation for two phases is expressed as

$$\rho \frac{\partial \mathbf{u}}{\partial t} + \rho(\mathbf{u} \cdot \nabla)\mathbf{u} = \quad (1)$$

$$\begin{aligned} \nabla \cdot \left[-p\mathbf{I} + \mu \left(\nabla \mathbf{u} + (\nabla \mathbf{u})^T \cdot \frac{2}{3} (\nabla \cdot \mathbf{u})\mathbf{I} \right) \right] \\ - \nabla \cdot [\rho X(1-X)\mathbf{u}_{slip}\mathbf{u}_{slip}^T] \\ + \rho \mathbf{g} + F \end{aligned}$$

where X and \mathbf{u}_{slip} are the vapor quality and the relative velocity vector between two phases, respectively. The flow is assumed homogeneous and then the relative velocity between the phases is zero. Density and viscosity of two-phase flow are calculated with the volume averaged model as

$$\rho = \phi_l \rho_l + \phi_v \rho_v \quad (2)$$

$$\mu = \phi_l \mu_l + \phi_v \mu_v \quad (3)$$

A single continuity equation is written for the continuous (liquid) and dispersed (vapor) phases as:

$$\begin{aligned} (\rho_l - \rho_v) \left\{ \nabla \cdot [\phi_v(1-X)\mathbf{u}_{slip}] + \frac{m_{lv}}{\rho_v} \right\} \\ + \rho_l(\nabla \cdot \mathbf{u}) = 0 \end{aligned} \quad (4)$$

m_{lv} is mass transfer rate from the liquid to the vapor. It is also related to the volume fraction of dispersed phase (ϕ_v) as:

$$\begin{aligned} \frac{\partial \phi_v}{\partial t} + \nabla \cdot \{ \phi_v(\mathbf{u} + (1-X)\mathbf{u}_{slip}) \} \\ = - \frac{m_{lv}}{\rho_v} \end{aligned} \quad (5)$$

The mass transfer rate is determined in terms of the transferred heat from the wall to the refrigerant for evaporation and the latent heat of the refrigerant as:

$$m_{lv} = \frac{Q_{evp}}{h_{fg}} \quad (6)$$

Same temperature is assumed for the liquid and vapor phases. In other words, the temperature of the fluid remains constant and it equals to the saturation temperature.

On the other hand, the temperature of microchannel walls rises as the heat is applied to the bottom wall of the heat sink. Hence there will be a discontinuity just at the walls of microchannels. To address this issue, new parameter is defined in which it consists of the saturation temperature in the fluid and the superheated temperature on the walls of the microchannel as boundary conditions. The temperature of walls are obtained by solving the energy equation for the heat sink as

$$\rho C_p \frac{\partial T}{\partial t} + \rho C_p u \cdot \nabla T + \nabla(-k\nabla T) = Q \quad (7)$$

2.2 Wall Heat Flux Partitioning

To determine the wall heat flux, numerous experimental and theoretical studies propose so-called heat partitioning which consists of three components of wall heat fluxes for low-pressure subcooled boiling flow [18-22]. The heat flux components include the single-phase turbulent convection, transient conduction due to the departing bubbles (quenching), and evaporation. Generally, the fluid flow in the microchannels is laminar and the effect of the turbulence is negligible. Moreover, available studies of the convective boiling in the literature concluded diverse outcomes in the microchannels. Some of the studies reported the dominance of the nucleate boiling in the microchannels [23,24]. Conversely, some other studies concluded the dominant mechanism is convective boiling [25,26]. In addition, the effect of the both of the nucleate and convective boiling mechanism has been reported [27,28]. Type of the boiling mechanism will result in different boiling flows as bubbly flow, slug flow, annular flow and film boiling in microchannels. Evaporation heat flux at the walls is calculated from [29]:

$$Q_{evp} = nf \left(\frac{\pi}{6} d^3\right) \rho_v h_{fg} \quad (8)$$

There are various correlations in the literature to predict the density of active nucleation sites, n , for pool boiling and fluid flow in macroscale [30-32]. It mostly depends on the wall superheat and surface parameters. Lemmert and Chwala [30] considered the wall superheat to correlate n as

$$n = [210(T_w - T_{sat})]^{1.805} \quad (9)$$

Benjamin and Balakrishnan [32] remarked n in terms of the wall superheat and the surface roughness as

$$n = 218.8 Pr^{1.63} \left(\frac{1}{\gamma}\right) \theta^{-0.4} (\Delta T_{sat})^3 \quad (10)$$

Where θ and γ are calculated as

$$\theta = 14.5 - 4.5 \left(\frac{RaP}{\sigma}\right) + 0.4 \left(\frac{RaP}{\sigma}\right)^2 \quad (11)$$

$$\gamma = \left(\frac{k_v \rho_v C_{pv}}{k_l \rho_l C_{pl}}\right)^{\frac{1}{2}} \quad (12)$$

Bubble departure frequency, f , is a complex function of the bubble formation process. Available studies in the literature concluded that the bubble departure frequency is a fluctuating parameter [33].

It is assumed that a bubble grows uniformly to the internal diameter of the microchannel before departing. Therefore, the model of Plesset and Zwick [34] to predict the bubble departure frequency is given as:

$$f = \left(\frac{\rho_l C_{pl} \Delta T_{sat}}{\rho_v h_{fg} R}\right)^2 \frac{12\alpha_l}{\pi} \quad (13)$$

When a nucleated bubble grows, it departs from the surface and fresh fluid, comes into contact with the wall surface. The heated fluid by the transient conduction has been predicted by Mikic and Rohsenow [33] and the heat flux is considered as:

$$Q_q = \frac{2}{\sqrt{\pi}} \sqrt{f} \sqrt{k_l \rho_l C_{pl} A_q} (T_w - T_l) \quad (14)$$

where, A_q is expressed as

$$A_q = nK \left(\frac{\pi d^2}{4}\right) \quad (15)$$

K is a constant and is greater than unity. The heat flux due to the convection is calculated as:

$$Q_c = St \rho_l C_{pl} u_l (T_w - T_l) (1 - A_q) \quad (16)$$

Finally, the total wall heat flux, Q_w , is calculated as sum of evaporating, quenching and convection heat fluxes as:

$$Q_w = Q_{evp} + Q_q + Q_c \quad (17)$$

3. Geometry and Computational Domain

The viscosity effect on the lateral sides of the bubbles is neglected in 2D simulation; therefore, it would be less accurate than 3D. The computational domain is three-dimensional microchannel as depicted in Figure 1. In order to compare the simulation results with available experimental data in the literature, the computational domain and boundaries are defined same as the condition of the microchannel of heat sink experimented by Jafari et al. [5]. The height, width and length of the microchannel are 700 μm , 250 μm and 19 mm, respectively. Thermal properties of copper are used for the walls, except the top wall, which is assumed adiabatic. Coolant is refrigerant R134a with the inlet quality of 0.5 and the mass flux of 200 $\text{kg/m}^2\cdot\text{s}$. The saturation temperature is 10°C and it is assumed the outlet pressure remains at the saturation pressure. The thickness of the side walls is considered 53.5 μm which is half of the walls in the heat sink; hence, symmetry thermal boundary condition is applied to the outer sides of the walls. The initial and boundary conditions including the inlet quality and heat flux were selected respectively 0.5 and 20 W/m^2 to compare the results with the previous experimental study [5]. The dimensions of the heat sink and properties of the coolant are summarized in Table 1.

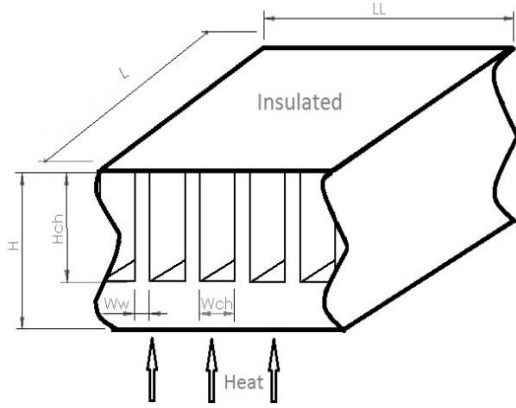


Figure 1. Heat Sink Geometry

Table 1. Dimensions of the heat sink and thermal properties of the refrigerant

Heat Sink		R134a	
L	19 mm	T_{sat}	10 °C
LL	14.4 mm	h_{lg}	189.460 KJ/kg
H	1 mm	k_l	0.092 W/m·K
Microchannel		k_v	0.014 W/m·K
L	19 mm	μ_l	0.00024 Pa.s
W _{CH}	0.250 mm	μ_v	0.0000567 Pa.s
H _{CH}	0.700 mm	ρ_l	1261 kg/m ³
Applied Heat Flux	20 W/cm ²	ρ_v	23.74 kg/m ³
G	200 kg/m ² ·s		

Since there is a little variation in the results by elapsing time, the steady-state solver failed. Therefore, the simulations have been conducted transient. A simulation has been implemented for applied base heat flux of 200 kW/m² for 5 seconds to distinguish the steady-state region. Table 2 illustrates number of meshes and sizes of the smallest grid. The grids sizes are determined finer in the domain of fluid than the solid part. Also, to take more accurate results at the corner of the microchannel, the smaller grids are distributed as well. The average wall temperature and average exit quality at different time steps are depicted in Figure 2 and Figure 3, respectively. It is obvious that after one second, the results converge to steady values. Furthermore, the results of meshing with four different mesh sizes are compared to evaluate the grid sizes on the outcomes.

Since the variation of the vapor quality is negligible for all the mesh sizes except the coarser mesh, the simulations

are proceeded with coarse mesh to save the computational time and power.

Figure 4 illustrates the temperature and vapor quality distributions along the microchannel. Figure 4a shows that the temperature decreases from the bottom wall to the side walls of the microchannel about one kelvin. On the other hand, since the refrigerant temperature remains uniform at the saturation temperature along the microchannel specified by the blue color, temperature of the walls is nearly constant along the fluid flow, which is the advantage of the two-phase flow boiling comparing the single-phase flow. Based on the numerical model, it is assumed that the heterogeneous nucleation occurs on the walls of the microchannel. Therefore, the vapor quality rises along the microchannel. Figure 4b displays that the vapor quality increases gradually along the fluid flow as the saturated liquid gains heat from the walls and is converted to the saturated vapor.

Table 2. Number of grids for various meshing

Meshing	Number of tetrahedral elements	Minimum element quality (mm)
Coarser	204364	1.2×10^{-3}
Coarse	395443	1.2×10^{-3}
Fine	755271	0.16×10^{-3}
Finer	998242	0.16×10^{-3}

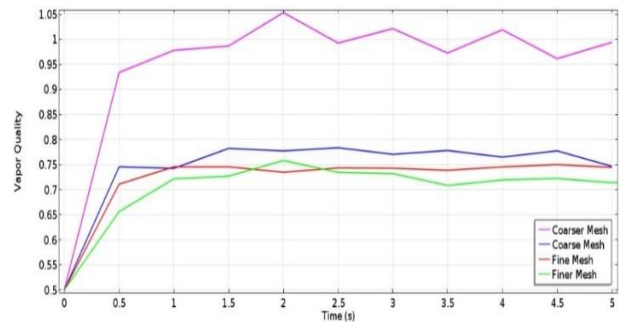


Figure 2. Variation of average wall temperature for two different sizes of grids by elapsing time ($\dot{q} = 20W/cm^2$)

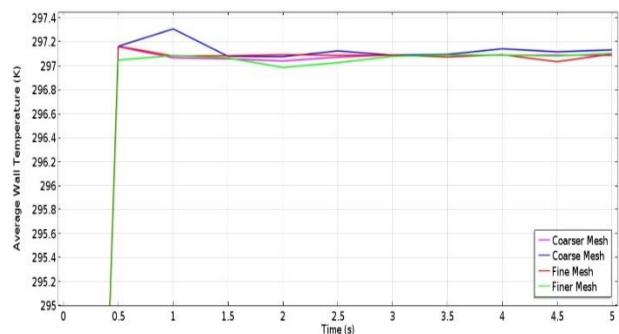


Figure 3. Variation of exit vapor quality for two different sizes of grids by elapsing time ($\dot{q} = 20W/cm^2$)

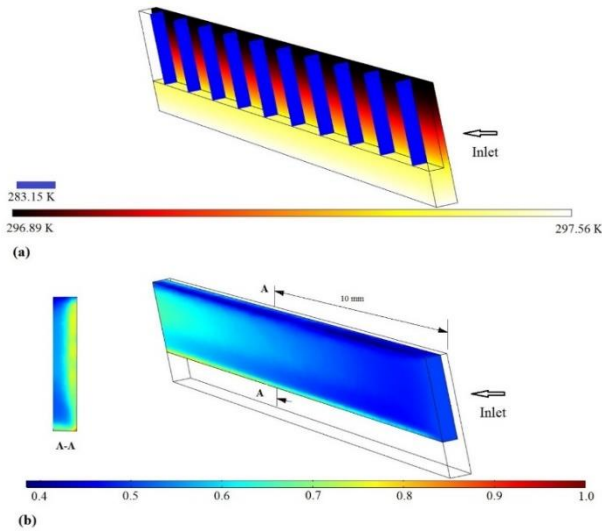


Figure 4. Temperature and (b) vapor quality distribution along the microchannel (Axisymmetric view)

4. Results and Discussion

4.1 Validation of the Numerical Model

The computational domain is selected such that determined in section 3. In addition, various heat fluxes from 5 W/cm^2 to 45 W/cm^2 have been applied to the base plane. This way, the initial and boundary conditions are identical with the conditions experimented by Jafari et al. [5]. Figure 5 illustrates the average HTC with respect to the applied base heat flux obtained with the present simulation and the experimental correlations available in the literature [5, 35-37].

The HTC grows strongly with increase of the corresponding heat flux. It is accordant with the experimental studies on the microchannels [39,40]. At low heat fluxes, the HTC of the present simulation and the experimental correlation of Kim and Mudawar [38] are in good agreement. The simulation results approached the experimental correlation of Lee and Mudawar [36] obtained from high heat fluxes as the applied heat flux grows. Since it has been assumed that bubbles nucleate uniformly along the walls and also the bubble departure diameter is restricted to the hydraulic diameter of the microchannel, the heterogeneous nucleate boiling is considered dominant in the simulations; however, based on the observation of the author from the previous experimental study [5] and also the captured flow patterns by Thiangtham et al. [41] for the applied ranges of heat flux, the dominant pattern in the experiments is annular flow. Therefore, employing of the proposed method to optimize the MHS with boiling flow at high heat fluxes will be much more realistic.

In order to evaluate the mass transfer from the liquid to the vapor, the average quality at the exit is calculated by first law of thermodynamics as:

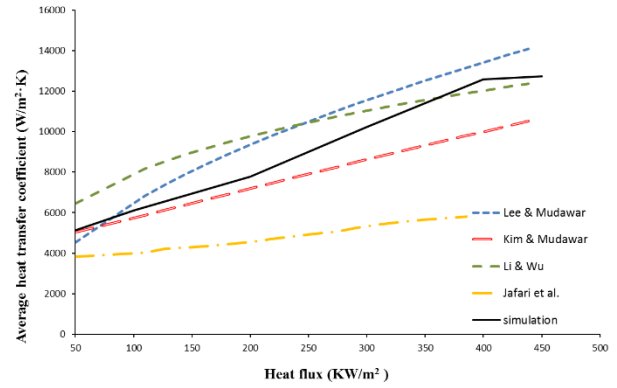


Figure 5. Comparison of the HTC between the experimental data and the proposed model

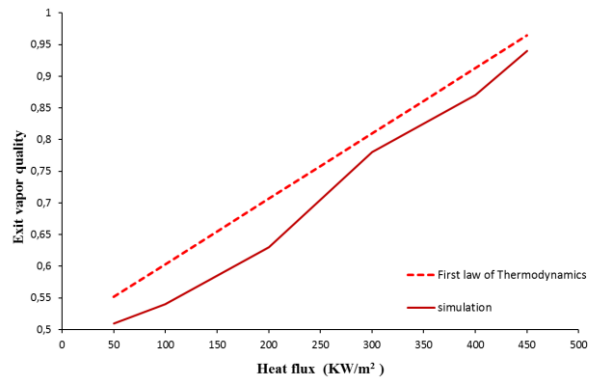


Figure 6. Comparison of exit vapor quality between the results of first law of thermodynamics and the present study

$$X_{out} = X_{in} + \frac{Q}{m_w h_{fg}} \quad (18)$$

Figure 6 depicts the comparison of exit vapor quality with respect to the base heat flux between the simulation and Equation 18. The result shows a good agreement in the exit vapor quality between the simulation and the calculated values from Equation 18.

Although the length of the microchannels is some millimeters in the previous studies with phase-field method [10,11] and ALE method [12], the computational time of the proposed method is about one third of the phase-field method and half of the ALE method.

4.2 Optimization of the Geometry

The heat sink mounted on the backside of an Intel Core i7-900 Desktop Processor is considered for optimization. The overall dimensions of the heat sink are $19 \text{ mm} \times 14.4 \text{ mm} \times 1 \text{ mm}$. The heat flux of 50 W/cm^2 is specified to be dissipated from the chip, which is a little greater than the actual generated heat (130 W). Two geometrical control variables, width and height of the microchannels, are used in the optimization. The optimization lower bound of the width and height are selected $100 \mu\text{m}$. The lower bound is specified based on the manufacturing constraints. The upper bounds of the width and height are determined 500

μm and 700 μm, respectively. The upper limit of the width restricts the dimension to the microscale size. Besides, minimum thickness of 300 μm is considered to satisfy the strength of the bottom wall of the microchannel. The initial wall thickness of the microchannel is assumed constant and takes the value of 100 μm. This value is based on the manufacturing constraints to fabricate MHSs from copper using wire electro-discharge machining (WEDEM) [5]. The wall thickness would change a little due to obtain integer value for the number of the microchannels at each simulation. Initial and boundary conditions are stated in Table 3. The objective variable is determined the average walls temperature, which is interested parameter to minimize. Besides, the only property constraint is the exit vapor quality that should be less than 1 to assure the prevention of superheating in the microchannels.

The employed optimization method is BOBYQA, Bound Optimization BY Quadratic Approximation, which is an iterative algorithm to find a minimum of an objective function $F(x)$, $x \in R^n$. It is subjected to specified bounds on the variables as $a_i < x_i < b_i$, $i = 1, 2, \dots, n$, in which n refers to the number of variables. A quadratic approximation at the beginning of the k -th iteration has the form

$$Q_k(y_i) = F(y_i), \quad i = 1, 2, \dots, m \tag{19}$$

m is a constant integer and equals $2n+1$. It is needed an initial control variable inside the specified bounds to begin the optimization. The interpolation points of first quadratic model (y_j , $i = 1, 2, \dots, m$) are specified as

$$y_1 = x_0$$

$$y_{i+1} = x_0 + \Delta_1 e_i \quad \text{and} \quad y_{n+i+1} = x_0 - \Delta_1 e_i \quad a_i < (x_0)_i < b_i$$

$$y_{i+1} = x_0 + \Delta_1 e_i \quad \text{and} \quad y_{n+i+1} = x_0 + 2\Delta_1 e_i \quad (x_0)_i = a_i \tag{20}$$

$$y_{i+1} = x_0 - \Delta_1 e_i \quad \text{and} \quad y_{n+i+1} = x_0 - 2\Delta_1 e_i \quad (x_0)_i = b_i$$

where Δ_1 and e_i are the initial trust region radius and the i -th coordinate vector in R^n , respectively. The algorithm of the method is described in detail in references [42, 43] and the overall flowchart of the computational algorithm is represented in Figure 7.

Since just one of the microchannels of the heat sink is considered to be optimized, the misdistribution of the flow, which would lead temperature variation over the heat sink surface is ignored. The optimization is carried out for two sets of initial control variables. The results of the optimization for initial values of $H = 200 \mu\text{m}$, $W = 100 \mu\text{m}$ and $H = 500 \mu\text{m}$, $W = 500 \mu\text{m}$ are provided in Tables 4, 5, respectively. The results show that the minimum wall temperature equals 288.6 K and is obtained for the channels with width and height of 100 μm and 700 μm, respectively. Moreover, it is concluded that the optimized value does not change by varying the initial control

variables. The optimization results are also employed to investigate the effects of the dimensional variations on the heat transfer and fluid flow parameters. Figure 8 shows the contour plots of the average wall temperature, average HTC, mass flow rate and exit vapor quality versus the width and height of the microchannels. It shows that the wall temperature decreases by increase of the aspect ratio (Height/Width). However, decrease in the average wall temperature does not comply with the increase in the average HTC.

Table 3. Dimensional ranges of microchannel and boundary conditions of optimization

Microchannels Height, μm	Upper bound	700
	Lower bound	100
Microchannels Width, μm	Upper bound	500
	Lower bound	100
Length, mm		14.4
Inlet quality		0.1
Mass flux, kg/m ² ·s		500
Heat flux, KW/m ²		500
Saturation temperature, K		283.15

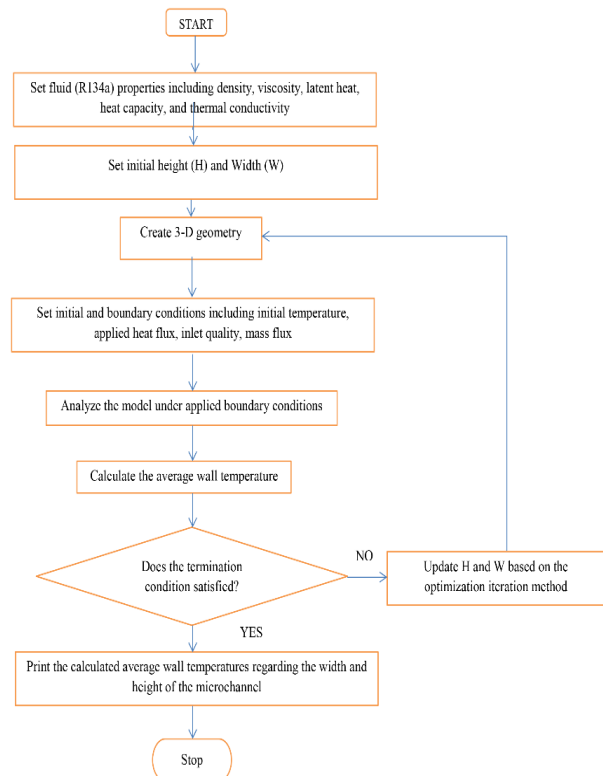


Figure 7. Flowchart of the computational algorithm

Table 4. Optimization results for $q''= 50 \text{ W/cm}^2$, $G = 500 \text{ kg/m}^2\text{s}$ and initial $W = 100 \mu\text{m}$, $H = 200 \mu\text{m}$

Number	Width (μm)	Height (μm)	Width of walls (μm)	Number of channels	Ave. Walls temp. (K)	Mass flow rate (g/s)
1	100	200	98.9	95	295.3	0.95
2	140	200	99.2	79	298.0	1.10
3	100	240	98.9	95	293.5	1.14
4	180	200	102.0	67	299.3	1.20
5	100	160+	98.9	95	296.1	0.76
6	100	700	98.9	95	288.6	3.32

Table 5. Optimization results for $q''= 50 \text{ W/cm}^2$, $G = 500 \text{ kg/m}^2\text{s}$ and initial $W = 500 \mu\text{m}$, $H = 500 \mu\text{m}$

Number	Width (μm)	Height (μm)	Width of walls (μm)	Number of channels	Ave. Walls temp. (K)	Mass flow rate (g/s)
1	500	500	109.3	63	301.6	3.87
2	460	500	112.3	66	301.4	3.80
3	500	540	109.3	31	301.2	4.18
4	420	500	104.8	40	300.9	3.78
5	500	460	109.3	57	302.1	3.57
6	100	700	98.9	37	288.6	3.32

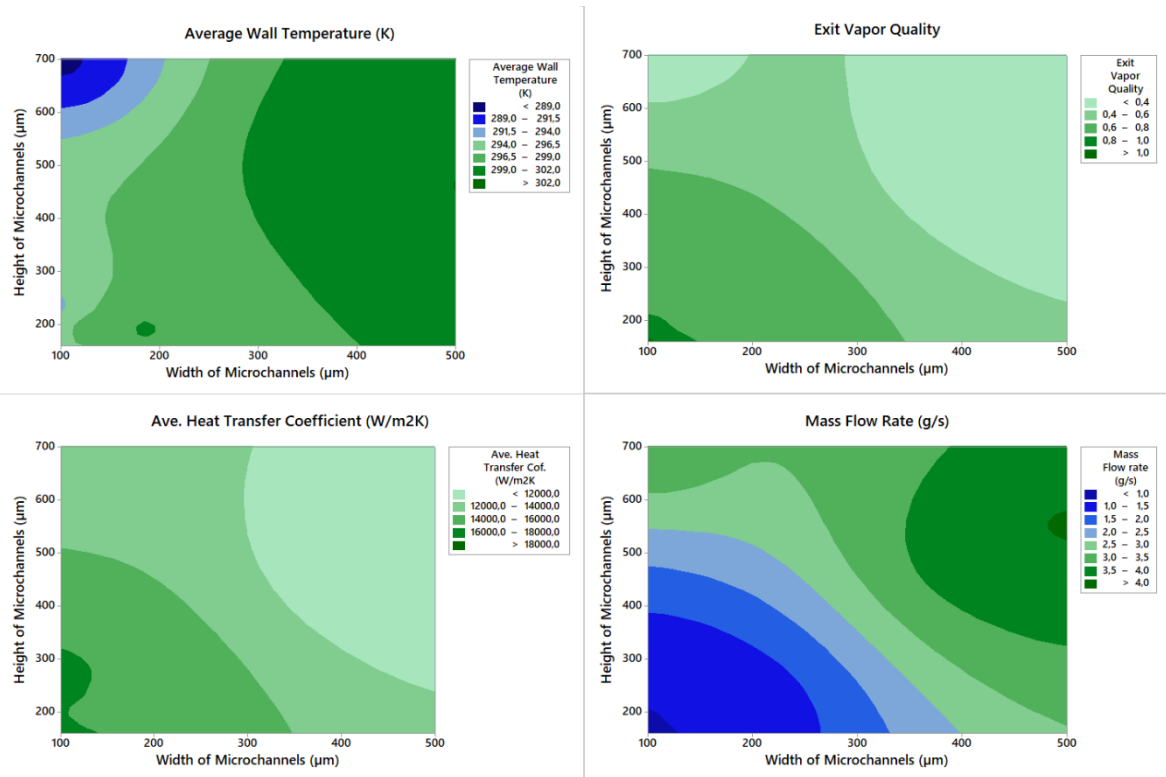


Figure 8. Contour plots of average wall temperature, average HTC, mass flow rate and exit vapor quality versus the width and height of the microchannels

Because of the reduction in applied heat to the walls of the microchannels, the exit vapor quality decreases as the sizes of the microchannels grow. The mass flow rate, which is proportional to the energy consumption by the compressor also rises by increment of microchannel size.

5. Conclusion

The mixture two-phase method along with the wall heat flux partitioning have been used to analyze two-phase flow boiling in MHSs. Intel Core i7-900 Desktop Processor has been considered as a heat source contained the overall area of $19\text{mm} \times 14.4 \text{ mm}$ and the maximum dissipated heat of 130 W. The average HTC and exit vapor quality have been

determined according to the different applied heat fluxes. The HTC and the vapor quality rise by increasing the heat flux at the constant mass flux of $G = 200 \text{ kg/m}^2\text{s}$. The results have complied with the available experimental data and first law of thermodynamics. The constructed model has been extended to optimize the width and height of the microchannels for the maximum generated heat flux of 50 W/cm^2 , which is a little more than the maximum generated heat flux from the aforementioned processor. The mass flux of $500 \text{ kg/m}^2\text{s}$ and the wall thickness of just about $100 \mu\text{m}$ have been supposed to be the constant values. The minimum wall temperature of 288.6 K has been gained for the maximum aspect ratio with the width and height of 100

μm and $700\ \mu\text{m}$, respectively. Türkakar and Okutucu-Özyurt also concluded that the channel height should be kept as high as the available volume permits. However, the average HTC restricts its value up to about $300\ \mu\text{m}$ with the constant mass flux. The proposed model would be an appropriate method to optimize microchannels heat sinks dimensionally.

Declaration

The author(s) declared no potential conflicts of interest with respect to the research, authorship, and/or publication of this article. The author(s) also declared that this article is original, was prepared in accordance with international publication and research ethics, and ethical committee permission or any special permission is not required.

Author Contributions

All the numerical analysis, validation and writing of the article have been done by R. Jafari.

Nomenclature

A_q	: Fraction of wall area cooled by quenching
C_p	: Specific heat capacity, [J/kg·K]
D	: Bubble departure diameter, [m]
f	: Bubble departure frequency, [Hz]
F	: External forces vector, [N/m ³]
G	: Gravity acceleration vector, [m/s ²]
G	: Mass flux [kg/m ² ·s]
h_{lg}	: Latent heat, [J/kg]
H	: Height [m]
I	: Identity matrix
K	: Thermal conductivity, [W/m·K]
L	: Length [m]
m_{iv}	: Mass rate of evaporation, [kg/s]
n	: Density of active nucleation sites
p	: Pressure, [Pa]
Pr	: Prandtl number
R	: Hydraulic diameter, [m]
Re	: Reynolds number
u	: Velocity vector, [m/s]
W	: Width [m]
X	: Vapor quality
t	: Time, [s]
T	: Temperature, [K]
Q	: Heat [W]
α	: Thermal diffusivity, [m ² /s]
Δ	: Radius of trust region, [m]
μ	: Viscosity, [Pa·s]
ρ	: Density, [kg/m ³]
σ	: Surface tension coefficient, [N/m]
ϕ	: Volume fraction
ch	: Channel
l	: Liquid
q	: Quench
sat	: Saturation

v : Vapor

w : Wall

References

1. Roadmap, IN, International Technology Roadmap for Semiconductors, 2006 Semiconductor Industry Association, 2009, <http://www.itrs.net/> Last visited on August 30, 2015.
2. Krishnan, S., S. Garimella, G. Chrysler, and R. Mavajan, *Towards a thermal Moore's law*, IEEE Transactions on Advanced Packaging, 2007. **30**(3): p. 462-474.
3. Price, D. C., *A review of selected thermal management solutions for military electronic systems*, IEEE Transactions on Components and Packaging Technologies, 2003. **26**(1): p. 26-39.
4. Çengel, Y. A., and A. J. Ghajar, *Heat and mass transfer: fundamentals and applications*. 2014, McGraw-Hill Education.
5. Jafari, R., T. Okutucu-Özyurt, H. Ünver, and Ö. Bayer, *Experimental investigation of surface roughness effects on the flow boiling of R134a in microchannels*, Experimental Thermal and Fluid Science, 2016. **79**: p. 222-230.
6. Lee, J., and I. Mudawar, *Two-phase flow in high-heat-flux micro channel heat sink for refrigeration cooling applications Part II—Heat transfer characteristics*, International Journal of Heat and Mass Transfer, 2005. **48**(5): p. 941–955.
7. Kim, S.M., and I. Mudawar, *Universal approach to predicting saturated flow boiling heat transfer in mini/micro-channels – Part II. Two-phase heat transfer coefficient*, International Journal of Heat and Mass Transfer, 2013. **64**: p. 1239–1256.
8. Zhou, S., X. Xu, B.G., and Sammakia, *Modeling of boiling flow in microchannels for nucleation characteristics and performance optimization*, International Journal of Heat and Mass Transfer, 2013. **64**: p. 706–718.
9. Akhlaghi Amiri, H.A., and A.A. Hamouda, *Evaluation of level set and phase-field methods in modeling two phase flow with viscosity contrast through dual-permeability porous medium*, International Journal of Multiphase Flow, 2013. **52**: p. 22–34.
10. Zu, Y.Q., Y.Y. Yan, S. Gedupudi, T.G. Karayiannis, and D.B.R., Kenning, *Confined bubble growth during flow boiling in mini-micro-channel of rectangular cross-section part II: approximate 3-D numerical simulation*, International Journal of Thermal Sciences, 2011. **50**(3): p. 267-273.
11. Jafari, R., and T. Okutucu-Özyurt, *Phase-field modeling of vapor bubble growth in a microchannel*, Journal of Computational Multiphase Flows, 2015. **7**(3): p. 143–158.
12. Jafari, R., and T. Okutucu-Özyurt, *Numerical simulation of flow boiling from an artificial cavity in a microchannel*, International Journal of Heat and Mass Transfer, 2016. **97**: p. 270–278.
13. Jafari, R., and T. Okutucu-Özyurt, *3D numerical modeling of boiling in a microchannel by arbitrary Lagrangian–Eulerian (ALE) method*, Applied Mathematics and Computation, 2016. **272**: p. 596–603.
14. Gong, S., and P. Cheng, *Numerical investigation of saturated flow boiling in microchannels by the Lattice Boltzmann method*, Numerical Heat Transfer, 2014. **65**(7): p. 644–661.
15. Türkakar, G., and T. Okutucu-Özyurt, *Dimensional optimization of micro-channel heat sinks with multiple heat sources*, International Journal of Thermal Sciences, 2012.

- 62: p. 85–92.
16. Turkakar, G., T. Okutucu-Ozyurt, and S.G. Kandlikar, *Entropy generation analysis of a microchannel-condenser for use in a vapor compression refrigeration cycle*, International Journal of Refrigeration, 2017. **70**: P. 71–83.
 17. Crowe, C., M. Sommerfeld, and Y. Tsuji, *Multiphase Flows with Droplets and Particles*, 1998. CRC Press.
 18. Cooper, M.G, *The microlayer and bubble growth in nucleate pool boiling*, International Journal of Heat and Mass Transfer, 1969. **12**(8): p. 915–933.
 19. Fath, H.S., and R.L. Judd, *Influence of system pressure on microlayer evaporation heat transfer*, ASME Journal of Heat Transfer, 1978. **100**(1): p. 49–55.
 20. Victor, H., M. Del Valle, and D.B.R. Kenning, *Subcooled flow boiling at high heat flux*, International Journal of Heat and Mass Transfer, 1985. **28**(10): p. 1907–1920.
 21. Hsu, Y.Y. and R.W. Graham, *Transport Processes in Boiling and Two-phase Systems*, 1976. Hemisphere, Washington, DC.
 22. Graham, R.W., and R.C. Hendricks, *Assessment of convection and evaporation in nucleate boiling*, 1967. NASA TN D-3943.
 23. Anwar, Z., B. Palm, and R. Khodabandeh, *Flow boiling heat transfer and dryout characteristics of R152a in a vertical mini-channel*, Experimental Thermal and Fluid Science, 2014. **53**: p. 207–217.
 24. Bao, Z.Y., D.F. Fletcher, and B.S. Haynes, *Flow boiling heat transfer of freon R11 and HCFC123 in narrow passages*, International Journal of Heat and Mass Transfer, 2000. **43**(18): p. 3347–3358.
 25. Qu, W., and I. Mudawar, *Flow boiling heat transfer in two phase microchannel heat sinks: I. Experimental investigation and assessment of correlation methods*, International Journal of Heat and Mass Transfer, 2003. **46**(15): p. 2755–2771.
 26. Boye, H., Y. Staate, and J. Schmidt, *Experimental investigation and modelling of heat transfer during convective boiling in a minichannel*, International Journal of Heat and Mass Transfer, 2007. **50**(1): p. 208–215.
 27. Lin, S., P.A. Kew, and K. Cornwell, *Flow boiling of refrigerant R141b in small tubes*, Transactions of the Institution of Chemical Engineers, 2001. **79**(A): p. 417–424.
 28. McNeil, D.A., A.H. Raeesi, P.A. Kew, and R.S. Hamed, *Flow boiling heat-transfer in micro to macro transition flows*, International Journal of Heat and Mass Transfer, 2013. **65**: p. 289–307.
 29. Bowring, R.W., *Physical model based on bubble detachment and calculation of steam voidage in the subcooled region of a heated channel*, Report HPR-10, Institute for Atomenergies, Halden, Norway, 1962.
 30. Lemmert, M.,J., and J.M. Chwala, *Influence of flow velocity on surface boiling heat transfer coefficient*, in: E. Hahne, U. Grigull (Eds.), *Heat Transfer in Boiling*, Academic Press and Hemisphere, 1977. New York and Washington, DC.
 31. Wang, C.H., and V.K. Dhir, *Effect of surface wettability on active nucleation site density during pool boiling of water on a vertical surface*, Journal of Heat Transfer, 1993. **115**(3): p. 659-669.
 32. Benjamin, R.J., and A.R. Balakrishnan, *Nucleation site density in pool boiling of saturated pure liquids: effect of surface microroughness and surface and liquid physical properties*, Experimental Thermal and Fluid Science, 1997. **15**(1): p. 32-42.
 33. Yoo, J., C.E. Estrada-Perez, and Y.A. Hassan, *A proper observation and characterization of wall nucleation phenomena in a forced convective boiling system*, International Journal of Heat and Mass Transfer, 2014. **76**: p. 568–584.
 34. Plesset, M.S., and S. A. Zwick, *The growth of vapour bubble in superheated liquid*, Journal of Applied Physics., 1954. **25**(4): p. 493–500.
 35. Mikic, B.B., and W.M. Rohsenow, *A new correlation of pool walking data including the fact of heating surface characteristics*, ASME Journal of Heat Transfer, 1969. **91**(2): p. 245–250.
 36. Lee, J., and I. Mudawar, *Two-phase flow in high-heat-flux micro-channel heat sink for refrigeration cooling applications: Part II—heat transfer characteristics*, International Journal of Heat and Mass Transfer, 2005. **48**(5): p. 941–955.
 37. Li, W., and Z. Wu, *A general correlation for evaporative heat transfer in micro/minichannels*, International Journal of Heat and Mass Transfer, 2010. **53**(9-10): p. 1778–1787.
 38. Kim, S.M., and I. Mudawar, *Universal approach to predicting saturated flow boiling heat transfer in mini/micro-channels – Part II. Two-phase heat transfer coefficient*, International Journal of Heat and Mass Transfer, 2013. **64**: p. 1239–1256.
 39. Agostini, B., J.R. Thome, M. Fabbri, B. Michel, D. Calmi, and U. Kloster, *High heat flux flow boiling in silicon multi-microchannels - Part I: Heat transfer characteristics of refrigerant R236fa*, International Journal of Heat and Mass Transfer, 2008. **51**(21-22): p. 5400-5411.
 40. Bertsch, S., E.A. Groll, and S.V. Garimella, *Refrigerant flow boiling heat transfer in parallel micro channels as a function of local vapor quality*, International Journal of Heat and Mass Transfer, 2008. **51**(19-20): p. 4775-4787.
 41. Thiangtham, P., C. Keeapaiboon, P. Kiatpachai, L.G. Asirvatham, O. Mahian, A.S. Dalkilic, and S. Wongwises, *An experimental study on two-phase flow patterns and heat transfer characteristics during boiling of R134a flowing through a multi-microchannel heat sink*, International Journal of Heat and Mass Transfer, 2016. **98**: p. 390-400.
 42. Powell, M.J.D., *The BOBYQA algorithm for bound constraint optimization without derivatives*, Report DAMTP 2009/NA06, University of Cambridge, UK.
 43. Powell, M.D.J., *Developments of NEWUOA for minimization without derivatives*, IMA Journal of Numerical Analysis, 2008. **28**(4): p. 649-664.

**Research Article**

Structural analysis of embedded hollow tubes on straight and curved platforms under thermal loads

Mustafa Murat Yavuz ^a 

^a*İzmir Democracy University, Faculty of Engineering, Mechanical Engineering Department, İzmir, 35300, Turkey*

ARTICLE INFO*Article history:*

Received 11 August 2021

Revised 14 November 2021

Accepted 13 December 2021

Keywords:

Stress

Temperature

Thermal

Tubes

ABSTRACT

Tube systems are widely used in heat transfer and intensive research is being done on positioning tubes on a platform. The platform structure is constantly exposed to thermal changes under operating conditions and the resulting stresses cause damage to existing systems. In this study, 8 thin-walled tubes were positioned on flat and curved platforms that were widely used and the stress behavior under thermal effects was investigated. Finite element analysis was used, and steady-state thermal condition was considered in the numerical investigation. The effects of temperature difference between platform surfaces and the thermal conductivity at the tube surfaces were investigated. It has been determined that the stress on the platform is higher than the stress on the tubes and the increase in the temperature difference on the platform surfaces increases the stress drastically. The increased thermal conductivity coefficient on the tube surface reduced the stresses on the platform and increased fatigue performance. Flat platform has lower contact pressure and platform stresses and better fatigue behavior. Results are discussed in detail.

1. Introduction

Tube systems are generally used to obtain heat from solar energy or to transfer heat from one heat source to another. Environmental conditions and thermal effects are dominant, and these factors exhibit an unstable attitude. Considering these factors, different geometric shapes, material types, various surface conditions and mounting structures are investigated. Studies in the literature focus on increasing efficiency in thermal solar panels, especially on thermal performance. Tube systems were systematically examined on the panels, and various geometric and material analyses were made. Flat plate was the most preferred in terms of ease of maintenance and production and cost in various tube panel systems such as flat plate, compound parabolic, evacuated tube, parabolic trough, Fresnel lens, parabolic bowl and heliostat field collectors [1-2]. The iso-scale trapezoidal absorber plate [3] developed for collector efficiency in flat plates reached 62% efficiency. Concentrated radiation applied to the tube along the focal line [4] increased the efficiency. Efficiency increased when the flow [5] was supported by homogeneous temperature distribution and simpler tube system structures [6] can be used to achieve homogeneous

temperature distribution, further reducing the production cost. The numerical investigation method [7] is sufficient and efficient to investigate the properties of thermal devices, and this method has been applied with the ANSYS simulation program [8] to avoid large deformation of absorbent flat plates. A 3D mathematical model of flat plate collectors [9] has been developed and applied in different collector types and flow conditions. The finite volume method (FVM) and Monte Carlo Ray-Trace (MCRT) [10] were combined for 3D computational solar collector analysis to obtain detailed flow and temperature results. The mechanical behavior of potential sealing materials [11] used in tube connections were investigated under the effects of atmospheric pressure and thermal expansion. In the study using the finite element method, it was determined that the low temperature bonding process provided sufficient strength. In the investigation of the heat losses between the absorber and the glass, the effects of the temperature difference were investigated [12] and it was determined that the thermal expansion and stresses formed affect the insulating epoxy material. The thermal stress analysis of the tube receiver [13] with focused radiation was investigated for different material conditions and it was more appropriate to use

* Corresponding author. Tel.: +90-232-260-1001 ; Fax: +90-232-260-1004.

E-mail addresses: murat.yavuz@idu.edu.tr (M.M. Yavuz)

ORCID: 0000-0002-5892-0075 (M.M. Yavuz)

DOI: 10.35860/iarej.981796

© 2021, The Author(s). This article is licensed under the CC BY-NC 4.0 International License (<https://creativecommons.org/licenses/by-nc/4.0/>).

copper material instead of stainless steel. For a parabolic collector, thermal stress analysis [14] was carried out on absorber tubes and it was seen that the highest tube deformation occurred in the supports. For a circular tube, heat transfer and thermal stresses [15] were investigated and it was determined that there was a relationship between the resulting stresses and the Biot number. Thermal-mechanical effects [16] have been investigated in the design of a central receiver for tubes. It [17-19] was seen that the bearing effects dominate the stress formation in the tube, and it was determined that the axial stresses formed were much larger than the stresses in the radial direction. It was predicted that thermal bending can be prevented with the support type. The thermal loads [20] for collector tubes in solar power buildings, which are complex to measure experimentally, were investigated with computer aided numerical methods and it was seen that thermal effects doubled the maximum equivalent stress. A new bayonet tube receiver [21] was designed to avoid the stress increase and compared it with a simple solar collector tube. Von-Mises stresses were significantly reduced as a result of the eccentricity of the bayonet tube. In the thermal stress analysis of bimetallic receivers, the double-layer absorber tube [22] created less stress than the single-layer absorber tube. Thermal and mechanical effects [23] were investigated in the absorber tube of the parabolic trough solar collector (PTSC) made of steel, copper, aluminum, Cu-Fe and four-layer laminate (Cu-Al-SiC-Fe). Although steel is strong in terms of strength, copper shows better thermal effects in thermal conditions. The most optimal material in all conditions was the four-layer laminate and the deflection in the tube was reduced by up to 49% compared to standard steel. In the solar tower research with molten salt receiver, it [24] was observed that the stress distribution and the inner-outer wall temperature difference distribution were similar. The similarity of the stress formed in the tube and the temperature distribution [25] was also seen in another study examining the deformation and stress errors in the absorber tube of parabolic trough collectors. The radial thermal stresses [26] occurred so low that they could be neglected in the thermal stress analysis for non-solar receiver tubes. It has been emphasized that different designs continue to be made in flat and curved panel systems and that mechanical effects in designs should be examined structurally.

In this study, platforms designed as flat and curved and the tubes connected between them were examined considering the thermal-mechanical effects. The effect of the temperature difference at the pipe ends and the heat transfer coefficient, which were known as the dominant effect of the working and environmental conditions, on the tube surfaces has been investigated. The results obtained show where and how intense the stresses were as a result

of thermal effects. Fatigue results, which took up little space in the literature, were made in detail with the fatigue analysis applied in this study, and the working life and safety were shown in the results.

2. Method and Tube System Models

It is difficult to produce thin-walled tube systems used in heat transfer and to examine their various parameters. Parametric studies should be carried out in these systems operating under variable temperature and convection effects. In the literature summary, since experimental studies have difficulties in thermal-mechanical investigations, the finite element method was used in this study because it has provided ease of parametric analysis. ANSYS package software was used in the research. A numerical model was created for the finite element method and the stresses created by the temperature and convection effects in the tube were investigated by defining the ideal boundary conditions.

Formation of the finite element model to be used in the analysis dominantly affects the solution accuracy. Therefore, a validation study was carried out before examining the tubes and the results were compared with an analytical solution found in the literature. In Figure 1, one tube used for the validation study was examined in the bending condition. The hollow tube has an inner radius of 35 mm and an outer radius of 37 mm. For the 800 mm long tube, the back surface was fixed and a force of 100 N was applied on the front surface for the bending condition. The bending stress for this condition was shown in Equation (1).

M was the moment due to the force; c was the distance between the cylinder centre and the cylinder outer surface; I was the moment of inertia for the cylinder geometry and was shown in Equation (2).

Thermal tube profiles were prepared in two different mounting arrangements and computer-aided models were created. The tubes are the same as the validation study model shown in Figure 1.

$$\sigma_{analytical} = \frac{M \cdot c}{I} \quad (1)$$

$$I = \frac{\pi}{4} (r_{out}^4 - r_{in}^4) \quad (2)$$

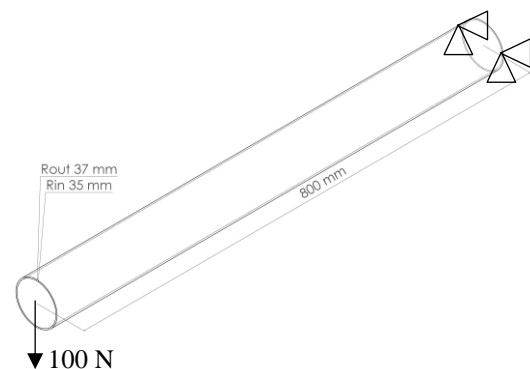


Figure 1. The used validation model

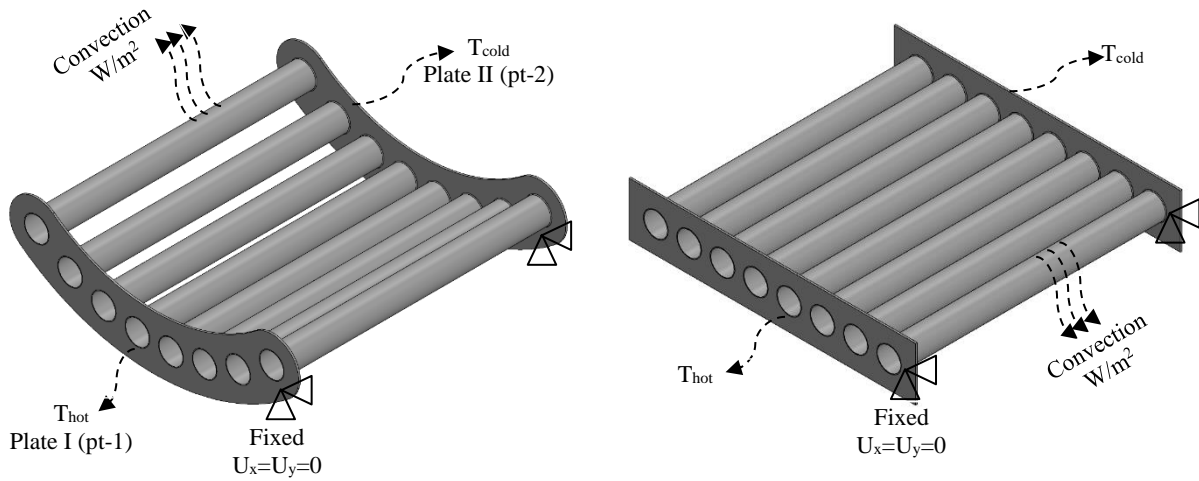


Figure 2. Curved and flat tube platforms and boundary conditions

Central distance between tubes are 100 mm. The used plate dimensions were $860 \times 160 \times 5$ mm. Thermal and structural boundary conditions were given in Figure 2. $T_{hot}=80^\circ\text{C}$ was used and it was changed to observe temperature difference effects. T_{cold} was set as 22°C , and it was constant in whole analyses. Convection on outer surface of tubes was considered. Side edges of platforms were fixed in structural analyses and bonded contact was used in contact definition. The used contact was suitable for the assembly of tubes and platforms. Standard steel properties were [27] used to define material properties that have modulus of elasticity 200 GPa, Poisson ratio of 0.3 and thermal expansion coefficient of $1.2 \times 10^{-6}/^\circ\text{C}$. Modulus of elasticity and thermal expansion coefficient [28-30] were used as constants, since tubes were not studied at high temperature ranges and the mechanical-thermal properties of the steel material did not vary much up to 200°C . Stress results were given in Von-Mises stresses. The used stress formulation [27, 31] was given in Equation (3). Soderberg fatigue theory [32-33] was used in fatigue analyses, and it was given in Equation (4).

$$\sigma_{mises} = \frac{1}{\sqrt{2}} \sqrt{(\sigma_1 - \sigma_2)^2 + (\sigma_2 - \sigma_3)^2 + (\sigma_3 - \sigma_1)^2} \quad (3)$$

$$\frac{\sigma_a}{S_e} + \frac{\sigma_m}{S_y} = \frac{1}{n} \quad (4)$$

σ_1 , σ_2 and σ_3 were principal stresses, σ_a and σ_m are alternating and mean stresses. For fatigue analysis, The used parameters and coefficients [34] were; standard strength coefficient (σ'_f), 920 MPa, strength exponent (b), -0.106, ductility coefficient (ϵ'_f), 0.213, ductility exponent (c), -0.47, cyclic strength (K'), 1000 MPa, cyclic strain hardening exponent (n'), 0.2 and yield strength (S_y), 250 MPa.

3. Results and Discussion

For the verification study shown in Figure 1, the stress result available in the literature [27, 35] was calculated in

Equation (1). The tensile stress formed in the middle of the tube geometry was found to be 5.04 MPa. The result of the finite element analysis was shown in Figure 3. The result obtained was similar to the analytical solution and the inspection method can be used to calculate the tube stress.

Figure 4 shows the stress and contact pressure due to convection for the curved and flat platform. Platform geometry has the highest stress value of all convection results. Another study [36] in the literature stated that a similar stress concentration occurs on the platform surface and its edges. The applied convection reduced the stress and contact pressure. There was no direct correlation between increasing convection value and decreasing stress value.

The application of convection only to the tube outer surfaces was more effective in reducing the stresses in the tube in Figure 4. Locally occurring high stresses are much lower in most sections. However, the highest values were used in the graph, since the onset of fracture mostly occurred where local stress values were high. Considering the convection effects for the flat platform, the stresses decreased similar to the curved structure. Although the plate (pt-1) stress and contact pressure were higher on the curved platform, the stress within the tube occurred more on the flat platform. Using the curved platform was safer in terms of stresses on the tube body.

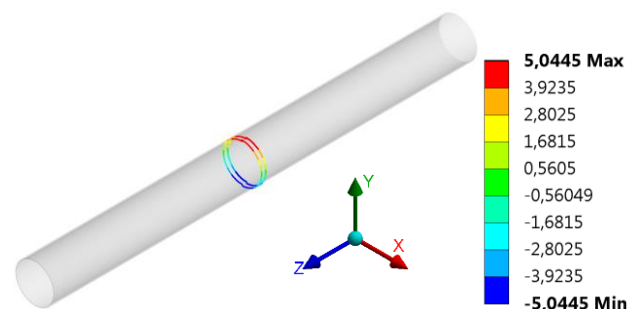


Figure 3. Bending (axial) stresses of a hollow cylinder in the middle of the length (in MPa)

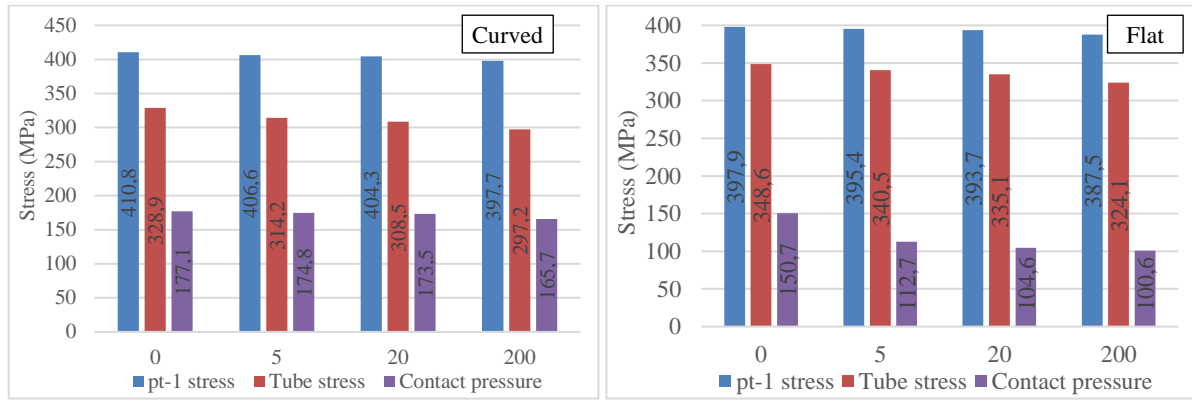


Figure 4. Effect of convection coefficient (0, 5, 20, 200 W/m².°C) on Von-Mises stresses and contact pressure in curved and flat system components

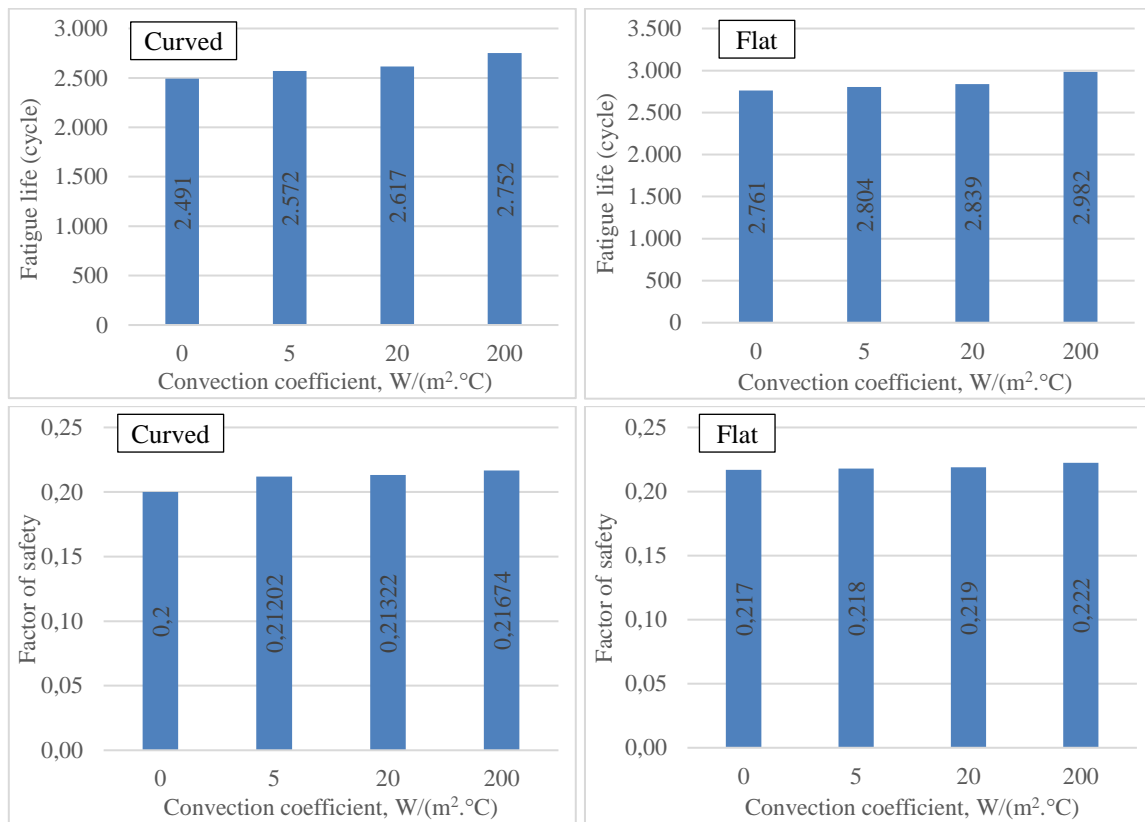


Figure 5. Effect of convection on fatigue life and factor of safety in curved and flat system

Figure 5 showed fatigue life and safety factor for full load/unload condition on curved and flat platform. The stresses were decreased by the convection effect and accordingly the fatigue life and safety factor increased. As the convection coefficient increased from 0 W/m².°C to 200 W/m².°C, the fatigue life increased 10% and the safety factor increased by 8% on the curved platform. Increased convection on flat platform increased 8% fatigue life and 2.5% safety factor. Flat platform showed more positive effect in terms of fatigue behavior. It was observed that the convection effect and the increase in fatigue results were not directly proportional.

The stresses occurring at the contact edge of the tube and

the curved/flat platform were shown in Figure 6. While the stresses on the side edges were higher, the stress values on the lower and upper edges were lower. Stress values decreased with the effect of convection. The difference between the 5, 20 and 200 W/m² convection values was small. As a result of the convection, the stresses decreased 6% on the curved platform and 8% on the flat platform.

The stresses formed as a result of the effect of different temperature differences were shown in Figure 7. Convection value was used as 0 W/m².°C. The increase in temperature difference predominantly caused an increase in stresses and contact pressure. As the pt-1 temperature increased from 80°C to 120°C, stress value on platform increased by 70%.

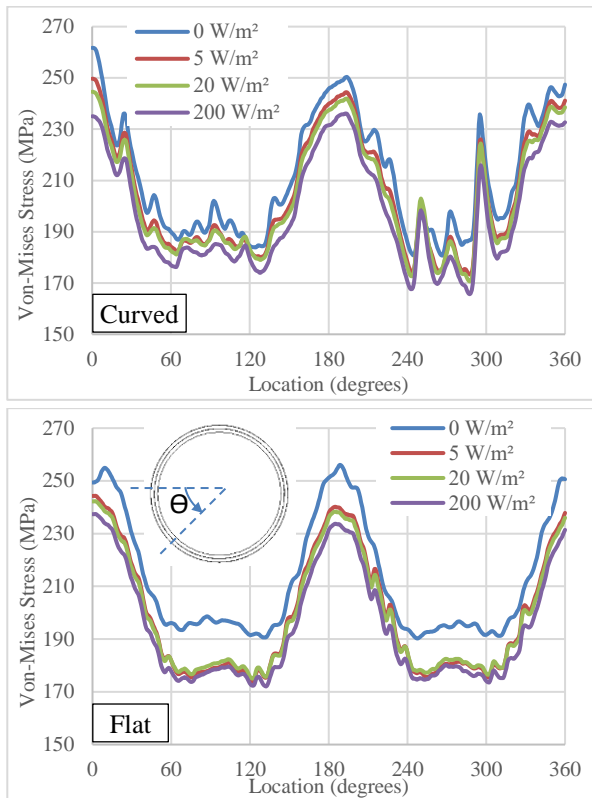


Figure 6. Effect of convection on Von-Mises stress distribution at circumference of 4th tube edge

The fact that the increase rate has been higher than the other results was due to the support effects on the platform in Figure 7. In the curved platform, the platform stress and contact pressure were higher, and the tube stress was lower than the flat platform.

The effect of pt-1 temperature for fatigue behaviour was shown in Figure 8. Higher stresses due to increasing temperature difference have been found to shorten the fatigue life. Increased temperature difference from 80°C to 120°C reduced fatigue life by 61% and coefficient of safety by 30% on both platforms.

Figure 9 showed the stresses that occurred at the edge of the tube as a result of the temperature difference. The temperature distribution in the platform results was similar and it was determined that the values increased predominantly as a result of the temperature change. Higher stresses were observed at the lateral edges of the tube contact area, and lower stresses were observed in the lower-upper contact edge region. The use of bonded contacts caused small fluctuations in the stress results, and this seems more evident on the curved platform.

4. Conclusions

In this study, the thermal-mechanical properties of a tube system operating under thermal conditions on two different

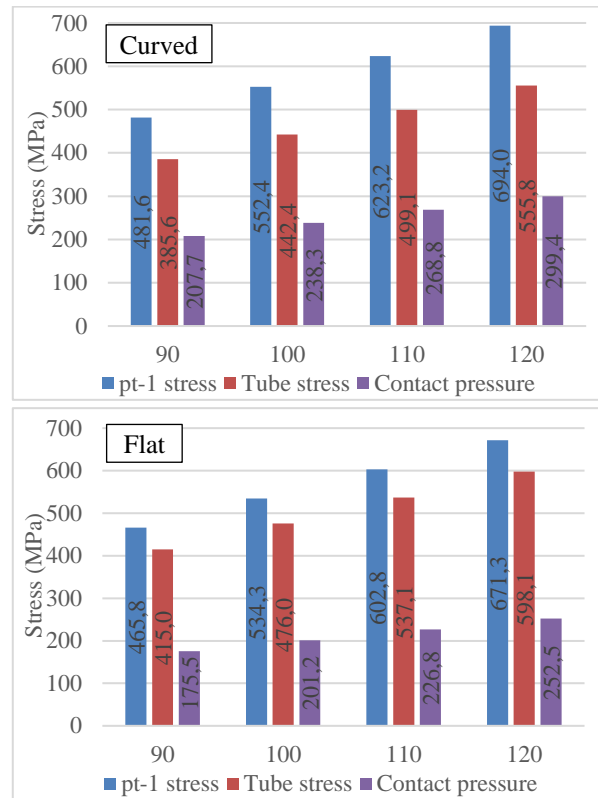


Figure 7. Effect of pt-1 plate temperature (90, 100, 110 and 120°C) on Von-Mises stresses and contact pressure in curved and flat system components

platforms were investigated by computer aided analysis. The effects of temperature difference and convection coefficient in operating conditions were investigated and the results were shown with graphics. If the main findings of the study are summarized;

- Increasing the convection coefficient has a reducing effect on the stress, increased the fatigue life and safety factor, but this effect is quite low.
- Local contact stresses and bearing effects dominate the stress due to thermal expansion.
- The variation of stresses caused by convection is not directly proportional.
- While tube stress is higher in flat platform, platform stress and contact pressure are lower.
- The fatigue behaviour of the flat platform is longer and safer than the curved platform.
- The increase in temperature difference predominantly caused an increase in stresses and contact pressure.
- Changing the platform temperature from 80°C to 120°C increased the stresses by 70%, reduced the fatigue life by 61% and the safety factor by 30%.

The findings show that thermal-mechanical examination should be done for each new design. Numerical methods are sufficient in terms of both solution time and accuracy.

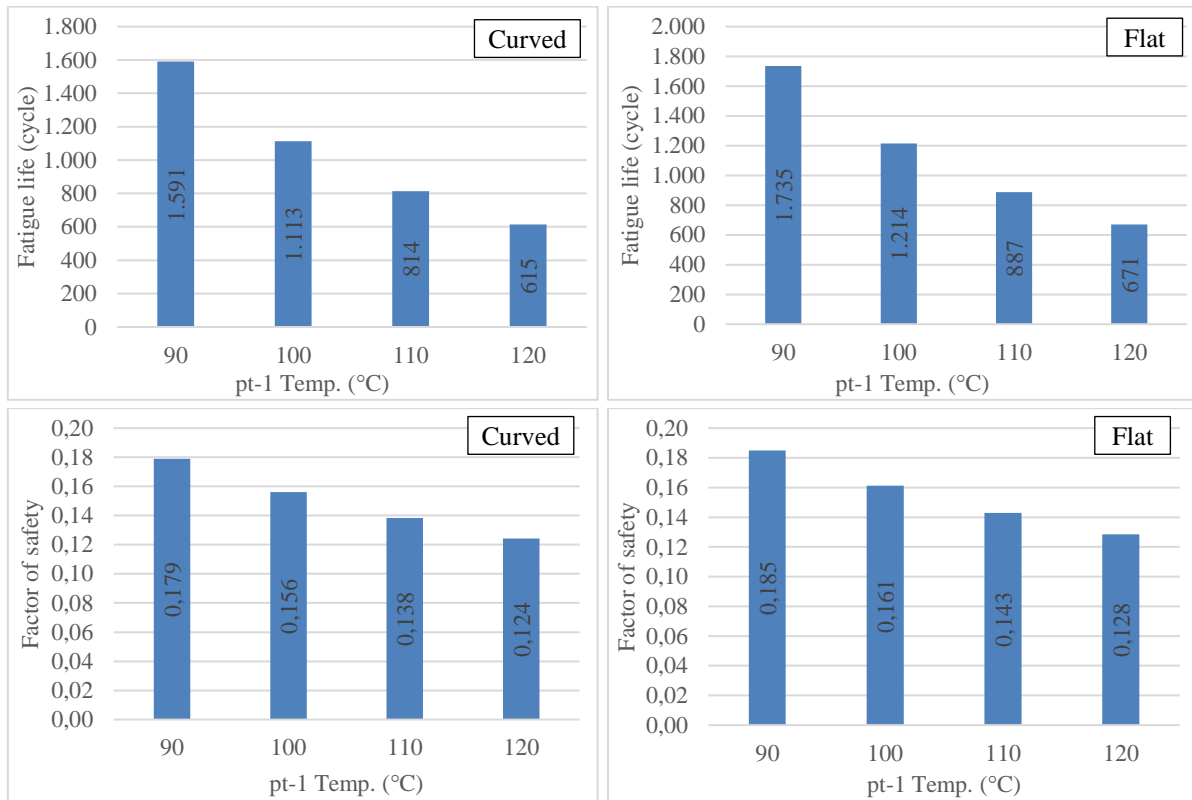


Figure 8. Effect of pt-1 plate temperature on fatigue life and factor of safety in curved and flat system

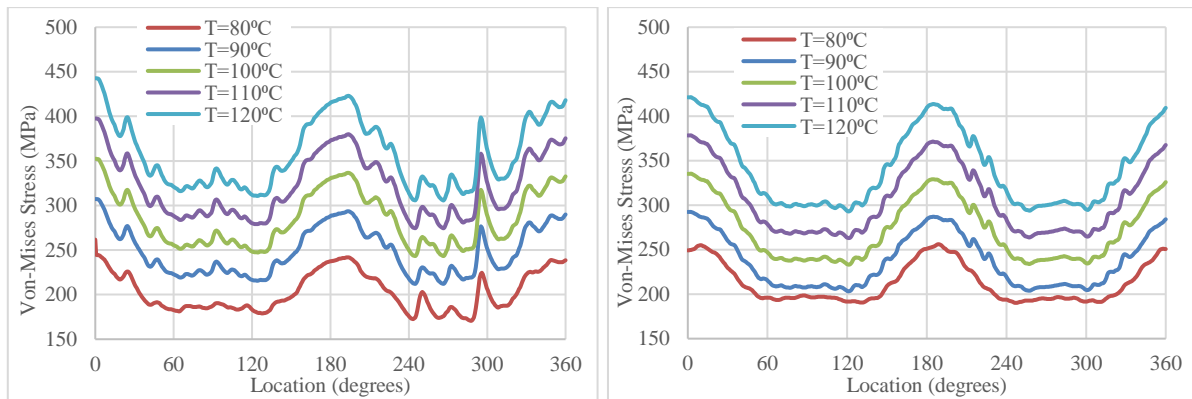


Figure 9. Effect of pt-1 plate temperature on Von-Mises stress distribution at circumference of 4th tube edge at curved and flat system

Declaration

The author declared no potential conflicts of interest with respect to the research, authorship, and/or publication of this article. The author also declared that this article is original, was prepared in accordance with international publication and research ethics, and ethical committee permission or any special permission is not required.

Author Contributions

M.M. Yavuz performed the analysis and wrote the whole manuscript.

References

1. Kalogirou, S.A., *Solar thermal collectors and applications*. Progress in Energy and Combustion Science, 2004. **30**: p. 231-295.
2. Alghoul, M.A., Sulaiman, M.Y., B.Z. Azmi, and M.A. Wahab, *Review of materials for solar thermal collectors*. Anti-Corrosion Methods and Materials, 2005. **52**(4): p. 199-206.
3. Visa, I., Duta, A., Comsit, M., Moldovan, M., Ciobanu, D., R. Saulescu, and B. Burduhos, *Design and experimental optimisation of a novel flat plate solar thermal collector with trapezoidal shape for facades integration*. Applied Thermal Engineering, 2015. **90**: p. 432-443.
4. Kalogirou, S.A., *A detailed thermal model of a parabolic trough collector receiver*. Energy, 2012. **48**: p. 298-306.
5. Facao, J., *Optimization of flow distribution in flat plate solar thermal collectors with riser and header arrangements*. Solar Energy, 2015. **120**: p. 104-112.
6. Cadafalch, J., *A detailed numerical model for flat-plate solar thermal devices*. Solar Energy, 2009. **83**: p. 2157-2164.

7. Visa, I., M. Moldovan, and A. Duta, *Novel triangle flat plate solar thermal collector for facades integration*. Renewable Energy, 2019. **143**: p. 252-262.
8. Villar, N.M., Lopez, J.M.C., Munoz, F.D., E.R. Garcia, and A.C. Andres, *Numerical 3-D heat flux simulations on flat plate solar collectors*. Solar Energy, 2009. **83**: p. 1086–1092.
9. Cheng, Z.D., He, Y.L., Cui, F.Q., R.J. Xu, and Y.B. Tao, *Numerical simulation of a parabolic trough solar collector with nonuniform solar flux conditions by coupling FVM and MCRT method*. Solar Energy, 2012. **86**: p. 1770–1784.
10. Colangelo, G., Favale, E., P. Miglietta, and A. Risi, *Innovation in flat solar thermal collectors: A review of the last ten years experimental results*. Renewable and Sustainable Energy Reviews, 2016. **57**: p. 1141–1159.
11. Henshall, P., Eames, P., Arya, F., Hyde, T., R. Moss, and S. Shire, *Constant temperature induced stresses in evacuated enclosures for high performance flat plate solar thermal collectors*. Solar Energy, 2016. **127**: p. 250–261.
12. Mossa, R., Shire, S., Henshall, P., Arya, F., P. Eames, and T. Hyde, *Performance of evacuated flat plate solar thermal collectors*. Thermal Science and Engineering Progress, 2018. **8**: p. 296–306.
13. Wang, F., Shuai, Y., Y. Yuan, and B. Liu, *Effects of material selection on the thermal stresses of tube receiver under concentrated solar irradiation*. Materials and Design, 2012. **33**: p. 284–291.
14. Abedini-Sanigy, M.H., Ahmadi, F., E. Goshtasbirad, and M. Yaghoubi, *Thermal stress analysis of absorber tube for a parabolic collector under quasi-steady state condition*. Energy Procedia, 2015. **69**: p. 3–13.
15. Marugán-Cruz, C., Flores, O., D. Santana, and M. García-Villalba, *Heat transfer and thermal stresses in a circular tube with a non-uniform heat flux*. International Journal of Heat and Mass Transfer, 2016. **96**: p. 256–266.
16. Rodríguez-Sánchez, M.R., Marugán-Cruz, C., A. Acosta-Iborra, and D. Santana, *Thermo-mechanical modelling of solar central receivers: effect of incident solar flux resolution*. Solar Energy, 2018. **165**: p. 43–54.
17. Montoya, A., Rodríguez-Sánchez, M.R., J. López-Puente, and D. Santana, *Numerical model of solar external receiver tubes: Influence of mechanical boundary conditions and temperature variation in thermoelastic stresses*. Solar Energy, 2018. **174**: p. 912–922.
18. Laporte-Azcué, M., González-Gómez, P.A., M.R. Rodríguez-Sánchez, and D. Santana, *Deflection and stresses in solar central receivers*. Solar Energy, 2020. **195**: p. 355–368.
19. Qaisrani, M.A., Wei, J., Fang, J., Jin, Y., Z. Wan, and M. Khalid, *Heat losses and thermal stresses of an external cylindrical water/steam solar tower receiver*. Applied Thermal Engineering, 2019. **163**: 114241.
20. Montoya, A., Rodríguez-Sánchez, M.R., J. López-Puente, and D. Santana, *Thermal stress variation in a solar central receiver during daily operation*. AIP Conference Proceedings, 2019. **2126**: 030038.
21. Pérez-Álvarez, R., Laporte-Azcué, M., A. Acosta-Iborra, and D. Santana, *Effect of eccentricity on the thermal stresses in a bayonet tube for solar power tower receivers*. AIP Conference Proceedings, 2019. **2126**, 030041.
22. Khanna, S., Sharma, V., Newar, S., T.K. Mallick, and P.K. Panigrahi, *Thermal stress in bimetallic receiver of solar parabolic trough concentrator induced due to non uniform temperature and solar flux distribution*. Solar Energy, 2018. **176**: p. 301–311.
23. Tripathy, A.K., Ray, S., S.S. Sahoo, and S. Chakrabarty, *Structural analysis of absorber tube used in parabolic trough solar collector and effect of materials on its bending: a computational study*. Solar Energy, 2018. **163**: p. 471–485.
24. Du, B., He, Y., Z. Zheng, and Z. Cheng, *Analysis of thermal stress and fatigue fracture for the solar tower molten salt receiver*. Applied Thermal Engineering, 2016. **99**: p. 741–750.
25. Wu, S., Luo, J., L. Xiao, and Z. Chen, *Effect of different errors on deformation and thermal stress of absorber tube in solar parabolic trough collector*. International Journal of Mechanical Sciences, 2020. **188**: 105969.
26. Zhou, H., Li, Y., Zuo, Y., Zhou, M., W. Fang, and Y. Zhu, *Thermal performance and thermal stress analysis of a 600 MWth solar cylinder external receiver*. Renewable Energy, 2021. **164**: p. 331-345.
27. Hibbeler, R.C., *Mechanics of materials*. 2018: 10e, Pearson Education.
28. American Society of Mechanical Engineers, 2010. ASME Boiler and Pressure Vessel Code II, part D: Properties (Metric) Materials. Tech. Rep., ASME, New York, USA.
29. Li, H., Hu, J., Li, J., G. Chen, and X. Sun, *Effect of tempering temperature on microstructure and mechanical properties of AISI 6150 steel*. J. Cent. South Univ., 2013. **20**: p. 866–870.
30. Kodur, V., M. Dwaikat, and R. Fike, *High-Temperature properties of steel for fire resistance modeling of structures*. Journal of Materials in Civil Engineering, 2010. **22**(5): p. 423-434.
31. Chandrupatla, T.R. and A.D. Belegundu, *Introduction to finite elements in engineering*. 2012: fourth edition, Pearson Education Limited.
32. Budynas, R.G. and J.K. Nisbett, *Shigley's mechanical engineering design*. 2011: ninth edition, McGraw-Hill
33. Zhang, Z., Qiao, Y., Sun, Q., C. Li, and J. Li, *Theoretical estimation to the cyclic strength coefficient and the cyclic strain-hardening exponent for metallic materials: preliminary study*. JMEPEG, 2009. **18**: 245–254.
34. ASME BPV Code, Section 8, Div 2, Table 5-110.1, 1998.
35. Beer, F.P., Johnston, E.R., J.T. Dewolf, and D.F. Mazurek, *Mechanics of materials*. 2015: SI 7th Ed., McGraw-Hill Education.
36. Fang, J., Zhang, C., Tu, N., J. Wei, and Z. Wan, *Thermal characteristics and thermal stress analysis of a superheated water/steam solar cavity receiver under non-uniform concentrated solar irradiation*. Applied Thermal Engineering, 2021. **183**: 116234.